ABSTRACT

Title of Dissertation: ANALOG–DIGITAL QUANTUM SIMULATIONS WITH TRAPPED IONS

Katherine S. Collins
Doctor of Philosophy, 2023

Dissertation Directed by: Professor Christopher Monroe
Department of Physics

Since its inception in the early 1920s, the theory of quantum mechanics has provided a framework to describe the physics of nature; or at least our interpretations about systems in nature. However, even though quantum theory works, the unsettling question of "why?' still remains. The field of quantum information science and technology (QIST) has brought together a collection of disciplines forming a united multidisciplinary collaborative effort towards realizing a large-scale quantum processor as an attempt to understand quantum mechanics better. It has been established in the field that the most efficient architectural design of this quantum processor would be composed of numerous individual quantum computers, quantum simulators, quantum networks, quantum memories, and quantum sensors that are "wired" together creating just the hardware layer in the full stack of the machine. Realizing a module-based quantum processor on such a macroscopic scale is an ongoing and challenging endeavor in itself.

However, existing noisy intermediate-scale quantum (NISQ) devices across all the quantum applications above are still worth building, running, and studying. NISQ quantum computers can

still provide quantum advantages over classical computation for given algorithms, and quantum simulators can still probe complex many-body dynamics that remain improbable to consider even on the best supercomputer. One such system is the trapped-ion quantum simulator at the center of this dissertation. Using $^{171}Yb^{+}$ ions, we expand our "analog" quantum simulation toolbox by incorporating "digital" quantum computing techniques in each of the three experiments presented in this work.

In the first experiment, we perform a quantum approximate optimization algorithm (QAOA) to estimate the ground-state energy of a transverse-field antiferromagnetic Ising Hamiltonian with long-range interactions. For the second project, we develop and demonstrate dynamically decoupled (DD) quantum simulation sequences in which the coherence in observed dynamics evolving under the unitary operator of the target Hamiltonian is extended while the known noise is suppressed. Finally, in the third project, we implement an experimental protocol to measure the spectral form factor (SFF) and its generalization, the partial spectral form factor (PSFF), in both an ergodic many-body quantum system and in a many-body localized (MBL) model. As a result, a quantum simulator can be utilized to test universal random matrix theory (RMT) predictions, and simultaneously, probe subsystem eigenstate thermalization hypothesis (ETH) predictions of a quantum many-body system of interest.

ANALOG–DIGITAL QUANTUM SIMULATIONS WITH TRAPPED IONS

by

Katherine S. Collins

Dissertation submitted to the Faculty of the Graduate School of the
University of Maryland, College Park in partial fulfillment
of the requirements for the degree of
Doctor of Philosophy
2023

Advisory Committee:
Dr. Christopher Monroe, Chair/Advisor
Dr. Zohreh Davoudi
Dr. Alexey Gorshkov
Dr. Christopher Jarzynski
Dr. Qudsia Quraishi

© Copyright by
Katherine S. Collins
2023

Dedication

For my mother, Lisa

Acknowledgments

I am truly grateful to Chris Monroe for introducing me to the quantum systems of trapped ions as an undergraduate freshman. I appreciate your continued support in allowing me to pursue research in your group after deciding to stay at UMD for graduate school. This experience has given me the opportunity to develop the skills needed as a researcher and to further my knowledge of trapped ion systems in the quantum information field.

In regards to my work in the lab, QSIM, I would like to say a special thanks to our post-doc Will Morong and fellow graduate student Arinjoy De. I appreciate your all-hands-on-deck approach in keeping the experiment running and collecting the necessary data for the spectral form factor project.

To Allison Carter, Wen Lin Tan, and Crystal Noel I enjoyed your friendship and mentoring in navigating the complexities of pursuing a Ph.D. as a woman in the field of physics.

I also want to thank all of the members of the Trapped Ion Quantum Information group, both current and past, for their help, and for taking the time to answer the countless physics questions I pestered you with. It was a fantastic experience working with you all.

To my good and longtime friend, Emily Ackerman, thank you for your support and for being there at a moment's notice. Thank you to David, Sherry, and my extended family, for being in my life and providing friendship over the years.

Most of all, thank you to my Mom. I am grateful for all of the opportunities, the endless

support, and the love you have given me. I am lucky to have been adopted by you and that you became my Mom. In the ultimate roll of the dice, you refused the Welfare Institute's effort to swap me out for a "healthy girl" instead choosing to stick with the "sick one."

Table of Contents

Dedication ii

Acknowledgements iii

Table of Contents v

List of Tables viii

List of Figures ix

List of Abbreviations xi

Chapter 1: Introduction 1
- 1.1 Trapped Ion Quantum Simulators . . . 4
- 1.2 Outline . . . 5

Chapter 2: Ytterbium Ions 9
- 2.1 Continuous Wave Lasers Required for $^{171}Yb^{+}$ . . . 14
  - 2.1.1 Photoionization . . . 15
  - 2.1.2 Repumping Light . . . 16
  - 2.1.3 Doppler Cooling . . . 17
  - 2.1.4 Optical Pumping . . . 19
  - 2.1.5 Detection . . . 20
- 2.2 The CW Lasers . . . 22
  - 2.2.1 399 nm Optical Path . . . 23
  - 2.2.2 935 nm Optical Setup . . . 24
  - 2.2.3 369 nm Beam Paths . . . 26
  - 2.2.4 739 nm Laser . . . 28
- 2.3 Trapping Our Friends the Ions . . . 43
- 2.4 Difficulty in Loading Ions Troubleshooting . . . 45

Chapter 3: Components of the Experimental System 46
- 3.1 Ion Trap and Vacuum Chamber . . . 46
- 3.2 Coherent Manipulation via Stimulated Raman Transitions . . . 55
  - 3.2.1 Carrier Transitions . . . 58
  - 3.2.2 Sideband Transitions . . . 58
  - 3.2.3 Resolved Sideband Cooling . . . 60

3.3 Mølmer-Sørenson Interaction to the Long-Range Ising Model . . . 61
3.3.1 Tuning J_{ij} to Change α . . . 65
3.4 355 nm Pulsed-Laser . . . 66
3.4.1 Beam-Pointing Stabilization . . . 69
3.4.2 Individual Addressing Beam . . . 72
3.5 Experimental Control Program . . . 77
3.5.1 Calibrating the Individual Addressing Beam . . . 79

Chapter 4: A Hybrid Quantum-Classical Algorithm 86
4.1 Quantum Approximate Optimization Algorithm . . . 87
4.2 The QAOA Protocol and Experimental Implementation . . . 88
4.3 $p=1$ QAOA . . . 92
4.3.1 $p=1$ QAOA Exhaustive Search . . . 94
4.3.2 $p=1$ QAOA System Size Performance . . . 95
4.4 $p=2$ QAOA Exhaustive Search . . . 96
4.5 Closed-Loop QAOA Gradient Descent Search . . . 98
4.6 QAOA Sampling . . . 101
4.7 Summary of the QAOA Experiment . . . 104

Chapter 5: Dynamically Decoupling Quantum Simulations 105
5.1 Dynamical Decoupling . . . 105
5.2 Principles of Dynamical Decoupling . . . 106
5.3 Implementing DD Sequences in QSim . . . 110
5.4 Application to Trapped Ions and Example Sequences . . . 112
5.4.1 Example 1: A CMPG Sequence . . . 114
5.4.2 Example 2: A XY Sequence . . . 115
5.4.3 Example 3: A Decoupled Heisenberg Model . . . 116
5.5 Two-Ion Tests of Pulse-Sequence Parameters . . . 117
5.5.1 Pulse Shaping . . . 120
5.5.2 Drive Rate . . . 121
5.5.3 Detuning . . . 123
5.5.4 Noise Model . . . 123
5.6 Multi-Ion Dynamically Decoupled Realizations . . . 125
5.6.1 11 Ion Dephasing Suppression . . . 126
5.6.2 Realizing an Approximate Haldane-Shastry Model . . . 128
5.7 Summary: Adding Dynamical Decoupling to the Simulation Toolbox . . . 135

Chapter 6: Spectral Form Factor 137
6.1 What is the Spectral Form Factor? . . . 137
6.2 Characteristic Properties of the SFF and PSFF . . . 139
6.3 Proposed Protocol and Requirements for Measuring SFF and PSFF . . . 141
6.3.1 Estimators of the SFF and PSFF Observables . . . 143
6.3.2 General Requirements . . . 143
6.4 Two Methods to Rescale the Raw Data from Decoherence Errors . . . 145
6.4.1 Imperfections from U and $U^\dagger$ . . . 146

6.4.2 Imperfections During $T(t)$ . . . 147
6.5 Implementing the SFF Sequence in QSim . . . 149
6.5.1 Implementing and Testing the Individual RUs . . . 153
6.5.2 Implementing Local Random Disorders . . . 165
6.5.3 SFF Purity Sequence and Calculating the Purity . . . 167
6.6 $N=5$ SFF . . . 170
6.7 Variations of the Purity Sequence . . . 171
6.8 $N=4$ SFF Results . . . 178
6.8.1 Disorder-Averaged Ergodic SFF . . . 179
6.8.2 Disorder-Averaged Localized SFF . . . 181
6.8.3 Single-Disorder Localized SFF . . . 182
6.9 Summary . . . 183

Bibliography 187

List of Tables

2.1 Isotopes of neutral Ytterbium 9
2.2 Some angular momentum quantum numbers 10
2.3 Iodine VCO control signal parameters 43

3.1 Static voltage parameters 53

4.1 $N = 20$ QAOA exhaustive search performances 98

5.1 Signs of uniform magnetic field terms for Hamiltonians in XY sequence 116

6.1 LabView SFF sequence 152
6.2 Measure X, Y, Z experimental sequences 161
6.3 LabView state overlap sequence 165
6.4 LabView purity sequence 168

List of Figures

2.1 $^{171}Yb^{+}$ energy level diagram . . . 13
2.2 369 nm Doppler cooling transitions . . . 18
2.3 369 nm optical pumping transitions . . . 19
2.4 369 nm detection transitions . . . 21
2.5 Optical paths of $^{171}Yb^{+}$ CW lasers . . . 22
2.6 399 nm optical path . . . 23
2.7 935 nm optical path . . . 25
2.8 369 nm optical path . . . 27
2.9 739 nm beam path . . . 30
2.10 PDH current and grating locks . . . 34
2.11 Iodine SAS optical setup . . . 35
2.12 Feature 5 of the iodine error signal . . . 37
2.13 Feature 4 of the iodine error signal . . . 40
2.14 Iodine AOM RF source signal comparison . . . 42
2.15 CW optics right before the chamber . . . 44

3.1 QSim vacuum chamber . . . 47
3.2 The QSim ion trap . . . 50
3.3 Iseg LabView control program . . . 52
3.4 Λ system . . . 56
3.5 355 nm optics outside of Raman enclosure . . . 68
3.6 Beam-pointing optical system . . . 72
3.7 Raman beam paths . . . 72
3.8 Individual addressing beam path, part 1 . . . 75
3.9 Individual addressing beam path, part 2 . . . 76
3.10 Pulse sequence experiment control window . . . 78
3.11 Individual addressing beam calibrations with one ion . . . 80
3.12 Single ion Stark shift versus AWG amplitude . . . 81
3.13 Camera calibration for $N=4$ ions using the experimental control program . . . 82
3.14 AOD frequency scan with $N=4$ ions . . . 83
3.15 Calibrating the individual Stark shift applied to each ion . . . 85

4.1 QAOA experimental sequence . . . 90
4.2 QAOA $p=1$ example energy landscape . . . 93
4.3 $N=20$ QAOA $p=1$ exhaustive search performance landscape . . . 94
4.4 QAOA $p=1$ performance as a function of system size . . . 95
4.5 $N=20$ QAOA $p=2$ exhaustive search . . . 97

4.6 $N=12$ QAOA $p=1$ gradient search . . . 99
4.7 $N=20$ QAOA $p=1$ gradient search . . . 100
4.8 Sampling from $p=1$ QAOA . . . 103

5.1 Generalized decoupling sequence for quantum simulation . . . 108
5.2 An example of dynamical decoupling for a two-ion interaction . . . 119
5.3 Dependence of dynamical decoupling pulse sequence parameters . . . 122
5.4 Relative contribution of the error terms in noise model . . . 125
5.5 Performance of many-body Hamiltonian evolution without and with dynamical decoupling . . . 127
5.6 Generalized imbalance comparison . . . 128
5.7 Quantum simulation of the approximate Haldane-Shastry model . . . 131
5.8 Haldane-Shastry numerics with decoherence . . . 132
5.9 Additional Haldane-Shastry data . . . 133
5.10 Modified Haldane-Shastry sequence results . . . 134

6.1 Uniform sampling of θ and ϕ but nonuniform distribution of points on a sphere . . . 156
6.2 Defined random angle functions . . . 156
6.3 Uniform sampling of points on the Bloch sphere . . . 157
6.4 Converting random Stark shifts to AWG amplitudes . . . 159
6.5 Converting Stark shifts to corresponding AWG amplitudes . . . 160
6.6 Individual ion average measure x, y, z results . . . 163
6.7 RU ensemble average connected correlations . . . 163
6.8 Individual ion average state overlap scan . . . 166
6.9 Converting random disorder strengths to AWG amplitudes . . . 166
6.10 $N=5$ ergodic SFF . . . 170
6.11 $N=5$ ergodic average subsystem size PSFF . . . 171
6.12 $N=5$ individual ion average fidelity . . . 172
6.13 $N=5$ ergodic SFF purity . . . 172
6.14 $N=5$ ergodic SFF purity sequence z-magnetizations . . . 174
6.15 Average z-magnetizations of dark product state . . . 175
6.16 Average z-magnetizations of bright product state . . . 175
6.17 Average z-magnetizations of arbitrary product state . . . 176
6.18 Average z-magnetizations of SFF purity sequence with only random disorders . . . 177
6.19 Average z-magnetizations of SFF purity sequence with only global interactions . . . 177
6.20 Average z-magnetizations of SFF purity sequence with only global interactions take two . . . 178
6.21 $N=4$ dynamically decoupled results . . . 179
6.22 $N=4$ ergodic disorder-averaged average subsystem size PSFF . . . 180
6.23 $N=4$ ergodic SFF purity and individual ion average fidelity. . . . 181
6.24 $N=4$ localized disorder-averaged average subsystem size PSFF . . . 182
6.25 $N=4$ localized disorder-averaged SFF purity . . . 183
6.26 $N=4$ localized single-disorder unitary-averaged average subsystem size PSFF . . . 184
6.27 $N=4$ localized single-disorder SFF purity . . . 185

List of Abbreviations

AC	Alternating Current
AHT	Average Hamiltonian Theory
AMO	Atomic Molecular and Optical
AOD	Acousto-Optic Deflector
AOM	Acousto-Optic Modulator
AWG	Arbitrary Waveform Generator
BSB	Blue Sideband
BS	Beam Splitter
BW	Bandwidth
CA	Central Average
CD	Central Difference
CPMG	Carr-Purcell-Meiboom-Gill
COM	Center-of-Mass
CW	Continuous Wave
DAC	Digital-to-Analog Converter
DC	Direct Current
DD	Dynamical Decoupling
EA	End Average
ECDL	External Cavity Diode Laser
EMCCD	Electron Multiplying Charge-Coupled Device
ENVD	End Near Vertical Difference
EOM	Electro-Optic Modulator
ETH	Eigenstate Thermalization Hypothesis
FM	Frequency Modulation
FP	Fabry-Perot
FPGA	Field-Programmable Gate Array
FWHM	Full Width Half Maximum
GR(s)	Global Rotation(s)
HV	High Voltage

HWP Half-Wave Plate

MBL Many-Body Localization
MS Mølmer-Sørensen

NA Numerical Aperture
NISQ Noisy Intermediate-Scale Quantum
NMR Nuclear Magnetic Resonance

PBS Polarizing Beam Splitter
PDH Pound Drever Hall
PID Proportional Integral Differential
PM Phase Modulation
PMT Photo-Multiplier Tube
PSFF Partial Spectral Form Factor

QAOA Quantum Approximate Optimization Algorithm
QIST Quantum Information Science and Technology
QWP Quarter-Wave Plate

RD(s) Random Disorder
RF Radio Frequency
RMT Random Matrix Theory
RSB Red Sideband
RU(s) Random Unitary
RWA Rotating-Wave Approximation

SAS Saturated Absorption Spectroscopy
SB(s) Sideband(s)
SBC Sideband Cooling
SD Standard Deviation
SEM Standard Error of the Mean
SFF Spectral Form Factor
SHG Second Harmonic Generation
SIR(s) Single Ion Rotation(s)
SM Supplementary Material
SS(s) Stark Shift(s)

TA Tapered Amplifier
TTL(s) Transistor-Transistor Logic
TVD Total Variation Distance

UHV Ultra High Vacuum
UV Ultra-violet

VQE Variational Quantum Eigensolver
VCA Voltage-Controlled Amplifier
VCO Voltage-Controlled Oscillator

XHV Extreme High Vacuum

Yb Ytterbium

Chapter 1: Introduction

The field of quantum information science brings together the disciplines of physics, engineering, computer science, mathematics, and information science all in the pursuit of understanding quantum mechanics.Since multiple areas of study are involved in this quest, there are, of course, many different questions that exist and numerous research avenues to explore. The common "object" that is shared amongst all fields involved is a *large-scale quantum computer*.

The physics that describes a quantum computer is the theory of quantum mechanics which describes the physics of particles (molecules, atoms, electrons, protons, neutrons, etc.) and photons (light) at a microscopic scale as opposed to the theory of classical mechanics that governs the physics of macroscopic objects. As my research advisor (Chris Monroe) says, "There are two rules in quantum physics. (1) Everything is a wave and can exist in superposition, (2) until you look and then, the system randomly assumes a definite state." The first rule refers to the fact that a particle (assumed to be in a quantum system) at some time t is described by its wavefunction $|\psi(t)\rangle$ that corresponds to single quantum state or occupying several quantum states simultaneously, also known as *a quantum superposition*. However, when the particle's state is measured, the quantum superposition is destroyed, and the particle will be measured in only one of the possible states. Rule 1 highlights the "quantumness" of the particle existing in more than one state at time t which under classical physics is physically impossible. Rule 2 summarizes two concepts

in quantum physics. The first is that the act of measuring the quantum system (the particle) collapses the wavefunction such that the particle is detected in only a single state which reassuringly agrees with classical expectations. Second, measurements in quantum systems are probabilistic in nature. There exists uncertainty in the measurement, an associated probability in measuring the particle in a given state. Because of the uncertainty in the measurement, the inability to place the result in context, multiple measurements must be made (assuming the quantum particle can be prepared in the same state $|\psi(t)\rangle$, which we will assume that it can) of the particle's wavefunction $|\psi(t)\rangle$ at time t, forming a probability distribution of the measured outcomes.

Keeping these two rules of quantum physics in mind, let us return to the discussion of a *quantum computer*. A quantum computer is the quantum version of the "classical" computer. Computers encode information in computer bits: 0s and 1s. In a similar fashion, a quantum processor encodes its quantum information in quantum bits, or *qubits*. Unlike a classical bit, a qubit can be in a superposition of $|0\rangle$ *and* $|1\rangle$, in addition to occupying only $|0\rangle$ or only $|1\rangle$. A qubit can be any two-state quantum system in which information between the qubit states can be accessed. The strength of a quantum processor is demonstrated when the size of the quantum system consists of N qubits. For N qubits, there are 2^N quantum states in which quantum information can be stored due to the property of quantum superposition and something called *quantum entanglement* can be generated which is still a process to be understood. In comparison, a classical computer would need 2^N bits to store just the information whereas the storage capabilities already exist in a system of N qubits. However, having an isolated system of N qubits is different from performing a set of coherent operations on the N qubits for a long enough time while minimizing any unwanted disturbances or decoherence to the system.

The quantum computer and quantum simulator are very similar in foundation; however, a

quantum computer has universal control, access to any quantum state, while a quantum simulator is restricted in the types of operations that can be performed. Both represent quantum systems with realizable qubits that can be well-controlled, coherently manipulated, and measured. On a quantum computer, a series of quantum gates similar to classical computer gates are executed in order to realize a specific quantum algorithm or procedure. The quantum circuit picture often comes to mind in which each qubit is placed on its own row connected to a wire. The wires are connected to different gates or operations allowing the quantum information to flow through the circuit before a measurement is made. This description is similar to boolean operations that might be executed on a computer processor. However, in quantum simulators, interactions described by a Hamiltonian are applied to the qubits in which the dynamics are allowed to evolve for varying amounts of time before measuring the system.

The quest of developing a large-scale quantum computer is still an ongoing process. Many technical challenges exist when designing a quantum processor large enough that can run the already identified algorithms in which a quantum system outperforms the current classical supercomputer. An early question proposed in the quantum information science community was whether it would be better to create one large quantum device or connect together many smaller devices. I believe it has been answered. The modular approach seems to be the way to go for many reasons that are not discussed here. Another question still remains regarding whether the quantum architecture should be based only on a specific quantum platform that has already been demonstrated at a smaller scale or on a combination of different quantum systems. The jury is still out on that verdict. Regardless, there is still much of work to be done to realize fully a useful large-scale quantum processor. Not only is there the needed improvement of the performances of existing quantum platforms in what has been coined noisy intermediate-scale quantum (NISQ)

devices [1], there is also the question of the connection to the different modular systems. Many experiments exist that examine quantum communication and networking in which the qubit is entangled with an information bus or carrier of the information such as a photon, a phonon or some other degree of freedom. Experiments have already demonstrated the *quantum teleportation* of information rather than matter and have shown that quantum information can be sent and received between different modules that are not physically connected; assuming that there was prior interaction and classical communication between the modules.

Despite the ongoing quest for the creation a large-scale quantum processor and determining useful applications for the device to run, there still remain the current NISQ-era quantum computers and simulators. Several experimental platforms exist in which qubits can be realized: trapped ions, ultra-cold neutral atoms, Rydberg atoms, superconducting transmons, solid-state nitrogen-vacancy centers in diamond, photon-coupled cavity systems, as well as possibly-to-be-determined topological qubits or further experimental development of vibrational modes of molecules. There are pros and cons (or challenges) for each of these systems. However, the quantum platform of interest in this dissertation focuses on trapped-ion qubits.

1.1 Trapped Ion Quantum Simulators

Experiments using trapped ions for quantum information processing have been in existence for over three decades and counting. There are many ion species that can be chosen: Beryllium (Be^+), Magnesium (Mg^+), Calcium (Ca^+), Strontium (Sr^+), Barium (Ba^+), Zinc (Zn^+), Cadmium (Cd^+), Mercury (Hg^+), Boron (B^+), Aluminum (Al^+), Gallium (Ga^+), Indium (In^+), Thallium (Tl^+), Ytterbium (Yb^+), and Lutetium (Lu^+). The research presented in this disser-

tation focuses on using trapped $^{171}Yb^{+}$ ions as the qubits in a quantum simulator. The atomic structure of $^{171}Yb^{+}$ makes it a good qubit candidate. The large fine-structure splitting of the P-orbital excited states and the large hyperfine splitting between different F levels in the atom's ground state level are well suited for both coherent and incoherent manipulation of its internal states.

1.2 Outline

The experimental apparatus at the heart of this dissertation is the trapped-ion quantum simulator system in Chris Monroe's Trapped Ion Quantum Information group originally located in the Atlantic Building on the University of Maryland, College Park campus. The current experimental system has been well documented in recent dissertations, [2] and [3], which includes the presentation of the redesign of the Raman optical setup. This dissertation will talk a little bit more about the quadrant photodetector and the output voltage amplifying gain circuits that were designed for the active stabilization of the lateral beam-pointing of the Raman beams at the plane of the ions.

In addition, this dissertation presents three different quantum simulation experiments realized in QSim. The brief topics of the three projects are in order: (1) implementing a quantum approximate optimization algorithm (QAOA) in order to estimate the ground-state energy of a transverse field antiferromagnetic Ising Hamiltonian with long-range interactions; (2) developing and demonstrating dynamically decoupled (DD) quantum simulation sequences to extend the coherence of the intended simulation Hamiltonian dynamics; and (3) implementing the experimental sequence measuring the spectral form factor (SFF) as well as its generalization, the

partial spectral form factor (PSFF), in different types of many-body systems and demonstrating the feasibility of incorporating both of these observables into the quantum simulation toolbox which can be used directly to probe predictions of random matrix theory (RMT) and predictions from the eigenstate thermalization hypothesis (ETH). Although all three of these experiments are still evolving the quantum spin system under a Hamiltonian, aspects from quantum computations arise in both. "Digital" operations on individual ions are interwoven with the "analog" time evolution of the Ising-like Hamiltonians in the last project while the quantum circuit representation of the experimental sequence is present in all three projects. By this statement, I mean that the Hamiltonian interactions are segmented into chunks of operations as opposed to a continuous quench. Also, the third project utilizes the individual addressing beam to incorporate methods from the random operation toolbox instead only being used for state preparation. The SFF project has tested the QSim apparatus like no other in both experimental complexity of the implementation as well as the computational demands on the compiling of the waveforms. The SFF project is an example of some of the challenges that must be faced in order to create a large-scale quantum module-based processor.

Chapter 2 begins by introducing the Ytterbium atom and its 171-isotope ion, $^{171}Yb^{+}$. The qubit states and the energy levels are presented leading to an overview of how the internal energy levels of $^{171}Yb^{+}$ ions can be controlled and manipulated. The different continuous-wave lasers are introduced which are a crucial component to address the trapped-ion system. In context to $^{171}Yb^{+}$ ions, laser cooling, state preparation, and state-dependent detection of the qubit states are discussed as well as their corresponding experimental implementation for the trapped-ion quantum simulator.

Chapter 3 presents the other components of the experimental system which combined make

up a tunable quantum simulator of trapped $^{171}Yb^{+}$ ions. The vacuum chamber and its history are briefly introduced before discussing the important ingredients housed inside the chamber: the linear RF Paul trap and the atomic sources of neutral Yb. Following the ion trap design and features, we break take a break from the physical implementation of the experiment to discuss the physics of the atom-laser interactions describing coherent manipulation of a single ion's qubit states. Generalizing the coherent control from one ion to N ions, spin-spin interactions are derived in which the collective transverse modes of motion are coupled to the internal degrees of freedom to create what is called the long-range antiferromagnetic Ising Hamiltonian. After introducing the atom-laser interactions, the quantum simulation toolbox of Hamiltonian terms is presented since it provides background for the experiments presented in Ch. 4, Ch. 5, and Ch. 6. In the remaining sections of Ch. 3, the experimental setups for realizing the coherent interactions are presented as well as the experimental control software interface connecting all the optical and electrical components together.

Chapter 4 demonstrates the first implementation of using QAOA to approximate the ground-state energy specifically of a transverse-field antiferromagnetic long-range Ising Hamiltonian. Focusing on this quantum many-body Hamiltonian, the scaling of the optimal QAOA performance is investigated in both the number of layers of the routine and the number of ions in the system. In addition, both a brute-force approach and a closed-loop gradient descent was used in experimentally determining the optimal QAOA variational parameters. Lastly, QAOA was used to sample the optimized solution to a classical combinatorial problem in which it has already been proved to be inefficient to realize by a computer.

Chapter 5 develops a general strategy for dynamically decoupling (DD) a quantum simulation experiment from a known error while preserving the intended coherent interactions of

the quantum many-body system that are described by the unitary operator of the desired target Hamiltonian. We demonstrate this technique on our trapped-ion quantum simulator in which AC Stark shift noise is identified as the primary cause of decoherence observed in the measured time-evolved dynamics. With a multi-ion system evolving under the simple long-range Ising Hamiltonian, we experimentally demonstrate that our method can suppress the noise and, in fact, extend the coherence of the time-evolved dynamics by more than a factor of 5 in comparison to coherence observed in the non-decoupled sequence. Lastly, combining of dynamical decoupling technique with Floquet Hamiltonian engineering, we realize an approximate Haldane-Shastry model that would be difficult to simulate without the decoupling.

Chapter 6 lastly implements a proposal for measuring the SFF and PSFF of the time-evolution operator for two known types of quantum many-body spin models: an ergodic system and a many-body localized (MBL) one. Both the SFF and PSFF observables will be explained and how they are related to RMT and ETH. This experiment is a prime example of the "analog-digital" quantum simulation in which single-ion operations are applied not only for state preparation but also as part of the Hamiltonian interactions that we wish to simulate. Combining methods from the random measurement toolbox, we demonstrate that universal predictions of RMT and properties of ETH properties can be probed experimentally. These demonstrations will expand the quantum simulation toolbox of today's current quantum simulators.

Chapter 2: Ytterbium Ions

The atom of choice for the trapped-ion system discussed in this dissertation is Ytterbium (Yb). Yb is a lanthanide rare-earth metal whose atomic number is $Z = 70$ and whose ground-state electron configuration is $[\mathrm{Xe}]\, 4f^{14}\, 6s^2$. As seen in Table 2.1, neutral Yb has seven stable isotopes [4]. Five of these isotopes have a spinless nucleus while the other two isotopes have a nonzero nuclear spin. We primarily trap Ytterbium-171 ions ($^{171}\mathrm{Yb}^{+}$); however, Ytterbium-174 ions ($^{174}\mathrm{Yb}^{+}$) can also be trapped as well under given circumstances that are discussed in Sec. 2.4. The significance in writing out the electron configuration for the ground state of the

Isotope	**Abundance (%)**	**Nuclear Spin (I)**
168	0.13	0
170	3.05	0
171	14.30	1/2
172	21.90	0
173	16.12	5/2
174	31.80	0
176	12.70	0

Table 2.1. Isotopes of neutral Ytterbium. The isotopes of Yb are listed in ascending order. The natural abundance and the spin of the nucleus, represented by the quantum number I, are specified for each of the seven isotopes. The natural abundance values listed in the table are from [4].

neutral atom, Yb, is to highlight the similarities in the atomic structure of a $^{171}\mathrm{Yb}^{+}$ ion to that of a Hydrogen (H) atom. In fact, if one disregards the principal number quantum number n, then

the low-energy electronic states in $^{171}Yb^{+}$ ions are labeled by the exact same quantum numbers as that of Hydrogen, obviously, with different hyperfine splittings.

The electronic states (or internal energy levels) of an atom are usually denoted by "good" quantum numbers which provide a complete description of the atom's angular momentum. Table 2.2 defines some of these different quantum numbers and the corresponding total angular momentum vector operator. In addition to the quantum numbers listed in Table 2.2, there are "mag-

Quantum Number	**Angular Momentum Quantity**
F	magnitude of the total atomic angular momentum $\vec{F}$ of the atom
I	magnitude of the nuclear spin $\vec{I}$
J	magnitude of the total electronic angular momentum $\vec{J}$
L	magnitude of the total electronic orbital momentum $\vec{L}$
S	magnitude of the total electronic spin $\vec{S}$

Table 2.2. Some angular momentum quantum numbers. Often, the internal energy states of an atom are specified by a set of "good" quantum numbers that are simultaneous eigenstates of the corresponding angular momentum operators.

netic" or Zeeman quantum numbers corresponding to the spatial component of the total angular momentum vector that is parallel to the direction of an externally applied magnetic field $\vec{B}_{ext}$. Typically, these magnetic quantum numbers are defined as the z-component of the relavent total angular momentum vector. For example, quantum number m_F corresponds to the z-component of the atom's total angular momentum, $\vec{F}_z$ which is better defined in the presence of an magnetic field. In general, the internal states of an atom with hyperfine structure are denoted by $|F,\, m_F\rangle$ and their associated energy level (or orbital shell) that is, usually, denoted by the Russel-Saunders term symbol without the principal quantum number n, i.e. $^{2S+1}L_J$. This is the notation that is adopted for this dissertation when discussing the atomic structure of $^{171}Yb^{+}$ ions unless explicitly

stated otherwise.

A $^{171}\mathrm{Yb}^{+}$ ion has a nuclear spin of $I=1/2$ and, together with its unpaired valence electron that has a spin angular momentum of $S=1/2$, gives rise to the hyperfine structure of its internal energy levels. As a result, the fine structure $6\,^2\mathrm{S}_{1/2}$ ground state for even-isotope Yb^{+} ions is split into two $6\,^2\mathrm{S}_{1/2}$ hyperfine ground states, $|F=0\rangle$ and $|F=1\rangle$, for $^{171}\mathrm{Yb}^{+}$ ions. The quantum number $F=I+J$ denotes the total angular momentum of the atom due to the hyperfine interaction between the nucleus and the electron $(\vec{F}\propto\vec{I}\cdot\vec{J})$ where $J=L+S$ is the total angular momentum of the electron and L is its orbital angular momentum. From principles governing the addition (or coupling) of angular momenta [5], each hyperfine level with quantum number F has $(2F+1)$ sublevels or Zeeman states denoted by "magnetic" quantum number m_F whose value, typically, corresponds to the magnitude of $\vec{F}_z$, the z-component of the atom's total angular momentum vector operator. In the absence of an externally applied magnetic field, Zeeman sublevels with the same F are degenerate in energy. Thus, the $^2\mathrm{S}_{1/2}\ |F=1\rangle$ hyperfine ground state has three Zeeman (sub)levels, $m_F=-\{1,0,1\}$, whereas the $^2\mathrm{S}_{1/2}\ |F=0\rangle$ hyperfine ground state remains a singlet with $m_F=0$. The degeneracy within each hyperfine manifold is easily lifted by applying an external magnetic field that occurs due to the Zeeman effect.

In the presence of an external magnetic field, $\vec{B}_{ext}=B_{ext}\hat{z}$, Zeeman levels within the same F-manifold experience an energy shift, or a Zeeman shift away from the energy eigenstates at zero-field, also known as the *Zeeman effect*. When the interaction between the atom's magnetic dipole moment and the external magnetic field is much weaker than the hyperfine interaction between the nucleus and the electron, $-\hat{\vec{\mu}}_m\cdot\vec{B}_{ext}\ll$, the degeneracy of the Zeeman sublevels within the same F manifold is lifted and F, m_F, I, and J are still good quantum numbers that describe the electronic states of the atom. In this weak-field limit, sublevels with nonzero m_F

numbers experience a first-order correction to their zero-field energies:

$$\Delta E_{\text{Zeeman}} = \mu_B g_F m_F |\vec{B}_{ext}|, \tag{2.1a}$$

$$g_F = g_J \frac{F(F+1) + J(J+1) - I(I+1)}{2F(F+1)}, \tag{2.1b}$$

$$g_J = 1 + \frac{J(J+1) + S(S+1) - L(L+1)}{2J(J+1)}. \tag{2.1c}$$

In Eq. (**??**), $\mu_B \equiv e_0\hbar/(2m_e)$ is the Bohr magneton [6] with elementary charge e_0 and electron mass m_e, g_F is the Landé g-factor [7] for hyperfine structure defined in Eq. (2.1b), and m_F is the total atom angular momentum component parallel to the direction of external field with magnitude B_{ext}. For example, the $\Delta m_F = \pm 1$ Zeeman splittings of the $^2\mathrm{S}_{1/2}$ $|F=1\rangle$ sublevels corresponds to $\mu_B/\hbar = \pm 1.4$ MHz/Gauss. In comparison, the two $m_F = 0$ hyperfine ground states are first-order magnetic-field insensitive and do not experience a first-order Zeeman shift. Instead, the lowest-order Zeeman correction to the qubit hyperfine splitting is a second-order term,

$$\delta_{2Z} = 310.8 \times B_{ext}^2, \tag{2.2}$$

where B_{ext} is the magnitude of the applied magnetic field in Gauss (1 Gauss$=1\times10^{-4}$ Tesla) corresponding to a total hyperfine qubit splitting of $\omega_{hf}/(2\pi) = 12.642812118466 + \delta_{2Z}$ GHz [8]. This large separation in the $^2\mathrm{S}_{1/2}$ $m_F=0$ states as well as other desired properties of the atomic structure of $^{171}\mathrm{Yb}^+$ (see Fig. 2.1) which will be discussed shortly, allow us to define an effective two-level spin-1/2 system in each trapped ion. The $^{171}\mathrm{Yb}^+$ hyperfine qubit states are defined in the $^2\mathrm{S}_{1/2}$ ground-state manifold as:

$$|0\rangle \equiv |\downarrow\rangle \equiv |\downarrow\rangle_z \equiv \left|^2\mathrm{S}_{1/2}\, F=0, m_F=0\right\rangle, \tag{2.3a}$$

$$|1\rangle \equiv |\uparrow\rangle \equiv |\uparrow\rangle_z \equiv \left|^2\mathrm{S}_{1/2}\, F=1, m_F=0\right\rangle. \tag{2.3b}$$

Resonant transitions between these qubit states can conveniently be addressed by a ∼12.6 GHz

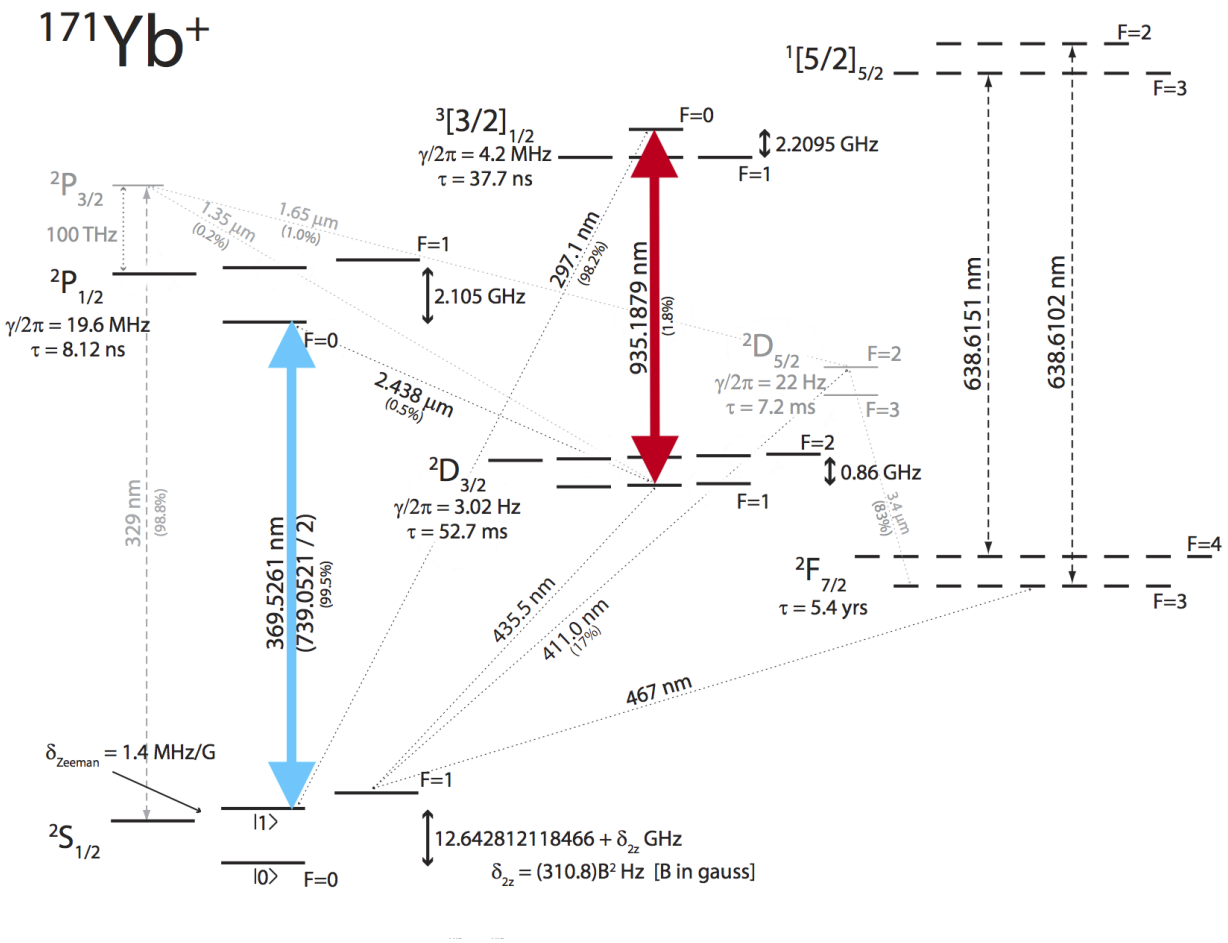


Figure 2.1. $^{171}Yb^{+}$ energy level diagram. This diagram displays an extensive energy levels in $^{171}Yb^{+}$ The atomic transitions between different hyperfine states are given with respect to wavelength of the optical light while the hyperfine splitting between different F quantum numbers (within each energy level) is specified by a (linear) frequency. The magnitude of the Zeeman shift with respect to the externally applied magnetic field strength (MHz/G) for the $^{2}S_{1/2}$ $|F=1,\ m_F=\pm1\rangle$ levels are also displayed. Lastly, the blue and red arrows denote the primary electric dipole transitions that we drive with the 369 nm and 935 nm lasers, respectively.

microwave source or by way of two-photon processes called stimulated Raman absorption and emission. In QSim, we use two 355 nm pulsed-laser beams to transfer the population coherently between the two qubit states. Further discussion about these stimulated Raman transitions and the way they are experimentally implemented are discussed in the next chapter, Ch. 3.

However, before we discuss the atom-laser interactions describing the coherent manipula-

tion of the qubit, we first present the required fundamental optical processes that enable basic control and manipulation of $^{171}Yb^{+}$ ions: laser cooling, state initialization, and state detection. In addition, photoionization of neutral Yb is also presented along with the other three processes in the next section.

2.1 Continuous Wave Lasers Required for $^{171}Yb^{+}$

As observed in Fig. 2.1, the atomic transitions between different energy levels of $^{171}Yb^{+}$ can be addressed by shining the appropriate optical wavelength of light on the ion. Fortunately, continuous-wave (CW) lasers at the wavelengths—λ =369 nm, λ =399 nm, λ =935 nm—are all now commercially available. The processes and atomic transitions that these three lasers drive are summarized next.

The 399 nm and 369 nm lasers are used to generate Yb^{+} ions from neutral Yb atoms through a two-step photoionization method [9]. Conveniently, the 369 nm laser also happens to be the wavelength of the light to laser cool the thermal average motion of these "hot" ions. The 369 nm laser addresses the main electric dipole transition in $^{171}Yb^{+}$ that connects the $^{2}S_{1/2}$ ground states to the $^{2}P_{1/2}$ first-excited states. Utilizing this nearly-closed cycling transition, we can Doppler cool the ions in their electronic ground states, optically pump the ions to prepare an initial product state of all spins down, and detect each qubit's state using a state-dependent protocol. Collected photons are imaged on an electron multiplying charge-coupled device (EMCCD), also known as a camera, or counted on a photomultiplier tube (PMT). The phrase "nearly-closed cycling transition" refers to the $\sim$0.005 branching ratio in which there exists a 0.5% probability that population in the $^{2}P_{1/2}$ state will decay to the metastable $^{2}D_{3/2}$ level instead of to the

$^2S_{1/2}$ level [10]. The lifetime of the $^2D_{3/2}$ level is $\tau_{D_{3/2}}$=52.7 ms [11] which is about $\sim 6\times10^6$ times longer than the lifetime of the $^2P_{1/2}$ state which is $\tau_{P_{1/2}}$=8.12 ns [12]. As a result, we use the 935 nm laser to repopulate (or repump) any population that has spontaneously decayed into the $^2D_{3/2}$ level back into to the $^2S_{1/2}$ ground state by driving it to the $^3[3/2]_{1/2}$ level [13] which has a natural lifetime of $\tau_{[3/2]_{1/2}}$=37.7 ns [14]. From the $^3[3/2]_{1/2}$ energy level, ions will primarily decay back to $^2S_{1/2}$ manifold allowing them to reenter the nearly-closed 369 nm cooling cycle [15].

Each of the atomic transitions using 399 nm, 935 nm, and 369 nm for $^{171}Yb^+$ are presented in more detail next. The optical paths of how these lasers were configured in the lab space at the University of Maryland will also be discussed.

2.1.1 Photoionization

The photoionization of neutral Yb atoms to obtain $^{171}Yb^+$ ions will now be discussed. We will assume that there exists an atomic oven containing some Yb metal that can be resistively heated to create a beam of neutral atoms. A discussion on the way we actually trap ions in the ion trap will be discussed later on after describing the relevant transitions in the ion and the experimental implementation. So assuming that a beam of Yb atoms is being ejected from the oven, these atoms can be ionized, using a two-step, or two-photon transition. First, the 399 nm wavelength laser is used to excite resonantly the $^1S_0 \leftrightarrow {}^1P_1$ transition in neutral Yb. Second, any laser beam with a wavelength λ<394.1 nm can be used to drive the electron from $^1P_1$ to the continuum resulting in a Yb^+ ion. Thus satisfying this wavelength requirement, the 369 nm laser cooling beam is used to promote the atoms in the first-excited state to become ions. The 355 nm

laser also satisfies the condition, and we actually quickly flash on and off one of the Raman beams to load ions faster into the trap.

This dichroic two-photon transition enables isotope selective trapping of Yb^+ ions [9] by tuning the frequency of the 399 nm to the resonance of the corresponding isotope that we wish to trap. We take care to have the alignment of the 399 nm beam roughly perpendicular to the direction of the Yb oven in order to minimize the Doppler shift in frequency observed by the high-velocity atoms. We have often observed in QSim that when the ion loading rate is very slow that it is due to a slight misalignment of the 399 nm beam.

2.1.2 Repumping Light

The 935 nm laser is used to "retrieve" ions that spontaneously decay from $^2\mathrm{P}_{1/2}$ to $^2\mathrm{D}_{3/2}$ which can occur one out of two hundred scattering events when the 369 nm laser is used to drive the $^2\mathrm{S}_{1/2} \leftrightarrow {}^2\mathrm{P}_{1/2}$ transition. The 369 nm laser does not does not interact with the $^2\mathrm{D}_{3/2}$ hyperfine states, and as a result, the fidelity of a given $^2\mathrm{S}_{1/2}$ to $^2\mathrm{P}_{1/2}$ transition would be reduced without the presence of the 935 nm laser. Fortunately, the electric dipole transition between the $^2\mathrm{D}_{3/2}$ and $^3[3/2]_{1/2}$ can be addressed using 935 nm light in which the natural lifetime in the $^3[3/2]_{1/2}$ energy level is $\tau_{[3/2]_{1/2}}$=37.7 ns [14], and thus, spontaneous emission happens quickly. The spontaneous emission from the bracket energy level has a strong branching ratio of 0.982 (98.2%) to the $^2\mathrm{S}_{1/2}$ manifold while the remaining branching ratio of 0.018 (1.8%) goes back to the $^2\mathrm{D}_{3/2}$ states [10, 13, 15]. Thus, the 935 nm laser acts to repump ions that have decayed into the $^2\mathrm{D}_{3/2}$ states back to the $^2\mathrm{S}_{1/2}$ manifold by driving the $^2\mathrm{D}_{3/2} \leftrightarrow {}^3[3/2]_{1/2}$ transition.

This repumping laser addresses both $\Delta F = 1$ $^2\mathrm{D}_{3/2} \leftrightarrow {}^3[3/2]_{1/2}$ transitions. The 935 nm

laser's (carrier) frequency, ω_{935}, resonantly addresses the ${}^2\mathrm{D}_{3/2}\ |F=1\rangle \leftrightarrow {}^3[3/2]_{1/2}\ |F=0\rangle$ transition and and an electro-optic modulator (EOM) is used to apply a negative first-order sideband at 3.0695 GHz to the 935 nm laser such that this second frequency tone at $(\omega_{935} - 2\pi \times 3.0695\,\mathrm{GHz})$ is resonant with the ${}^2\mathrm{D}_{3/2}\ |F=2\rangle \leftrightarrow {}^3[3/2]_{1/2}\ |F=1\rangle$ transition. The magnitude of the 935 nm EOM RF sideband is equal to the sum of the ${}^2\mathrm{D}_{3/2}$ hyperfine splitting and ${}^3[3/2]_{1/2}$ hyperfine splitting, whose values are 0.86 GHz and 2.2095 GHz, respectively. Ions in the ${}^3[3/2]_{1/2}\ |F=0\rangle$ level will spontaneously decay back down into one of the states in the ${}^2\mathrm{S}_{1/2}\ |F=1\rangle$ manifold while ions in any of the ${}^3[3/2]_{1/2}\ |F=1\rangle$ states can spontaneously decay to any of the ${}^2\mathrm{S}_{1/2}$ hyperfine levels, due to the selections rules of allowed transitions. The 935 nm laser remains on at all times, i.e. during the processes of loading, Doppler cooling, optical pumping, and detecting the ions.

2.1.3 Doppler Cooling

Conveniently, the 369 nm laser that is used in the second step of the ionization process of neutral Yb, described in Sec. 2.1.1, also happens to be the laser cooling beam. Thus, laser cooling of any trapped ions can occur simultaneously if more ions need to be trapped before the current to the Yb oven is turned off. We laser cool the ions using a well-known technique called Doppler cooling [16, 17]. This cooling method utilizes the Doppler effect to maximize the photon scattering rate of the ${}^2\mathrm{S}_{1/2} \leftrightarrow {}^2\mathrm{P}_{1/2}$ transition in order to reduce the average kinetic energy of the ion [16, 17].

The atomic transitions that are driven by the cooling beam in ${}^{171}\mathrm{Yb}^+$ are shown in Fig. 2.2. The blue arrows indicate the dipole allowed stimulated absorption and emission processes while

the gray arrows display only the spontaneous emission paths back to the $^2S_{1/2}$ states. A single

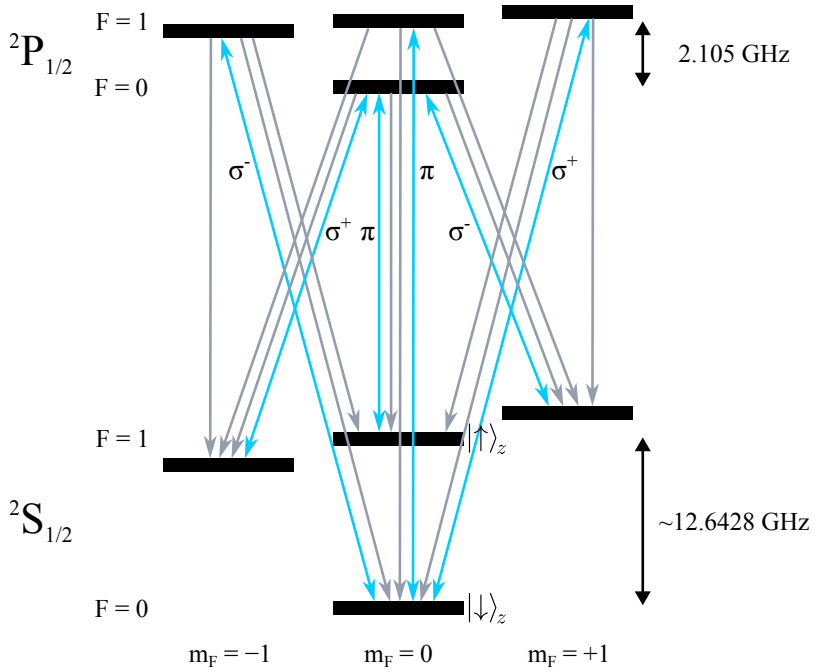


Figure 2.2. 369 nm Doppler cooling transitions. The 369 nm Doppler cooling beam off-resonantly drives both allowed $\Delta F = 1$ $^2S_{1/2} \leftrightarrow {}^2P_{1/2}$ transitions in order to cool efficiently both the $|\downarrow\rangle$ and $|\uparrow\rangle$ states in $^{171}Yb^+$. The blue arrows depict the stimulated absorption and emission processes from the $^2S_{1/2}$ while the gray arrows indicate spontaneous emission transitions. The cooling beam also contains all polarizations components in order to cool population that decays in the the nonzero $^2S_{1/2}$ Zeeman sublevels.

369 nm (cooling) beam is used to Doppler cool the ions by orienting it through the chamber and ion trap slot such that the beam's $\vec{k}$ has components along all three axes. The cooling beam frequency is red-detuned from the $^2S_{1/2}$ $|F=1\rangle \leftrightarrow {}^2P_{1/2}$ $|F=0\rangle$ resonant frequency by slightly more than half the linewidth, ∼15 MHz. In addition, we apply an external static magnetic field of about ∼5.22 G along the y principal axis of the ion trap (z axis in the lab frame). The externally applied B-field not only defines the spin quantization axis, but it also helps to prevent population from getting stuck in coherent dark states, superpositions of the $^2S_{1/2}$ $|F=1\rangle$ Zeeman levels, that exist in the absence of one [18]. The $|\vec{B}_{ext}|$ =5.22 G magnetic field shifts the Zeeman $|F=1,\ m_F=\pm1\rangle$ states, to first-order, by $\sim \pm 7$ MHz. In order to efficiently cool on both allowed

electric dipole transitions between the $^2S_{1/2}$ and $^2P_{1/2}$ states, the 369 nm cooling beam is sent through an EOM that applies a sideband frequency at 14.748 GHz that is red-detuned from the $^2S_{1/2}\,|F=0\rangle \leftrightarrow {}^2P_{1/2}\,|F=1\rangle$ transition. In addition, to the 369 cooling beam, the 935 nm beam is also critical in order to return population that spontaneously decays into the $^2D_{3/2}$ manifold from the $^2P_{1/2}$ states back to the main cooling transitions.

2.1.4 Optical Pumping

State preparation or initialization of a single trapped ion (or a linear chain of ions) is accomplished through the process of optical pumping. By applying a separate 369 nm laser beam (not the cooling beam) that addresses the $^2S_{1/2}\,|F=1\rangle \leftrightarrow {}^2P_{1/2}\,|F=1\rangle$ transition, the ion is efficiently prepared in the $|\downarrow\rangle$ state. The optical pumping beam frequency is 2.105 GHz shifted above

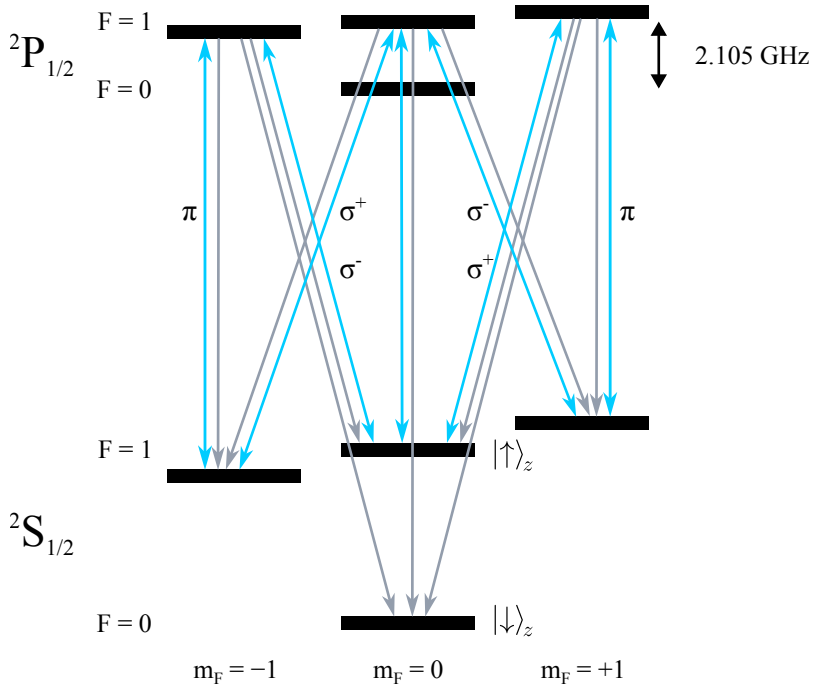


Figure 2.3. 369 nm optical pumping transitions. The 369 nm optical pumping beam frequency is resonant with the transition, $^2S_{1/2}\,|F=1\rangle \leftrightarrow {}^2P_{1/2}\,|F=1\rangle$. The stimulated absorption and emission transitions of the optical pumping process are represented by blue arrows while spontaneous emission from the $^2P_{1/2}\,|F=1\rangle$ excited states are represented by gray arrows.

the $^2S_{1/2}\ |F=1\rangle \leftrightarrow {}^2P_{1/2}\ |F=0\rangle$ resonant frequency and contains both π- and σ- polarizations as shown in Fig. 2.3. When the ion is pumped to any of the $^2P_{1/2}\ |F=1\rangle$ hyperfine states, selection rules dictate that the ion can spontaneously decay to a state in either $^2S_{1/2}$ F manifold or to a state in the $^2D_{3/2}\ |F=2\rangle$ level. If the ion decays back into any of the $^2S_{1/2}\ |F=1\rangle$ states, it will be optically pumped back to the $^2P_{1/2}\ |F=1\rangle$ manifold. However, if the ion spontaneously emits into the $^2S_{1/2}\ |F=0\rangle$ ($|\downarrow\rangle$) state, it will be unaffected by the optical pumping beam since the frequency of the beam is $\sim$12.6 GHz off-resonant from the $|\downarrow\rangle \leftrightarrow {}^2P_{1/2}\ |F=1\rangle$ transition. If the ion spontaneously emits into the $^2D_{3/2}\ |F=2\rangle$ level, the 935 nm beam will return the ion to the $|\downarrow\rangle$ state. The optical pumping beam only needs to be turned on for 15–25 µs before the ion is initialized in the $|\downarrow\rangle$ state.

2.1.5 Detection

We can determine the spin state of a single ion through a spin-dependent fluorescence method illustrated in Fig. 2.4. The 369 nm detection light frequency is exactly on resonance with the $|\uparrow\rangle \leftrightarrow {}^2P_{1/2}\ |F=0\rangle$ transition. If an ion is in the $|\uparrow\rangle$ state, then it will absorb a photon and transition to the $^2P_{1/2}\ |F=0\rangle$ state. As mentioned previously, an ion in the $^2P_{1/2}\ |F=0\rangle$ state will preferentially spontaneously decay back to one of the $^2S_{1/2}\ |F=1\rangle$ hyperfine states, scattering a photon in the process. The detection beam is composed of all three polarizations in order to address all three of the $^2S_{1/2}$ Zeeman states. In comparison, an ion that is in the $|\downarrow\rangle$ state will not be excited by the detection beam since the frequency of the light is $\sim$12.6 GHz off-resonant from the $^2P_{1/2}\ |F=0\rangle$ state, which is also a transition that is forbidden. In summary, when the detection beam is applied, an ion in the $|\uparrow\rangle$ state will fluoresce and appear "bright" while an ion

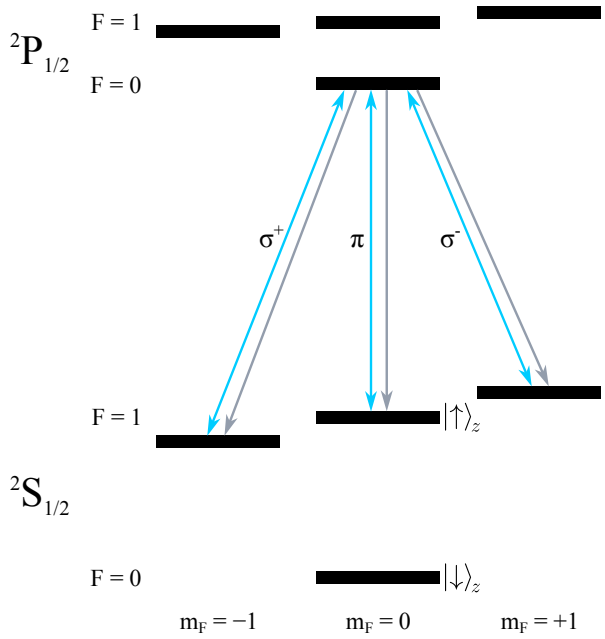


Figure 2.4. 369 nm detection transitions. The 369 nm detection beam frequency is resonant with the transition, $^2\mathrm{S}_{1/2}\,|F=1,\,m_F=0\rangle \leftrightarrow {}^2\mathrm{P}_{1/2}\,|F=0,\,m_F=0\rangle$. However, the detection beam polarization contains π and both σ polarizations in order to drive population from the $^2\mathrm{S}_{1/2}\,|F=1\rangle$ Zeeman levels as well. Stimulated absorption and emission transitions are represented by blue arrows while spontaneous emission from the $^2\mathrm{P}_{1/2}\,|F=0\rangle$ excited state are represented by gray arrows.

in the $|\downarrow\rangle$ state will not fluoresce and appear "dark." Further discussion regarding the collection of the photons and discriminating the measured counts for a single ion versus a linear chain of ions will be discussed in the following chapter in Sec. **??**. Off-resonant excitation to the $^2\mathrm{P}_{1/2}$ $|F=1\rangle$ states that spontaneously decay to either $^2\mathrm{D}_{3/2}$ F-manifold (due to selection rules) can cause detection errors since an ion decaying into $^2\mathrm{D}_{3/2}\,|F=2\rangle$ could be repumped back the $|\downarrow\rangle$ state. However, the 935 nm light is still needed to retrieve ions that decay from the $^2\mathrm{P}_{1/2}\,|F=0\rangle$ to $^2\mathrm{D}_{3/2}\,|F=1\rangle$. This type of spontaneous emission transition would not cause a detection error since the $^3[3/2]_{1/2}\,|F=0\rangle$ state can only decay back into the $^2\mathrm{S}_{1/2}\,|F=1\rangle$ manifold.

2.2 The CW Lasers

In this section, we will present how the atomic transitions in $^{171}Yb^{+}$ are physically implemented. Before presenting the beam paths of the 369 nm, 399 nm, and 935 nm lasers; I should mention that there is a fourth CW laser that is also utilized. This laser has a wavelength at λ=739 nm and it was the one that was alluded to back in Sec. 2.1. The reasons for why QSim uses this 739 nm laser system instead of a direct diode laser at 369 nm will be explained in Sec. 2.2.4.

Figure 2.5 displays the entire optical layout for the 369 nm, 399 nm, 739 nm, and 935 nm lasers that are before a dividing wall. This dividing wall is a composite aluminum panel, sold by the 8020 company, that separates the area surrounding the vacuum chamber from these optical elements that make up the beam paths for the CW lasers. As observed in Fig. 2.5, the optical

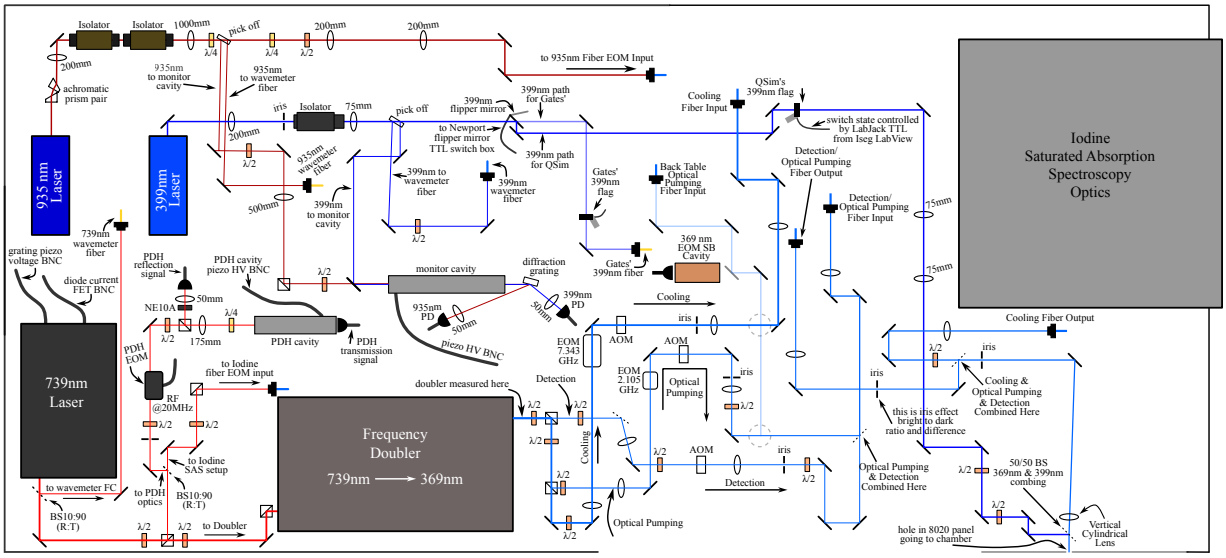


Figure 2.5. Optical paths of $^{171}Yb^{+}$ CW lasers. The beam paths for the 369 nm, 399 nm, 739 nm, and 935 nm laser light are displayed roughly to scale in the configuration that they were in at the University of Maryland.

paths are quite spread out. In the following subsections, each laser path will be discussed and the corresponding optical setup will be displayed again by itself so that it can be seen better.

2.2.1 399 nm Optical Path

The 399 nm laser is an off-the-shelf commercial continuous wave (CW) tunable diode laser from Toptica Photonics. A diagram of the 399 nm optical path is shown in Fig. 2.6. After the

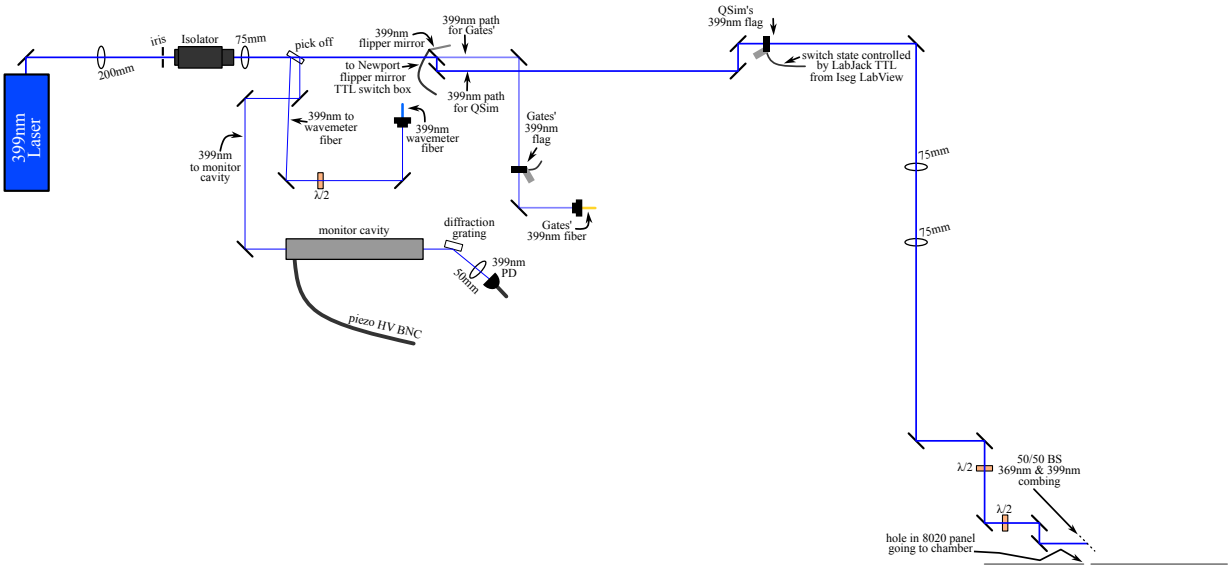


Figure 2.6. 399 nm optical path. The 399 nm beam is shared with another lab. There is a motorized flipper mirror that allows us to switch which the position that determines which way the main 399 nm light is directed.

399 nm light passes through an isolator and a couple of lenses, a small portion of the light is picked off from the main beam path. The beam that is reflected from the front surface of the optical element (labeled as "pick off" in Fig. 2.6 and referred to as such) goes to a fiber that is sent to a wavemeter that measures the frequency of the 399 nm laser. The beam that is reflected from the back surface of the pick off is aligned through a home-built scanning confocal "monitor" cavity in which a photodetector is used to measure the 399 nm light transmitted through the cavity. By scanning the length of the cavity via applying a triangle-ramp voltage to the cavity piezo, we can monitor whether the 399 nm frequency is single-mode or multi-mode.

Returning to the main 399 nm beam path, the next element in the beam path is a mirror

on a motorized flipper-mount allowing the beam to be shared with another lab that also traps $^{171}Yb^{+}$ ions. When the 399 nm flipper-mirror is flipped up into the beam path, the 399 nm light is directed to the rest of the free-space optical path. A 399 nm flag (or mechanical shutter) by default prevents (blocks) the beam from continuing to the rest of the beam path and whose positioned can be triggered by our experimental control software that raises the flag out of the 399 nm beam path when we wish to load ions into the trap. With the 399 nm flag raised out of the beam path, the beam passes through a couple of beam-shaping lenses and is eventually combined with the three 369 nm beam paths (cooling, optical pumping, and detection) at a non-polarizing beam splitter. The reflected 399 nm beam and the transmitted 369 nm beams pass through a small hole made in the 8020 aluminum composite panel that separates optical paths of the CW lasers from the remaining optics leading to the vacuum chamber and the vacuum chamber itself.

2.2.2 935 nm Optical Setup

The 935 nm laser is a CW tunable diode laser also from Toptica Photonics. A diagram of the 935 nm optical path is shown in Fig. 2.7. Similar to the 399 nm optical path, a small portion of the light is picked off soon after the isolators. The front surface of the pick off sends the light to the monitor cavity so that the 935 nm transmission peaks can be observed on an oscilloscope. Assuming that the 935 nm beam is well-coupled to the monitor cavity, we can look at the 935 nm oscilloscope signal to guarantee that the laser frequency is single mode. The back surface of the 935 nm pick off is coupled to a fiber that goes to the wavemeter in order to measure the value of the laser's frequency.

We use the wavemeter frequency reading of the 935 nm laser to stabilize the laser's fre-

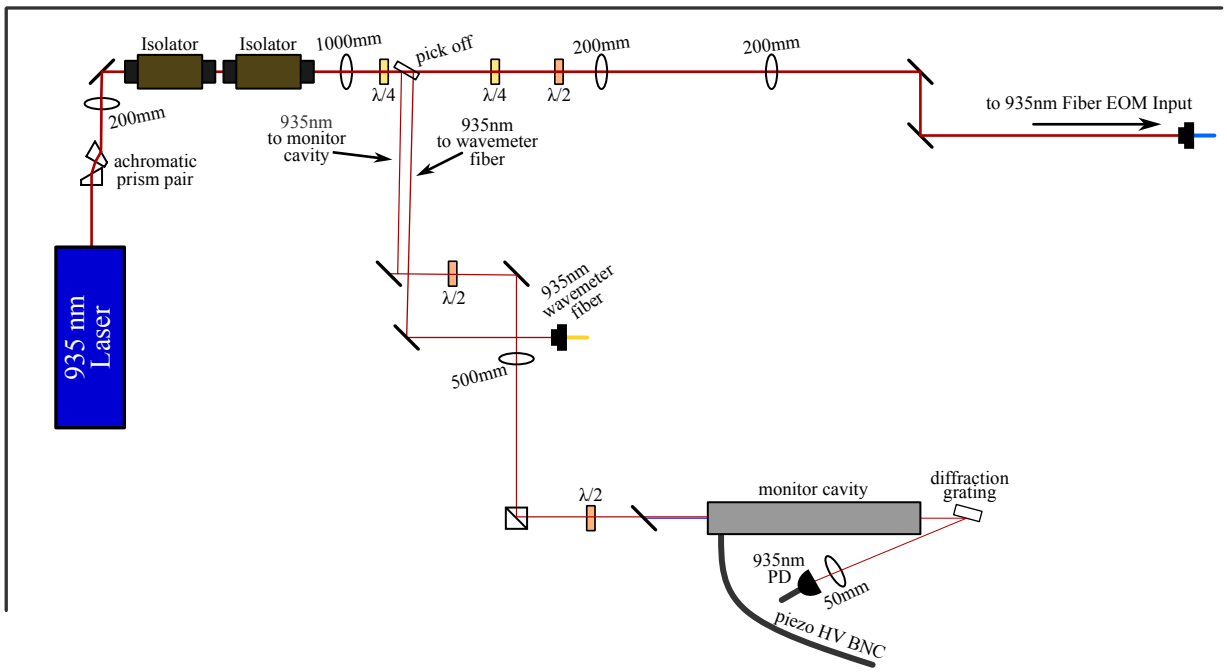


Figure 2.7. 935 nm optical path. The 935 nm optical path is very simple. The main beam path goes to a fiber coupler sending the light to the input of the fiber EOM. The other two beams paths are one that goes to the wavemeter to read and lock the laser frequency while the other path goes to a "monitor" cavity. The monitor cavity is used to determine ensure that the 935 nm laser is single mode.

quency with a software (or "wavemeter") lock. The 935 nm wavemeter lock compares the wavemeter measured frequency value of the laser to the set frequency that is typed into the web browser software interface. The wavemeter lock sends a feedback signal to the voltage control module that supplies the laser's grating piezo voltage. The wavemeter itself is calibrated with a laser whose frequency is stabilized to an absolute reference (the locked 739 nm laser, see Sec. 2.2.4.2). The 935 nm wavemeter lock set frequency is typically at 320.569251 THz which resonantly addresses the $^2\mathrm{D}_{3/2}\,|F=1\rangle \leftrightarrow {}^3[3/2]_{1/2}\,|F=0\rangle$ transition in $^{171}\mathrm{Yb}^+$.

Returning to the main 935 nm beam path, the light is coupled into the input port of a fiber EOM in which the negative first-order sideband at 3.0695 GHz is applied to the carrier frequency of the 935 nm light. The sideband frequency is the sum of the hyperfine splittings of the $^2\mathrm{D}_{3/2}$

and $^3[3/2]_{1/2}$ levels which enables the single 935 nm beam to re-pump ions from any of the $^2\mathrm{D}_{3/2}$ hyperfine states. The RF amplitude of the 935 nm sideband is about 2% of the initial carrier signal. The output port of the 935 nm fiber EOM is connected to a fiber coupler that is placed closer to the vacuum chamber, on the other side of the dividing 8020 panel, where the light is directed towards the entrance of the back chamber window.

2.2.3 369 nm Beam Paths

The 739 nm laser will be discussed in the next section, Sec. 2.2.4. The majority of the 739 nm laser light is sent to the input of a WaveTrain frequency doubler which outputs blue 369 nm light. Figure 2.8 shows the optical setup exiting from the doubler. The frequency of the light exiting the doubler is ~ 430 MHz red-detuned from the resonant frequency that addresses the $^2\mathrm{S}_{1/2}\ |F=1\rangle \leftrightarrow ^2\mathrm{P}_{1/2}\ |F=0\rangle$ transition. By splitting the 369 nm light into three different paths and using optical modulators to shift the frequency of (using an AOM) and/or apply additional frequency tones (using an EOM) to the original 369 nm light, we can use the 369 nm light to address transitions between the $^2\mathrm{S}_{1/2}$ and $^2\mathrm{P}_{1/2}$ hyperfine levels. Each of the 369 nm beam paths are separated into two parts in which a fiber is used to create the separation. The optics that lie before the corresponding fiber input, all have an EOM (except for detection) and an AOM in their path while the path after the fiber output provides the degrees of freedom to optimize the alignment of the beam interacting with the ions. We often find that the AOMs need to be recoupled or at least optimized slightly every few months, so having the defined separation ensures that the beams still remain aligned to the ions once the fiber coupling has been optimized.

We typically measure the 369 nm power coming out of the doubler each day and usually

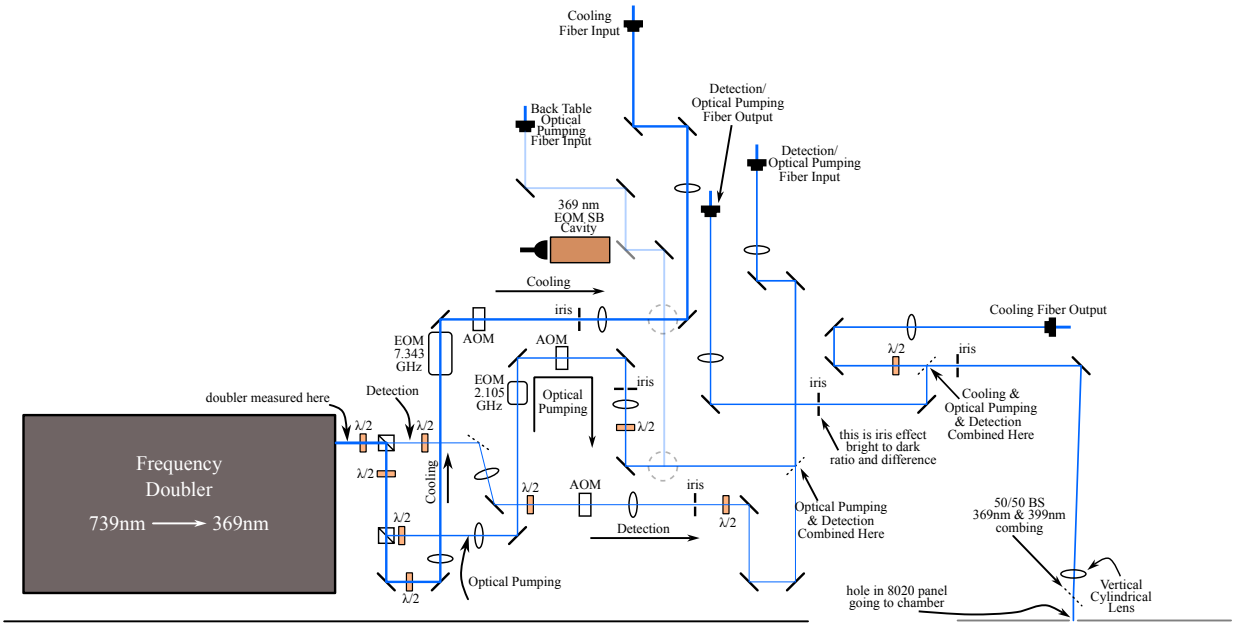


Figure 2.8. 369 nm optical path. The 369 nm beam paths is a lot more complicated in comparison to the 399 nm and 935 nm beam paths. The 369 nm light exiting the doubler system is immediately split into three beam paths: cooling, optical pumping, and detection.

the power coming out of the cooling fiber output if we do not see any of the usual background scattered cooling light on the camera. The detection beam transmits through the first PBS after the doubler while cooling and optical pumping are reflected by the PBS. The orange rectangles in Fig. 2.8 (and in the other beam path sketches) are half-wave plates (HWPs) and are used to control the power in each beam path such as the ones that are placed before PBSs or to set the polarization of the light.

The detection beam path only has an AOM in its path which shifts the frequency of the light to be resonant with the ${}^2\mathrm{S}_{1/2}\ |F=1\rangle \leftrightarrow {}^2\mathrm{P}_{1/2}\ |F=0\rangle$ transition, and it's AOM's RF power is kept lower than the max in order to not saturate the transition. In addition, less power in the detection beam helps to reduce off-resonantly scattering to the ${}^2\mathrm{P}_{1/2}\ |F=1,\ m_F=\pm 1\rangle$ sublevels which can off-resonantly decay into either F hyperfine level in the ${}^2\mathrm{D}_{3/2}$ spectrum. Unlike the off-resonant process that can occur during cooling and optical pumping, if an ion is off-resonantly

pumped into either of the decays into the $^2\mathrm{P}_{1/2}$ $|F=1,\, m_F=\pm 1\rangle$ states and ends up decaying into one of the $^2\mathrm{D}_{3/2}$ $|2,\, m_F\rangle$ sublevels, it will transition to the $^3[3/2]_{1/2}$ $|F=1\rangle$ in which the only decay path back to the ground state manifold is to $|\downarrow\rangle$ due to selection rules. This particular process with correspond to a detection error in which an ion that is detected "bright" becomes stuck in the "dark" state.

In the 369 nm beam path, shown in Fig. 2.8, there are two removable mirror mounts that can be placed in the cooling and optical pumping paths which are depicted as grey dashed circles. These are convenient to have in place. The removable mirror in the cooling beam path that is after the AOM but before the cooling fiber input allows us to direct the beam into a scanning confocal cavity to check the the second-order EOM sideband (2×7.374 GHz=14.748 GHz) coupling while the other removable mirror mount enables us to redirect the optical pumping beam. The optical pumping light goes to a fiber coupler that is connected to a fiber nicknamed, the "back table optical pumping fiber" (see Fig. 2.8) which delivers the optical pumping beam across the back of the optics table, naturally, to be combined with the individual addressing beam. It has been very handy to have the optical pumping beam to be able to realign that 355n̈m beam since it is a tightly focused beam going down the objective lens stack to the trap. The procedure for overlapping the back-table optical pumping beam with the individual addressing beam is discussed in Ref. [3].

2.2.4 739 nm Laser

As previously mentioned, the electric dipole transitions between the hyperfine levels, $^2\mathrm{S}_{1/2}$ and $^2\mathrm{P}_{1/2}$, are addressable with a laser at 369 nm. However, we use Toptica Photonics TA739, a tapered amplifier (TA) external cavity diode laser (ECDL), that is at a wavelength of $\lambda=739$ nm.

The 739 nm laser is sent through a frequency doubler in which 369 nm light is generated at exactly twice the frequency of the fundamental 739 nm frequency. Frequency doublers, generally, use a nonlinear optical crystal to provide the second-harmonic generalization (SHG) or frequency doubling when a high intensity laser traverses through the crystal and utilize optical resonators to amplify SHG converted power.

The 739 nm laser can also be used to probe absorption features in molecular iodine that are within ± 20 GHz of the 739 nm light. Molecular iodine has an "atlas" of narrow absorption lines that can be used as a frequency reference. Accordingly, the 739 nm laser frequency can be stabilized by referencing its frequency to an absorption line in molecular iodine which will be inherited by the SHG 369 nm light coming out of the doubler system.

The 739 nm optical setup is shown in Fig. 2.9. The light from the 739 nm laser diode is coupled into a tapered amplifier (TA) chip which is an active gain-medium that produces a high-power output typically between 450 mW to 520 mW (depending on the laser mode). The first element in the 739 nm beam path is a 10:90 beam splitter (BS) that reflects about 10% of the light exiting from the laser system, to a single-mode fiber that goes to the wavemeter, allowing us to observe the laser's frequency. The remaining 90% of the laser light is transmitted through the BS. We measure and record the output power of the 739 nm laser after the first mirror which has a typical value of $\sim$470 mW. The main beam path is split in two by a PBS in which the reflected beam path leads to the optical setups for the PDH and iodine locks while the transmitted beam path directs the light to the input of the doubler. Before the PBS, we have a 739 nm half-wave plate (HWP) in an adjustable rotation mount. By rotating the HWP, we can change the polarization of the light, resulting in how much power is reflected by and/or transmitted through the PBS. We typically send the majority of the 739 nm power to the doubler input in which typical

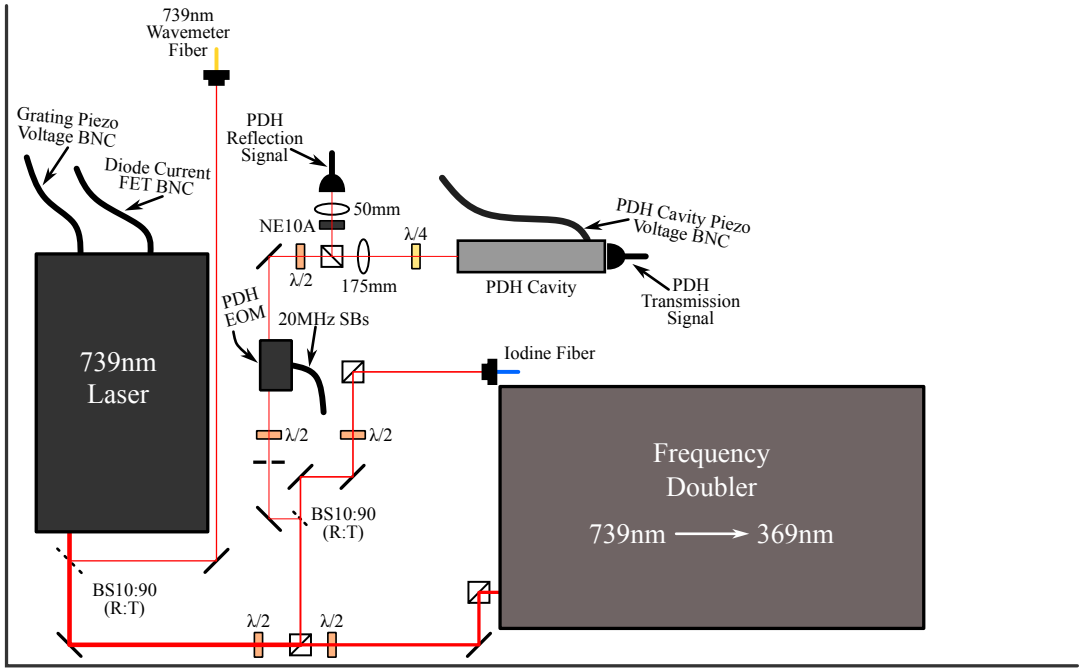


Figure 2.9. 739 nm beam path. 739 nm beam path is the only one of the four CW lasers that has a nice compact beam path excluding the molecular iodine saturated absorption spectroscopy setup. The majority of the 739 nm light is sent to the input of the doubler system while the remaining light is reflected by a PBS for the 739 nm laser locks.

values of the power measured after the second HWP are between 365–420 mW depending on the total output power from the laser and the amount of power is reflected by the PBS for the locks. The power measured in the PBS reflected path is typically set to a value between 45–110 mW. The PBS reflected beam path is further split in two by another 10:90 BS and distinguishes the PDH optical setup from the iodine setup. Thus, the majority of the light designated for the 739 nm stabilization locks is sent to the input of a fiber that delivers the light to the iodine SAS system. The discussion of locking the 739 nm laser current, piezo grating voltage, and laser frequency will be presented next.

Unlike the 935 nm laser whose frequency is locked using the wavemeter, the stabilization of the 739 nm laser is slightly more complicated. We use the Pound-Drever-Hall (PDH) technique [19, 20] to lock the 739 nm laser frequency to a scanning confocal cavity. In turn, the

length of this PDH cavity is stabilized using a Doppler-free saturated absorption spectroscopy (SAS) signal from a heated cell of molecular iodine. The following sub-subsections detail the PDH and iodine SAS optical setups in which the signals obtained are used to stabilize the 739 nm laser.

2.2.4.1 739 nm PDH Locks

The frequency of the 739 nm laser is mainly controlled by the amount of current supplied to the laser diode and the angular position of the diffraction grating. The temperature of the laser diode is another parameter that can be adjusted to tune the frequency but generally is not the first "knob" of choice. From day-to-day operation, the laser frequency is usually tuned by finely adjusting the angular position of the diffraction grating with respect to the incident light emitted from the laser diode. The grating itself is epoxied onto to the front surface of a flexure mount in which the flexure angle can be opened or closed by tightening or loosening a piezo actuated screw, respectively. The grating flexure angle can be adjusted to a finer degree by changing the voltage applied to the piezoelectric material of the actuated screw. By scanning the voltage of the grating piezo, the laser's frequency can be tuned at the MHz resolution and over a range of a few GHz. Frequency tuning the laser via the piezo voltage is slow in comparison to scanning the laser diode's current which also changes the intensity of the laser. Thus, in order to guarantee a stable laser frequency, both the current of the laser and the grating piezo voltage must be controlled.

The PDH technique [19, 20] provides a straightforward solution for stabilizing a laser's frequency using a Fabry-Perot (FP) cavity. The PDH method provides a protocol to measure the derivative of the cavity-reflected intensity with respect to changes in the laser's frequency

which indicates how the frequency of the laser should be corrected to remain on-resonance with the cavity. By using the reflected intensity to measure the frequency of the laser, the signal is decoupled from fluctuations in the laser's intensity which is not the case when measuring the transmitted cavity signal. The implementation of the PDH optical setup is shown in Fig. 2.9 in which the beam path is defined by the reflected 739 nm beam from the half-inch diameter 10:90 BS. The 739 nm beam in the PDH path is phase-modulated using a resonant EOM that adds weakly-coupled frequency sidebands at ± 20 MHz about the carrier frequency of the beam. Our setup differs from previous implementations of the 739 nm PDH lock, discussed in dissertations of former group members [21, 22], in which previous schemes frequency-modulated (FM) the current of the laser diode.

The phase modulated (PM) 739 nm light is aligned to the PDH scanning confocal cavity in which photodetectors before and after the cavity have been positioned to measure the reflected and transmitted intensity signals, respectively. The HWP before the PBS ensures that the modulated beam incident from the left is transmitted through the PBS while the QWP just before the PDH cavity ensures that the reflected signal from the cavity is reflected by the PBS and directed towards the PDH reflection photodetector. The PDH cavity itself has one of its mirrors epoxied on the outside of the hollow Invar-36 rod which has a low coefficient of thermal expansion. The piezoelectric tube and the other cavity mirror are mounted inside the Invar-36 rod. A homebuilt electronics board supplies the high-voltage (HV) to the piezo enabling the length of the PDH cavity to be scanned using the electronic board's tunable *internal ramp signal* or with an *external signal* that can be fed as an input connection to HV board. Which ramp setting is determined by the internal/external toggle switch on the HV board. This manual control allows us to optimize the PDH signal when the switch is set to the internal setting, and then, have the length of the

cavity itself be locked to a stable reference frequency when the switch is flipped to the external state.

Before we are able to reference the length of the PDH cavity using a Doppler-free saturated absorption signal from molecular iodine, the 739 nm laser's current and grating piezo voltage must first be locked to the PDH cavity. Figure 2.10 shows the electronic diagram of the PDH lock. The PDH cavity reflection signal is compared to the 20 MHz local oscillator signal using a frequency mixer. The output of the mixer is sent through a low-pass filter resulting in the PDH error signal. This error signal is split and sent to the inputs of two different proportional integral differential (PID) servo controllers that are used to stabilize the laser's frequency. The PDH error signal that is sent to the PID controller used for the grating piezo voltage passes through another low-pass filter before entering the controller's input. The *grating PID* stabilizes the 739 nm laser's frequency against slow drifts while the *current PID* counteracts faster noise. The 739 nm laser frequency is locked to the length of the PDH cavity after engaging the grating and current PID controllers. However, the PDH cavity length is still susceptible to slow thermal drifts and as a result, stabilization of its length is required in order to maintain frequency stability of the 739 nm laser which is imparted in the resulting 369 nm light exiting the doubler.

2.2.4.2 739 nm Iodine Reference Frequency Lock

The PDH cavity length is referenced to a narrow absorption line in molecular iodine. More specifically, our lab has an optical setup to perform Doppler-free SAS of a heated glass cell of molecular iodine. Conveniently, molecular iodine has three absorption lines that are within $\pm$ 15 GHz of the 739 nm laser frequency value required to address $^{171}Yb^{+}$ ions. However, the

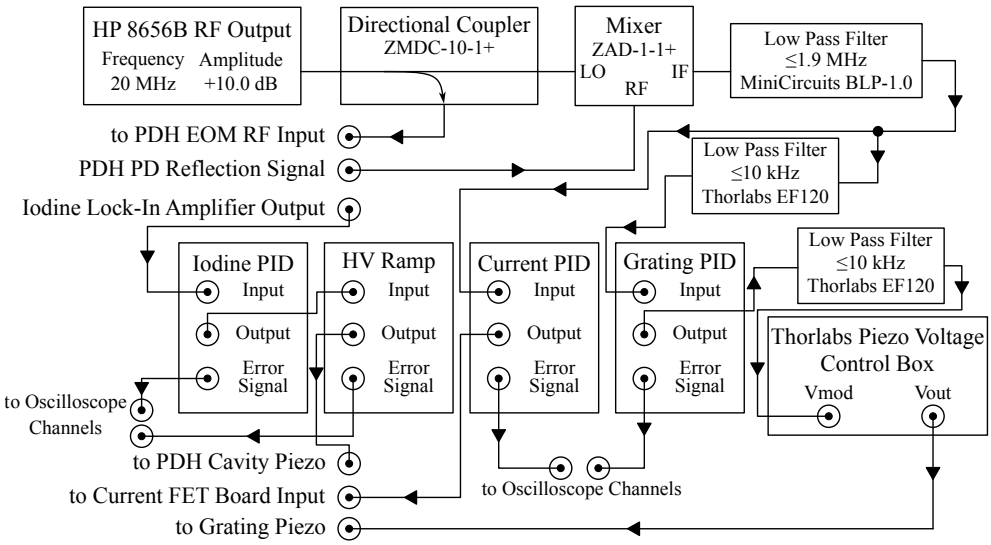


Figure 2.10. PDH current and grating locks. These are the electronic components of the PDH stabilization scheme used to lock the 739 nm laser diode's current and grating piezo voltage. The four PIDs are a type of rack mount card that can be plugged into a Toptica controller main-frame slot.

strengths of these absorption lines are quite weak with the iodine cell at room-temperature. As a result, our iodine cell, shown in Fig. 2.11, is heated to a temperature of about 560 °C. This section will highlight improvements that have been made to both the optical and electrical components of the iodine lock during my time in the lab. For more information about the design and theoretical principles of SAS, please refer to [21–23].

I will first summarize the iodine SAS setup. The 739 nm light is sent through a fiber EOM shifting the 739 nm frequency on the order of GHz in order to address the desired iodine line. The EOM fiber output is connected to a fiber coupler located at the top right corner of the elevated breadboard platform, the input of the iodine SAS setup. Immediately, the 739 nm beam is split into two beams in which the higher-intensity beam is transmitted through the pick off and is denoted as the *pump beam*. The beam reflected from the pick off is further split in two by a BS in which the reflected beam is the *reference* and the transmitted beam is the *probe*. The reference beam is aligned to the *reference input* of a balanced photodetector. Meanwhile, the probe beam

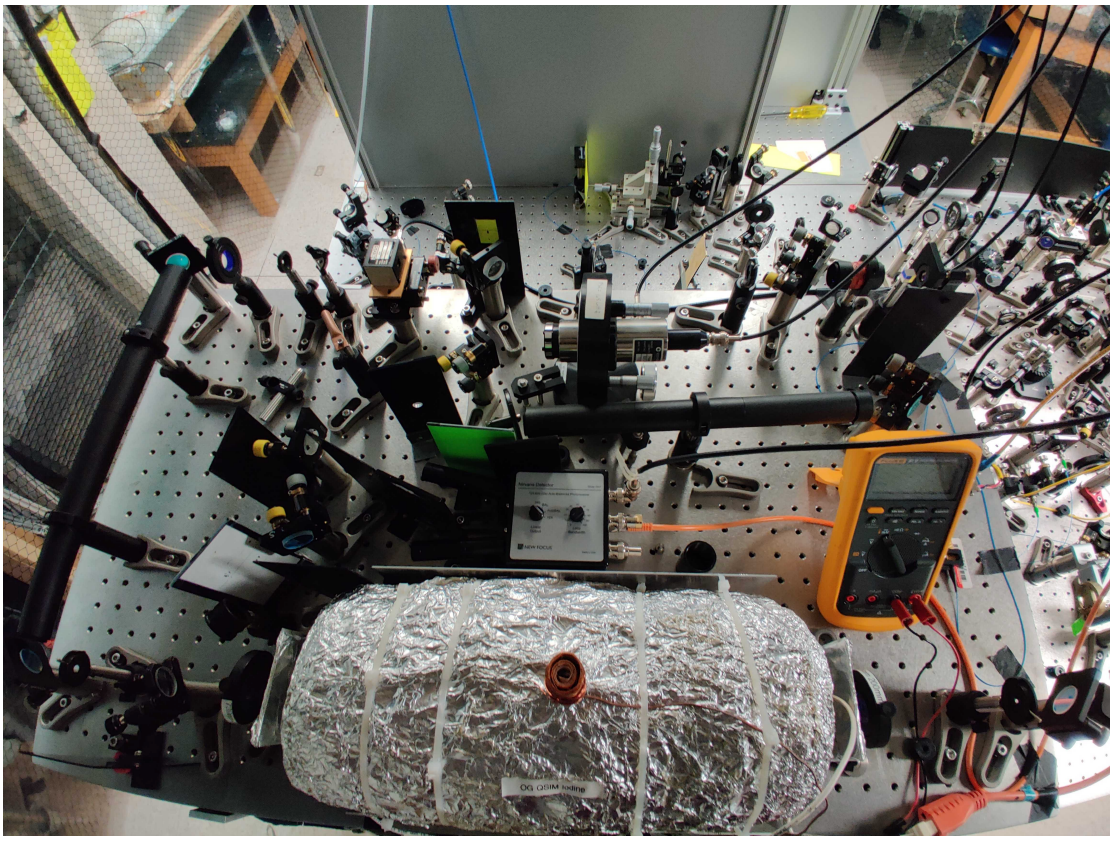


Figure 2.11. Iodine SAS optical setup. The large cylinder blob that is wrapped in aluminum, a good thermal conductor, is the molecular iodine cell. In order to be able to see an absorption feature of molecular iodine at room temperature it must be heated to over 500 °C. The 739 nm light that has sidebands that are on the order of 13 GHz enters the iodine SAS setup in the top right corner of the elevated bread board. The probe beam goes through the cell from right to left with respect to this image and the pump goes from left to right.

travels through the iodine cell from right to left and is aligned to the *signal input* of the balanced photodetector. Returning to the pump beam path, a small portion of the light is picked off and aligned to a FP cavity. By observing the FP transmission signal, we can check the 739 nm laser mode and measure the GHz sidebands that are applied to the light from the fiber EOM. The carrier peak should be suppressed and only the first-order sidebands peaks should be observed in the transmission signal. The majority of the pump light is sent to the input of an AOM that has a center frequency at 80 MHz and the optimized first-order diffracted beam is used as the pump. The RF signal applied to the AOM is frequency modulated by a 11 kHz sine wave. The

modulated pump beam is aligned through the iodine cell traveling left to right. In our setup, the ratio between the intensities of pump and probe beams is about 3.5:1. The power in each beam is measured right before it enters the iodine cell which corresponds to the position just before the spherical lens.

The signal from the balanced photodetector and the 11 kHz modulation signal are sent to the input and reference ports of a lock-in amplifier electronics box, respectively. The output from the lock-in amplifier is the derivative of the Doppler-free signal measured by the balanced photodetector. This iodine reference frequency error signal is sent to the input of another PID servo controller that is used to lock the length of the PDH cavity. More specifically, the iodine error signal as a function of the 739 nm laser frequency can be observed on an oscilloscope. Once the 739 nm current and grating piezo are locked to the PDH cavity, scanning the PDH cavity length results in scanning the frequency of the 739 nm laser. Thus, by scanning the 739 nm frequency, the scanned iodine error signal will show the derivative of the Doppler-free iodine signal as a function of the laser frequency. The PDH cavity length is locked to the zero-crossing of the Doppler-free derivative iodine signal using the iodine PID controller. The output of the iodine PID is sent to the control port of the PDH HV ramp card that sends the voltage signal to the cavity as shown in Fig. 2.10.

The frequency detuning with respect to the 739 nm frequency of the three closest iodine absorption lines are about -5 GHz, +10 GHz, and +13 GHz and correspond to transitions at 13530.6745 cm^{-1}, 13531.1823 cm^{-1}, and 13531.2773 cm^{-1} respectively [24]. Further spectroscopy at each absorption line was performed in Ref. [21] to determine which hyperfine-structure feature would be the best to use as an absolute reference. The lock-in amplifier output signal which is equivalent to the derivative of the Doppler-free hyperfine-structure of the +13 GHz

line and the +10 GHz line is plotted in Ref. [23] and Ref. [10], respectively. Reference [22] has the signal of the largest hyperfine structure feature of the -5 GHz line.

Figure 2.12 displays the trace of the observed unlocked iodine error signal as the 739 nm laser frequency is changed by scanning the PDH cavity length and it corresponds to "Feature 5" of the lock error signal plotted in Ref. [23]. Feature 5 is one of six features that are observed in the +13 GHz absorption line. This iodine absorption feature has the largest amplitude, and as a result, the zero-crossing of the furthest right positive slope of Fig. 2.12 was chosen as the absolute frequency reference to stabilize the 739 nm laser. Originally in QSim, we used the second zero-



Figure 2.12. Feature 5 of the iodine error signal. Sweeping the unlocked iodine error signal over the doublet feature in the +13 GHz absorption line. The PDH cavity length is referenced to the zero-crossing that's farthest to the right (or the second zero-crossing). When the iodine PID is locked, the frequency of the 739 nm laser is stabilized at 405.644325 THz, the value measured on the wavemeter.

crossing in the doublet feature, shown in Fig. 2.12, in the +13 GHz detuned iodine absorption line as the lock-point of the iodine PID. To observe this feature, 13.315 GHz was the RF frequency applied to the iodine fiber EOM in which the first-order sideband was optimized and the carrier amplitude suppressed.

In December 2019, we took some time to optimize the Doppler-free iodine signal measured by the balanced photodetector since we had noticed that the unlocked iodine error signal had become smaller and noisier leading to the iodine PID unlocking shortly after being locked. Several improvements were made to the iodine optical setup:

1. Improved the polarization stability of the 739 nm light entering the iodine setup. The polarization of the 739 nm light entering the iodine setup is set such that the light coupled through the fiber EOM maximizes the power in the first-order sideband while minimizing the power in the carrier frequency. Fluctuations in the polarization of the 739 nm light entering the iodine setup will cause the optimized first-order sideband signal to decrease and the carrier peak to emerge. We noticed this polarization instability when we were looking at the transmitted FP signal. The amplitude of the sideband became noisy as we wiggled iodine EOM's fibers. We improved the polarization stability of the entering light by taping down the EOM's input and output fibers making sure the fibers secure but not under strain. In addition, we used some optical clamps from Thorlabs to "hold" the EOM body itself to the elevated optical breadboard. Lastly, we switched out the single-mode fiber delivering the 739 nm light to the fiber EOM input with a polarization maintaining fiber and we made sure that this fiber was secured well.

2. Removed the nonzero offset observed in the error signal. We discovered that a small amount of scattered light from the pump beam was being measured by the balanced photodetector. As a result, the iodine error signal had an overall offset from zero. We added lens tubes about the reference and probe paths leading to the balanced photodetector. In addition, black plates were placed about these paths in locations where space was limited. Lastly, we made sure that the zeroth and other diffracted orders of the modulated 80 MHz AOM were picked off from the main pump path and truly centered in the copper beam dump.

3. Optimized the alignment of the pump and probe beams through the cell. We added a x2 beam expander which defocused the pump and probe beams inside the cell and increased their beam sizes. Previously, the alignment of the pump beam inside the iodine cell crossed

the probe beam at a small angle. The beam expander increased the waists of the pump and probe beams enabling their alignment to be fully overlapped inside the cell. Increasing the spatial overlap between the two beams inside the cell helped to enhance the size of the Doppler-free signal.

4. Increased the temperature of the iodine cell. Originally, the iodine cell was heated to a temperature of 400 °C. After reviewing the iodine setups previously implemented in other labs within the group, we realized that temperature of the cell could be heated to a higher temperature as long as the value was below 600 °C. Increasing the cell's temperature beyond 600 °C, one risked cracking the iodine cell. As a result, we slowly increased the temperature of the iodine cell, and at each temperature increment, we observed the strength of the error signal once the cell temperature reached equilibrium. We decided to keep the iodine cell temperature heated to 560 °C since the largest error signal was observed at this location, and we didn't want to risk heating the cell temperature any higher.

After incorporating all of the changes made to the iodine setup, we obtained an improved error signal that had a larger peak-to-peak amplitude, no offset from zero, and less noise. It was easier to identify the correct zero-crossing, and once the iodine PID was engaged, the lock remained locked for a longer period of time. However, despite having the PDH and iodine PIDs all locked, thus locking the frequency of the 739 nm and 369 nm light, we still had the issue of iodine frequency reference jumping from the second to the first positive slope zero-crossing observed in Fig. 2.12. The doublet structure of this fifth feature had two positive slope zero-crossings that were separated by about 15 MHz. When the iodine PID locked to the lower frequency zero-crossing, the frequencies of 369 nm beams for cooling, optical pumping, and detection were all red-detuned from their set values and the efficiency of these processes decreased. To solve this problem, we decided to change the iodine feature that we used as the absolute reference. We chose the fourth feature ("Feature 4") appearing in the +13 GHz absorption line Doppler-free

signal as a function of detuning frequency [23]. Figure 2.13 shows the oscilloscope trace of the unlocked iodine error signal in which the length of the PDH cavity has been scanned to show Feature 4. Locking the PDH cavity length to the absolute frequency reference now corresponds

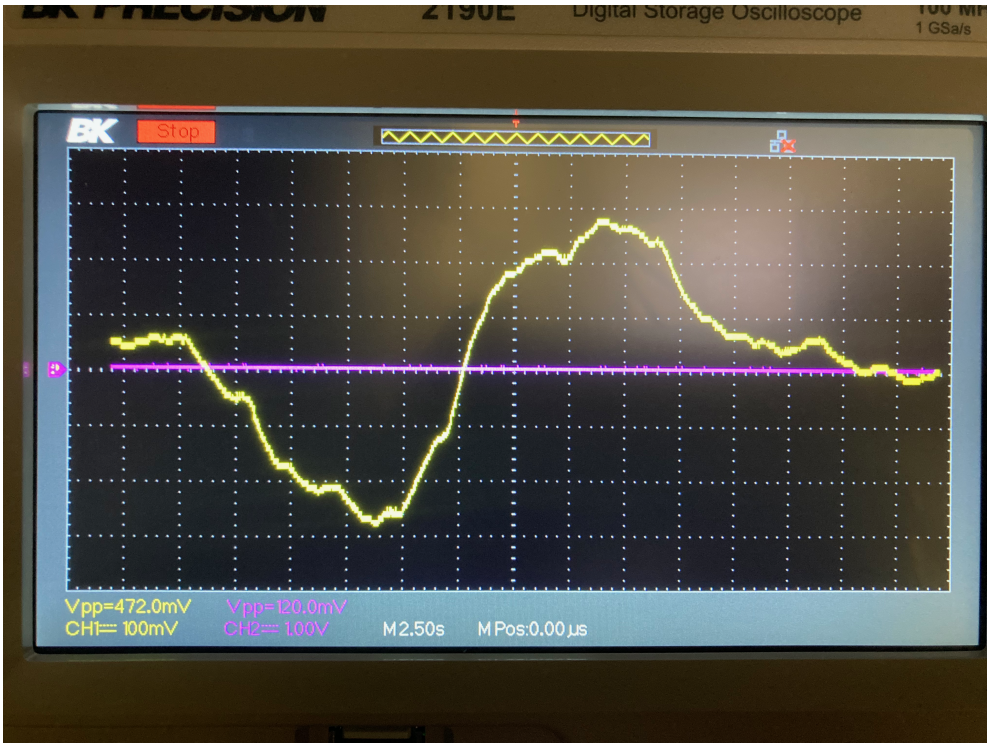


Figure 2.13. Feature 4 of the iodine error signal. The unlocked iodine error signal is the derivative of the swept over the Doppler-free doublet feature in the +13 GHz absorption line. The PDH cavity length is referenced to the zero-crossing of the positive slope in which only one exists. When the Iodine PID is locked, the frequency of the 739 nm laser is stabilized at 405.644318 THz, the value measured on the wavemeter.

to locking the iodine PID at the single zero-crossing that the feature possess. In switching from the fifth to fourth feature in the spectroscopy of the +13 GHz absorption line, the iodine fiber EOM RF frequency was changed from 13.315 GHz to 13.161 GHz. This change in the iodine lock has made it more robust and corresponds to having only to lock once or twice a day the three PIDs required to stabilize the 739 nm laser frequency.

The last major change to the iodine reference frequency lock that has occurred during my time in QSim is the RF source used for the 80 MHz AOM. Originally, a HP8660C synthesized

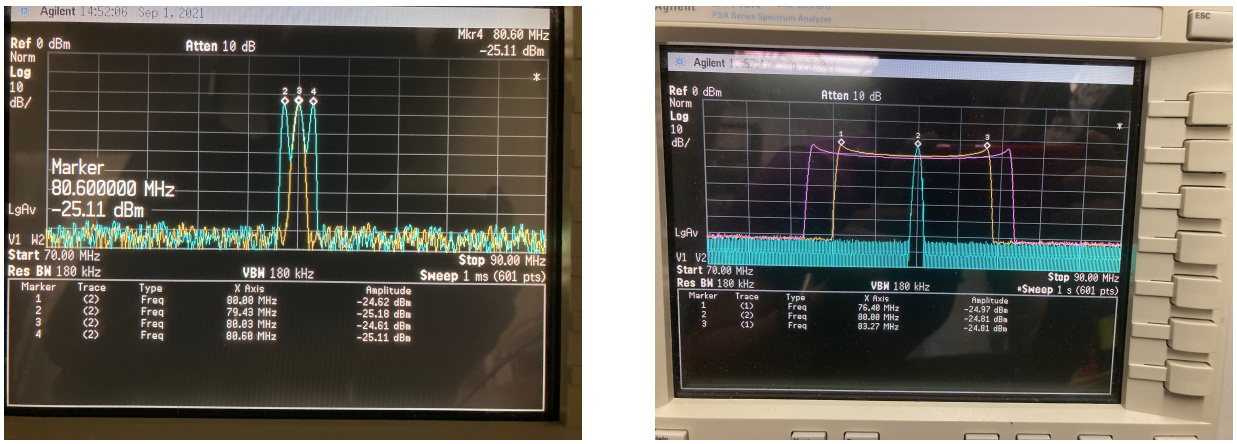
signal generator along with its modules (HP86635A modulation selection and HP86602B RF selection) was used to generate the frequency modulated RF signal for the iodine AOM. Unfortunately, the modulation section of the RF unit stopped working in May 2021. We were able to use a spare HP8640B, a standard RF source, to supply the 80 MHz frequency and apply the 11 kHz frequency modulation to the iodine AOM. However, the maximum peak deviation that the HP8640B unit could supply was $\pm$640 kHz (based on the electronic control box specifications). In comparison, the maximum peak deviation of the HP8660C system was set at $\pm$1.2 MHz. It is important to note here that both the modulation bandwidth and intensity of the pump beam influence the size of the error signal [23]. The bandwidth, f_{BW}, of a FM signal is related to the frequency of the modulation, f_{FM}, and the maximum peak deviation, Δf, from the center frequency and is given by the following equation:

$$f_{BW} = 2(\Delta f + f_{FM}). \tag{2.4}$$

Based on Eq. (2.4), the modulation bandwidth of the HP8640B RF source was slightly more than half of the modulation bandwidth that was achieved with the now broken HP8660C RF source. In order to compensate for the the reduced modulation bandwidth, we increased the amount of power going to the 739 nm iodine fiber so that the power measured on the iodine breadboard platform was twice the original value.

The solution of using a HP8640B to supply the RF signal to the iodine AOM with having more power sent to the iodine setup worked temporarily. Diverting the increased amount of power to the iodine system consequently reduced the amount of power being sent to the frequency doubler corresponding to a reduced doubler output power (less 369 nm power). So instead of using a HP8640B to provide the iodine AOM RF frequency signal, I specifically figured out the param-

eters required to use a voltage controlled oscillator (VCO) that could be used instead. Figure **??** shows the RF output at 80 MHz with and without the 11 kHz frequency modulation generated by the HP8640B (left) versus a VCO (right) using a spectrum analyzer (Agilent E4440A) to measure the average trace "max-hold" signal. In Fig. 2.14a, the yellow trace shows the unmodulated



(a) RF signal from the HP8640B

(b) RF signal from the ZOS-150+ VCO

Figure 2.14. Iodine AOM RF source signal comparison. (a)

80 MHz output while the blue trace displays the average maximum FM signal generated from the HP8640B source. From the x-axis value of markers '4' (80.60 MHz), the measured maximum peak deviation is about 600 kHz, corresponding to a modulation bandwidth of $\sim$1.2 MHz.

In comparison, the yellow trace of the FM signal in Fig. 2.14b has a measured maximum peak deviation of 3.6 MHz, corresponding to a modulation bandwidth of $\sim$7.2 MHz. An even larger maximum peak deviation of the FM signal centered at 80 MHz could be achieved, indicated by the pink trace in Fig. 2.14b, by tuning the control voltage signal that's sent to the input of the VCO (Mini Circuits part number: ZOS-150+). However, we chose to use the control voltage settings that produced the VCO RF output with a maximum peak deviation of 3.6 MHz since this peak deviation value was three times the original peak deviation produced by the HP8660 system. The FM signal parameters that were sent to the control port of the VCO are displayed in Table 2.3.

Since implementing the VCO to send the RF signal to the iodine AOM, we have been able to

Type	**Frequency (kHz)**	**Amplitude (V_{pk-pk})**	**Offset (V_{pk-pk})**	**Phase (°)**
sinusoidal	11.0	0.60	1.268	0.0

Table 2.3. Iodine VCO control signal parameters. The parameters of the FM signal sent into the control port of the VCO are displayed. A Stanford Research System function generator was used to generate this input signal. V_{pk-pk} represents the peak-to-peak voltage.

reduce the power measured on the iodine platform while still maintaining an adequate iodine error signal in which the measured 739 nm locked laser frequency on the wavemeter fluctuates less than 2 MHz.

2.3 Trapping Our Friends the Ions

The 935 nm beam size is much larger than the beam sizes of the 399 nm and all the 369 nm laser beams. All three beams are combined on the other side of the 8020 wall. In a similar manner, even though they have not been discussed yet, both Raman beams, named "Raman 1" and "Raman 2" also enter and exit the chamber. Raman 1 is usually the beam 355 nm that is used to load ions faster. In QSim, the vacuum chamber contains two ovens filled with neutral Yb metal flakes [25]. One of these ovens is filled with naturally abundant Yb while the second oven is filled with isotopically enriched ^{171}Yb. We primarily use the latter oven but have the capability of quickly switching over to use the naturally abundant atomic oven under particular circumstances.

To trap $^{171}Yb^{+}$, we first turn on the isotopically enriched oven power supply, sending about 2.5 A of current through it in order to generate a thermal beam of neutral Yb via resistive heating. This oven is aligned such that the beam of neutral Yb atoms are directed towards the center of the ion trap. In addition, we unshutter the 399 nm beam path by raising a small metal flag that

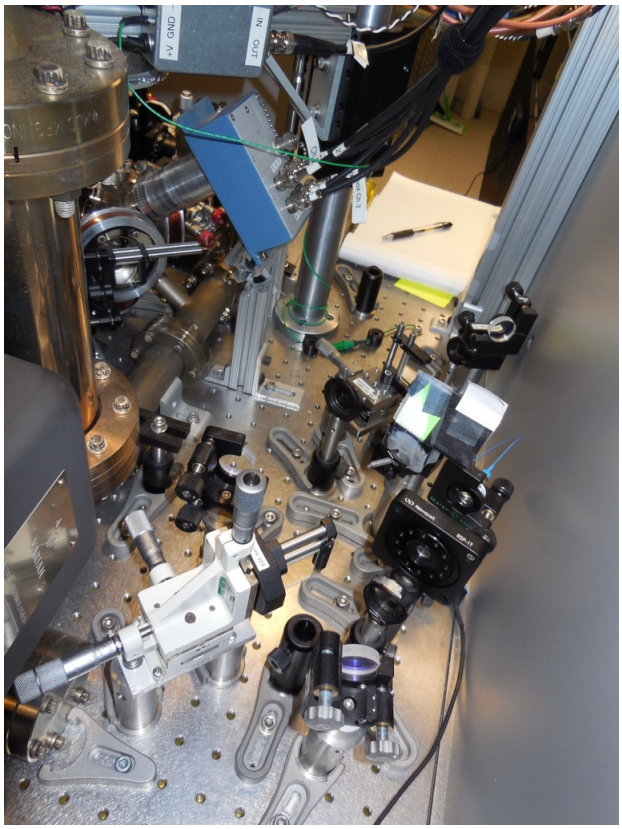


Figure 2.15. CW optics right before the chamber. These are the 369 nm 399 nm and 935 nm optics that are on the other side of the 8020 panel that direct the beams to the center of the ion trap.

blocks the beam path. It takes about 30–45 s before neutral atoms begin spewing out of the oven.

All three CW lasers, the 369 nm, 399 nm, and 935 nm beams are all involved in the process for trapping. Usually, we lower the RF potential of the ion trap since we find it is easier to load, cool, and keep a larger chain as we raise the RF back up to its nominal "high" position compared to its "low" RF value. The static electrode voltages are also changed to compensate a looser axial confinement for loading. This entire lowering, turning the oven on, unshuttering the 399 nm has been integrated in what we call the "Iseg LabView" experiment control software which will be discussed in the next chapter.

2.4 Difficulty in Loading Ions Troubleshooting

Usually, the most common problem with loading is the 399 nm laser alignment or either the 399 nm or the 935 nm laser not being single-mode. We can usually still trap an ion even if the 935 nm power out of the fiber is only on the order of 5 mW in comparison to its 10 mW value.

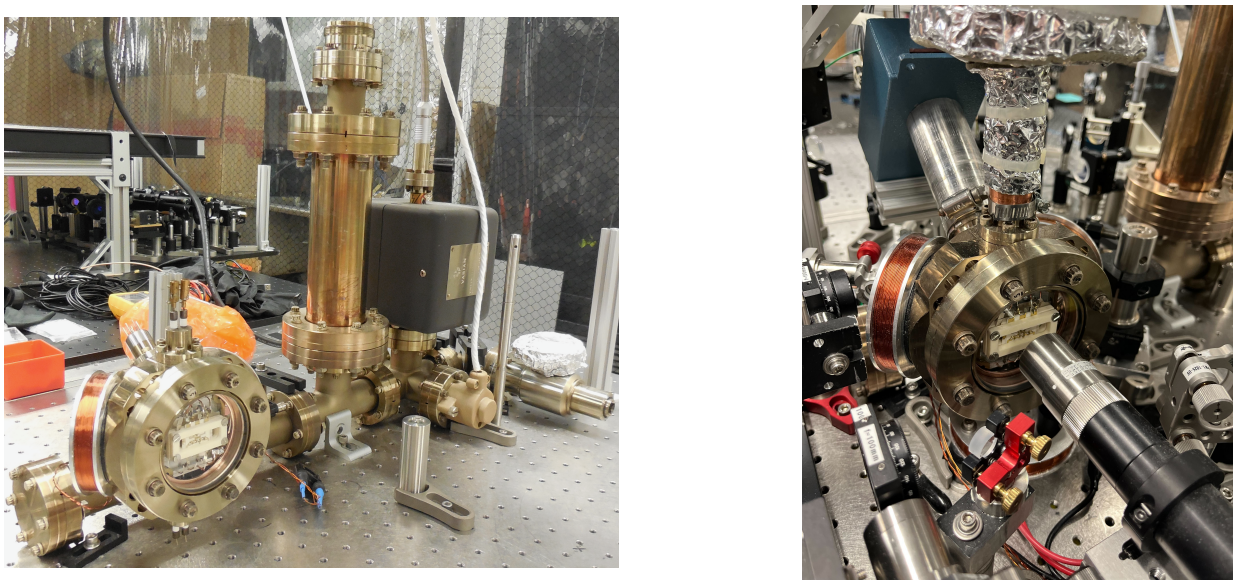
Chapter 3: Components of the Experimental System

This chapter discusses the remaining components of the trapped ion experiment in QSim which altogether form an experimental quantum simulator.

3.1 Ion Trap and Vacuum Chamber

In order to trap an ion or multiple ions in a region of free space, a three-dimensional confining potential must exist in that area. An arrangement of electrodes can be used to create this confinement in all three directions and as a result are called ion traps. However, from Earnshaw's theorem [26], static voltages alone cannot be used to create a potential minimum (nor maximum) in free space, and as result, both static and oscillating fields are required. There are two types of ion traps that are primarily used for trapping ions: the linear radio-frequency (RF) Paul traps and the Penning trap [27]. In linear RF Paul traps, both oscillating and static electric fields are used, in combination, to create an effective pondermotive transverse confinement potential and an axial confining potential respectively [27, 28]. In a Penning trap, both a static uniform magnetic field along the axial direction and a static electric field that traps the ions in the axial direction are used to generate the confining potential. This transverse potential arises from the cross product of the two fields $(\vec{E}\times\vec{B})$ in which trapped ions undergo cyclotron motion, rotating about the axial direction of the trap [6, 29].

In QSim, we use a linear RF Paul trap that is housed inside the vacuum chamber, displayed in Fig. 3.1, that is at one end of the ultra-high vacuum (UHV) assembly. Placing an ion trap in an UHV environment helps to isolate the system of trapped ions from the surrounding room environment as well as reducing the rate of collisional bombardment from background gas particles that are inside the chamber. An ion pump, shown in Fig. 3.1a, is actively "pumping" on the entire



(a) **(b)**

Figure 3.1. QSim vacuum chamber. **(a)** The entire UHV chamber assembly having had all of its surrounding optics surround it cleared and ready to be moved. The RF can and the DC electrode filter box which are both normally attached to the chamber (see picture on the right) have been removed in order to transport the entire assembly. **(b)** QSim's trapezoidal-shaped vacuum chamber. The QSim chamber only has three available optical axes and there is not a direct way to access the y direction of the ion trap's principal axis which corresponds to the conventional z axes of a Cartesian coordinate system.

chamber assembly in order to maintain the low vacuum pressure. Based on the display of the MidiVac ion pump controller supplying the HV to the ion pump and the controller manual, we estimate that the pressure inside the UHV system is on the order of $\sim 1 \times 10^{-11}$ Torr. The QSim vacuum assembly has remained under vacuum for more than fourteen years and counting ever since the chamber was opened around 2008 to replace the Cadmium oven with two Yb ovens. In

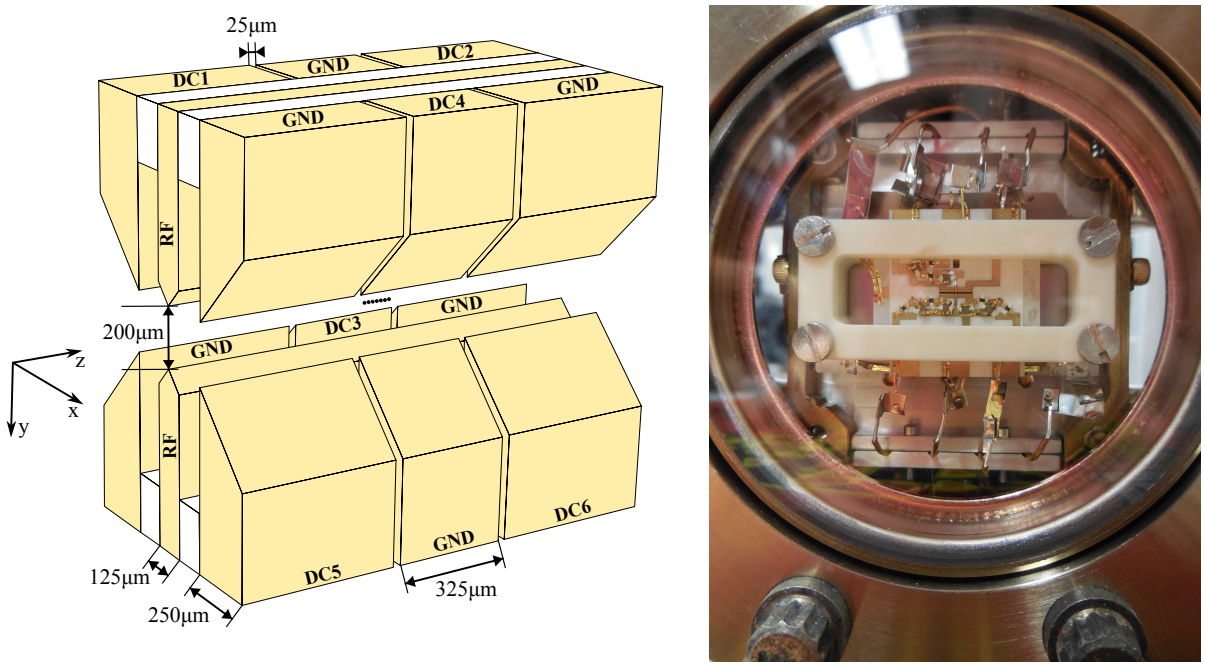
fact, the QSim chamber assembly was recently moved from the University of Maryland to Duke University (Summer 2023) and still remains under vacuum.

In addition, contained inside the vacuum chamber are two atomic source ovens containing Yb^+ metal flakes [25]. One atomic source is isotopically enriched with ^{171}Yb while the other is just a naturally abundant Yb source, i.e. ^{174}Yb. Both oven feedthrough connections exit from the bottom of the chamber (see Fig. 3.1a). The alligator connections (the two pairs of red and black wires) of the BNC-to-alligator cables can be seen in Fig. 3.1b; however, output of the power supply for the oven is only connected to the cable for the isotopically enriched oven. The left feedthrough pin is attached to the isotopically enriched Yb source. The QSim ion trap is centered just inside in the large diameter viewport flange, and there are two smaller diameter viewport windows mounted inside the two vacuum flanges that are each individually surround by a magnetic coil. A third coil is underneath the chamber (see Fig. 3.1b). The sum of the constant currents supplied to each coil generates an externally applied magnetic field that lifts the degeneracy between the Zeeman states within each hyperfine F manifold. The direction of this field defines the quantization axis for the ion(s).

Before moving on to discuss some features of the QSim ion trap, I would like to briefly mention some of the other visible components that are part of the experimental apparatus. In Fig. 3.1b, there are two different connections around the top of the vacuum chamber that supply the static (DC) and RF voltages to the corresponding trap electrodes, respectively. We have a 0.4 NA (numerical aperture) objective that is used to collect the emitted fluorescence from the ions. The collected light is imaged and focused onto either a EMCCD (electron multiplying charge-coupled device) camera or defocused and counted by a single-channel PMT (photomultiplier tube). A mirror that is mounted on a motorized flipper mount, placed in the imaging path,

enables us to easily switch between these two devices. We usually use the PMT to run daily calibrations for the experiment with one ion before switching over to the camera to take data with N trapped ions. Lastly, the final optical elements in each of the beam paths can be glimpsed. The half-inch diameter mirror that is closest to the imaging objective directs the beam called "Raman 1" to the ions while the other half-inch mirror that has a red thumb-screw aligns the beam called "Raman 2."

A linear RF trap confines ions in free space using both static and oscillating electric fields forming an effective 3D potential. QSim's linear RF trap was designed and hand-assembled by Martin Madsen [30]. The three-layer gold-plated segmented electrode trap geometry is illustrated in Fig. 3.2a. The front and back layers each have two segmented rows of static (DC) electrodes separated by a 5 mm by 200 µm rectangular gap. The DC layers are 25 mm$\times$20 mm$\times$0.25 mm alumina substrates in which the rectangular gap and the four additional slits separating the six electrodes in each layer were machined in the center. Only six out of the twelve DC electrodes are required to form the harmonic potential that confines the ions in the axial direction of the trap. As a result, the front and back layers of the ion trap each have three electrodes that are grounded and three electrodes that are wired to receive static voltages. In Fig. 3.2a, the static electrodes are labeled DC 1-DC 6 while the grounded electrodes are labeled "GND". The middle layer of the ion trap contains the two RF electrodes whose tips are separated by 200 µm. The voltage signals that are supplied to the RF electrodes form the oscillating quadrupole potential which confine the ions in the transverse direction. The RF electrodes are also machined in the center of a 20 mm$\times$25 mm$\times$0.125 mm alumina substrate. Uncoated alumina substrate spacers that are also 125 µm thick are placed in between the electrode layers to isolate electrically the gold-plated DC electrodes from the gold-plated RF electrodes. Finally, all five alumina substrate layers are held



(a) **(b)**

Figure 3.2. The QSim ion trap. **(a)** A sketch of QSim's ion trap electrode geometry is zoomed-in on the central region of the ion trap in order to see the three separate electrode layers better. Also, shown are the principle axes of the trap which are different from and not to be confused with the usual Bloch sphere (lab-frame) axes. **(b)** A close-up image of the actual trap in which one can observe the front layer of DC electrodes.

in place by two ceramic 4 mm thick mount bars that have four through-holes enabling the entire assembly to be mounted inside the vacuum chamber and centered in the 4.5 in diameter viewport flange window as shown in Fig. 3.2b.

Typically, the ion trap anisotropy is set such that the confining potential is much weaker in the axial direction in comparison to the transverse directions. As a result, trapped laser cooled ions form a 1D linear chain along the axial (z) direction of the ion trap. The electrode geometry of QSim's ion trap was designed to give full control of the position of the ions along all three directions of the trap. More specifically, by adjusting the static voltages applied to the DC electrodes, it allows us to rotate independently the principal axes of the trap and minimize micromotion from RF heating experienced by the ions. Generally, ions are aligned along the z axis in which micro-

motion is nulled. An eight channel Iseg EHS-80-05XK3 HV module supplies the static voltages to the six DC electrodes. This Iseg HV module is plugged into a MPOD mini-crate which can be connected to a network and interfaced with LabView. As a result, we have a LabView project that interfaces with the Iseg crate that allows us to actively set and observe the sensed values (voltage and current) on each Iseg HV channel output. Figure 3.3 displays screenshots of the LabView program that is used to control the ion trap's static voltages. The left-half of Fig. 3.3a shows two methods, "Set by Function" and "Set Directly" in which the static components of the confining trap potential can be controlled. The "Set Directly" method obviously corresponds to setting directly the voltage V_i on static electrode DC i whose positions are shown in Fig. 3.3c and where $i = 1, \ldots, 6$. In Fig. 3.3a, the area that is dimmed at the bottom corresponds to the "Set Directly" control. The "Set by Function" method which is selected and visible in Fig. 3.3a corresponds to changing the value of defined voltage parameters that are defined in terms of linear combinations of the DC electrodes. We primarily use the "Set by Function" method to configure the desired axial confinement of the trap and the additional electric field compensation. Table 3.1 highlights the voltage parameters that we call "Z push", "End Average" (EA), "Central Average" (CA), "End Near Vertical Difference" (ENVD), and "Central Difference" (CD) and shows how changing these values allows us to control the strength of the trap's axial confinement, to rotate the trap's transverse principle axes to minimize y mode coupling from the Raman beams, and to enable us to minimize the micromotion coupled to the x mode of motion. Figure 3.3c displays the set voltage of each static electrode as well as the actual sensed voltage and current measured by the Iseg crate which is a window tab shown in Fig. 3.3d.

Figure 3.3b displays the software control that is used when we wish to load ions into the trap. In addition to communicating with the Iseg crate, this LabView program is also connected to

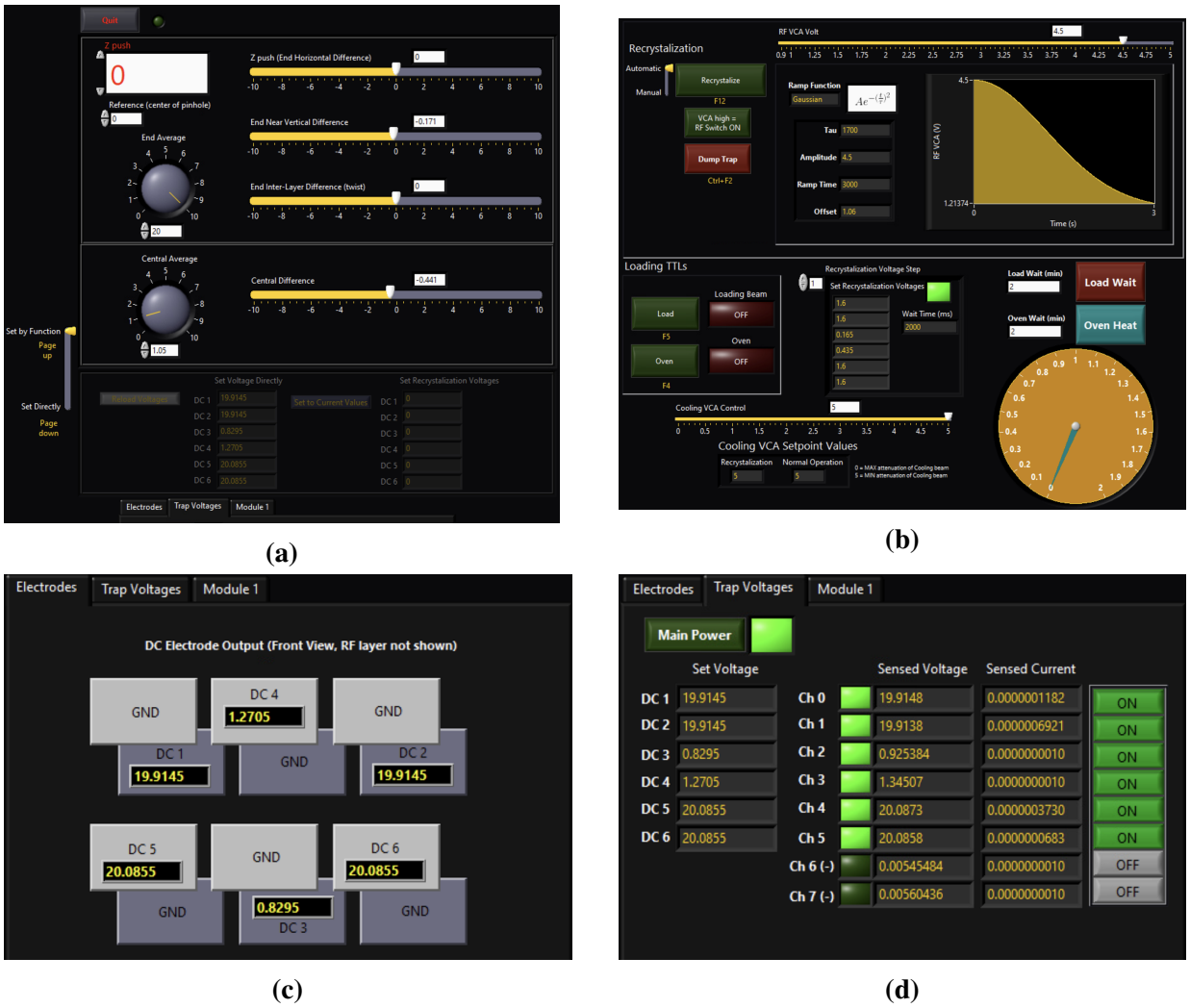


Figure 3.3. Iseg LabView control. **(a)** The DC electrode voltages can be changed either by using the "Set by Function" or the "Set Directly" method. **(b)** LabJack UE9 controls that send TTL triggers specific for loading ions. **(c)** The "Electrode" tab shows the set voltages on each DC electrode. Only the DC electrodes are drawn in the control program. The light gray-colored electrodes correspond to DC electrode layer observed in the objective window. The dark gray-colored electrodes, thus, correspond the DC electrode layer that the CW lasers pass through first. **(d)** The "Voltages" tab, also shows the set voltages on the six electrodes in addition to displaying the actual (sensed) voltages as measured by the MPOD crate. The sensed current values on each Iseg HV channel also shown on this tab.

a device called, a LabJack UE9, which is a commercial ethernet/USB data acquisition and control device. Two analog ports of the LabJack are used to unshutter the 399 nm beam path ("Load" button in Fig. 3.3b) and to turn on the current supplied to the oven ("Oven" button) when loading ions. When current is allowed to flow to the oven, the "Oven" button color changes to the bright

Parameter	Function	Use
End Average	$V_{\mathrm{EA}} = \frac{1}{4}(V_1+V_2+V_5+V_6)$	Controls the strength of the axial confinement of the ions.
Central Average	$V_{\mathrm{CA}} = \frac{1}{2}(V_3+V_4)$	Rotates the trap's transverse principal axes. Value is adjusted to minimize coupling to the y mode.
End Near Vertical Difference Central Difference	$V_{\mathrm{ENVD}} = \frac{1}{2}[(V_1+V_2) - (V_5+V_6)]$ $V_{\mathrm{CD}} = V_3 - V_4$	Controls the position of the ion along the x axis. Values of these two parameters are changed by the same amount and in the same direction in order to minimize micromotion along the x axis.
Z-push	$V_Z = \frac{1}{2}[(V_1+V_5) - (V_2+V_6)]$	Controls the position of the ion along the z axis. Typically, $V_Z = 0$ corresponding to the position of an ion centered at $z = 0$.

Table 3.1. Static voltage parameters. These are the voltage function definitions corresponding to the "Set by Function" method. We generally use these voltage variables to change the trap settings.

LED green and the needle of the yellow two minute countdown timer is engaged. The LabJack also has two 0–5 V DACs which are each connected to a voltage-controlled amplifier (VCA). One VCA controls the amount of RF power delivered to the Doppler cooling AOM while the other VCA is used to lower the RF power applied to the RF electrodes. In QSim, we have historically found that it is necessary to reduce both the RF and DC voltages applied to the trap electrodes resulting in a looser confining trap potential in order to load and initially cool larger numbers of ions. In the lab, we call this process recrystallization. When the "Recrystallize" button is pressed in the LabView program, the trap RF power is exponentially ramped down and the voltages on the DC electrodes are changed to the recrystallization values shown underneath the RF ramp profile on the right-side of Fig. 3.3b. It is important to remember to unlock the trap RF voltage PID just before lowering the RF and to remember to lock it again once all the ions have crystalized into a

linear chain.

In QSim, the oscillating RF potential is driven at about $\Omega_{RF}/(2\pi) \sim$38.8 MHz. The trap RF signal is generated from a HP8640B signal generator and is inductively coupled to a quarter-wave helical coaxial resonator (RF can) that is attached to a vacuum feedthrough located at the top of the vacuum chamber (see Fig. 3.1b). The RF can is a compact step-up transformer that amplifies the input RF voltage that is proportional to the resonator's quality factor Q. The RF can also acts as a bandpass filter in which transmission through the can is maximized when the frequency of the RF signal is at the resonant frequency of the can and filters out frequencies that are outside the can's frequency bandwidth.

The combination of using a static axial potential and oscillating RF quadrupole potentials in the transverse direction creates a confining pseudo-potential that is described by the 3D simple harmonic oscillator potential,

$$U_{trap} = \frac{m}{2}\left(\omega_x^2\, x^2 + \omega_y^2\, y^2 + \omega_z^2\, z^2\right), \tag{3.1}$$

where ω_x, ω_y, and ω_z are the trap secular frequencies along the principal axes of the trap. The values of the secular frequencies of the trap are dependent on the voltage on the RF electrodes, V_{RF}, and trap RF frequency, Ω_{RF}.

Unfortunately, fluctuations in both of these trap RF parameters can occur due to thermal and/or mechanical changes in the RF can which ends up altering the trap frequencies. In addition, when we load ions, the ion trap potential is relaxed by reducing the confinement in both the axial and transverse directions of the trap. In addition, we have found that it is easier to trap larger numbers of ions when the trap potential is weaker. As a result, both the DC and RF voltages applied to the trap electrodes are reduced when we load ions and then returned to their typical

values once the desired number of ions has been trapped. The changing of the trap parameters required for loading as well as turning on the oven and unshuttering the 399 nm beam is also controlled using the same LabView program, previously mentioned. The lowering and raising of the RF power going to the RF can introduce small changes in the trap frequencies. As a result, we lock the RF drive frequency from the HP8640B source to the resonance frequency of the RF can. In addition, when the power going to the RF electrodes is set at its high value which typically is the default position, the power flowing into the RF can is also stabilized. The implementation of both trap RF locks are discussed in Jake Smith's dissertation [31]. In addition, there are two temperature heating elements in order to keep the RF can and rectifier package (used for the RF power lock) temperatures stabilized. These temperature controllers are from Thorlabs.

3.2 Coherent Manipulation via Stimulated Raman Transitions

Having introduced how we can ionize, load, cool, initialize, and detect $^{171}Yb^{+}$ ions, this section presents the atom-laser interaction theory (the math) that describe coherent transitions between: only the spin (qubit) states, the spin states and one motional mode sideband, and lastly the spin states and two sidebands of motion.

The coherent laser interactions are described by stimulated Raman transitions in which two lasers at optical frequencies ω_1 and ω_2 are used. Consider the following three-level system shown in Fig. 3.4 in which Raman 1 off-resonantly couples the qubit $|\downarrow\rangle$ state to some intermediary excited state $|e\rangle$. Similarly, Raman 2 off-resonantly couples the qubit $|\uparrow\rangle$ state to the same intermediary excited state $|e\rangle$. The derivation of how the intermediary excited state $|e\rangle$ can be adiabatically eliminated resulting in an effective two-level system between the qubit states will

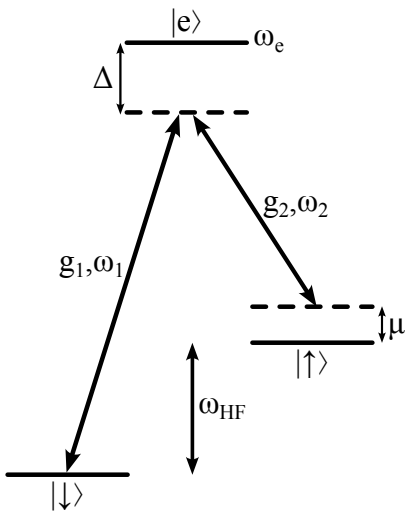


Figure 3.4. Λ system. The Λ system is used to describe how stimulated Raman transitions are driven between two low-lying levels which in this case are the qubit states of the ion, $|\downarrow\rangle$ and $|\uparrow\rangle$ by off-resonantly coupling each state to an intermediary excited state labeled $|e\rangle$. ω_{hf} is the hyperfine splitting between the two qubit states. Δ is the frequency detuning away from $|e\rangle$ and μ is the frequency detuning away from $|\uparrow\rangle$. g_1 and g_2 are the single-photon Rabi oscillation frequencies of Raman 1 and Raman 2, respectively.

not be derived here. Some good derivations of the stimulated Raman transitions can be found in Refs. [25, 32]. Instead, I will just briefly summarize how one goes from the three-level system, shown in Fig. 3.4, to an effective two-level system. In addition, the following is assumed unless explicitly stated otherwise: $\boldsymbol{\hbar = 1}$.

When the frequency detuning Δ from the excited state is sufficiently large compared to the single-photon Rabi frequencies g_1 and g_2 of the two lasers, coupling to the excited state can be adiabatically eliminated and the initial three-level system reduces to an effective two-level one. The atom-light interaction Hamiltonian for a single trapped ion is,

$$H = \frac{\Omega}{2}\left[S_+ e^{i(\boldsymbol{\Delta k}\cdot\boldsymbol{r}-\mu t+\phi)} + S_- e^{-i(\boldsymbol{\Delta k}\cdot\boldsymbol{r}-\mu t+\phi)}\right], \tag{3.2}$$

where Ω is the two-photon Rabi oscillation frequency, S_+ and S_- are the spin-1/2 raising and lowering operators respectively, $\boldsymbol{\Delta k}$ is the wave vector difference between the two Raman beams,

$\boldsymbol{r}$ is the position vector of the ion, $\mu = \omega_{hf} - \omega_L$ is the detuning of the Raman beat-note $\omega_L = \omega_1 - \omega_2$ from the hyperfine splitting ω_{hf} , and lastly, ϕ is the phase difference between the beams. In Eq. (3.2) the $S_\pm$ spin-1/2 operators act on the spin state of the ion while the $e^{\pm i\boldsymbol{\Delta k}\cdot\boldsymbol{r}}$ terms represents the coupling to the ion's motion. In QSim, the two Raman beams are oriented 45° to the ion(s) and 90° with respect to each other, resulting in a wave vector difference along the x-axis: $\boldsymbol{\Delta k} = \Delta k\,\hat{x}$. Taking into account the alignment of the Raman beams, the exponential terms that couple to the ion's motion become,

$$\begin{aligned}\exp\left[\pm i\boldsymbol{\Delta k}\cdot\boldsymbol{r}\right] = &\exp\left[\pm i\Delta k x\right] = \exp\left[\pm i\Delta k\left(x_0[ae^{-i\omega_x t} + a^\dagger e^{i\omega_x t}]\right)\right] \\ \approx &1 \pm i\eta\left(ae^{-i\omega_x t} + a^\dagger e^{i\omega_x t}\right),\end{aligned} \tag{3.3}$$

where the ion's position operator x has been expressed in terms of the phonon annihilation (a) and creation ($a^\dagger$) operators of its single vibrational mode, $x_0 = \sqrt{\hbar/(2M\omega_x)}$ is the zero-point spatial spread of the phonon normal mode that oscillates at the trap's secular frequency, ω_x, M is the mass of the $^{171}\mathrm{Yb}^+$ ion, and $\eta \equiv \Delta k x_0$ is defined as the Lamb-Dicke parameter. In writing Eq. (3.3), it is assumed that the ion has been well-cooled making its temperature low such that the Lamb-Dicke criterion is met in which the ion's motional wavepacket is much smaller than the Raman beat-note wavelength. The Lamb-Dicke limit can also be expressed as $\eta^2(2\bar{n}+1) \ll 1$ where $\bar{n}$ is the average phonon number of the vibrational mode. Under this limit, transitions that change the ion's $\bar{n}$ by zero or one quanta are dominant. Substituting Eq. (3.3) into Eq. (3.2) the Hamiltonian describing the interaction between the two Raman beams and the single trapped ion becomes:

$$\begin{aligned}H = \frac{\Omega}{2}\Big[&S_+\left(1 + i\eta\left[ae^{-i\omega_x t} + a^\dagger e^{i\omega_x t}\right]\right)e^{-i\mu t + i\phi} \\ &+ S_-\left(1 - i\eta\left[ae^{-i\omega_x t} + a^\dagger e^{i\omega_x t}\right]\right)e^{i\mu t - i\phi}\Big].\end{aligned} \tag{3.4}$$

3.2.1 Carrier Transitions

When $\mu = 0$, the Raman beat-note ω_L is set to ω_{HF}. Plugging $\mu = 0$ into Eq. (3.4) and applying a rotating-wave approximation (RWA) to ignore the phonon terms, the following Hamiltonian obtained is,

$$\begin{aligned} H_{carrier} \approx & \frac{\Omega}{2}\left[S_+ e^{i\phi} + S_- e^{-i\phi}\right] = \frac{\Omega}{2}\left[e^{i\phi}\left|\uparrow\right\rangle\left\langle\downarrow\right| + e^{-i\phi}\left|\downarrow\right\rangle\left\langle\uparrow\right|\right] \\ = & \frac{\Omega}{2}\left[X\cos\left(\phi\right) - Y\sin\left(\phi\right)\right] \\ = & \frac{\Omega}{2}\sigma_\phi, \end{aligned} \tag{3.5}$$

where σ_ϕ is defined as a spin operator, $X \equiv \sigma_x$ is the Pauli x matrix, and $Y \equiv \sigma_y$ is the Pauli y matrix. The resulting Hamiltonian, given by Eq. (3.5) describes a resonant carrier transition between the qubit states where ϕ, defines the rotation axis of the spin vector.

3.2.2 Sideband Transitions

When the Raman beat-note detuning frequency is tuned near a vibrational mode frequency, also known as a sideband mode, the stimulated Raman transition will couple to both the ion's spin and motion. For one ion in the x direction, there is only a single vibrational mode, and thus, only two sidebands: a red sideband (RSB) and a blue sideband (BSB). For a linear chain of N ions in the x direction, there are N normal vibrational modes where the center-of-mass (COM) x vibrational mode frequency, $\omega_{x_{COM}}$, has the largest magnitude (sideband is the furthest away from the carrier) while the zig-zag x vibrational mode frequency, $\omega_{x_{zig-zag}}$, has the smallest magnitude. For the moment though, we will continue to discuss applying sideband transitions to one ion.

Driving a RSB transition corresponds to a red beat-note detuning, $\mu_r = -\omega_x - \delta$, where $\delta \ll \omega_x$ and corresponds to flipping the ion's spin as well as decreasing the vibrational quanta of the ion's x-motional mode by one. The frequency δ in the expression for μ_r detunes the red Raman beat-note from driving the RSB transition on-resonance. Using Eq. (3.4), the single ion Hamiltonian for driving an off-resonant RSB transition is,

$$\begin{aligned} H_{rsb} = \frac{\Omega_r}{2}\Big[&S_+\left(1 + i\eta\left[ae^{-i\omega_x t} + a^\dagger e^{i\omega_x t}\right]\right)e^{-i\mu_r t + i\phi_r} \\ &+ S_-\left(1 - i\eta\left[ae^{-i\omega_x t} + a^\dagger e^{i\omega_x t}\right]\right)e^{i\mu_r t - i\phi_r}\Big] \end{aligned} \tag{3.6a}$$

$$\begin{aligned} = \frac{\Omega_r}{2}\Big[&S_+\left(e^{i(\omega_x+\delta)t + i\phi_r} + i\eta a e^{i\delta t + i\phi_r} + i\eta a^\dagger e^{i(2\omega_x+\delta)t + i\phi_r}\right) \\ &+ S_-\left(e^{-i(\omega_x+\delta)t - i\phi_r} - i\eta a e^{-i(2\omega_x+\delta)t - i\phi_r} - i\eta a^\dagger e^{-i\delta t - i\phi_r}\right)\Big] \end{aligned} \tag{3.6b}$$

$$\approx \frac{i\eta\Omega_r}{2}\left[ae^{i(\delta t+\phi_r)}|\uparrow\rangle\langle\downarrow| - a^\dagger e^{-i(\delta t+\phi_r)}|\downarrow\rangle\langle\uparrow|\right], \tag{3.6c}$$

where ϕ_r is the RSB beat-note phase and a RWA was applied to obtain Eq. (3.6c).

Driving a BSB transition corresponds to a blue beat-note detuning, $\mu_b = +\omega_x + \delta$, where $\delta \ll \omega_x$ still is the case and corresponds to the ion's vibrational quanta increasing by one quanta as well as flipping the spin. Similarly, the frequency δ in the expression for μ_b detunes the blue Raman beat-note from driving the BSB transition on-resonance. Using Eq. (3.4), the single ion Hamiltonian for driving an off-resonant BSB transition is,

$$\begin{aligned} H_{bsb} = \frac{\Omega_b}{2}\Big[&S_+\left(1 + i\eta\left[ae^{-i\omega_x t} + a^\dagger e^{i\omega_x t}\right]\right)e^{-i(\mu_b t - \phi_b)} \\ &+ S_-\left(1 - i\eta\left[ae^{-i\omega_x t} + a^\dagger e^{i\omega_x t}\right]\right)e^{i(\mu_b t - \phi_b)}\Big] \end{aligned} \tag{3.7a}$$

$$\begin{aligned} = \frac{\Omega_b}{2}\Big[&S_+\left(e^{-i(\omega_x+\delta)t + i\phi_b} + i\eta a e^{-i(2\omega_x+\delta)t + i\phi_b} + i\eta a^\dagger e^{-i\delta t + i\phi_b}\right) \\ &+ S_-\left(e^{i(\omega_x+\delta)t - i\phi_b} - i\eta a e^{i\delta t - i\phi_b} - i\eta a^\dagger e^{i(2\omega_x+\delta)t - i\phi_b}\right)\Big] \end{aligned} \tag{3.7b}$$

$$\approx \frac{i\eta\Omega_b}{2}\left[a^\dagger e^{-i(\delta t-\phi_b)}|\uparrow\rangle\langle\downarrow| - ae^{i(\delta t-\phi_b)}|\downarrow\rangle\langle\uparrow|\right], \tag{3.7c}$$

where ϕ_b is the BSB beat-note phase and a RWA was applied to obtain Eq. (3.7c).

In Eq. (3.6c) and Eq. (3.7c) the ion's spin raising and lowering operators have been rewritten in Dirac notation which makes the action of driving an off-resonant sideband transition clearer. When $\delta = 0$ in these equations, the Raman beat-note is tuned to the resonant frequency of the sideband transition.

3.2.3 Resolved Sideband Cooling

So far, we have already discussed Doppler cooling the qubit states of the ion, but this process doesn't cool the ion's vibrational modes of motion. We can further cool the ion's vibrational mode in the x-direction to its motional ground state using a technique called resolved sideband cooling. From Eq. (3.6c), a RSB transition will flip the spin state and remove one quanta from the ion's motional mode. The ground state of the motional mode corresponds to $\bar{n} = 0$. Once the ion is optically pumped into its $|\downarrow\rangle$ state, the sideband cooling process is as follows:

1. A resonant RSB transition is applied for a duration equivalent to a π pulse such that the ion's spin flips completely from "down" to "up" in addition to decreasing the phonon number: $|\downarrow, n\rangle \longrightarrow |\uparrow, n-1\rangle$.

2. Then, a resonant carrier π pulse is applied which changes the ion's state from $|\uparrow, n-1\rangle$ to $|\downarrow, n-1\rangle$.

The sequence of a RSB π pulse followed by a carrier π pulse is continued until the ion's state is $|\downarrow, 0\rangle$. Alternatively, the optical pumping beam can be applied instead of a carrier π pulse to return the ion's spin state back to $|\downarrow\rangle$ without changing its the motional quanta. In practice, the sideband cooling process consists of 16 cycles of applying the alternating sequence of a RSB π

pulse and optical pumping. In addition, the duration of the RSB π pulse is varied in order to efficiently cool the motional mode initially starting from any value of n [33].

3.3 Mølmer-Sørenson Interaction to the Long-Range Ising Model

So far, we have only been discussing applying the Raman beams at a single beat-note frequency that is tuned to off-resonantly drive a RSB, carrier, or BSB transition with one ion. When both the red and blue Raman beat-notes are applied at the same time, a bichromatic spin-dependent force is exerted on the ion. Utilizing the Mølmer-Sørenson (MS) scheme [34], effective Ising interactions can be generated by shining the bichromatic laser tones on a linear chain of N ions. The MS Hamiltonian of this interaction for a single ion will be derived next, and then generalized for N ions.

We will first consider the Hamiltonian describing the single ion-light interaction stemming from two Raman beat-notes which are symmetrically detuned from the carrier and off-resonantly detuned from the first-order sidebands. The bichromatic spin-dependent force Hamiltonian is just the sum of the RSB Raman transition, Eq. (3.6a), and the BSB Raman transition, Eq. (3.7a). Comparing the expressions of the red and blue beat-note detunings, we see the following relation: $\mu = \mu_b = -\mu_r$. Let us also assume that the two-photon Rabi frequencies, Ω_r and Ω_b, are the same: $\Omega = \Omega_b = \Omega_r$. Adding Eq. (3.6a) and Eq. (3.7a) together, the MS Hamiltonian for one ion using Ω and μ is:

$$\begin{aligned} H_{MS} =& H_{rsb} + H_{bsb} \\ =& \frac{\Omega}{2}\Big[S_+\left(1 + i\eta\left[ae^{-i\omega_x t} + a^\dagger e^{i\omega_x t}\right]\right)\left(e^{i\mu t + i\phi_r} + e^{-i\mu t + i\phi_b}\right) \\ &+ S_-\left(1 - i\eta\left[ae^{-i\omega_x t} + a^\dagger e^{i\omega_x t}\right]\right)\left(e^{-i\mu t - i\phi_r} + e^{i\mu t - i\phi_b}\right)\Big] \end{aligned}$$

$$
\begin{aligned}
=\frac{\Omega}{2}\Big[& S_+\left(e^{i\mu t+i\phi_r}+e^{-i\mu t+i\phi_b}\right)+S_-\left(e^{i\mu t-i\phi_b}+e^{-i\mu t-i\phi_r}\right) \\
& +\eta\left(ae^{-i\omega_x t}+a^\dagger e^{i\omega_x t}\right)\Big(S_+\left[e^{i\mu t+i\phi_r+i\frac{\pi}{2}}+e^{-i\mu t+i\phi_b+i\frac{\pi}{2}}\right] \\
& +S_-\left[e^{i\mu t-i\phi_b-i\frac{\pi}{2}}+e^{-i\mu t-i\phi_r-i\frac{\pi}{2}}\right]\Big)\Big],
\end{aligned}
\tag{3.8}
$$

where the factors of $\pm i$ in the second line are rewritten as factors of $e^{\pm i\frac{\pi}{2}}$ in the following line. As seen in the last line of Eq. (3.8), the first term of H_{MS} is a carrier term without phonon operators while the second term couples to both the ion's spin and motion. At this point, it becomes more convenient to replace ϕ_r and ϕ_b in Eq. (3.8) with ϕ_s and ϕ_m using the following relations:

$$
\phi_r+\pi/2=\phi_s+\phi_m \qquad \& \qquad \phi_b+\pi/2=\phi_s-\phi_m. \tag{3.9}
$$

Using Eq. (3.9) and some simplifying, H_{MS} becomes,

$$
\begin{aligned}
H_{MS} &= \frac{\Omega}{2}\Big[\left(S_+e^{i(\phi_s-\frac{\pi}{2})}+S_-e^{-i(\phi_s-\frac{\pi}{2})}\right)\left(e^{i(\mu t+\phi_m)}+e^{-i(\mu t+\phi_m)}\right) \\
&\qquad +\eta\left(ae^{-i\omega_x t}+a^\dagger e^{i\omega_x t}\right)\left(S_+e^{i\phi_s}+S_-e^{-i\phi_s}\right)\left(e^{i(\mu t+\phi_m)}+e^{-i(\mu t+\phi_m)}\right)\Big] \\
&= \Omega\cos\left(\mu t+\phi_m\right)\Big[\sigma_{\phi_s-\frac{\pi}{2}}+\eta\sigma_{\phi_s}\left(ae^{-i\omega_x t}+a^\dagger e^{i\omega_x t}\right)\Big],
\end{aligned}
\tag{3.10}
$$

where σ_ϕ is the spin operator, ϕ_s is called the spin phase, and ϕ_m is known as the motion phase. Phases ϕ_s and ϕ_m are defined in terms of the RSB and BSB beat-note phases as:

$$
\phi_s=\frac{\phi_r+\phi_b+\pi}{2} \qquad \& \qquad \phi_m=\frac{\phi_r-\phi_b}{2}. \tag{3.11}
$$

The spin phase defines the angle of the spin operator in the xy-plane of the Bloch sphere while the motion phase describes the phase of the optical beat-notes. These expressions for ϕ_s and ϕ_m assume a "phase-sensitive" Raman beam geometry which is the configuration in this lab. A phase-sensitive configuration means that the RSB and BSB beat-note wave vectors propagate in the same direction while a "phase-insensitive" geometry is the opposite. In QSim, we have

defined the phases of the red and blue beat-notes as $\phi_r = 0$ and $\phi_b = \pi$ resulting in $\phi_s = \pi$ and $\phi_m = -\pi/2$. Substituting in these phase values into Eq. (3.10), we obtain:

$$H_{MS} = -\Omega \sin(\mu t)\left[Y + \eta X\left(a e^{-i\omega_x t} + a^\dagger e^{i\omega_x t}\right)\right]. \tag{3.12}$$

In general, we usually work with N ions corresponding to N vibrational modes in the x direction. All of the single ion Hamiltonians that have been discussed so far can be generalized for a system of N ions. The i^{th} ion x-coordinate position operator, x_i and the product $\Delta k x_i$ are written as,

$$x_i = \sum_{m=1}^{N} b_{im} x_{0m}\left(a_m e^{-i\omega_m t} + a_m^\dagger e^{i\omega_m t}\right), \tag{3.13}$$

$$\Delta k x_i = \sum_{m=1}^{N} \eta_{im}\left(a_m e^{-i\omega_m t} + a_m^\dagger e^{i\omega_m t}\right), \tag{3.14}$$

where b_{im} is the normal mode eigenvector component for ion i in mode m, $x_{0m} = \sqrt{\hbar/(2M\omega_m)}$ is the zero-point spatial spread of the m^{th} mode with frequency ω_m, M is still the mass of a single $^{171}\text{Yb}^+$ ion, $\eta_{im} = \Delta k b_{im} x_{0m}$ is the Lamb-Dicke parameter for ion i in mode m, and a_m, $a_m^\dagger$ are the mode m phonon annihilation and creation operators. Finally, the Mølmer-Sørenson Hamiltonian describing one pair of off-resonant symmetrically detuned sideband beat-notes, $\pm\mu$, applied to a linear chain of N ions is,

$$H_{MS} = -\sum_{i,m} \eta_{im}\Omega_i \sin(\mu t) X_i\left(a_m e^{-i\omega_m t} + a_m^\dagger e^{i\omega_m t}\right), \tag{3.15}$$

where Ω_i is the two-photon sideband Rabi frequency of the i^{th} ion and $X_i \equiv \sigma_i^x$ is the Pauli x operator for ion i. In comparison to the single ion H_{MS}, the generalization of the off-resonant carrier term for N ions, $-\Omega_i \sin(\mu t) Y_i$ where $Y_i \equiv \sigma_i^y$ is the Pauli y operator for ion i, has been dropped in Eq. (3.15) since $\Omega \ll \mu$.

The time-evolution of H_{MS} (Eq. (3.15)) is described by the Magnus expansion of the unitary operator, $U(t)$:

$$U(t) = \exp\left[-i\int_0^t H_{MS}(t_1)\,dt_1 - \frac{1}{2}\int_0^t dt_1 \int_0^{t_1} \left[H_{MS}(t_1),\, H_{MS}(t_2)\right]\,dt_2\right], \tag{3.16}$$

where only the first two terms of the Magnus expansion are non-zero. Now in QSim, in which we are interested in the dynamics as a function of time, it is the second term in Eq. (3.16) that contains the spin-spin interactions. By operating in the "dispersive" regime ($|\delta_{im}| \gg \eta_{im}\Omega_i$) in which the Raman beat-note detuning is far away from any of the motional sideband frequencies in comparison to any of the sideband Rabi frequencies and taking the long time limit, the unitary time-evolution operator of the N ion Mølmer-Sørenson Hamiltonian can be approximated as,

$$U(t) \approx \exp\left[-i\left(\sum_{i<j,m} \frac{\Omega_i\Omega_j\eta_{im}\eta_{jm}\omega_m}{\mu^2-\omega_m^2} X_iX_j\right)t\right] = \exp\left[-i\left(\sum_{i<j} J_{ij}X_iX_j\right)t\right], \tag{3.17}$$

where J_{ij} is the Ising coupling, or spin-spin interaction strength, between ion i and j and X_i, X_j are the x Pauli operators of the i^{th} and j^{th} ion, respectively. Equation (3.17) describes the time-evolution of a static long-range Ising Hamiltonian,

$$H_{Ising} = \sum_{i<j} J_{ij}X_iX_j, \tag{3.18}$$

$$J_{ij} \sim \frac{J_0}{|i-j|^\alpha}, \tag{3.19}$$

where J_{ij} as a function of ion separation can be approximated as a decaying power law described by exponent α and interaction strength J_0. Eq. (3.18) is the "native" Hamiltonian that arises from the simultaneous application of off-resonantly detuned RSB and BSB beat-notes illuminating a linear chain of N ions.

As a word of caution, J_0 is not often used to represent the same descriptor of how spin-spin interactions. By "descriptor," I mean that sometimes J_0 is defined in a paper as representing

the average coupling, and in another paper, it might represent the maximum Ising coupling. J_0 sometimes is used to denote the decaying power-law fit amplitude. However, in this dissertation and in the last few published papers in QSim, we have been consistent with defining J_0 as the average nearest-neighbor coupling, often denoted as J_{avgNN}.

3.3.1 Tuning J_{ij} to Change α

Equation (3.20) gives the mathematical expression for the Ising coupling strength between the i^{th} and j^{th} ion:

$$\begin{aligned} J_{ij} &= \Omega_i \Omega_j \sum_{m=1}^{N} \frac{\eta_{im}\eta_{jm}\omega_m}{\mu^2 - \omega_m^2}, \\ &= \Omega_i \Omega_j \Omega_R \sum_{m=1}^{N} \frac{b_{im} b_{jm}}{\mu^2 - \omega_m^2}, \end{aligned} \tag{3.20}$$

which corresponds to the coefficient in Eq. (3.17) that is multiplied to $X_i X_j$ in the summation. In Eq. (3.20), $\Omega_R = \hbar(\Delta k)^2/(2M)$ denotes the recoil frequency associated with the transfer of momentum $\hbar\,\Delta k$ to a single $^{171}\text{Yb}^+$ ion. The expressions for the Lamb-Dicke parameters describing the coupling of each ion (i and j) in mode m is utilized to rewrite the following product in the summation, $\eta_{im}\eta_{jm}\omega_m = \Omega_R b_{im} b_{jm}$. As a result, the expression for J_{ij} given in terms of the second line of Eq. (3.20) provides a clearer intuition for understanding the Ising interaction between different pairs of ions.

An important characteristic to note about Eq. 3.20 is the dependence of the Raman beat-note detuning μ. This beat-note detuning is the symmetric off-resonant detuning from the first-order sidebands. The first-order motional mode RSB and BSB correspond to COM x transverse normal mode which is the furthest away from the carrier. Recall that μ is defined as, $\mu = \pm(\omega_x + \delta)$, where frequency δ is the symmetric detuning from the sidebands (SB). In practice, we make sure

to keep the value of δ at least three times the average SB on-resonance Rabi frequency. This setting usually corresponds to an inverse power-law exponent $\alpha \sim 1$.

However, δ is one of two parameters for fixed N that can be used to tune the spin-spin interactions in order to tune α which describes the range of interactions. Increasing δ also increases α, but the average nearest-neighbor coupling, J_{avgNN}, becomes slower. If the value of J_{avgNN} becomes too slow, for instance $\leq 2\pi\times(200\,\mathrm{Hz})$, then we risk not being able to observe the full evolution of the dynamics since the experiment must be run longer. Unfortunately, decoherence sets a limit to the maximum evolution time in which a signal is distinguishable from noise.

The other parameter that can be used to tune the J_{ij} interactions is the strength of the axial confining potential, also known as the axial COM trap frequency ω_z. The axial trap frequency is set by the end average voltage function V_{EA}. In general, we usually set the V_{EA} based on how many ions with which we wished to run experiments. For example, the end average voltage of the trap electrodes for 15 ions to be held in a linear chain is about 7 V, corresponding to a medium axial confining potential and a trap frequency $\omega_z \sim$0.5 MHz. In comparison, for 25 ions the end average voltage is decreased to 3 V and $\omega_z \sim 0.34\,\mathrm{MHz}$. However, for tuning the Ising interactions, decreasing ω_z for fixed N and δ will increase both α and J_{avgNN}. Weakening the axial trap potential decreases the transverse normal mode frequency bandwidth in which more motional modes participate in the interaction.

3.4 355 nm Pulsed-Laser

We use a 4 W 355 nm mode-locked pulsed-laser (a Coherent Paladin) to drive coherent Raman operations and to generate site dependent fourth-order AC Stark shifts that directly change

the addressed ion's qubit frequency by the strength of the AC SS. The laser pulses, or comb teeth, exiting from the output of the Paladin system have a pulse duration of about $\sim$14 ps and a repetition rate, $\omega_{rep}/(2\pi) \sim$120.245 MHz.

I will begin by first giving a brief general overview of the different parts of the 355 nm optical setup and the reason that they are important before presenting the actual design. I generally tend to think about the 355 nm pulsed-laser as if it were a CW laser even though it is not one. As a result, I will tend to discuss the 355 nm laser as a "beam" or as an individual laser pulse rather than as a "frequency comb" or a train of pulses. However, I will stick to the frequency comb representation when I discuss the beat-note stabilization feed-forward lock which is crucial for maintaining the optical coherence between the Raman 1 and Raman 2 since the coherence in the interactions is imparted onto the coherence of the ions.

The 355 nm optical setup can be broken down into two categories: beams and locks. From the previous discussion about the coherent manipulation of a system of trapped ions, we know that the main (or global) 355 nm beam path must be broken up into two paths. One path is for the individual addressing beam that applies a fourth-order differential Stark shift to the illuminated ion's qubit splitting. The individual addressing beam is used to drive single ion rotations (SIRs), enabling the ability to initialize an arbitrary N-ion product state [35] or to probe correlation spreading using local interferometric schemes [36]. In addition, the individual addressing beam can be used to generate an arbitrary ion-dependent z magnetic field term expanding the quantum Hamiltonian simulation toolbox [36, 37]. The other beam path is for driving global (illumination of all the ions) stimulated Raman transitions in order to generate pure collective-spin rotations, generate long-range spin-spin interactions, or a combination of both. To realize these kinds of interactions requires that the global Raman path be further split into two, forming the

paths of Raman 1 and Raman 2 which each pass through AOMs. Now focusing on the stabiliza-

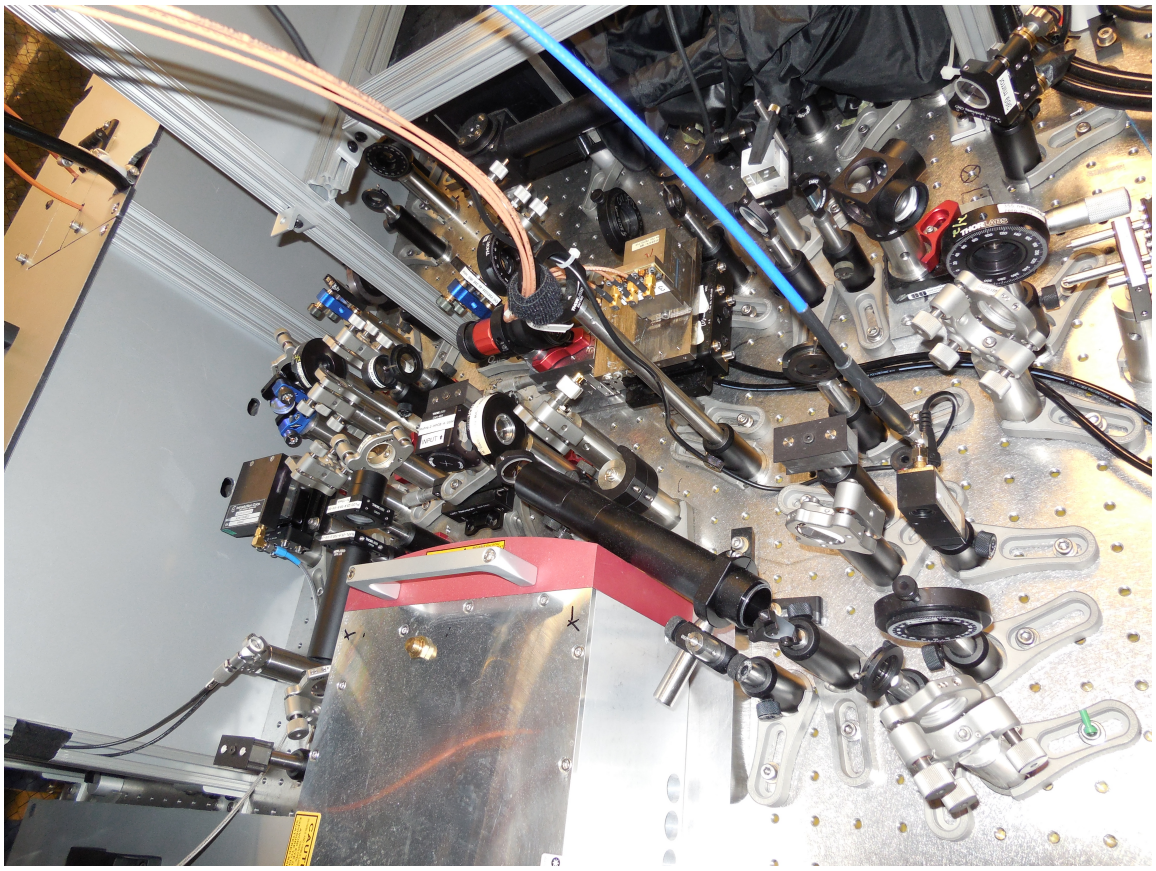


Figure 3.5. 355 nm optics outside of Raman enclosure.

tion locks in the 355 nm optical layout, there are three main factors that will affect our ability to realize coherent atom-laser interactions. These elements, primarily with respect to the global Raman beams, are the beat-note frequency, beam intensity and beam pointing. In regard to the individual addressing beam, laser intensity is an important factor, but this aspect will be discussed later in the section dedicated to the beam. The beat-note frequency or rather the phase coherence requirement for the individual addressing beam is less stringent in comparison to stimulated Raman transitions [35]. Both individual addressing beam's phase coherence and beam-positioning aspects can be provided for through the control of the acousto-optic deflector (AOD) that is an essential part of its optical setup. Similarly, these details will also be discussed in the individual

addressing beam section of the dissertation. Returning to the brief discussion of the three major properties influencing the applied Raman interactions, we incorporate three active stabilization schemes to address each factor. The active stabilization of the beat-note frequency and the noise-eater intensity lock will be briefly discussed first since these schemes have been well-documented by previous members of the lab.

The beat-note frequency between the two Raman frequency combs is stabilized by feeding forward any change in the measured Paladin repetition rate to the RF frequency of Raman 1's AOM. This beat-note feed forward lock is based on the beat-note stabilization scheme proposed in Ref. [38] and is well documented in Ref. [32]. The intensity stabilization lock also involves an AOM that "eats" the noise measured on the zeroth-order beam (the main global 355 nm beam) and instead puts the noise in the first-order diffracted beam which is not used at all in the setup. When the noise-intensity is locked, the overall power transmitted to the Raman beams is a few percent lower than when the intensity is unlocked, but we observe a more consistent Rabi frequency throughout the day especially if we let the 4 W laser thermalize at full power for at least an hour before trying optimizing any alignment or beginning calibrations for the day. For a more complete discussion regarding the noise-intensity lock that has relatively recently been implemented please see Ref. [3].

3.4.1 Beam-Pointing Stabilization

The last active stabilization lock addresses beam-pointing fluctuations at the position of the trapped ions that was realized by redesigning the Raman optics. When I first joined QSim, the lab was beginning to think about redesigning their current, now previous, Raman setup. A redesign

of the Raman optics was desired due to several factors. First, the beam paths of Raman 1 and Raman 2 were very long and, as a result, the interferometric area enclosed by the two paths was large. See Jake Smith's dissertation for a diagrams of the previous Raman setup [31]. This configuration is problematic for the coherence of the phase-sensitive Mølmer-Sørenson interactions realized in the experiment. Longer path lengths are sensitive to air flow, thermal fluctuations, and mechanical drifts that can result in beam pointing, phase, and intensity noise. Another problematic feature in the previous design, was astigmatism of the beam profile at the ion plane. The location of the beam's horizontal waist versus its vertical waist corresponded to displacing the last focusing lens along the optical axis by about 0.426 in=10.82 mm [31]. Lastly, the alignment of the Raman beams to the ions was difficult since the final mirror in each path was quite a distance away from the chamber. See Fig. 3.4 in Ref. [31] for a diagram of the previous Raman beam path leading up to the chamber and Sec. 3.2.3.2 in Ref. [32] regarding aligning the beams in the previous design. A redesign of the 355 nm optics was clearly needed and was installed in May 2018. Many passive measures were included in the new design to improve the overall stability of the setup, in addition to, achieving a larger horizontal focused beam waist at the ion plane. These elements include:

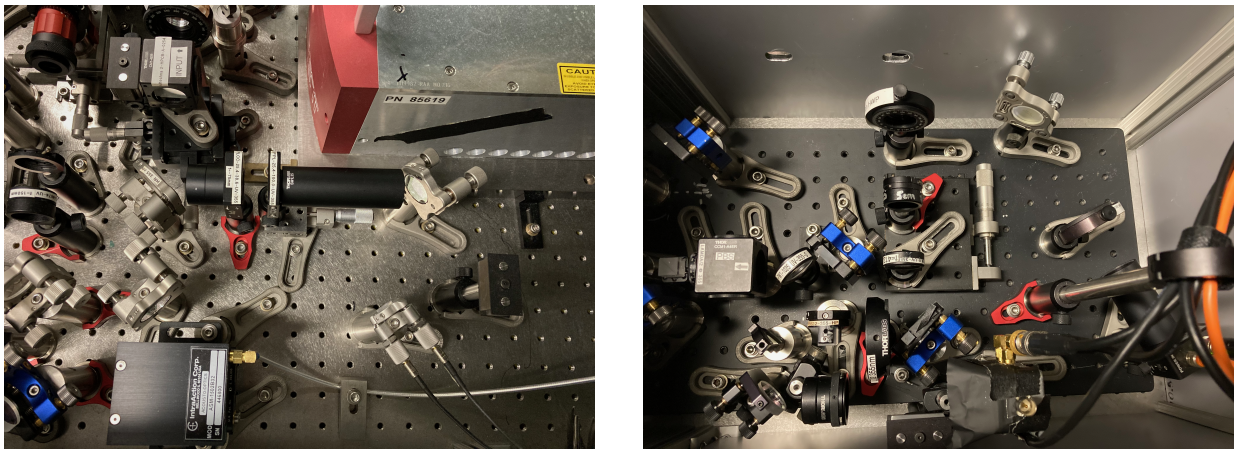
- shortening the overall length of each Raman path,
- minimizing the interferometric area enclosed by the two paths,
- mounting the 355 nm pulsed-laser on a thicker aluminum baseplate designed by Joe Britton,
- placing the new Raman optical setup on a custom-shaped Thorlabs breadboard and enclosing the design in an 8020 "castle,"
- using optics with higher-quality surfaces and better damage thresholds for pulsed high-power UV light at 355 nm,

- water cooling the Raman AOMs,
- assembling the Raman optics in a configuration that is easier to align or to optimize the alignment of,
- utilizing two sets of beam shaping optics that shape the horizontal beam profile separately from the beam's vertical profile, and
- incorporating 4f optical relays enabling the plane each Raman AOM's center to be imaged onto the plane of the ions.

A 4f system represents two telecentric configurations placed back-to-back. Each lens of focal length f, is placed such that there is one focal length separation in the front and in the back. This configuration allows the mapping of lateral displacement to angular deviations, or vice versa. Using this mapping and following a similar technique used by the Laser Interferometer Gravitational-Wave (LIGO) system [39], we implement a beam-pointing stabilization scheme that locks the beam pointing at a plane corresponding to the center of each Raman AOM. In turn each Raman AOM center's plane is imaged at the plane of the ions in both the horizontal and vertical directions by configuring the beam shaping lenses in "4f" optical relays.

In order to stabilize the beam pointing at the plane of the AOMs, three additional optical elements are required: a focusing lens, a quadrant detector, and a mirror mounted in an optical mount that has piezo-actuated horizontal and vertical knobs. Any angular deviation from the laser output is transformed into lateral displacements using a spherical lens whose quoted focal length is f =412.3 mm that is placed one focal length before the AOMs. A quadrant photodetector is also placed one focal length away from this f=412.3 mm lens in order to measure the changes in the beam. Figure 3.6 shows the corresponding optical setup broken up into two chunks: global optics that are outside of the "Raman castle" and optics that immediately on the other side of the

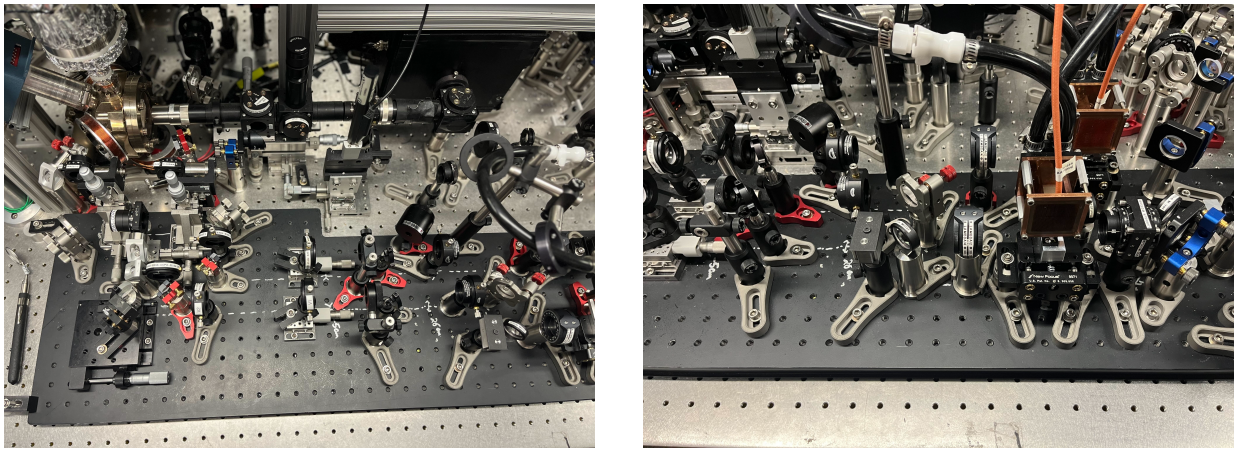
8020 panel. The ion plane is then mapped to the focus of the Raman AOMs by utilizing a 4f



(a) **(b)**

Figure 3.6. Beam-pointing optical system.

optical relays for shaping the beam profiles in the horizontal and vertical directions. Figure 3.7 shows pictures of the Raman beam shaping optics that are after the Raman AOMs.



(a) **(b)**

Figure 3.7. Raman beam paths.

3.4.2 Individual Addressing Beam

We have a tightly focused individual addressing beam, nicknamed “the poke beam,” that is sent down the imaging objective and applies a fourth-order AC Stark shift (SS) [35] to a specified

ion i in the trapped N-ion chain. The derivation of this fourth-order SS can be found in Ref. [35] and will not be discussed in this work. Instead, the implementation and application of the individual SS beam will be presented since it plays an essential role in the experiment presented in Ch. 6. The beam path of the individual addressing beam will be summarized first.

As previously mentioned, the main 355 nm beam is separated into two paths by the first PBS cube inside the Raman enclosure. The HWP that is immediately in front of this PBS is set such that the majority of the 355 nm light is reflected into the global Raman path. The poke beam path continues through the first PBS to a D-mirror which directs the beam out of the Raman castle by means of a small hole that was drilled in the 8020 panel. This is the same 8020 panel that the global 355 nm beam uses to enter the Raman box. When the poke beam exits the Raman enclosure it is guided by several mirrors to the input of the AOD. The amount of power that is typically sent/measured going to the poke beam path is about $\sim$50 mW. Generally, when we wish to measure the power being sent to the poke beam AOD, it is easier to measure the power right before the beam exits through the 8020 panel. Assuming that the high-power HWP is rotated such that the majority of the power is transmitted through the high-power PBS, it is highly recommend that the power be minimized by rotating the HWP before taking that section of the Raman enclosure wall out. At high power, the power measured after the noise easter AOM at the entrance of the Raman box can be about 3 W. It is also recommended that once the global 355 nm power is at a minimum, that either the high-power power meter be secured to the Raman breadboard using a slotted base with the post holder attached so that one can safely focus on rotating the HWP without mishap, or have a second person rotate the HWP and read the power measurement while the other person holds the power meter head in the poke beam path. Unless the 355 nm optical setup is changed from how it was setup at the University of Maryland, there is not enough space

to safely measure the poke beam path power holding the power meter and rotating the HWP all while trying to read the power measurement. Something will get bumped, burnt, or both.

Unlike in the Raman beam paths that have the centers of the AOMs placed at the focus of the 412.3 mm lens, the individual addressing beam's AOD is placed well after the focus of that lens. The AOD is not imaged to the plane of the 412.3 mm lens. As a result, the individual addressing beam can be aligned to a specific ion by setting the RF frequency of the AOD's diffracted first-order beam. Correspondingly, the strength of the SS experienced by the ion can be tuned by adjusting the RF power at that center frequency. The RF signal sent to the individual addressing beam AOD is generated by the second output channel of the same AWG that controls Raman 2's AOM. Since both the global Raman interactions and the individual Stark shifts are generated using the same clock reference of the AWG, synchronization between the two operations is easily satisfied through the AWG. In addition, the poke beam directly shifts the qubit's hyperfine frequency by the AC SS that is applied. The individual addressing beam does not generate an actual coherent population transfer, such as a spin flip, but rather, an "effective" or approximated "spin flip" since the individually addressed ion's qubit splitting is no longer resonant with the detection beam. As a result if one were to try to measure the Stark shifted ion, it would appear "dark." This result will become clearer when we, later on, discuss the calibration and application of the poke beam on a single ion.

Since the frequency applied to the AOD will map to a specific ion's position in a chain of N ions, the individual addressing beam must be tightly focused. When the poke beam exist the Raman enclosure, it is collimated by a f=150 mm lens (LA4874-UV) before going through a x5 beam expander (BE05-355) that is mounted of a three-axis translation stage. We have not had to adjust the micrometers on this translation stage very often. We do adjust the focus of the

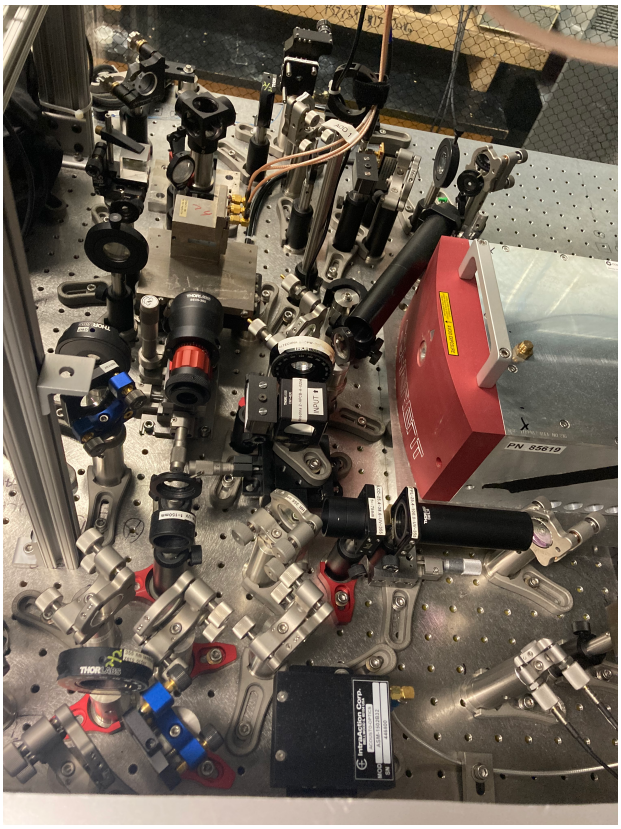
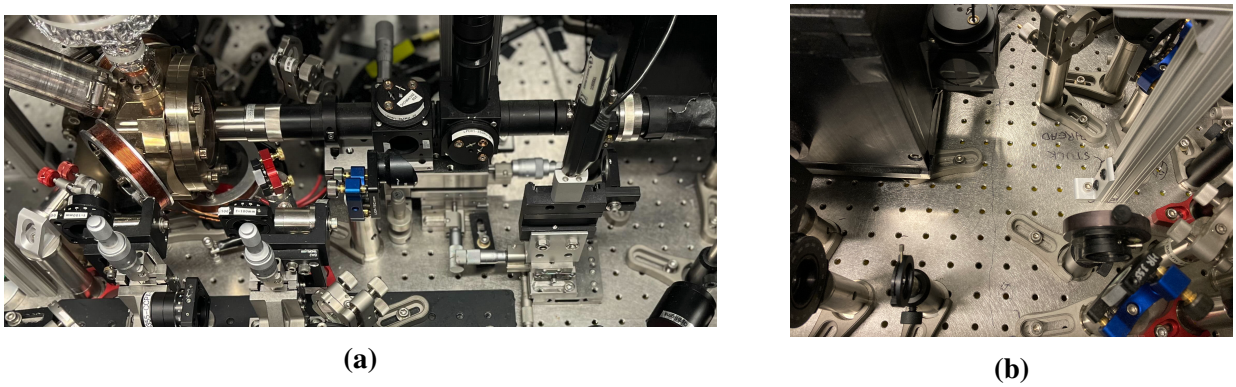


Figure 3.8. Individual addressing beam path, part 1.

x5 beam expander itself when we need to optimize the width of the individual addressing beam. This optimization procedure is done using an ion. After the beam expander, the poke beam is coupled into the AOD made by L3 Harris. The first-order diffracted beam continues straight head to a delay stage which was placed in the beam path if we need to have the poke beam temporally overlapped with the Raman beams. We have not optimized the individual addressing beam's delay stage since there has not been need for that ability yet. The zeroth-order AOD is picked off by the D-mirror after the delay stage while the first order continues past and is reflected by the large 1 in beam cube. The beam path that approaches this cube from behind aligns light exiting the fiber in which we send optical pumping light through. This fiber is called the "back-table optical pumping fiber" since we place a removable turning mirror into the optical pumping path to direct the light to the input fiber coupler located in the 369 nm optical layout. Overlapping the

back-table optical pumping light to the individual addressing beam has been very helpful when the beam has become horribly misaligned. A procedure for the process of aligning the poke beam to the ions from scratch is laid out in Ref. [3].

The poke beam passes through another telescope coming back towards the Raman castle as seen in Fig. **??** in which it is directed with two mirrors, a blue mirror mount that is closes to the 8020 profile and a second mirror that cannot be seen in the picture, to a third mirror just slightly to left of the silver mirror mount that is clearly visible in the bottom left corner. These last two mirrors can be observed better in Fig. 3.9b. This third mirror is used to center the poke



(a) **(b)**

Figure 3.9. Individual addressing beam path, part 2.

beam through some polarization wave plates and to what is called "the intermediate focus lens;" a f=100 mm lens that maps the beam to an intermediate focus that is just after this lens but before the beam is combined into the imaging objective assembly. The imaging objective which has an NA=0.4 maps the intermediate focal plane to the plane of the ions. A dichroic filter reflecting the 355 nm light down the objective not only helps to send the laser to the ions but also lets 369 nm fluorescence from scattered photons transmit through the dichroic to the EMCCD camera or PMT.

It is worth noting that the f=100 mm lens is mounted of a two-axis translation stage that

can be moved along the optical axis or vertically (up and down) with respect to the incident beam. The vertical micrometer is motorized and is connected to the computer which has the Iseg LabView control software via a USB and USB extension cord. The motorized micrometer is from Newport and there is a control program that we use to adjust the vertical position of the lens. Optimizing the vertical position of this 100 mm lens is the usual "knob" that we like to use as a method to optimize the Stark shift experience by a single ion.

3.5 Experimental Control Program

We use LabView as the software control program to run the quantum simulator. LabView provides a convenient way to interface with many different types of devices and enable the ability to "interface" with the trapped ions by applying different operations via turning on and off different lasers. In addition, scans can be formed with "live" results. However, none of us are fluent in LabView so when there is a software bug or a new sequence that needs to be implemented figuring out how to do it in LabView can be very time consuming. Especially, when there isn't any explanation why a specific chapter index will not work in what we call the "Trotter Chapter" in which at least two different operations are applied for varying repetitions. Despite challenges in trying to add new features without having to become a LabView expert it suffices for the job since no one has bothered to implement a different software control program. Having LabView as the experimental control software does date QSim since there are many other ways that one can interface with the experiment.

- FPGA Sequencer
- Andor Camera (the EMCCD)

- Single-Channel PMT
- Agilent AWG

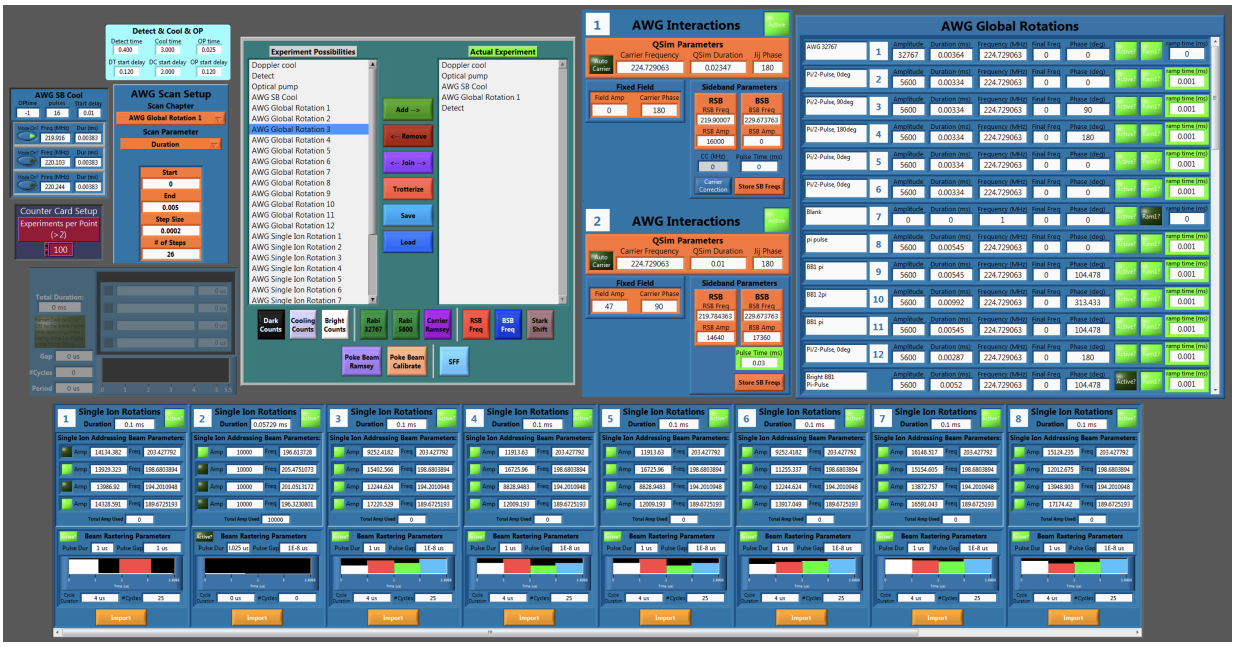


Figure 3.10. Pulse sequence experiment control window.

A typical experimental sequence has three parts: preparation, interaction, and measurement. We have now discussed all of the "preparation" part of an experimental sequence which consists of the following processes: Doppler Cooling $\rightarrow$ Optical Pumping $\rightarrow$ Sideband Cooling. At the end of the preparation sequence, the ion is well-cooled and is initialized in its spin down motional ground state, $|\downarrow_z, 0\rangle$. If required, a global rotation, $R(\theta, \phi)$, can be applied to prepare the ion's spin in the $|\uparrow\rangle$ state or in the σ_x or σ_y basis. Otherwise, the interaction part of the experimental sequence begins in which the Raman beams are turned on for some duration t and the coherent interaction is described by the time-evolution of the applied Hamiltonian. The interaction is the quantum simulation. After coherently manipulating the ion, a measurement of the ion's spin state is made by turning on the detection beam. The result of the measurement is recorded as 0 or 1 corresponding to detecting the ion in $|\downarrow\rangle$ or $|\uparrow\rangle$. State discrimination, determining whether the

ion is in the $|\downarrow\rangle$ ("dark") state or $|\uparrow\rangle$ ("bright") state, from the collected fluorescence or lack of fluorescence. If we wish to measure the ion's spin in a different basis (σ_x or σ_y), a $\pi/2$-global rotation is applied to the ion about the y or x axis before the measurement part of the experimental sequence.

The entire experimental sequence, just described above, is repeated many times in order to build up statistics about the measurement for the given interaction duration. A "scan" of an experimental sequence involves changing a parameter of the interaction such as the duration in which many shots are collected of the experimental sequence at each value of the parameter that is being changed. The number of steps in a scan is dependent on the parameter range and the resolution desired. We usually set the number of experiments per scan step to either 50 or 100 shots.

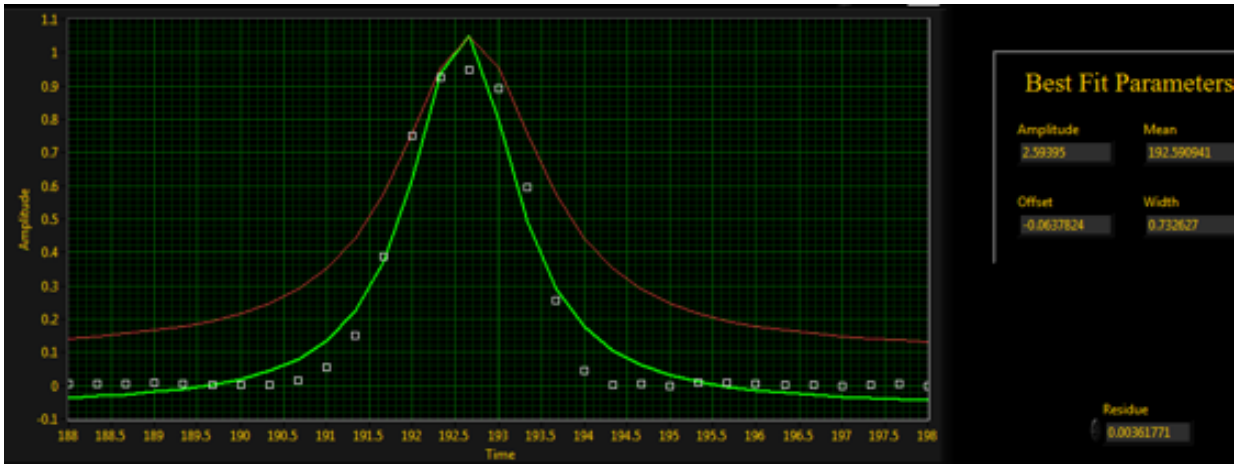
There are three types of scans that are usually run throughout a typical day in the lab. We call these scans a "dummy scan," a "frequency scan," and a "duration scan." A dummy scan is basically applying the sequence as you see it and measuring the result. The dummy scan can have steps in it such as two steps in which the scan consists of applying the specified experimental sequence some number of times before the averaged result is placed on the plot in the experimental control program software and the scan increments to the next step. None of the parameters within the experimental sequence is being "scanned" or varied.

3.5.1 Calibrating the Individual Addressing Beam

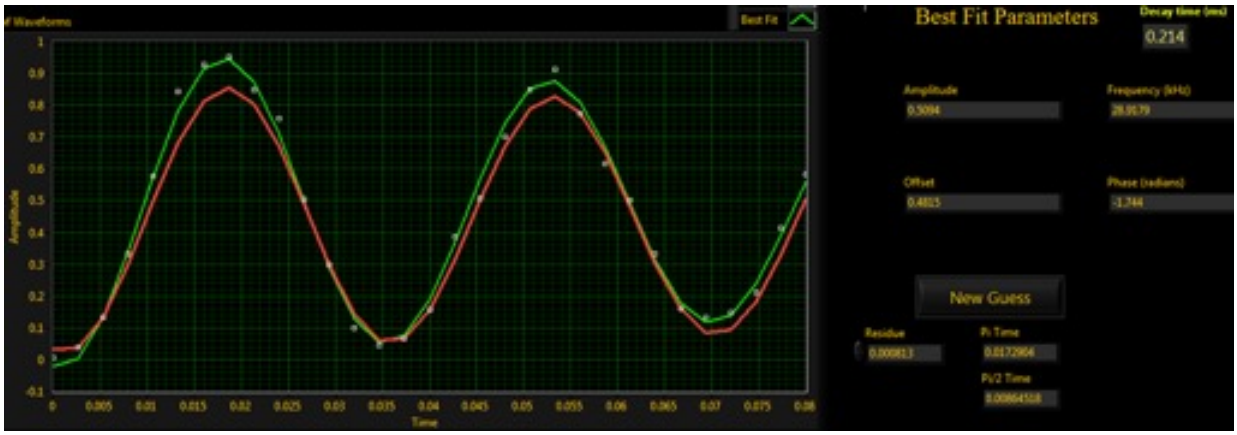
In this subsection, the general procedure for calibrating the individual addressing beam for a N ion chain is discussed. First, there are a few single-ion calibration sequences that need to be

run before loading more ions. These sequences will be presented first.

We usually run an AOD frequency scan to determine the AOD's center frequency value that corresponds to the position of one ion. Usually, we know roughly where the AOD single-ion center frequency is from a previous day's measurement and only run a frequency scan that is about 10 MHz wide about the center frequency value. To determine the center frequency initially, we can either drag the vertical cursor to be aligned by eye with the peak, or we can fit the scan to a Lorentzian function to extract the peak frequency as shown in Fig. 3.11a. After determining



(a)



(b)

Figure 3.11. Individual addressing beam calibrations with one ion. **(a)** Lorentzian frequency fit of the optimized single ion AOD center frequency. **(b)** Corresponding optimized single ion individual addressing beam applied Stark shift. Both of these sequences are measured with the AWG amplitude set at 7000 AWG amplitude units.

the center frequency of the AOD to "poke" a single ion, we need to measure the corresponding Stark shift experienced by the ion. This measurement is done by turning the individual addressing beam on with the RF waveform frequency set at the determined center frequency of the AOD and varying the duration that the beam is turned on for. A Rabi flopping signal is observed, as shown in Fig. 3.11b, the duration of the poke beam is scanned. We often fit this individual addressing SS scan to a sinusoidal function to extract the frequency of the Stark shift.

Both of the individual addressing beam sequences were run with the AWG (Ch.2) set at 7000 amplitude units. Usually, the default AWG amplitude for these poke beam measurements is set at 10,000 amplitude units. The last set of measurements that is necessary to collect is the single ion SS as a function of the individual addressing beam's AOD's AWG amplitude which we can control in the LabView control program (in the pulse sequence window). Figure 3.12 displays a plot of the relationship between the RF amplitude sent to the individual addressing beam AOD and the measured Stark shift experienced by a single ion. The purple-colored data

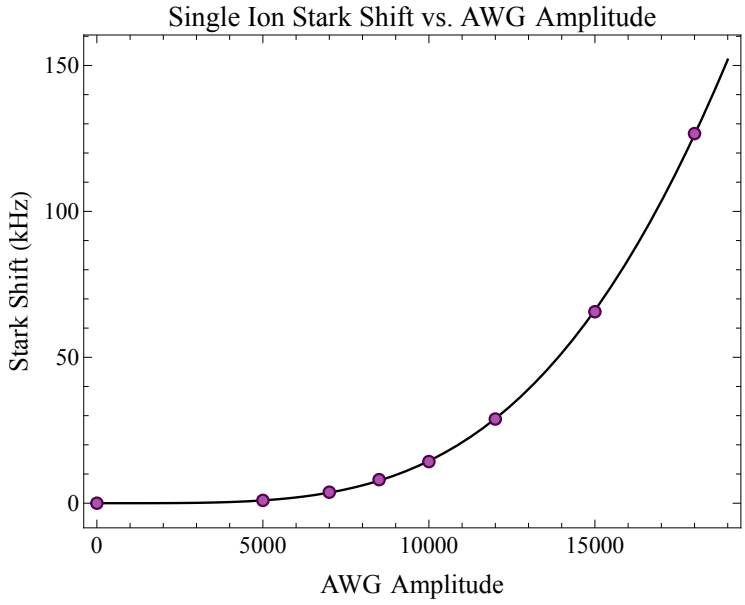


Figure 3.12. Single ion Stark shift versus AWG amplitude.

points are fit to a sine-to-the-fourth function described by the following equation:

$$f(SS) = A\sin\left(k \times power\right) + B, \tag{3.21}$$

where $\{A, k, B\}$ are the fit parameters whose values are found through a nonlinear model fit using a Mathematica notebook that has been created specifically for calibrating the individual addressing beam.

After the individual addressing beam is optimized using one ion, it is time to run a SIR-Ramsey sequence scanning the AOD center frequency at a fixed SIR duration across a chain of N ions. Before running the frequency scan, this calibration requires loading N ions and running a camera calibration, or the "Camera ROI Finder" resulting in a region of interest (ROI) that is defined for each ion and a corresponding threshold value for each ROI. As an example, a screenshot of the "Ion ROI Finder" experiment control window results of a $N = 4$ camera calibration is shown in Fig. 3.13. "Camera" Running a N ion camera calibration is mainly for

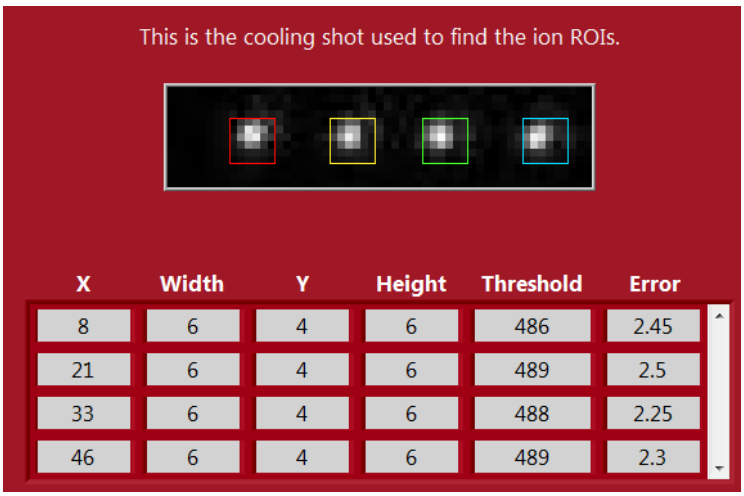
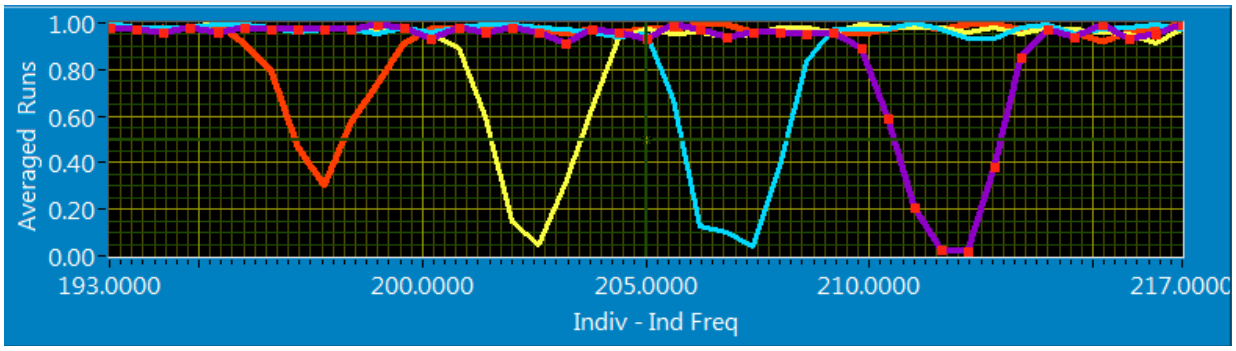


Figure 3.13. Camera calibration for $N = 4$ ions using the experimental control program.

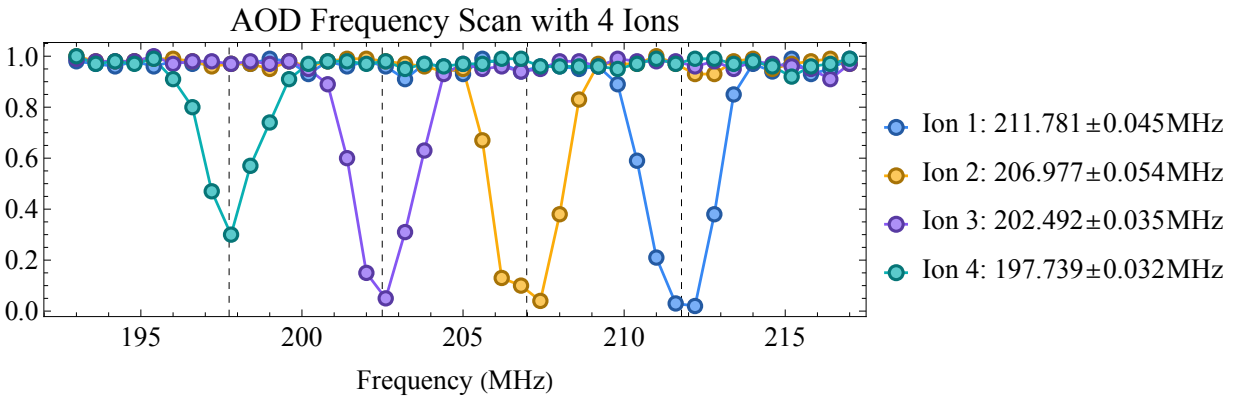
the benefit of being able to detect what each ion is doing in "real time" during any experiment sequence. Performing this calibration allows parameters such as $\pi/2$- or π-times to be adjusted

right away instead of running sequences "blindly" and realizing in the post-processing of the collected results that the data was "bad" because of imperfect rotations.

Figure 3.14a of an $N = 4$ ion AOD frequency scan using the camera to collect the fluorescence and the "Ion State Scan" tab in the LabView experimental control program to see the results in "real time." The rightmost dip (highest center frequency) corresponds to the leftmost ion in



(a)



(b)

Figure 3.14. AOD frequency scan with $N = 4$ ions. The center frequency of the individual addressing beam is varied while the duration and AWG amplitude of the single-ion rotation are fixed. The AWG amplitude is set at 10,000 and the duration is set a π time. **(a)** Screenshot of the AOD frequency scan plotted in "real-time" looking at the "Ion State Scan" window tab on the *Experiment Control* window of the LabView control software. **(b)** Calibrated AOD frequencies to address each ion in a four-ion chain.

the chain when viewed on the "Continuous Camera" window, i.e. the camera in the LabView control program. The leftmost ion in the chain is what we would naturally label as "ion 1" while the rightmost ion would correspond to the N^{th} ion, or in this case "ion 4". Referring back to the

$N = 4$ ion AOD frequency scan, the lowest frequency (the leftmost dip) belongs to ion 4 while the highest frequency (rightmost dip) belongs to ion 1. Each resonance dip is fit to a Lorentzian function in order to extract the frequency that the AOD needs to be set at in order to address each of the four ions.

Now that the AOD frequencies have been calibrated to a given ion positioned in the linear chain, the RF amplitude applied of each AOD frequency must be calibrated. When we wish to use the individual addressing beam to address multiple ions at the same time, we must "raster" or quickly sweep the AOD frequency across the calibrated values in sequential order. This rastering process is required since the overall optical power in the beam path is now divided by $N = 4$. Figure 3.15 shows the results of two sequences that are executed.

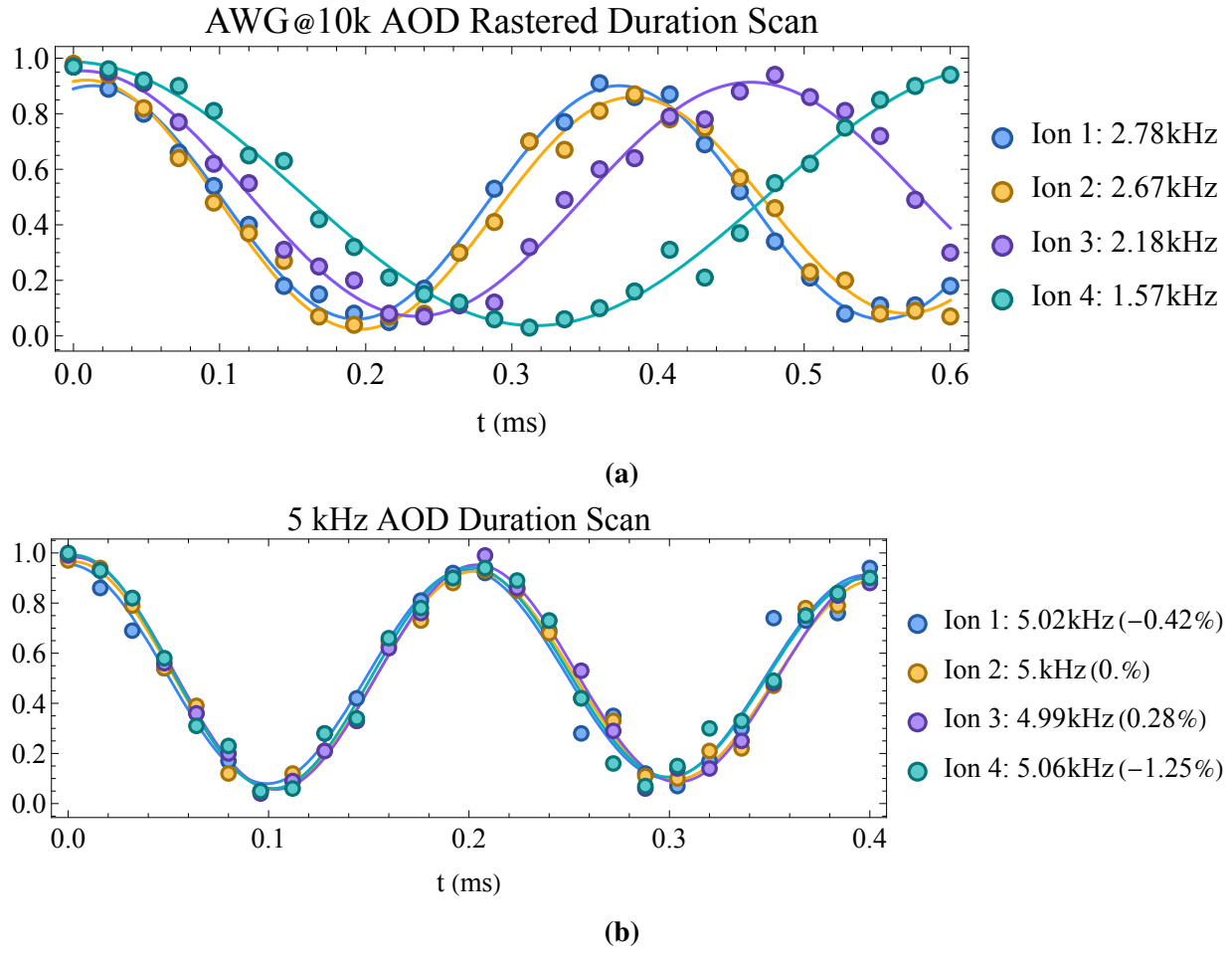


Figure 3.15. Calibrating the individual Stark shift applied to each ion. **(a)** An initial duration scan with the AWG amplitude for each AOD frequency set at 10000 AWG units. **(b)** Calibrating the individual Stark shifts to 5 kHz.

Chapter 4: A Hybrid Quantum-Classical Algorithm

Having introduced the high-degree of control, manipulation, and detection of a linear chain of trapped ions and discussed the native long-range spin-spin interactions that together form the underlying framework of the quantum simulator presented in this dissertation, one would naturally expect to know what types of problems can be experimentally implemented and what are the results?

Quantum computers offer potentially more significant advantages in solving certain types of computationally difficult problems than classical devices. Recently, there has been a growing interest in investigating the open question of whether quantum devices provide shortcuts for finding approximate solutions to classical combinatorial optimization problems. One option is to utilize a quantum annealing protocol, which in some cases has demonstrated an advantage over its classical counterparts. However, the adiabaticity requirements of quantum annealing hinder its applicability for existing quantum systems that have finite coherence times. Another promising option is to use a variational method such as a variational quantum eigensolver or a quantum approximate optimization algorithm.

Chapter 4 focuses on a specific instance of the latter, experimentally implemented on the trapped-ion quantum simulator, presented in this dissertation as well as on a cryogenic trapped-ion quantum simulator [40, 41]. This research was published in an article entitled, "Quantum

approximate optimization of the long-range Ising model with a trapped-ion quantum simulator" [42]. The goal of this experiment was to approximate the ground state energy of an antiferromagnetic transverse-field Ising Hamiltonian with long-range spin-spin interactions which also happens to be a type of Hamiltonian native to our trapped-ion system.

4.1 Quantum Approximate Optimization Algorithm

Preparing a quantum product state of all spins down, $|\downarrow\downarrow \ldots \downarrow\downarrow\rangle_z$ is trivial. One just simply Doppler cools, optically pumps, and then applies resolved sideband cooling to the chain of ions. In comparison, preparing a many-body quantum ground state, such as the ground state of the transverse-field antiferromagnetic Ising Hamiltonian with long-range interactions, is more complicated. One solution is to utilize adiabatic quantum computing to prepare the desired non-trivial Hamiltonian ground state [43, 44]. Under this method, the quantum system is initially prepared in the ground state of a trivial, easy-to-prepare Hamiltonian before the target Hamiltonian is adiabatically turned on. Under the adiabatic approximation, if the switching process is slow enough, the initial trivial ground state will evolve adiabatically to the ground state of the hard-to-prepare Hamiltonian. The key phrase in the previous sentence is, "slow enough." Coherence times of current experimental quantum systems are often too short for these strict adiabatic requirements.

An alternate solution is to implement a quantum approximate optimization algorithm. This method, abbreviated as QAOA, was developed by Farhi *et al.* to provide approximate solutions to combinatorial optimization problems [45]. QAOA, is similar in spirit to quantum algorithms called variational eigensolvers which is used in the quantum chemistry community as a way to approximate chemical binding energies [46]. QAOA has also been identified as a time-efficient

protocol to prepare non-trivial quantum entangled states [47]. In addition, QAOA is an example of a hybrid quantum-classical variational algorithm. Further details regarding the QAOA protocol and its hybrid nature are elaborated next.

4.2 The QAOA Protocol and Experimental Implementation

To further illustrate QAOA, the protocol will be presented within the context of the long-range antiferromagnetic transverse-field Ising Hamiltonian H:

$$H = \overbrace{\sum_{i<j} J_{ij} X_i X_j}^{H_A} + \overbrace{B \sum_i Y_i}^{H_B}, \tag{4.1}$$

where H can be expressed as the sum of two Hamiltonians H_A and H_B. In Eq. (4.1), $\hbar = 1$. H_A is the antiferromagnetic Ising Hamiltonian with long-range interactions where $J_{ij} > 0$ represents the Ising coupling between the i^{th} and j^{th} ions. These spin-spin interactions approximately fall off as a decaying power law which is described by the power-law exponent α and J_0, the average nearest-neighbor strength. X_i and X_j are the x Pauli spin-1/2 operators for ion i and j, respectively. H_B, the second term in Eq. (4.1), is the global (uniform) transverse-field Hamiltonian where $B < 0$ denotes the strength of the field and Y_i is the y Pauli spin-1/2 operator of ion i. In this experiment, we implement QAOA to approximate the ground state energy of H with N ions (up to $N = 40$) at the critical point, $(B/J_0)_c$, of the quantum-phase transition that this Hamiltonian is known to exhibit [48]. In addition, we will use QAOA to sample the output of the combinatorial optimization of the classical Hamiltonian H_A, in which $B = 0$ in the cost function Eq. (4.3).

The QAOA sequence involves alternating the noncommuting unitary time-evolution operators of H_A and H_B applied to an easy-to-prepare initial state $|\psi_0\rangle$. Each application of the pair of

unitary operators for H_A and H_B represent a layer or step, and, in general, the QAOA sequence is made up of integer p layers. The final state after a p-layer QAOA protocol is given by:

$$\begin{aligned} |\vec{\beta},\vec{\gamma}\rangle &= \prod_{k=1}^{p} e^{-i\beta_k(H_B/J_0)} e^{-i\gamma_k(H_A/J_0)} |\psi_0\rangle \,, \\ &= e^{-i\beta_p(H_B/J_0)} e^{-i\gamma_p(H_A/J_0)} \ldots e^{-i\beta_1(H_B/J_0)} e^{-i\gamma_1(H_A/J_0)} |\psi_0\rangle \,, \end{aligned} \tag{4.2}$$

where the k^{th} layer durations, β_k and γ_k, correspond to the amount of time that H_B and H_A are applied for, respectively. As seen in Eq. (4.2), the final state $|\vec{\beta},\vec{\gamma}\rangle$ is described by and depends on a set of evolution times (or angles) denoted by $\vec{\beta}=\{\beta_1,\beta_2,\ldots,\beta_p\}$ and $\vec{\gamma}=\{\gamma_1,\gamma_2,\ldots,\gamma_p\}$. Therefore, a QAOA sequence composed of p layers has a total of $2p$ variational parameters that can be optimized by evaluating the energy expectation value of the final state:

$$E(\vec{\beta},\vec{\gamma}) = \langle\vec{\beta},\vec{\gamma}|H|\vec{\beta},\vec{\gamma}\rangle. \tag{4.3}$$

A quantum simulator can run the QAOA sequence shown in Eq. (4.2) for a given set of parameters $(\vec{\beta},\vec{\gamma})$. The results from the quantum simulator can be used to evaluate, classically, a cost function of interest, such as Eq. (4.3), and to obtain a new set of variational parameters. This hybrid quantum-classical procedure is repeated until the cost function has been optimized, such as approximating the ground state energy of H [Eq. (4.1)] . Alternatively, if the optimal values of the variational parameters are known for p layers of alternating the time-evolution operators, QAOA can be used as a tool to prepare the corresponding quantum state $|\vec{\beta},\vec{\gamma}\rangle$, that can measured (or sampled) or as the initial state of another quantum simulation experiment. QAOA has, in fact, been proposed as an efficient method to produce non-trivial entangled states [47].

Implementing the QAOA sequence of p-layers is experimentally fairly straightforward, as illustrated by Fig. 4.1. To begin, we initialize a system of N ions in the ground state of H_B, namely, $|\uparrow\ldots\uparrow\rangle_y \equiv |+\rangle^{\otimes N} = |\psi_0\rangle$, where $|\uparrow\rangle_y \equiv (|\uparrow\rangle_z + i\,|\downarrow\rangle_z)/\sqrt{2}$, and the global transverse

field strength, B, is assumed to be negative. Next, after preparing $|\psi_0\rangle$ the first layer of QAOA

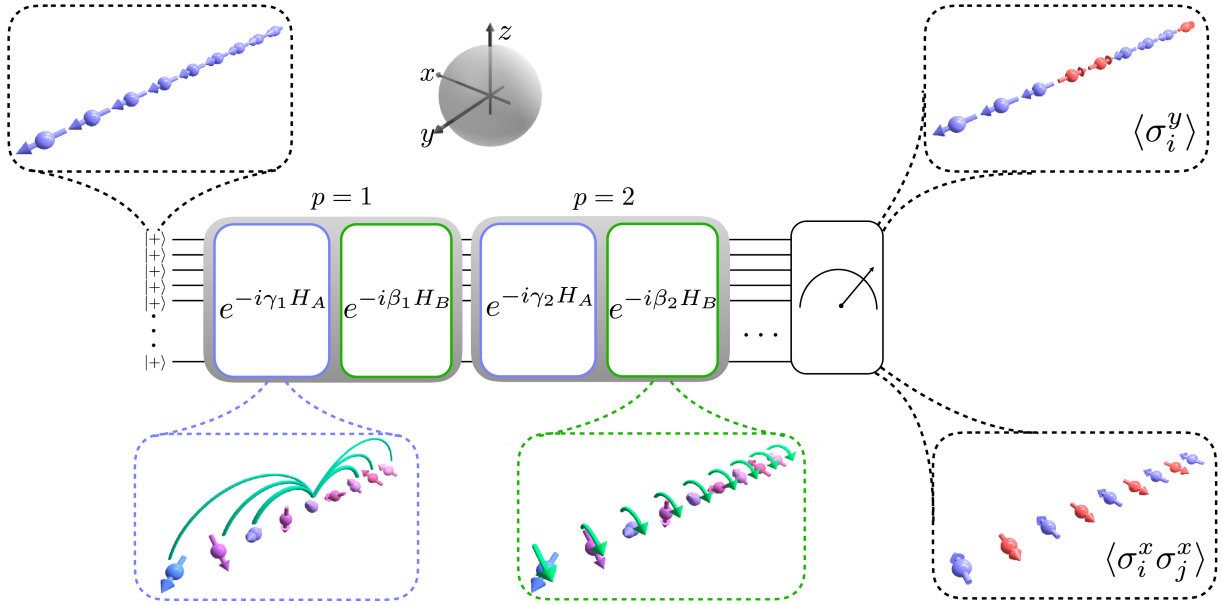


Figure 4.1. QAOA experimental sequence. N ions are initialized in a product state along the positive y axes of the Bloch sphere. Unitary evolution under Hamiltonians H_A and H_B are applied for durations corresponding to angles γ_i and β_i, respectively for each i^{th} layer ($i = 1, 2, \ldots, p$) in a p-layer QAOA sequence. Finally, projective measurements along the x and y bases are performed in order to calculate the average energy $\langle H\rangle = E(\vec{\beta}, \vec{\gamma})$.

is applied beginning with unitary evolution under H_A for a duration γ_1 followed by unitary evolution under H_B for a duration β_1. H_A is realized by generating spin-spin interactions through spin-dependent optical dipole forces as described in Ch. 3 while H_B is generated by applying a resonant carrier transition corresponding to a global rotation around the y axis of the Bloch sphere. The remaining QAOA steps are then applied similarly until all p layers have been performed. Finally, after each run of the algorithm projective measurements of the individual ion magnetizations along the x or y axis are made in order to measure $\langle H_A\rangle$ and $\langle H_B\rangle$, respectively for the corresponding $(\vec{\beta}, \vec{\gamma})$ parameters. The phrase, "QAOA sequence" will now refer to and represent the running of the experimental sequence in which measurements in both the x and y bases have been realized for a given set of variational parameters.

At this point in the discussion about the implementation of QAOA on a trapped-ion sim-

ulator, it is important to note that this project actually employed two different $^{171}Yb^{+}$ quantum-simulator apparatuses depending on the number of qubits and measurements required. In Ref. [42], these two simulators are referred to as "system 1" [49] and "system 2" [40] also known as "WarmQSim" and "CryoQSim"', respectively. WarmQSim or QSim is of course the lab nickname of the trapped-ion quantum simulator utilized in this entire dissertation. CryoQSim is the lab nickname of the trapped-ion quantum simulator enclosed in a 4 K cryostat which was another experimental system of the Monroe Group [41]. Both systems use linear RF Paul traps and use the same ion isotope, $^{171}Yb^{+}$. Because of the extreme-high-vacuum (XHV) environment surrounding the ion trap in the cryogenic apparatus, larger ion chains can be trapped and held for hours in a linear configuration [40]. The ion trap system in QSim is held in a UHV chamber, in which the environment surrounding the outside of the vacuum chamber is at room-temperature. Hence the origin of the nickname WarmQSim. As a result, both systems are used to study different aspects of the implementation of QAOA with trapped ions. For both systems, the power-law exponent used is $\alpha \sim 1$ and the average nearest-neighbor Ising coupling strengths vary in the range $J_0/(2\pi) = (0.3 - -0.57)$ kHz, depending on the system size and experimental realization.

The energy corresponding to a set of $(\vec{\beta}, \vec{\gamma})$ is calculated by combining the measurements of the two-body correlators $\langle X_i X_j \rangle$ and the total magnetization along the y axis, $\sum_i \langle Y_i \rangle$ together using Eq. (4.1) where indices i, j range from one to N, the number of ions in the system. In order to quantify the performance of the QAOA sequence, we define the following dimensionless parameter, η (not to be confused with the Lamb-Dicke parameter):

$$\eta \equiv \frac{E(\vec{\beta}, \vec{\gamma}) - E_{max}}{E_{gs} - E_{max}}, \tag{4.4}$$

where $E(\vec{\beta}, \vec{\gamma})$ is the energy calculated from measurements from the quantum simulator for the

input $(\vec{\beta}, \vec{\gamma})$ values, E_{max} is the energy of the highest excited state of the target Hamiltonian, and E_{gs} is the actual ground state of the target Hamiltonian. E_{max} and E_{gs} are numerically calculated via exact diagonalization or by using the density matrix renormalization group (DMRG) method depending on the system size N. Eq. (4.4) maps the entire many-body spectrum to be bounded between 0 and 1. We will show that the best experimental performance, η^*, is close to the QAOA theoretical performance, η_{th}, which is less than 1 for finite values of p.

4.3 $p=1$ QAOA

We first focused on the $p=1$ optimization of the full quantum problem, approximating the ground state energy of the Hamiltonian H [Eq. (4.1)] describing a system of N ions. Since $p=1$, the QAOA sequence simplifies to a single layer, and thus, the subscript index denoting the QAOA steps will be dropped. In addition, Eq. (4.2) simplifies to

$$|\beta, \gamma\rangle = e^{-i\beta H_B} e^{-i\gamma H_A} |\uparrow\uparrow \ldots \uparrow\uparrow\rangle_y , \tag{4.5}$$

where the state $|\beta, \gamma\rangle$ is now parameterized by two angles: β and γ. For $p = 1$, β and γ are used to minimize $E(\beta, \gamma)$ in which the time-evolved one- and two-point correlation functions can be efficiently computed [50, 51]. Consequently, a general analytical formula for the energy expectation under a state produced by the QAOA $p=1$ protocol exists and can be used to compute the theoretical performance, η_{th}, of the algorithm (see the supplementary material, SM, of [42]). A couple of our theory collaborators on this project wrote a classical optimization code [52, 53] that returns the optimal QAOA parameters β_{opt} and γ_{opt} for a given system size N. The analytical form of $E(\beta, \gamma)$ is also included in the code which was extremely helpful for understanding and visualizing the $p=1$ QAOA energy "landscape". It was particularly useful to run this QAOA code

immediately after calibrating the trapped-ion system and experimental parameters required for the particular QAOA data run. More specifically, one part of calibrating a trapped-ion quantum simulator involves measuring experimental parameters whose values can be plugged in to the analytical form describing the spin-spin Ising interaction strength J_{ij}, and thus, a $N \times N$ J_{ij} matrix [see Eq (3.20)]. The classical optimizer outputs the QAOA parameters β and γ which

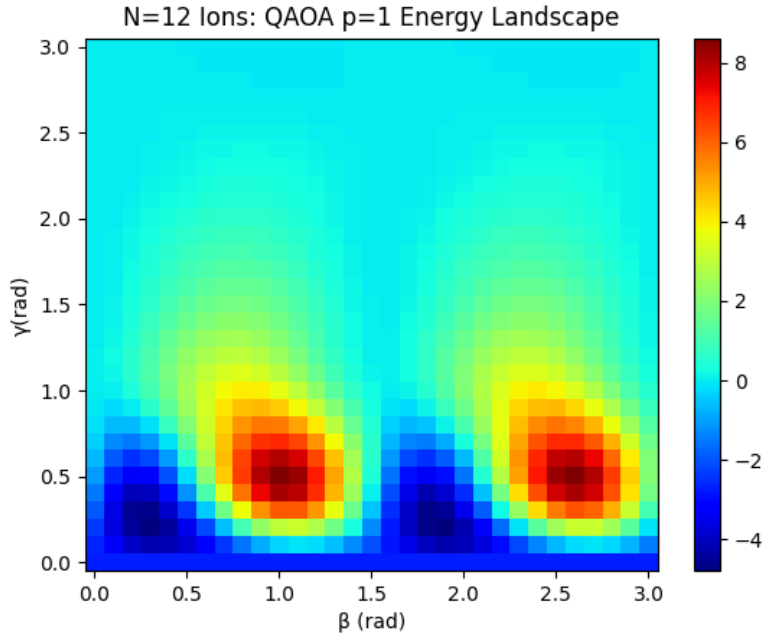


Figure 4.2. QAOA $p=1$ example energy landscape. This is an example energy landscape as a function the $p=1$ QAOA parameters.

have units in radians. These angles need to be converted into durations in order to be "useful" inputs to the QAOA sequence run on the quantum simulator.

$$t_\beta = \frac{2\beta}{2\pi B_{QAOA}} \qquad \& \qquad t_\gamma = \frac{\gamma}{2\pi} \tag{4.6}$$

Eq. (4.6) gives the transformation of the β and γ angles to t_β and t_γ times which are in milliseconds and B_{QAOA} denotes the measured value of the calibrated B_y field. Using Eq. (4.6) enables us to search experimentally for the optimum β and γ values by running the QAOA sequence

over a grid of the parameters around the expected values. In practice, we broadly searched β ($\beta = \{0.5, 0.75, 1.0, 1.25, 1.5\}\beta_{opt}$) and performed a finer scan over values of γ.

4.3.1 $p = 1$ QAOA Exhaustive Search

We first performed an exhaustive search for the variational parameters for $p = 1$ with $N = 20$ ions for the antiferromagnetic transverse-field Ising Hamiltonian. Fig. 4.3 shows the experimental performance landscape (left) and the theoretical performance landscape for the same β and γ values (right). For $N = 20$ the optimal performance η^* was $(93.8 \pm 0.4)\%$. In comparison, the theoretical performance of the algorithm was $\eta_{th} = 96.1\%$. The $p = 1$ exhaustive search for a system of $N = 20$ ions was measured using system 1.

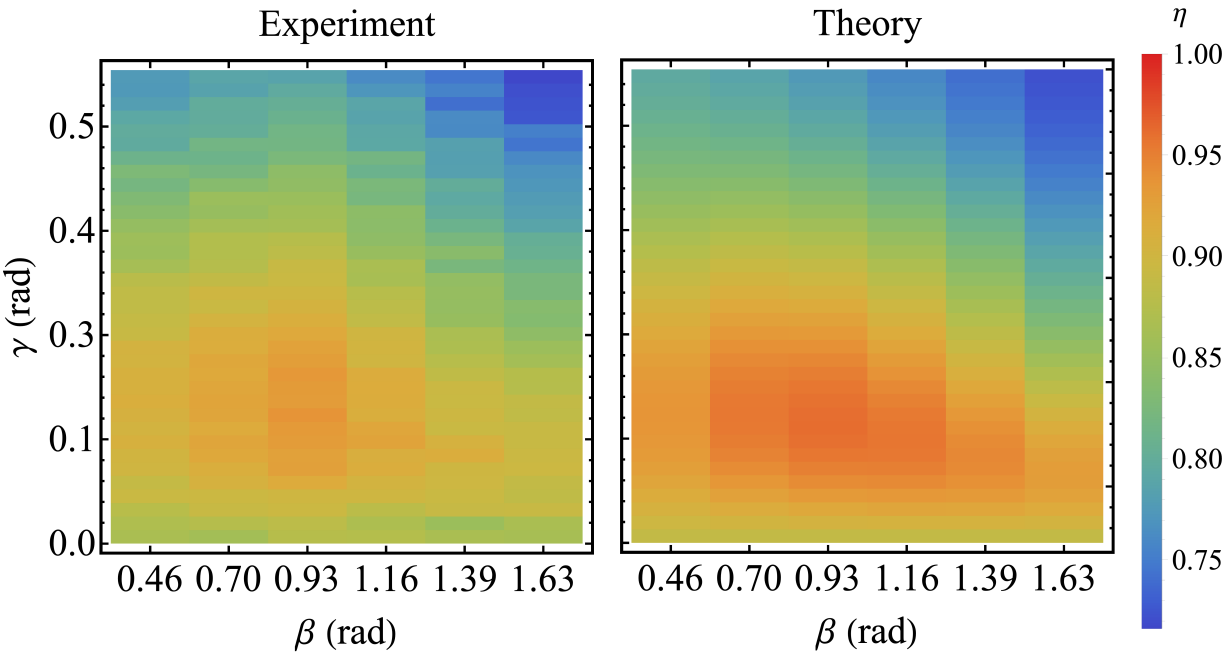


Figure 4.3. $N = 20$ QAOA $p = 1$ exhaustive search performance landscape. The experimental (left) and theoretical (right) performance landscapes are shown as a function of the variational parameters, β and γ. An exhaustive search was conducted over 210 different (β, γ) pairs in which the optimal performance was $\eta^* = (93.8 \pm 0.4)\%$. In comparison, the theoretical performance was $\eta_{th} = 96.1\%$.

4.3.2 $p=1$ QAOA System Size Performance

We benchmarked the performance of QAOA for $p=1$ for the antiferromagnetic transverse-field Ising Hamiltonian at the critical point, $B/J_0 \sim -0.3$ as a function of system size, N. For each of the system sizes, we tuned the ion-trap parameters in order to maintain the same value of the inverse power law exponent, α, that approximately describes the spin-spin coupling between ions i and j as a function of distance. In addition, this part of the QAOA experiment was done on the cryogenic quantum simulator (system 2) in which longer chains of ions can be trapped and manipulated in comparison to the room-temperature simulator (system 1). A quick exhaustive search was performed for each system size about the predicted optimal β and γ values, thus utilizing the quantum simulator to obtain the optimal angle values instead of a classical optimizer. Fig. 4.4, shows the QAOA performance η for five different system sizes, spanning the range from

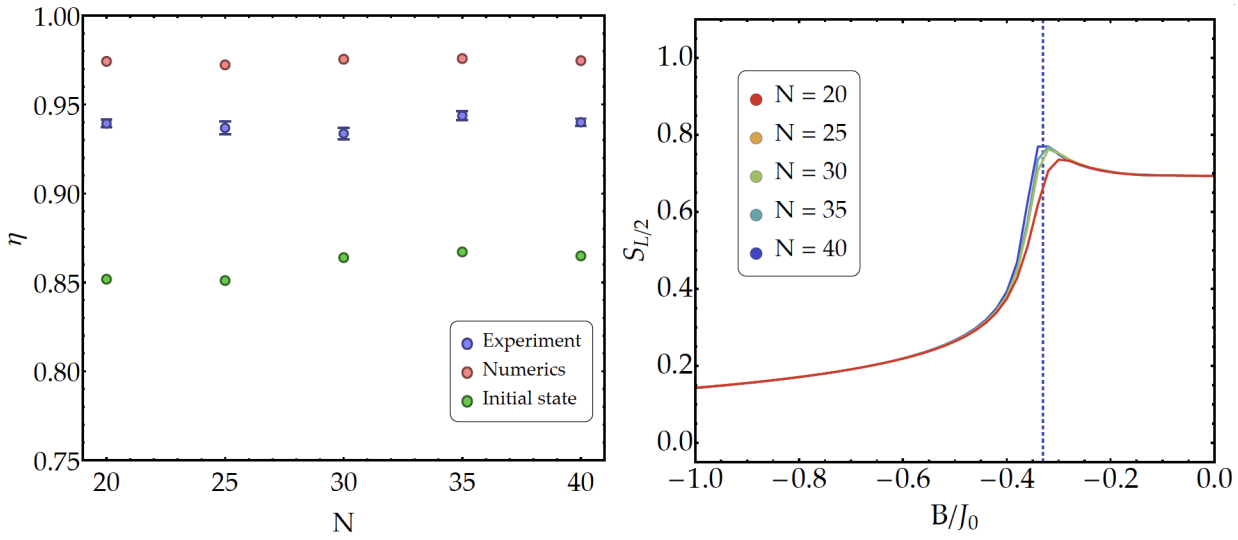


Figure 4.4. QAOA $p=1$ performance as a function of system size. The best experimental performance for one layer of QAOA is plotted in blue for each system size N that was investigated. The red points indicate the expected performance of the $p=1$ algorithm while the green points represent the performance of remaining in the prepared initial state.

$N=20$ to $N=40$. We observed that the best experimental performance, η^* (the blue points in

Fig. 4.4), remained constant across the various system sizes. In comparison, both the expected QAOA performance, plotted in red, and the initial state performance, plotted in green, improved as N was increased. The amount of time required to run the algorithm for each system size also remained constant.

4.4 $p=2$ QAOA Exhaustive Search

After observing promising $p=1$ QAOA results, we decided to study QAOA with $p=2$. The quantum state and the corresponding energy expectation value are now dependent on four variational parameters:

$$\begin{aligned} &\vec{\beta} = \{\beta_1, \beta_2\} \;\; \& \;\; \vec{\gamma} = \{\gamma_1, \gamma_2\} \\ &\xrightarrow{p=2} |\vec{\beta}, \vec{\gamma}\rangle = |\beta_2, \gamma_2, \beta_1, \gamma_1\rangle \;\&\; E(\vec{\beta}, \vec{\gamma}) = E(\beta_2, \gamma_2, \beta_1, \gamma_1), \end{aligned} \tag{4.7}$$

where there exists a pair of β_k and γ_k angles for the two applications of time-evolution operators for H_A and H_B. On another note, the optimal values for β_1 and γ_1 of the first-layer of the $p=2$ QAOA are generally not equivalent to the $p=1$ QAOA optimal angles, β_{opt} and γ_{opt}. In addition, unlike the $p=1$ case where an analytical form of the energy exists, there is not a known formula that can be used to calculate efficiently the energy for $p=2$. Visualizing a $p=2$ QAOA energy landscape is also challenging since it now resides in a four-dimensional space. Despite this, we used a bootstrapping heuristic method to obtain initial guess points for the four parameters and then used the experimental quantum simulator to fine-tune these values. More information regarding the bootstrapping heuristic method can be found in the supplementary information for [42].

Fig. 4.5 shows the results of the $p=2$ exhaustive search with $N=20$ ions. Figure. 4.5a

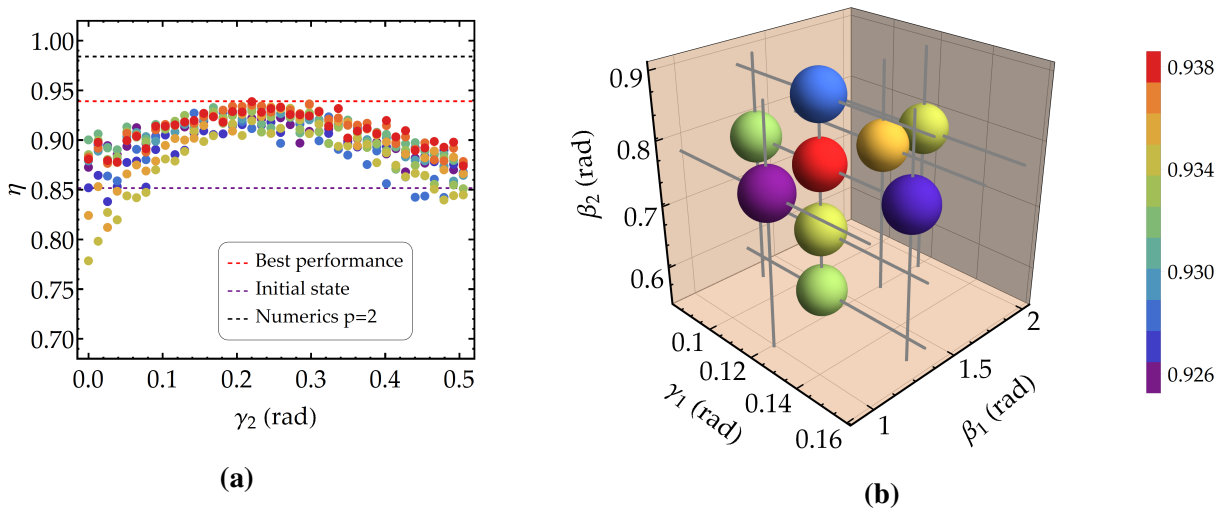


Figure 4.5. $N = 20$ QAOA $p = 2$ exhaustive search. An exhaustive search of all four variational parameters in $p = 2$ QAOA was examined for 20 ions in system 2. **(a)** The performance as a function of γ_2 was finely scanned for a fixed set of $\{\beta_1, \gamma_1, \beta_2\}$ QAOA angles. The different colored curves each represent a different set of $\{\beta_1, \gamma_1, \beta_2\}$ values. **(b)** This three-dimensional plot shows the best performance measured at the discrete values that the variational parameters $\{\beta_1, \gamma_1, \beta_2\}$ were searched over using the best γ_2 value measured in (a). The red ball represents the best experimental η^* obtained for a $p = 2$ $N = 20$ exhaustive search.

displays the performance η as a function of γ_2, the time evolution of the second application of H_A, where each color corresponds to a different set of $\{\beta_1, \beta_2, \gamma_1\}$ parameters. The right plot in Fig. 4.5b shows $p = 2$ QAOA performance as a function of $\{\beta_1, \beta_2, \gamma_1\}$ with the optimized γ_2 value found from the plot on the left. The best experimental $p = 2$ QAOA $\eta^* = (93.9 \pm 0.3)\%$ for 20 ions is shown in red whereas the theoretical performance has a value $\eta_{th} = 98.4\%$.

For $N = 20$ ions, the $p = 2$ η^* measured by system 2 is similar to the $p = 1$ η^* value measured by system 1. This similarity in the experimental performance is contrary to the gain that is expected in theoretical QAOA performance when number of layers is increased from $p = 1$ to $p = 2$. See Table 4.1 which summarizes the best exhaustive search performance and expected performance of QAOA for $p = \{1, 2\}$ with $N = 20$ ions. The expected 2.3% performance gain for running a $p = 2$ QAOA sequence is already counterbalanced by experimental errors arising from

p	η^*	η_{th}
1	$(93.8 \pm 0.4)\%$	96.1%
2	$(93.9 \pm 0.3)\%$	98.4%

Table 4.1. $N = 20$ QAOA exhaustive search performances.

bit-flip errors and decoherence that have accumulated during the longer second-layer evolution times.

4.5 Closed-Loop QAOA Gradient Descent Search

In many ways, a brute-force approach, i.e. exhaustively searching for the optimum QAOA parameters utilizing the quantum simulator, is inefficient. The QAOA experiments and results that have been presented so far in this chapter could be considered as an "open-loop" hybrid quantum-classical search procedure. The open-loop refers to the fact that the classical optimizer and the quantum simulator are not directly interacting with each other. To create a closed-loop search procedure, we wrote a gradient descent algorithm that is called by the experimental control software to return an optimized pair of variational parameters that minimizes the measured QAOA $p = 1$ energy results run on the quantum simulator. The closed-loop QAOA $p = 1$ search was performed on system 1.

We can use a theoretical energy landscape for $p = 1$ QAOA, to visualize the trajectory starting from an initial point, $(\beta^{(1)}, \gamma^{(1)})$ that is close to the maximum energy. Two additional points, $(\beta^{(1)}, \gamma^{(1)} + \delta\gamma)$ and $(\beta^{(1)} + \delta\beta, \gamma^{(1)})$, are chosen that are each orthogonal to the initial point. The first iteration of the closed-loop QAOA gradient descent experimental search is the following:

1. A $p=1$ sequence is run on the quantum simulator for each of the points in iteration 1.

2. Next, the gradient descent algorithm is called to calculate the corresponding energies—$E(\beta^{(1)}, \gamma^{(1)})$, $E(\beta^{(1)}, \gamma^{(1)}+\delta\gamma)$, and $E(\beta^{(1)}+\delta\beta, \gamma^{(1)})$ in order to compute the local energy gradient along each measured orthogonal direction.

3. The classical optimization returns the second iteration set of angles consisting of a new guess point $(\beta^{(2)}, \gamma^{(2)})$, an orthogonal point along constant β $(\beta^{(2)}, \gamma^{(2)}+\delta\gamma)$, and an orthogonal point along constant γ, $(\beta^{(2)}, \gamma^{(2)}+\delta\gamma)$.

4. The iteration 2 angle pairs are sent to the quantum simulator.

The QAOA sequences for iteration 1 will be run and the gradient descent optimizer will spit out the variational angle pairs for the second iteration. This closed-loop interaction will continue until the measured energy converges to a minimum.

We first implemented the closed-loop gradient descent search with $N=12$ ions. Figure 4.6

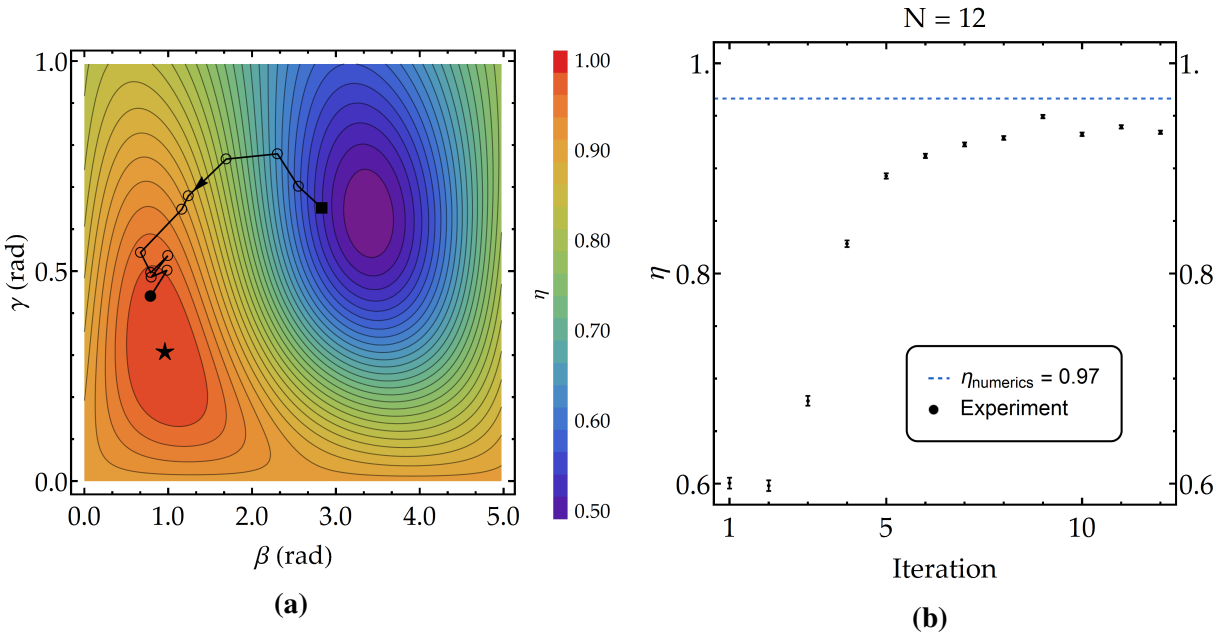


Figure 4.6. $N=12$ QAOA $p=1$ gradient search. **(a)** The gradient descent trajectory is plotted on top of the $p=1$ QAOA performance landscape for $N=12$ ions. **(b)** The same gradient descent performance is plotted as a function of iteration step.

shows the QAOA $p=1$ gradient descent search results for $N=12$ ions. The theoretical performance landscape, Fig. 4.6a, for one layer of QAOA is displayed with the trajectory suggested by the classical optimizer. The black square and circle represent the start and end points of the descent, respectively, while the point represented by a star corresponds to the expected performance $\eta^{th}=97\%$ for the optimum β^{th} and γ^{th} parameters.

Figure 4.6b displays the measured performance as a function of the iteration steps, in which we observe the best value occurs at iteration 9. The blue dashed line represents the expected QAOA performance. The value of the best experimental performance achieved for $N=12$ $p=1$ QAOA gradient descent was $\eta^{*}=(94.9\pm0.2)$.

After a successful closed-loop $p=1$ QAOA with $N=12$ ions we increased the size of the system back to $N=20$. A closed-loop descent was run with 20 ions and the results are displayed in Fig. 4.7. The gradient descent trajectory and the performance of each iteration step

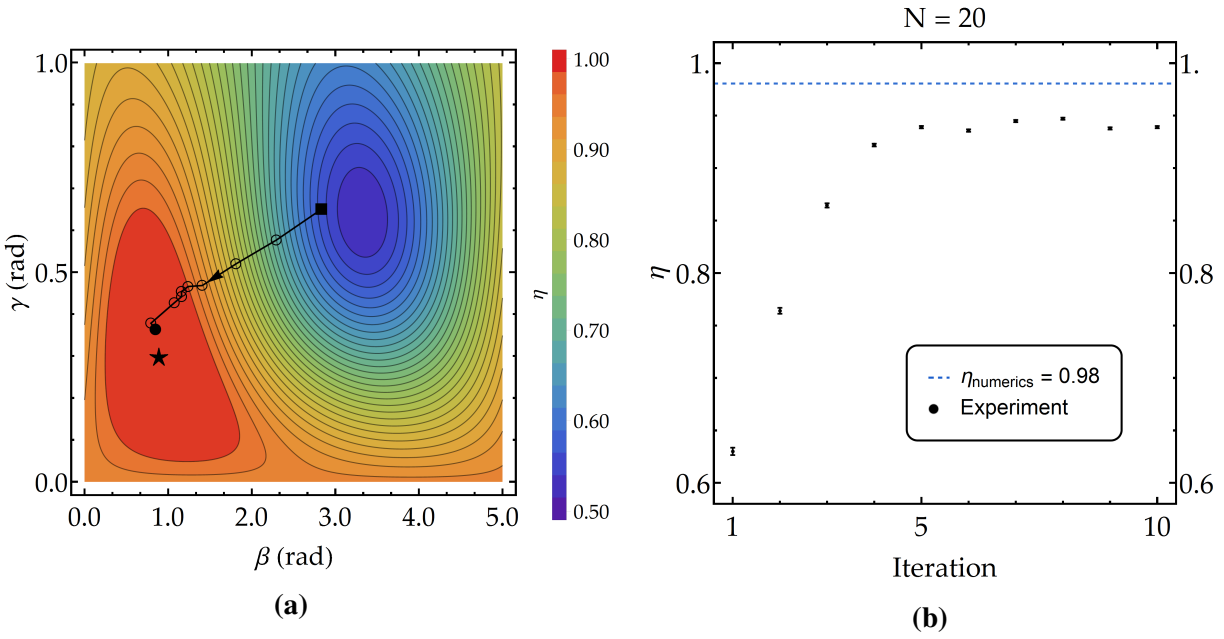


Figure 4.7. $N=20$ QAOA $p=1$ gradient search. **(a)** The gradient descent trajectory is plotted on top of the $p=1$ QAOA performance landscape for $N=20$ ions. **(b)** The same gradient descent performance is plotted as a function of iteration step.

are observed for 20 ions. The blue dashed line in Fig. 4.7b indicates the theoretical performance of the algorithm which corresponds to $\eta^{th} = 98\%$. The best experimental performance using the closed-loop method is $\eta^* = (94.7 \pm 0.1)$.

Observed in both closed-loop gradient descents, the optimal performance was reached before the tenth iteration and these performance values were slightly better than the values obtained through the exhaustive search method.

4.6 QAOA Sampling

Lastly, we investigated the combinatorial optimization of the classical Hamiltonian H_A, in which we now set $B = 0$ in Eq. (4.1), by approximately sampling the $p = 1$ QAOA output using high-fidelity, single-shot measurements of all the qubits. It has been proven, under reasonable complexity-theoretic assumptions, that no classical algorithm can efficiently sample exactly from a sufficiently general class of $p = 1$ QAOA circuits [54]. Recent results [55, 56], suggest that this could also hold in the case of approximate sampling (see SM of Ref. [42]). In our demonstration, by measuring in the x basis, it is possible to sample the probability distribution of all of the 2^N eigenstates $|x_i\rangle$ of the Hamiltonian H_A.

We performed this QAOA $p = 1$ sampling experiment with $N = 12$ ions so that we could both compute the expected QAOA theoretical output and also experimentally oversample the Hilbert space of all of the 4,096 ($= 2^{12}$) possible outcomes. In Fig. 4.8a, we show the experimentally sampled probability distribution of the QAOA eigenstates, plotted on a logarithmic scale, resulting from the optimized $p = 1$ sequence using the variational parameters β^* and γ^*. We compare the experimental eigenstate histogram with the exact diagonalization prediction of the

QAOA output state, sorting the eigenstates according to their energies.

However, sampling from the full QAOA output distribution is a daunting task since the experimental outcome is extremely sensitive to fluctuations in the Hamiltonian parameters and to experimental errors caused by detection and phonon-assisted bit-flip events as well as unwanted effective magnetic fields along the z direction of the Bloch sphere caused by uncompensated light shifts. Utilizing our measured experimental parameters, we can calculate the effect of these errors on the quantum evolution, resulting in a good agreement with the experimental outcome, as shown in Fig. 4.8a.

Another useful way to compare numerics and experimental data is to implement the coarse-graining procedure of the Hilbert space proposed in Ref. [57]. After sorting in decreasing order the observed states according to their experimental probability, we iteratively grouped the states into "bubbles" of Hamming distance L around the most probable state, producing a coarse-grained dataset. We then applied the same coarse-graining to the theoretical probability distribution and plotted the comparison in Fig. 4.8. In this procedure, the Hamming-distance radius was varied to ensure that each bubble contained a comparable number of experimental shots, leading to bubbles of average Hamming distance $\overline{L} = 2.5$. In order to quantitatively compare the coarse-grained experiment to the theory, we used two different metrics, namely, the total variation distance (TVD) and the Kullback-Leibler divergence ($\mathrm{D_{K\text{-}L}}$), defined as:

$$\mathrm{TVD} = \frac{1}{2}\sum_i |p_i - q_i|, \tag{4.8}$$

$$\mathrm{D_{K\text{-}L}} = -\sum_i p_i \log\left(\frac{q_i}{p_i}\right), \tag{4.9}$$

where p_i and q_i are the experimental and theoretical probability of observing the i^{th} outcome, respectively. As shown in Fig. 4.8, when the system is in the initial state, it is closer to a uniform

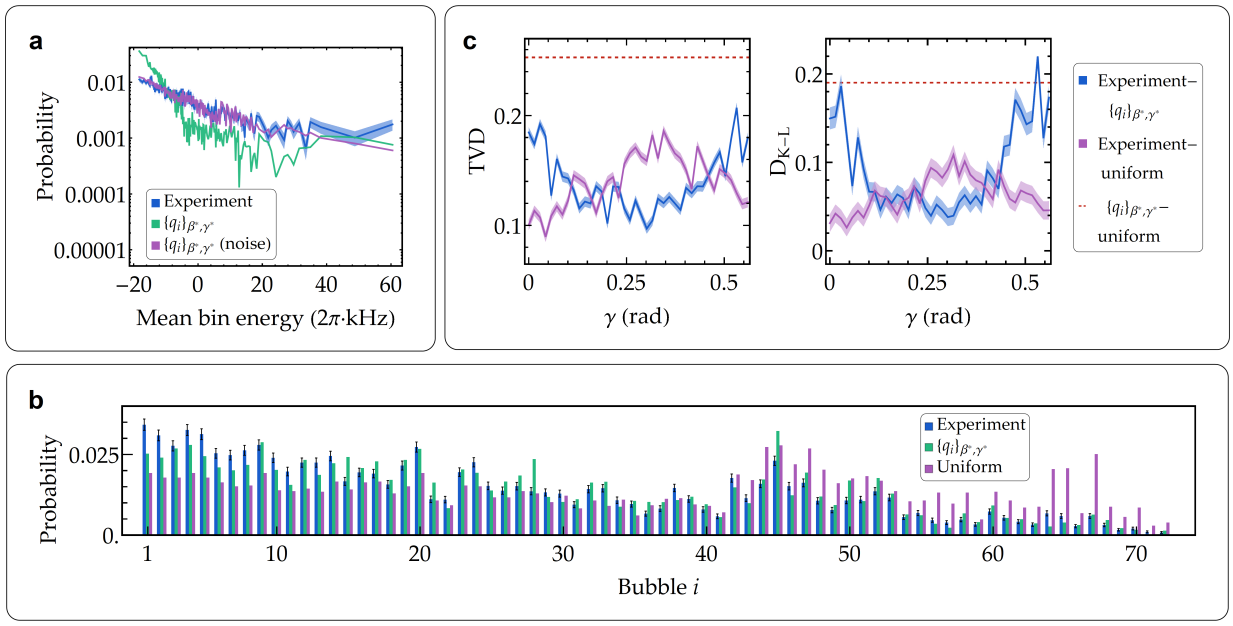


Figure 4.8. Sampling from $p = 1$ QAOA. All of the sampling data was taken on system 2. **(a)** Eigenstate probability histogram for 12 qubits with $B = 0$. The numerical histogram is computed by decomposing the ideal QAOA output state on the $\{|x_i\rangle\}$ basis. We performed 10,800 measurements to oversample the Hilbert space of dimension $2^N = 4,096$ at the optimal parameters $\beta^* = 0.25$ and $\gamma^* = 0.31$. The 4,096 eigenstates are grouped in bins of 20 for clarity purposes. The uncertainty bands follow the multinomial distribution standard deviation (SD). Here, $J_0/(2\pi) = 0.33\,\text{kHz}$ (see "Noise Sources" in the SM of Ref. [42] for details). **(b)** Histogram of coarse-grained distributions comparing data, theory, and the uniform distribution. The error bars here also represent the SD of the multinomial distribution. **(c)** TVD and Kullback-Leibler divergence as a function of γ, keeping β fixed at the optimal value (1,350 shots per time step). The nonzero TVD value of the violet curve at $\gamma = 0$ is due to state preparation and detection errors, as well as undersampling (see SM of Ref. [42]). The distance from the uniform distribution increases as the γ parameter reaches the optimal point γ^*. Dashed lines are the comparison between the ideal QAOA distribution $\{q_i\}_{\beta^*,\gamma^*}$ and the uniform distribution. The uncertainty bands are based on the aforementioned error in the probability of each state bubble for the experimental distribution, propagated to the TVD and the D_{K-L}, according to Eq. (4.8).

probability distribution since $|\psi(0)\rangle$ is an equal superposition of all of the eigenstates of H_A. Indeed, at $\gamma = 0$, the TVD between the data $\{p_i\}$ and the uniform distribution is smaller than one TVD between the data and the ideal QAOA distribution $\{q_i\}_{\beta^*,\gamma^*}$. On the other hand, as the γ parameter was scanned, we observed a net decrease of both the TVD and D_{K-L} between the experiment $\{p_i\}$ and the QAOA ideal distribution $\{q_i\}_{\beta^*,\gamma^*}$. This behavior in both metrics

is in agreement with the decrease in energy, computed by measuring the one- and two-body correlators.

4.7 Summary of the QAOA Experiment

We approximated the ground-state energy of a nontrivial quantum Hamiltonian, showing an almost constant time scaling with the system size. Single-shot, high-efficiency qubit measurements in different bases gave access to the full distribution of bit-strings that is generally difficult or potentially impossible to model classically. With the addition of individual control over the interactions between qubits, as well as improvements to fidelity and system size, the variational quantum-classical hybrid approach can be employed in a trapped-ion experimental platform to give insight into quantum chemistry [46, 58, 59] and hard optimization problems [60], such as maximum-satisfiability or exact cover [61], or be used for the production of highly entangled states of metrological interest [62].

Chapter 5: Dynamically Decoupling Quantum Simulations

The focus of this chapter theoretically examines and experimentally demonstrates how dynamical decoupling methods can be extended to quantum simulation experiments. In addition, we combine these dynamical decoupling principles with Floquet Hamiltonian engineering techniques to simulate approximately the spin-1/2 Haldane-Shastry model. This research was published in the article, "Engineering Dynamically Decoupled Quantum Simulations with Trapped Ions" [63] and this chapter presents the dynamical decoupling project in a similar manner.

5.1 Dynamical Decoupling

The coherence of a quantum system is crucial property. The coherence time of a quantum system is, however, finite and often sets a limit to how long dynamics can be observed or the number of operational gates that can be applied before decoherence dominates the system. Dynamical decoupling, driving a quantum system with global operations (rotations), is a targeted and well-known technique that is used to cancel out known noise sources in order to extend the quantum system's coherence [64–66]. This method has been utilized to preserve the coherence of a quantum state which is important for applications in quantum memories and quantum computations [67–71].

We are interested in developing dynamical decoupling experimental sequences that will

extend the coherence of a quantum system evolving under a target Hamiltonian. The dynamical decoupling sequence not only needs to reduce the influence of a known noise source, but it also should not alter the intended dynamics of the quantum simulation. This additional constraint is usually not present when dynamical decoupling is used to preserve the coherence of a quantum state. However, in a trapped-ion quantum simulator such as the one discussed in this dissertation, this constraint can be satisfied since we can periodically change the form and application of the Hamiltonians in sync with global rotations. These principles and general requirements for dynamically decoupled sequences suitable for quantum simulation experiments are presented next. Dynamical decoupling will also now be abbreviated by DD.

5.2 Principles of Dynamical Decoupling

The theoretical framework of the developed dynamical decoupling sequences examined in this chapter will be reviewed now. In this discussion, we will introduce the general requirements needed for a pulse sequence to decouple a quantum many-body system from certain noise terms without altering the intended dynamics. Analysis of these decoupling pulse sequences utilizes the framework of average Hamiltonian theory (AHT). Like the dynamical decoupling techniques, AHT is a prominent analytical method with origins stemming from the development of nuclear magnetic resonance (NMR) spin manipulation [72–74].

Under AHT, a static average Hamiltonian $\overline{\mathcal{H}}$ approximately describes the evolution resulting from an applied pulse sequence which is actually governed by a time-dependent Hamiltonian $\mathcal{H}(t)$ [75]. Essentially, instead of solving Schrödinger's time-dependent differential equation to obtain an expression for the time-evolution operator $U(t)$, AHT provides an approximate solu-

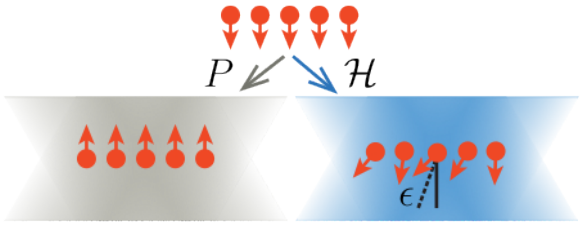
tion: $U(t) = e^{-i\overline{\mathcal{H}}t}$, where $\hbar = 1$. The effective Hamiltonian $\overline{\mathcal{H}}$ can be subjected to a series expansion known as the Magnus expansion where the n^{th} order term $\overline{\mathcal{H}}^{(n)}$ corresponds to the n^{th} order average Hamiltonian [76]. An important property of AHT, is that each order-term of the Magnus expansion is Hermitian and time-independent. These two properties are inherited by any truncation order n of the average Hamiltonian and guarantees that the time-evolution operator is unitary [75]. AHT can be extended to periodic (Floquet) sequences in which $\overline{\mathcal{H}}$ is the effective Hamiltonian corresponding to a single Floquet cycle [77].

Using the analysis tools from AHT, we consider a quantum (spin) system that can be subjected to two types of controllable operations: global rotations (P) and Hamiltonian evolution ($\mathcal{H}$), as depicted in Fig. 5.1a. An operation specified by P_n will uniformly rotate all the spins about either the x or y axis of the Bloch sphere by an angle θ. An operation governed by $\mathcal{H}_n$ turned on for duration t_n will generate spin-spin interactions, represented by fluctuating spin angles shown in Fig. 5.1a. However, $\mathcal{H}_n$ can induce an unwanted coherent error, denoted by ϵ. Over time these errors can accumulate contributing to decoherence. With this pretext, we examine a generic pulse sequence consisting of alternating applications of $\mathcal{H}$ and P can be described by the following unitary time-evolution operator,

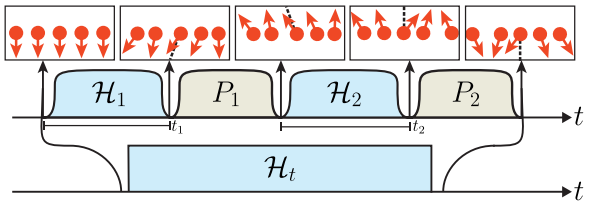
$$U_1 = P_n e^{-i\mathcal{H}_n t_n} \dots P_1 e^{-i\mathcal{H}_1 t_1}, \tag{5.1}$$

where $\hbar = 1$ and evolution under the n^{th} Hamiltonian $\mathcal{H}_n$ is applied for a duration t_n followed by a global rotation P_n (see Fig. 5.1b in which $n = 2$).

It is more convenient to analyze the dynamics of this pulse sequence given by Eq. (5.1) in the interaction frame, also known as the "toggling frame," in which operators act in a rotated frame determined by the previous pulses. The evolution operator of the pulse sequence expressed



(a)



(b)

Figure 5.1. Generalized decoupling sequence for quantum simulation. **(a)** We consider a spin system that can be subjected to two classes of controllable operations which are illustrated as a pair of laser beams: overall global rotation pulses (P_n) and Hamiltonian evolution ($\mathcal{H}_n$) for some period of time (t_n). The Hamiltonian evolution induces interactions (represented by fluctuating spin angles) but can also introduce a coherent error (represented by a tilt of ϵ in the average spin axis). **(b)** The goal of the dynamical decoupling sequence is to alternate periods of $\mathcal{H}_n$ and P_n operations, so that the final evolution after the pulse sequence corresponds to evolution (up to an overall rescaling) under a target Hamiltonian $\mathcal{H}_t$ while the error ϵ is canceled out.

in the interaction frame is,

$$U_1 = (P_n \dots P_1)\, e^{-i(\mathcal{H}'_n t_n)} \dots e^{-i(\mathcal{H}'_1 t_1)}, \tag{5.2}$$

$$\mathcal{H}'_n = (P_{n-1} \dots P_1)^{-1}\, \mathcal{H}_n\, (P_{n-1} \dots P_1)\,, \tag{5.3}$$

where the toggling-frame Hamiltonians $\mathcal{H}'_n$ are defined in Eq. (5.3). Invoking the framework of AHT, the resulting dynamics under the toggling-frame Hamiltonians $\mathcal{H}'_1$ to $\mathcal{H}'_n$ can be approximately described by evolution under a time-independent effective Hamiltonian $\overline{\mathcal{H}}$:

$$U_1 \approx (P_n \dots P_1)\, e^{-i\overline{\mathcal{H}}T}, \tag{5.4}$$

$$\overline{\mathcal{H}} = T^{-1} \sum_n \mathcal{H}'_n t_n, \tag{5.5}$$

where T is the total evolution of the pulse sequence including the durations of the global pulses. Equation (5.5) corresponds to the lowest-order term in a Magnus expansion of the effective Hamiltonian, which is simply the weighted average of the different rotated Hamiltonians that make up the pulse sequence. Within this context we define a dynamically decoupled sequence which eliminates an unwanted noise term denoted by operator $\mathcal{O}$, as a pulse sequence described

by $\overline{\mathcal{H}}$, an average Hamiltonian that does not include $\mathcal{O}$, despite the possible presence of $\mathcal{O}$ in the actual realization of an individual $\mathcal{H}_n$.

Having presented the initial formulation of a dynamically decoupled sequence, a couple more requirements are imposed such that the developed scheme is complimentary to quantum simulation experiments. First, in the absence of noise, we require that the unitary evolution governed by Eq. (5.1) is the same as evolution under the target Hamiltonian $\mathcal{H}_t$ up to an overall scaling factor. Second, we require that the frame at the end of the pulse sequence match the initial frame. Mathematically, these two conditions are represented by the following two equations, respectively:

$$\overline{\mathcal{H}} = \mathcal{H}_t, \tag{5.6}$$

$$P_n \dots P_1 = I. \tag{5.7}$$

These equations, in the absence of noise, imply that the average-Hamiltonian-theory description of the pulse sequence dynamics is exact. Higher-order corrections to $\overline{\mathcal{H}}$ can be calculated from the commutator $[\mathcal{H}'_n, \mathcal{H}'_m]$, which equates to zero. Importantly, the dynamics are guaranteed to follow the target Hamiltonian provided that the pulse sequence is fast enough to implement decoupling effectively. Lastly, we limit ourselves to decoupling sequences that are periodic in time T. This condition is a less stringent requirement. Accordingly, U_1 becomes the unitary evolution under one cycle, with the total evolution after m steps being:

$$U = \prod_m \left(U_1\right)^m. \tag{5.8}$$

Combined with the previous condition, this allows us to vary the total evolution time by integer cycles and observe time evolution matching $\mathcal{H}_t$, as long as decoupling is effective.

5.3 Implementing DD Sequences in QSim

We have now introduced a generalized dynamical decoupling scheme suitable for simulating dynamics described by a target Hamiltonian without specifying a particular quantum system. However, we now focus our attention to demonstrating this technique with a system of trapped ions. This section will introduce how briefly review how Hamiltonian interactions $\mathcal{H}$ and global rotations P are generated in our quantum simulator and some primary sources of decoherence.

Coherent operations, applied to a linear chain of N ions, are generated by uniformly illuminating the entire chain with two non-copropagating pulsed laser beams in order to drive stimulated Raman transitions between the collective spin states in which the Raman beat-note frequency is tuned to be resonant with the qubit splitting. The Raman beams are oriented such that the resulting difference wave vector is projected onto the x-axis of the ion chain's motion. This configuration paired with applying a beat-note tone tuned nearly resonant with a specific phonon normal mode frequency enables the ability to couple coherently both the collective motional mode and spin state together. More specifically, the application of a tone λ can be written as the following Hamiltonian term:

$$\mathcal{H}_{\lambda}(t) = \frac{\Omega_{\lambda}}{2} \sum_{j} \sigma_{j}^{+} \left(1 + i \sum_{m} \eta_{jm} \left[a_{m} e^{-i\omega_{m} t} + a_{m}^{\dagger} e^{i\omega_{m} t}\right]\right) e^{-i\mu_{\lambda} t + i\phi_{\lambda}} + h.c., \tag{5.9}$$

where the parameters Ω_{λ}, μ_{λ}, and ϕ_{λ} correspond to the Raman Rabi frequency, detuning from the qubit resonance and beat-note phase of tone λ, respectively. All three of these parameters can be precisely set. In Eq. (5.9), indices j and m denote a given ion and phonon normal mode of motion along the x-direction, respectively, while σ_{j}^{+} is the raising spin operator of the j^{th} ion, η_{jm} is the Lamb-Dicke parameter for ion j and phonon normal mode of motion m, and lastly,

a_m, $a_m^\dagger$, and ω_m correspond to the phonon ladder operators and normal mode frequency for mode m, respectively. See Ch. 3 for more about the interactions.

A common target Hamiltonian for trapped-ion quantum simulators is an Ising model that has long-range spin-spin interaction strengths, J_{ij}, paired with an effective magnetic field along direction k with a uniform magnitude B_k. One example is the long-range transverse field Ising model:

$$\mathcal{H} = \sum_{i<j} J_{ij} X_i X_j + B_y \sum_i Y_i. \tag{5.10}$$

However, several errors can cause the observed dynamics to deviate from evolution according to Eq. (5.10). Some types of decoherence errors include unwanted magnetic or electric fields, mode frequency drifts, off-resonant motional excitation, and spontaneous emission [27]. Errors that are more specific to our quantum system that can arise during evolution under $\mathcal{H}_n$ are:

- Fluctuations in the ratio between the on-resonance sideband Rabi frequencies generating the interactions causes the "nulled" fourth-order AC Stark term to drift away from zero. These fluctuations are of special concern because the AC Stark shifts, unlike the spin-spin couplings, are not suppressed by η^2. As a result, they are often much larger than the intended terms in the Hamiltonian (typically about an order of magnitude larger than $J_{i,i+1}$ for our experimental parameters) and therefore require a high degree of fractional stability.
- More generally, fluctuations in any of the laser intensities generating the Hamiltonian terms, causing the values of J_{ij} or B_y to vary over time.
- Errors arising from finite population of the motional states. These can occur from direct excitation of these transitions by the tones, or due to heating processes that these tones couple into the spin dynamics [27].

We will demonstrate, in the following sections, dynamical decoupling sequences that suppress the AC Stark noise, the dominating decoherence causing error, and show that these decou-

pling sequences leads to a large increase in coherence for sufficiently large detuning μ.

5.4 Application to Trapped Ions and Example Sequences

Having introduced the dynamical decoupling scheme suitable for quantum simulations and identified AC Stark noise as the type of error we wish to suppress, we will now layout example sequences applicable to trapped ion simulation experiments. AC Stark noise enters as an effective magnetic field along the z direction that can be written as an operator $\mathcal{O} = \sum_i \epsilon_i(t) Z_i$ [2]. The goal of the dynamical decoupling sequence applied to a quantum simulation experiment will be to suppress the influence of AC Stark noise in order to extend the coherence of the dynamics governed by the target Hamiltonian $\mathcal{H}_t$.

There are several features specific to trapped-ion platforms that happen to be very suitable in order to realize pulse sequences that meet this goal. First, the known noise varies relatively slowly compared to the duration of the applied pulses P_n. Second, both types of operations $\mathcal{H}_n$ and P_n are generated by laser tones that are highly controllable. More specifically, these operations can be turned on and off and modified one by one or together. Third, the noise only occurs when Hamiltonian interactions are applied and are not specific to the form of $\mathcal{H}_n$. The first and third features stem from experimental observations that have been documented informally and historically.

It is important to highlight two results from the second mentioned attribute of our trapped-ion system. First, during the application of the pulses P_n, no extraneous evolution occurs. Simply put the pulses rotate the spins from their current state to the intended state described by a rotation operator even though the pulses have a finite duration. In contrast, systems with fixed interactions

may produce undesired evolution from the application of the decoupling pulse. Second, because of the significant control and tunability of the individual Hamiltonians $\mathcal{H}_n$, we are able to generate an average Hamiltonian that in the static limit is inaccessible due to the physical realization of the interactions.

The following formula summarizes the explicit transformation of the Pauli operators under global π pulses:

$$R_k^{-1}(\pi)\sigma_{j'}^{k'}R_k(\pi) = (-1)^{1+\delta_{k,k'}}\sigma_{j'}^{k'}. \tag{5.11}$$

In Eq. (5.11), $\sigma_{j'}^{k'}$ denotes the individual ion j' Pauli operator in the k' direction while the global π pulse about the k-axis is represented by the rotation operator $R_k(\pi)$. As a reminder, the global rotation operator that rotates a system of N spins by an angle θ about the k^{th} axis is defined as,

$$R_k(\theta) = \exp\left[-i\sum_j \sigma_j^k\theta/2\right] = \mathbb{I}\cos(\theta/2) - i\sin(\theta/2)\sum_{j=1}^{N}\sigma_j^k, \tag{5.12}$$

where both the identity operator $\mathbb{I}$ and individual ion Pauli operators are written in the Hilbert space of the N-ion system. Geometrically, a π pulse flips the sign of the ion's Pauli operator unless the axis of rotation k and the Pauli operator direction k' coincide. This property enables the categorization of operators based on their parity under a given π rotation. More specifically, the difference in parity of spin-spin interactions versus single spin terms under a π rotation can be used to design dynamically decoupled pulse sequences such that the noise operator, $\mathcal{O}$, is cancelled at the end of the sequence while the desired evolution remains unchanged. Following, are three example sequences that incorporate our dynamical decoupling technique.

5.4.1 Example 1: A CMPG Sequence

As a minimal example of a decoupling sequence satisfying our requirements, we consider a typical asymmetric Carr-Purcell-Meiboom-Gill (CMPG) sequence [65]. The target Hamiltonian includes spin-spin interactions and uniform magnetic fields along each direction:

$$\mathcal{H}_t = \sum_{i<j} J_{ij} X_i X_j + \sum_i \Big[B_x X_i + B_y Y_i + B_z Z_i \Big]. \tag{5.13}$$

For this sequence, the number of alternating operations of $\mathcal{H}$ and P corresponds to $n = 2$ as illustrated by Fig. 5.1b. In an asymmetric CPMG $n = 2$ sequence, the two pulses, P_1 and P_2, are both π rotations along the y-axis and each occur after Hamiltonian evolution of $\mathcal{H}_1$ and $\mathcal{H}_2$, respectively, which have equal evolution durations, $t_1 = t_2$ [65]. A single cycle of this CPMG pulse sequence is the following:

$$U_1 = R_y(\pi) e^{-i\mathcal{H}_2 t_1} R_y(\pi) e^{-i\mathcal{H}_1 t_1}, \tag{5.14}$$

where Hamiltonians $\mathcal{H}_1$ and $\mathcal{H}_2$ are written as

$$\mathcal{H}_1 = \sum_{i<j} J_{ij} X_i X_j + \sum_i \Big[B_x X_i + B_y Y_i + B_z Z_i + \epsilon_i(t) Z_i \Big], \tag{5.15}$$

$$\mathcal{H}_2 = \sum_{i<j} J_{ij} X_i X_j + \sum_i \Big[(-B_x) X_i + B_y Y_i + (-B_z) Z_i + \epsilon_i(t) Z_i \Big]. \tag{5.16}$$

Note that we have explicitly included the noise term $\mathcal{O}_i = \epsilon_i(t) Z_i$ in both $\mathcal{H}_1$ and $\mathcal{H}_2$.

This asymmetric CPMG sequence satisfies our requirements for a suitable dynamically decoupled procedure for various reasons. First, the spin-spin interaction term has even parity under any π pulse and is therefore unchanged by $R_y(\pi)$. Second, the B_y term also has even parity under $R_y(\pi)$ since their axes are the same. Finally, despite the B_x and B_z terms having odd parities under $R_y(\pi)$, the signs of these terms are flipped between $\mathcal{H}_1$ and $\mathcal{H}_2$ ensuring the

preservation of these two terms by the end of the application of P_2. The frame in which the evolution of $\mathcal{H}_2$ occurs is rotated with respect to the initial frame but is returned after P_2. As a result, evolution under $\mathcal{H}_t$ given by Eq. (5.13) is achieved by the sequence evolution operator U_1 in which the dynamics are unchanged by the four pulses. In addition, this sequence decouples the target evolution from σ_z noise which has odd parity and is approximately canceled by the end of U_1. The exact degree of suppression depends on the power spectrum of $\epsilon(t)$ compared to the pulse sequence frequency as well as the commutator of the noise with the target Hamiltonian [63, 67].

This example sequence demonstrates that the ability to vary the Hamiltonian during the experimental realization expands the range of possibilities for $\overline{\mathcal{H}}$. If we were limited to a single Hamiltonian, such as $\mathcal{H}_1$, it would have been impossible to have terms proportional to X_i or Z_i in $\overline{\mathcal{H}}$ because they do not respect the symmetry of the pulse sequence. Thus, controllability of the Hamiltonian significantly expands the range of models amenable to dynamical decoupling. We introduce two more examples that demonstrate the freedom of changing the form of the Hamiltonian between global pulses extending the quantum simulation toolbox.

5.4.2 Example 2: A XY Sequence

The second protocol that we consider is a version of the XY dynamical decoupling sequence [65]. The target Hamiltonian for the quantum simulation remains the same, given by Eq. (5.13). The pulse sequence cycle length is $n=4$ and the unitary operator U_1 is given by:

$$U_1 = R_y(\pi)e^{-i\mathcal{H}_4 t_1}R_x(\pi)e^{-i\mathcal{H}_3 t_1}R_y(\pi)e^{-i\mathcal{H}_2 t_1}R_x(\pi)e^{-i\mathcal{H}_1 t_1}, \tag{5.17}$$

where all four Hamiltonians are evolved for a duration t_1 and the global π rotations are alternated about the x- and y-axis, respectively. This U_1 sequence, Eq. (5.17), traverses a slightly more

complicated rotating frame that only returns to the original frame after the fourth global π pulse. As a result, the form of the four Hamiltonians have global B-field terms with differing signs that must be cycled through in order not to alter the intended evolution described by $\mathcal{H}_t$ while ensuring the approximate zeroing of the σ_z-noise. The spin-spin Ising interaction term remains the same for $\mathcal{H}_1$, $\mathcal{H}_2$, $\mathcal{H}_3$, and $\mathcal{H}_4$ while the directions of the uniform magnetic fields are listed in Table 5.1.

	$\mathbf{B_x}$	$\mathbf{B_y}$	$\mathbf{B_z}$
$\mathcal{H}_1$	$+$	$+$	$+$
$\mathcal{H}_2$	$+$	$-$	$-$
$\mathcal{H}_3$	$-$	$-$	$+$
$\mathcal{H}_4$	$-$	$+$	$-$

Table 5.1. Signs of uniform magnetic field terms for Hamiltonians in XY sequence.

Compared to the CMPG sequence, the additional complexity of the XY sequence has the advantage of being insensitive to pulse-length errors [65], due to the chirality condition satisfied by the pulse sequence [78]. Another feature of this dynamical decoupling sequence is that noise along the x and y directions in addition to z is removed at the end of a single cycle. As a note, a similar robustness to pulse-length error can be achieved in the CPMG sequence given by Eq. (5.14) by alternating the sign of the π rotation along the y-axis between P_1 and P_2.

5.4.3 Example 3: A Decoupled Heisenberg Model

The first two dynamical decoupling sequence examples have so far obeyed our stringent requirement that the Hamiltonian operate exactly the same in each rotated frame. Satisfying this principle ensures that the dynamics are unchanged by the decoupled pulse sequence, removing any higher-order terms in the Floquet-Magnus expansion. However, this condition can be re-

laxed in order to engineer a desired average Hamiltonian that is not accessible in the static limit. For example, in the toggling frame in which X_iX_j is spanned by two $R_y(\pi/2)$ pulses, the Ising interactions along the x direction are rotated to the $-z$ direction, $-Z_iZ_j$, which is not physically realizable in our trapped-ion experimental system. Recently, this concept of Hamiltonian engineering has been used to extend the capability of quantum simulators [78–81]. While this imposes the extra condition that the cycle time or a Trotter step [82, 83] be sufficiently small, within this limit it is natural to combine this technique with dynamical decoupling.

The last example that we consider is a pulse sequence that realizes, in the limit of a high-frequency drive, a dynamically decoupled long-range Heisenberg model that is insensitive to pulse-length errors:

$$U_1 = R_y(-\pi/2)e^{-i\mathcal{H}_{XX}t_1/2}R_y(\pi)e^{-i\mathcal{H}_{XX}t_1/2}R_y(\pi/2)e^{-i\mathcal{H}_{YY}t_1}R_y(-\pi)e^{-i\mathcal{H}_{XX}t_1}, \tag{5.18}$$

where $\mathcal{H}_{XX}$ and $\mathcal{H}_{YY}$ are long-range Ising interactions along the x and y directions, respectively. Later on in this dissertation chapter, we apply this sequence to experimentally engineer the Haldane-Shastry model.

5.5 Two-Ion Tests of Pulse-Sequence Parameters

We initially experimentally optimized and benchmarked the effectiveness of dynamical decoupling with minimal tests using two ions. The sequence is a simplified version of the XY sequence:

$$U_1 = R_{-y}(\pi)e^{-i\mathcal{H}_{XX}t_1}R_x(\pi)e^{-i\mathcal{H}_{XX}t_1}, \tag{5.19}$$

where U_1 represents a single unit of the decoupled pulse sequence that has a cycle time, t_{U_1}, equal to twice the sum between t_1, the Hamiltonian evolution of $\mathcal{H}_{XX}$ and t_π, the small finite

duration of the global π pulse: $t_{U_1} = 2(t_1 + t_\pi)$. Referring back to Eq. (5.8), this XY sequence is performed for integer m cycles in which the corresponding t_m, the duration after m applications of U_1 is $t_m = mt_1$. In comparison, the continuous (uncoupled) version of Eq. (5.19) corresponds to evolving the two ions under simply $\mathcal{H}_{XX}$, also known as a two-ion Mølmer-Sørenson (MS) interaction [84], for a duration t.

Starting with both ions in the state $|\downarrow\downarrow\rangle$, the ideal state after turning on $\mathcal{H}_{XX}(t)$ has a simple form,

$$|\psi(t)\rangle = \cos\left(\overline{J_0}t\right)|\downarrow\downarrow\rangle - i\sin\left(\overline{J_0}t\right)|\uparrow\uparrow\rangle\,, \tag{5.20}$$

where $\overline{J_0}$ is the spin-spin coupling of the average Hamiltonian $\overline{\mathcal{H}}$. Compared to the general form of the XY sequence given in Eq. (5.17), both $\mathcal{H}_{XX}$ and the average ion z magnetization, $\langle Z\rangle = N^{-1}\sum_i \langle Z_i\rangle$, are symmetric under sign changes in x and y. This consequence allows us to use a fundamental time step with only two π pulses, rather than four, without changing any measurement outcomes. Besides representing a basic building block of our quantum simulations, unitary evolution under a MS interaction is highly sensitive to the dephasing noise that we are trying to suppress.

Figure 5.2 shows a typical example of this technique. The interspersed π pulses effectively cancel out the slow AC SS noise that is the primary cause of decoherence, while evolution under $\mathcal{H}_t$ is unaffected up to an overall scaling factor. Using the data of this type, we quantify the success of the dynamical decoupling using the quantity $\overline{J_0}\tau$ which is the product of the coherence time τ and $\overline{J_0}$. More specifically, we fit the average ion magnetization along the z direction to the function:

$$g(t) = A[1 - e^{t/\tau}\cos\left(2\overline{J_0}t\right)] - 1. \tag{5.21}$$

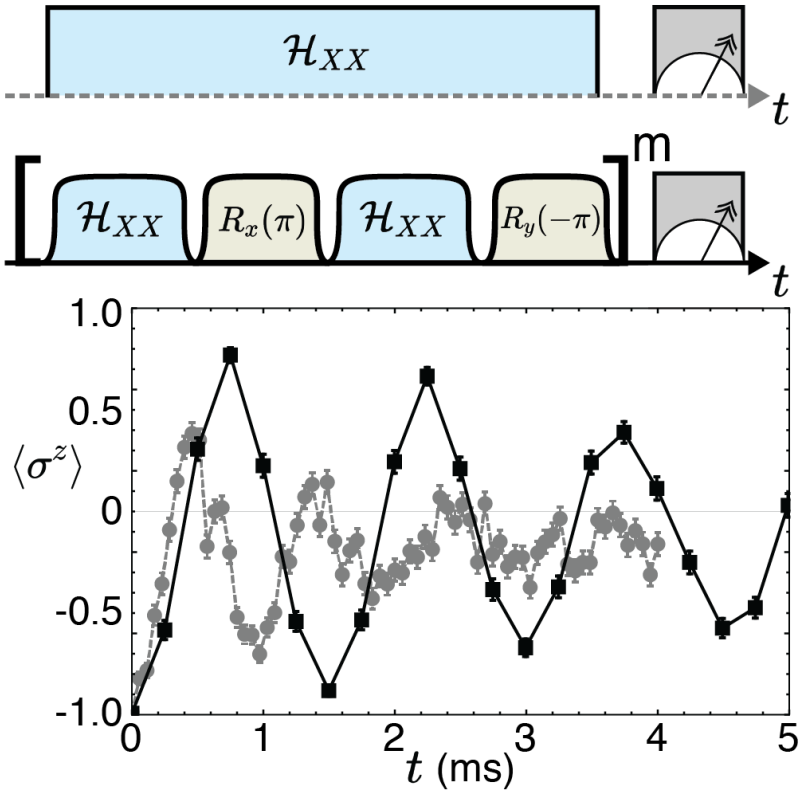


Figure 5.2. An example of dynamical decoupling for a two-ion interaction. Direct evolution of the average ion z-magnetization, $\langle Z\rangle$, under $\mathcal{H}_{XX}$ (gray dashed line) is quickly damped due to slow dephasing noise from fluctuating Stark shifts. In comparison, the dynamical decoupling scheme [Eq. (5.19)] consisting of alternating π pulses about the x and y axes (black solid line) preserves coherence to substantially longer times, even after accounting for the slowing of the averaged interactions, without otherwise altering the intended dynamics. Each point represents the mean of 300 experimental repetitions, with error bars of 1 SEM (standard error of the mean). The experimental parameters used for the decoupled sequence results are $t_p = 20\,\mu$s, $t_1 = 120\,\mu$s, and $\delta/(\eta\Omega) = 5.0$.

The AC SS noise leads to both a finite τ due to dephasing, and to $A < 1$, due to a nonzero average magnitude of the energy difference between the states $|\downarrow\downarrow\rangle$ and $|\uparrow\uparrow\rangle$.

For the data shown in Fig. 5.2, the fit values for $\overline{J_0}/(2\pi)$ are 0.52 kHz for the bare (non-decoupled) evolution and 0.33 kHz for the dynamical decoupling. Meanwhile, the fit values for τ are 1.2 ms and 7.5 ms for the evolution sequence without and with dynamical decoupling, respectively. The difference in fitted parameter values between the two sequences illustrates the central trade-off of dynamically decoupled procedures: overall slower dynamics but the potential

for an increase in the coherence time such that the product of the two improves (from $\overline{J_0}\tau = 3.9$ to 15.6). These best-fit functions are not plotted in Fig. 5.2.

We now describe a few parameters of the dynamical decoupling sequence that must be chosen for optimal performance, i.e. effective decoupling. A dynamically decoupled two-ion MS sequence, for example, is dependent on three parameters: the pulse-shaping properties, the drive rate of the interactions, and the detuning μ of the tones used to generate $\mathcal{H}_{XX}$. We examined and optimized each of these parameters separately, and this discussion follows next. Lastly, we will briefly discuss the noise model used in simulating the full two-ion Mølmer-Sørenson evolution.

5.5.1 Pulse Shaping

We smoothly turn on and off both the global interactions and the global rotations in order to reduce unwanted motional transitions resulting from spectral broadening of the pulses. This shaping of the pulses is especially crucial for interactions, which are relatively near detuned from motional transitions. We use a Tukey window [85] with a shaping parameter $\kappa = 2t_p/T$, where t_p is the pulse-shaping time that describes the amount of time for which the pulse is either being ramped up or down compared to the total pulse length denoted by T. For the interactions, the most relevant quantity is $t_p\delta$, the product of the pulse-shaping time and the detuning from the nearest motional resonance $\delta = (\mu - \omega_x)/(2\pi)$. The degree of spectral broadening is dependent on the value of t_p. We experimentally find that setting $t_p\delta \geq 3$ makes the induced error from motional excitations negligible, leading to a typical value of $t_p = 20\,\mu s$ for our parameters. The global rotations, while less sensitive to the shaping of their pulses, due to the fact that the RF amplitude is lower, has a corresponding pulse shaping parameter value of $\kappa = 0.4$.

The pulse shaping of the interactions leads to a decrease in the overall scale of the averaged Hamiltonian, which depends on the precise way in which the RF waveform is imprinted onto the laser intensity. This effective scaling can be theoretically predicted or determined with measurements of the *ex situ* beam power, but we chose to characterize it with *in situ* ion dynamics. This investigation was done by a process we call by experimentally determining comparing the difference in pulse area between an unshaped square pulse (ignoring the rise times of the AOMs) and a shaped interaction pulse with a shaping time t_p. We find that the averaged spin-spin coupling for a single pulse of the interactions obeys,

$$\beta = \int_0^{t_1} \frac{J(t)\,dt}{J_0 t_1} = 1 - 1.178\left(\frac{t_p}{t_1}\right), \tag{5.22}$$

where $J(t)$ ramps from 0 to J_0 and where $t_1 > 2t_p$. For our normal drive parameters, β is near 0.8, meaning that the pulse shaping removes about 20% of the area under $J(t)$. The pulse-averaged βJ_0 can then be used in the standard formulas of the average Hamiltonian theory. For example, in the XY sequence of Fig. 5.2, the average Hamiltonian for the two ions is,

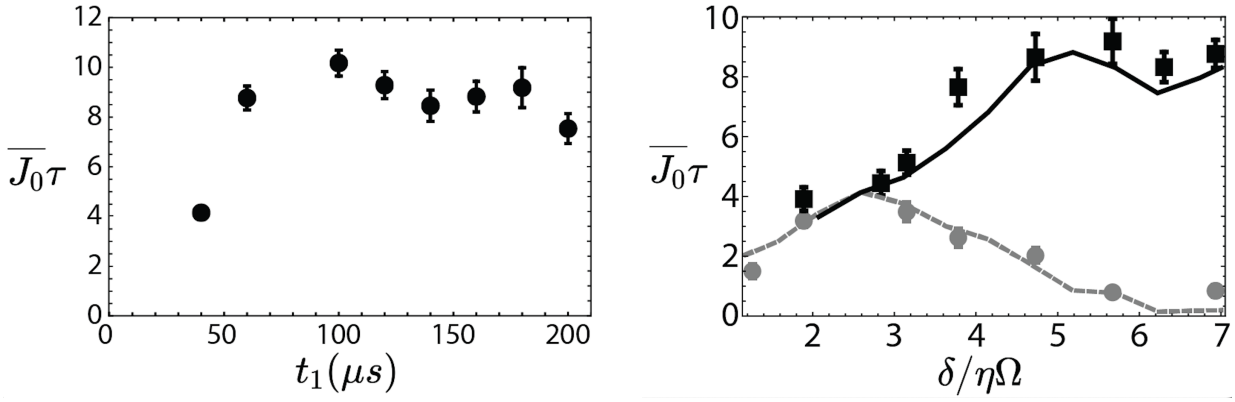
$$\overline{\mathcal{H}} = \overline{J_0} X_1 X_2, \qquad \overline{J_0} = \beta J_0 \left(\frac{t_1}{t_1 + t_\pi}\right), \tag{5.23}$$

simply reflecting the fraction of time during U_1 in which the interactions are applied. For a fuller discussion on the shaping of the laser interaction pulses and how the strengths of different terms in the Hamiltonian are affected, I recommend reading Sec. 3.2 of Ref. [2].

5.5.2 Drive Rate

The drive rate, or the value of $1/t_1$, is set by two considerations. The drive rate determines the bandwidth of noise that is suppressed and must be chosen to be fast enough for the observed

noise. The drive also sets the minimum time step, so it should be chosen in order that the dynamics of interest are resolved. On the other hand, increasing the drive rate does not lead indefinitely to better performance because it slows down the experimental timescale, increasing sensitivity to any slow drifts that are not decoupled.



(a) Interaction time t_1 dependence.

(b) Detuning dependence.

Figure 5.3. Dependence of dynamical decoupling pulse sequence parameters. **(a)** The dependence of dynamical decoupling on the pulse length t_1. The scaled coherence time $\overline{J_0}\tau$ is largely flat for pulses longer than 50 µs, suggesting that the noise is slow enough to be canceled out for any choice within this range. For this data, the detuning is fixed at $\delta/(\eta\Omega) = 4.1$. For sufficiently fast drives, we see a decrease in $\overline{J_0}\tau$, which is caused by a decreasing $\overline{J_0}$ without any compensating improvement in τ. **(b)** The dependence of $\overline{J_0}\tau$ on detuning δ, for both decoupled (black) and regular (gray) sequences. The points are experimental data, while the solid lines are numerics incorporating the dominant noise sources. Decoupling is most effective in the regime of large detuning, $\delta/(\eta\Omega) > 5$, in which the evolution without decoupling is nearly completely destroyed. For these data, the drive is fixed at $t_1 = 120$ µs, and the pulse-shaping is fixed at $t_p = 20$ µs throughout. The experimental data in both (a) and (b) are averaged over 300 shots, with error bars from the fit uncertainty.

Varying our experimental drive rate over the range of 40–200 µs (Fig. 5.3a), we observe nearly no decrease in $\overline{J_0}\tau$ with increasing t_1, indicating that the noise we are canceling out is mostly slower than the kHz scale. At sufficiently fast rates of driving, we see a decrease in $\overline{J_0}\tau$ because the fast drive leads to a reduction in the average Hamiltonian parameter $\overline{J_0}$, as seen from Eq. (5.23), without a corresponding improvement in τ.

5.5.3 Detuning

The Mølmer-Sørenson detuning δ is a key parameter in ion trap quantum simulations that determines the power-law range of the spin-spin coupling. It also controls the relative strengths of various sources of error. When δ is relatively small, coupling to the intermediate motional states is strong, and therefore errors associated with this motional coupling, such as fluctuations in the motional resonance frequencies, determine the coherence time. When δ is large, Stark shift noise becomes dominant, with the two being roughly equal near our normal point of operation of $\delta/(\eta\Omega) \approx 3$.

Figure 5.3b shows the dependence of $\overline{J_0}\tau$ on δ, for sequences with (in black) and without (in gray) dynamical decoupling. At small δ the two are similar, while at large δ, the dynamical decoupling begins to perform better. At the optimum value of $\delta/(\eta\Omega) \approx 5$, dynamical decoupling improves $\overline{J_0}\tau$ by over an order of magnitude. The dependence is captured well by a numerical model incorporating the relevant error sources (see Sec. 5.5.4 and Fig. 5.4). The significant improvement of the scaled coherence with dynamical decoupling (as opposed to not including DD) for $\delta/(\eta\Omega) \leq 5$ a suggests that this technique is especially valuable for quantum simulations requiring shorter-range interactions, which are reached with large δ.

5.5.4 Noise Model

For the noise model used in Fig. 5.3b, the full Mølmer-Sørenson evolution [Eq. (5.9)] is simulated for both the red and blue tones for a system of two ions. The maximum number of phonons allowed in each motional mode is truncated to two. The time step for the numerical evolution (using a Krylov subspace algorithm) is fixed at 15 ns. In addition, we add three types

of experimental noise:

1. Stark shift noise: consists of a random, independent intensity fluctuation on each of the two tones. These are constructed to have a power spectrum of $1/f^2$ over the bandwidth of [100 Hz, 1 MHz], and to have an overall fractional variation of $\sigma = 0.021$ over the total sample time of 100 ms.

2. Detuning noise: consists of a Gaussian random variable, with $\sigma = 4.5$ kHz, that is applied as a static shift to the detuning δ for each experimental run.

3. Motional heating: consists of a displacement operator with a random phase that is applied to the highest motional mode (the COM mode) every 1.5 µs, representing fast fluctuations of the global electric fields holding the ions [86]. The amplitude of these random displacements is set at 0.01 to match the decoherence observed in Fig. 5.3 and results in a simulated heating rate of roughly 50 quanta/s. Comparing this value used in the simulation to observed values of the heating rate (previous independent experimental measurements), which is typically between ∼100–200 quanta/s, indicates one way that we could further refine our noise models with independent characterizations of the various processes.

We note that all of these are technical noise sources. The fundamental limit to coherent Mølmer-Sørenson evolution, off-resonant Raman scattering, is several orders of magnitude below these for the chosen parameters. The strengths of the Stark shift noise and detuning noise were taken to match the data in Fig. 5.3b, as were the exact power spectra over the experimental timeframe (choosing from possibilities of $1/f$ noise, $1/f^2$ noise, and an ensemble average of constant values). The strengths are similar to previous estimations of our error sources [42, 87], while the power spectra over experimentally relevant times are not strongly constrained by our previous measurements. Simulations were run for evolution times up to 0.5 ms, and averaged over 20 random realizations of all the error sources, before being fit to extract $\overline{J_0}\tau$. For numeric simulations of the dynamically decoupled sequence, the form of the experimental pulse shaping of the inter-

actions was included, while we took the simplification of approximating the π pulses as perfect and instantaneous.

Fig. 5.4 shows the relative contribution of each of these noise sources to $1/(\overline{J_0}\tau)$, as a function of the detuning $\delta/(\eta\Omega)$. Consistent with our expectations, the decoupled dynamics effectively suppress the Stark shift noise without similarly affecting the other sources.

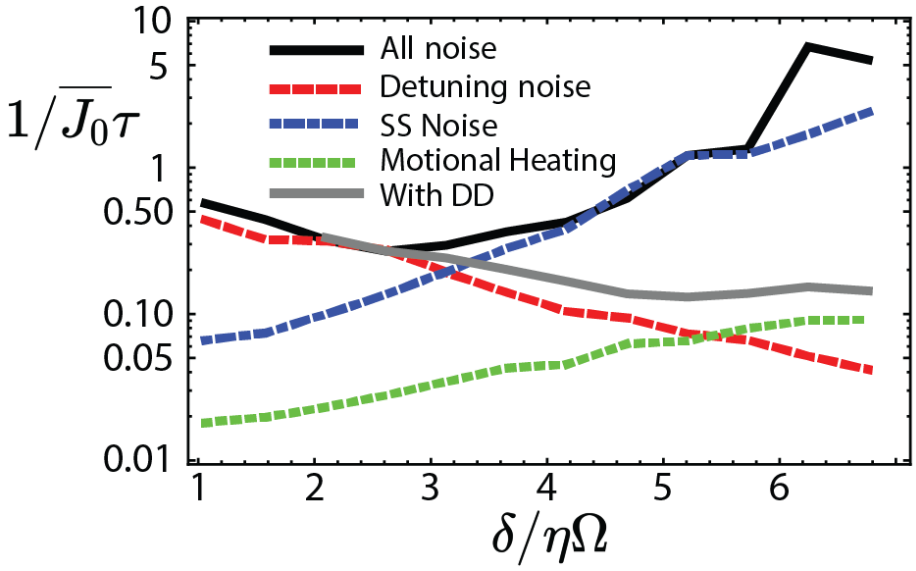


Figure 5.4. Relative contribution of the error terms in noise model. As δ increases, detuning noise decreases while Stark shift noise and motional heating errors increase. Dynamical decoupling effectively mitigates the Stark shift noise while having little effect on the other noise sources.

5.6 Multi-Ion Dynamically Decoupled Realizations

After investigating the effectiveness of a decoupled two-ion system as a function of each dynamical decoupling pulse sequence parameter individually, we next decided to extend this technique to systems with more than two ions. In order to scale our technique to larger system sizes, a change in methodology for determining $\overline{J_0}$ and τ is required. In the previous section, these two parameters were the corresponding best-fit values obtained from fitting the two-ion dynamics to the analytical form given by Eq. (5.21). For the following multi-ion studies, we

calibrate $\overline{J_0}$ using the Mølmer-Sørenson formula [Eq. (3.15)] and AHT, while τ is estimated from an exponential fit to an observable of the system that is conserved by the ideal Hamiltonian but that is modified by decoherence.

5.6.1 11 Ion Dephasing Suppression

We decided to extend the optimized two ion decoupled pulse sequence to a system with $N = 11$ ions. The ions are prepared in an initial product state $|\uparrow\uparrow\uparrow\uparrow\downarrow\downarrow\uparrow\uparrow\uparrow\uparrow\uparrow\rangle_x$, along the x-axis in which the individual addressing beam is utilized to prepare the fifth and sixth ions along the negative x-axis while the remaining spins are aligned along the positive x-direction. Once the initial product is prepared, the system is evolved under a CMPG-type sequence described by,

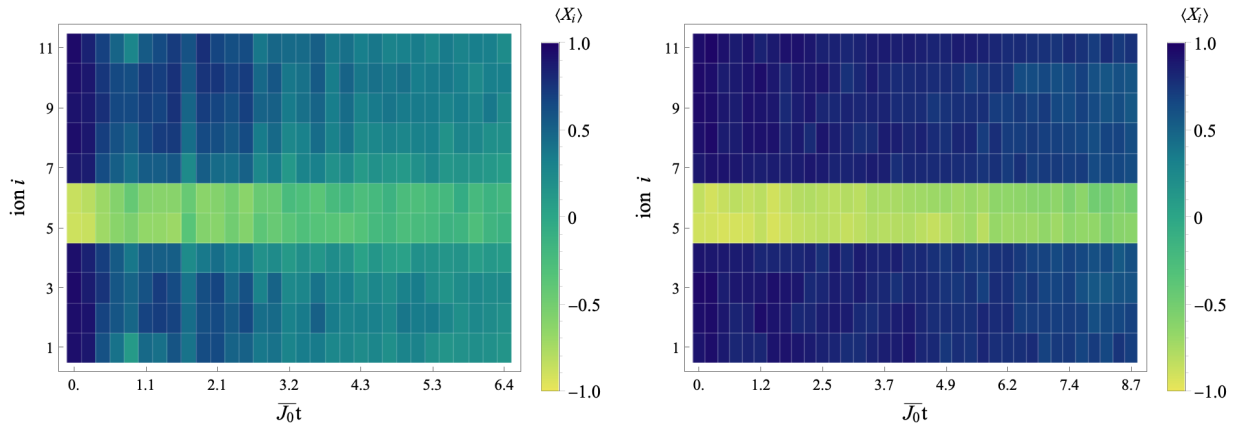
$$U_1 = R_{-y}^{\mathrm{BB1}}(\pi) e^{-i\mathcal{H}_{XX} t_1} R_{-y}^{\mathrm{BB1}}(\pi) e^{-i\mathcal{H}_{XX} t_1}, \tag{5.24}$$

where the coupling strength between spin i and spin j in the Ising Hamiltonian $\mathcal{H}_{XX}$ approximately follow an inverse power-law dependence often described by the formula $J_{ij} \approx J_0 / |i-j|^p$.

To avoid errors associated with the global rotations, we replace each bare rotation $R_{-y}(\pi)$ with a π-BB1 composite pulse denoted by $R_{-y}^{\mathrm{BB1}}(\pi)$ [88]. Ideally, there should be no observed dynamics under U_1 since the system is initialized in an eigenstate of $\mathcal{H}_{XX}$ making any effects of decoherence clearly identifiable. However, with the addition of a small B_y field, this system also exhibits domain wall confinement [89], which can result in nontrivial slow dynamics between the confined quasiparticles. As a result, we expect that this sequence provides a reasonable estimation of the coherence we can expect when studying an interesting many-body system.

Figure 5.5 displays the individual spin magnetizations along x, $\langle X_i \rangle$, as a function of the $\overline{J_0}t$ for both the 11-ion regular evolution under $\mathcal{H}_{XX}$ which is not protected from AC SS noise and

the corresponding dynamically decoupled realization. For this data, $J_0 = 2\pi \times 204\,\text{Hz}$, $\alpha = 1.32$, and $\delta/(\eta\Omega) = 7.5$. As seen in Fig. 5.5b, dynamical decoupling significantly improves the coherent evolution under the target Hamiltonian which corresponds to the preservation of the initialized product state. The improved coherence can be quantified with the general imbalance, $\mathcal{I}(t)$, a



(a) Regular sequence.

(b) Decoupled sequence.

Figure 5.5. Performance of many-body Hamiltonian evolution without and with dynamical decoupling. The 11 ions are initialized as either up or down along the x axis before a long-range spin-spin Hamiltonian $\mathcal{H}_{XX}$ is applied for variable time **(a)** without and **(b)** with CMPG decoupling pulses, before the x magnetization of the individual spins is read out. In the absence of decoupling, stray AC Stark shifts induce dynamics and dephasing, while with decoupling these are suppressed. The parameters are $\delta/(\eta\Omega) = 7.5$, $t_p = 20\,\mu\text{s}$, and $t_1 = 120\,\mu\text{s}$. The evolution time t is scaled by the effective average nearest-neighbor spin-spin coupling, $\overline{J_0}$.

spin-spin correlator that quantifies the memory of the initial state as a function of time [36]. The generalized imbalance is defined as,

$$\mathcal{I}(t) = \frac{\sum_i \langle X_i(t)\rangle\,(1+\langle X_i(0)\rangle)}{\sum_i (1+\langle X_i(0)\rangle)} - \frac{\sum_i \langle X_i(t)\rangle\,(1-\langle X_i(0)\rangle)}{\sum_i (1-\langle X_i(0)\rangle)}, \tag{5.25}$$

where $\mathcal{I}$ is constant under the target Hamiltonian, while dephasing or thermalizing dynamics will both drive it toward zero.

Figure 5.6 compares $\mathcal{I}(t)$ of the regular (gray circles) and decoupled (black squares) sequences. Fitting each calculated $\mathcal{I}(t)$ to an exponential decay, the scaled coherence time without dynamical decoupling is $\overline{J_0}\tau = 4.2$, while with dynamical decoupling, it is extended to $\overline{J_0}\tau = 22.1$,

showing that the benefit of dynamical decoupling demonstrated in two-ion tests persists in a much larger system. Addition of the decoupling pulses significantly extends the timescales accessible in this simulation, potentially improving the ability to resolve slow dynamics.

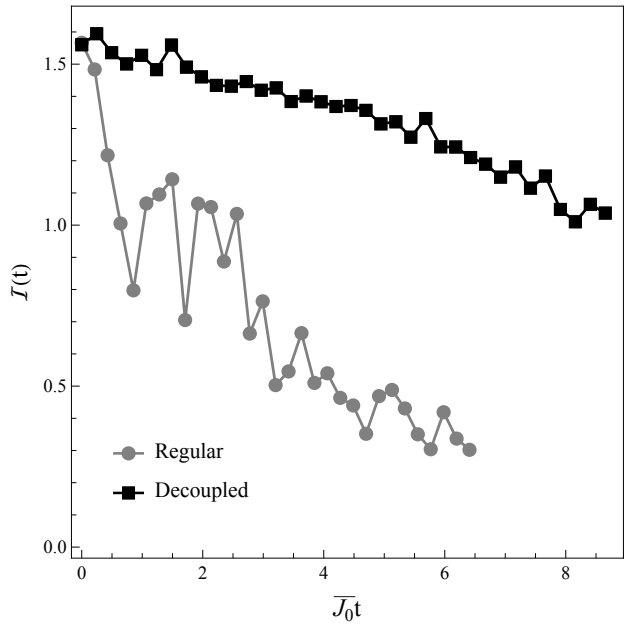


Figure 5.6. Generalized imbalance comparison. The generalized imbalance $\mathcal{I}(t)$ measures the preservation of the initial state which here is plotted as a function of the product $\overline{J_0}t$, the evolution time t scaled by the effective average nearest-neighbor spin-spin coupling $\overline{J_0}$ corresponding to each sequence. The gray circles represent the regular sequence $\mathcal{I}(t)$ while the decoupled $\mathcal{I}(t)$ are the black squares. The exponential decay fits of each imbalance are not plotted in the figure despite being discussed in the main text. Each of the points are the average of 500 experimental repetitions that have error bars smaller than the symbol size.

5.6.2 Realizing an Approximate Haldane-Shastry Model

As a final demonstration, we integrate our developed dynamical decoupling method with the technique of Floquet Hamiltonian engineering to realize a long-range Heisenberg model in the Haldane-Shastry regime. The Haldane-Shastry model [90, 91] can be formulated as a periodic spin-1/2 chain, in which the sites are evenly spaced around a circle, and with long-range

antiferromagnetic spin-spin interactions:

$$\mathcal{H}_{H\text{-}S} = \sum_{i<j} \frac{J_0\,\vec{\sigma}_i \cdot \vec{\sigma}_j}{3\,|i-j|^2} = \sum_{i<j} \frac{J_0}{3\,|i-j|^2}\,(X_iX_j + Y_iY_j + Z_iZ_j). \tag{5.26}$$

This model has attracted extensive interest because it is exactly solvable using the asymptotic Bethe ansatz and features a spin-liquid ground state and fractionalized spinon quasiparticles [92]. Previous work has proposed to create experimentally this model with trapped ions [93–95] or atoms in a photonic crystal waveguide [96]; however, to our knowledge this has not been demonstrated.

We approximately engineer the Haldane-Shastry model with four ions using the Heisenberg decoupling sequence, previously discussed in Sec. 5.4.3, described by Eq. (5.18) and whose sequence is sketched in Fig. 5.7a. Since this sequence now relies on a fast drive limit, we set $J_0 t_1 = 0.05$. In order to access spin-spin Ising interactions that are described by an inverse-square law, we must operate at a large detuning δ corresponding to $\delta/(\eta\Omega) = 9.9$. Unfortunately, increasing δ decreases the strength of the average nearest-neighbor coupling J_0, which often makes it challenging to observe the intended dynamics due to a finite coherence time. For example, with $\delta/(\eta\Omega) = 9.9$ the scaled coherence time without dynamical decoupling is $\overline{J_0}\tau < 1$, as suggested by Fig. 5.3b. However, from the same figure, the incorporation of dynamical decoupling at a large detuning is necessary to observe any nontrivial dynamics.

Before we discuss the results of our Floquet-engineered dynamically decoupled experiment, it is worth noting that our experimental realization deviates from the ideal Haldane-Shastry model in several ways. First, at the level of the Hamiltonian, the experiment has open boundary conditions, unlike the original version of this model, although open generalizations have also been previously studied [97, 98]. Furthermore, the spin-spin couplings in the ion chain do not

precisely obey an inverse square power-law dependence [27]. For the data shown in the rest of this section, the best-fit power law constant is actually $\alpha = 2.05$, and the largest deviation of a coupling from the fit is 0.08 J_0. Beyond the Hamiltonian form, the experiment also has decoherence, which, in this regime, is primarily due to motional heating. Averaging over the pulse sequence, this decoherence may be approximated as depolarizing noise. Despite these differences, we can experimentally and numerically observe key signs of proximity to the ideal Haldane-Shastry limit.

We began by preparing the four ions in a fully polarized product state $|i\rangle = |\uparrow\uparrow\uparrow\uparrow\rangle_i$ such that the spins are aligned along the positive i axis of the Bloch sphere. Once initialized in state $|i\rangle$, the decoupled approximate Haldane-Shastry sequence is applied for m cycles, shown in Fig. 5.7a, before measuring the individual spin states in the same basis as they were prepared in. Figure 5.7b shows the average ion magnetization along direction f for each polarized initial state i where $i = f = x, y, z$. Due to the Heisenberg symmetry, any finite initial magnetization along each direction is conserved up to a slow decay set by the decoherence as observed in Fig. 5.7b. We estimate the coherence time by a fit to the average of these decays, giving $\overline{J_0}\tau \approx 4.5$.

Meanwhile, preparing a Nèel state along z, $|i\rangle = |\uparrow\downarrow\uparrow\downarrow\rangle_z$, results in persisting and oscillatory nonthermalizing dynamics consistent with near-integrability as shown in Fig. 5.7c. Similar oscillations and recurrences are seen in numeric simulations of the experiment, which are performed by solving the Schrödinger's equation for $\overline{\mathcal{H}}$ using the experimental spin-spin couplings (Eq. 3.15), and in simulations of the exact Haldane-Shastry dynamics (Fig. 5.7d). We note that the inversion of the first recurrence, seen in experiment and experimental numerics but not the ideal Hamiltonian, is a boundary effect that is determined in an open chain by the parity of the number of ions. In addition, the discrepancy in the observed versus ideal experiment amplitudes

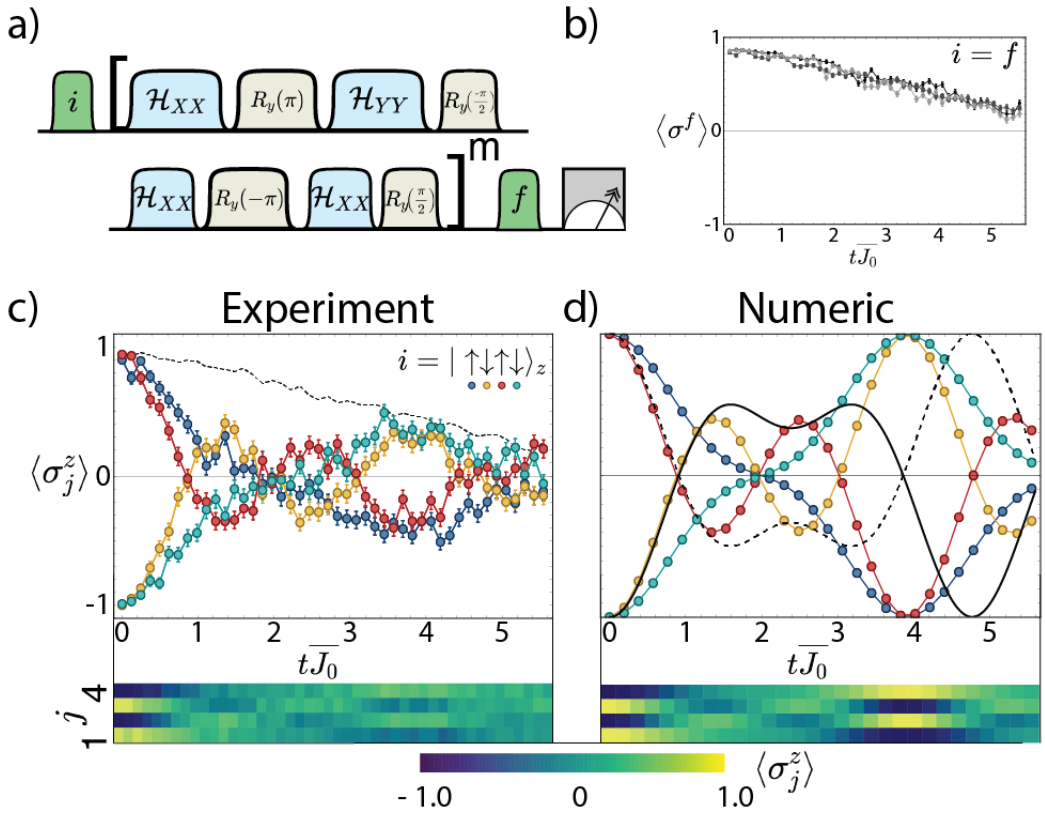


Figure 5.7. Quantum simulation of the approximate Haldane-Shastry model. **(a)** We prepare an initial state $|i\rangle$, apply the decoupled Floquet engineering sequence (Eq. 5.18) that results in $\overline{\mathcal{H}} \sim \mathcal{H}_{H\text{-}S}$, and measure in some basis f. **(b)** Creating a polarized state and measuring it in the same basis, a comparable slow decay of the average magnetization is seen for i along x, y, or z (dark to light). **(c)** Preparing a Nèel state, the dynamics measured along z (left) show complex oscillations and recurrences without thermalization. The average magnetization from (b) (dashed line) is provided as a guide to the eye indicating the approximate rate of depolarizing decoherence. **(d)** Numerics show very similar behavior as experiment up to the overall decoherence. Colored lines with markers (and lower heatplot) are a numerical simulation of the experimental Hamiltonian, while black lines (dashed for odd ions, solid for even ions) are the ideal, translationally symmetric Haldane-Shastry chain with the same number of ions and same average nearest-neighbor spin coupling. Experimental points are the average of 200 repetitions, with error bars of 1 SEM.

of the individual spin magnetizations dynamics is due to decoherence caused by motional heating.

From the noise model described in Sec. 5.5.4 and from Fig. 5.4, the dominant noice source for a decoupled simulation in the regime of the Haldane-Shastry data, $\delta/(\eta\Omega) = 9.9$ is expected to be motional heating. This noise source can be treated as a stochastic σ_x term [42], but after considering the overall global rotations about the Bloch sphere in the Haldane-Shastry sequence

the resulting decoherence can be reasonably approximated as a simple depolarizing model. The density matrix operator for the experimental system including this depolarizing noise can be approximated as,

$$\rho = [1 - p_1(t)]\, I + p_1(t)\, |\psi(t)\rangle \langle\psi(t)|\,, \tag{5.27}$$

where I is the diagonal fully mixed density matrix, $|\psi(t)\rangle$ denotes the desired evolution, and $p_1(t) = e^{-t/\tau}$. The motional heating decoherence rate can be estimated from the decay of the mean polarized data, the dashed black line in Fig. 5.7c. Mentioned previously, we extracted a scaled coherence time of $\overline{J_0}\tau = 4.5$ from the average of Fig. 5.7b allowing us to incorporate the depolarizing noise into the experiment numerics. Figure 5.8 displays the experimental results of

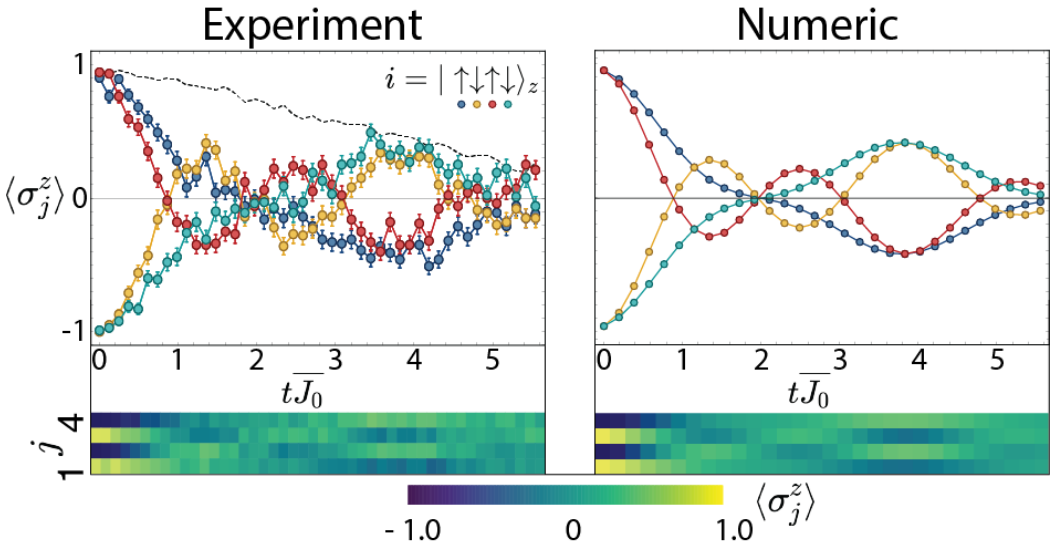


Figure 5.8. Haldane-Shastry numerics with decoherence. Comparison of experimental data with a minimal decoherence model based on depolarizing noise with $\overline{J_0}\tau = 4.5$. Inclusion of this effect results in numerics that have a strong agreement with experiment, suggesting that the primary influences on the experimental data have been accounted for.

the initialized Néel state evolution under the approximated Haldane-Shastry sequence in comparison to the numerical simulation of the experiment that now includes a simple depolarizing noise term. Reassuringly, these numerics which incorporate noise from motional heating, show a closer agreement with the measured experiment dynamics. This improvement in the corrected

numerics suggests that the primary influences on the experimental data have been accounted for.

In addition, to demonstrate that these oscillatory nonthermalizing dynamics are not unique to the initialized Néel state configuration, we prepare an alternative initial state configuration in which the net z magnetization is still zero. The four ions are prepared in $|i\rangle = |\uparrow\downarrow\downarrow\uparrow\rangle$ before applying the same Haldane-Shastry experimental sequence for integer m cycles and detecting along the z basis. Figure 5.9 displays the measured individual ion z magnetizations dynamics of the alternate initial state shown in comparison with the ideal experiment simulation that does not incorporate the depolarizing noise model discussed previously. We still observe signatures of the

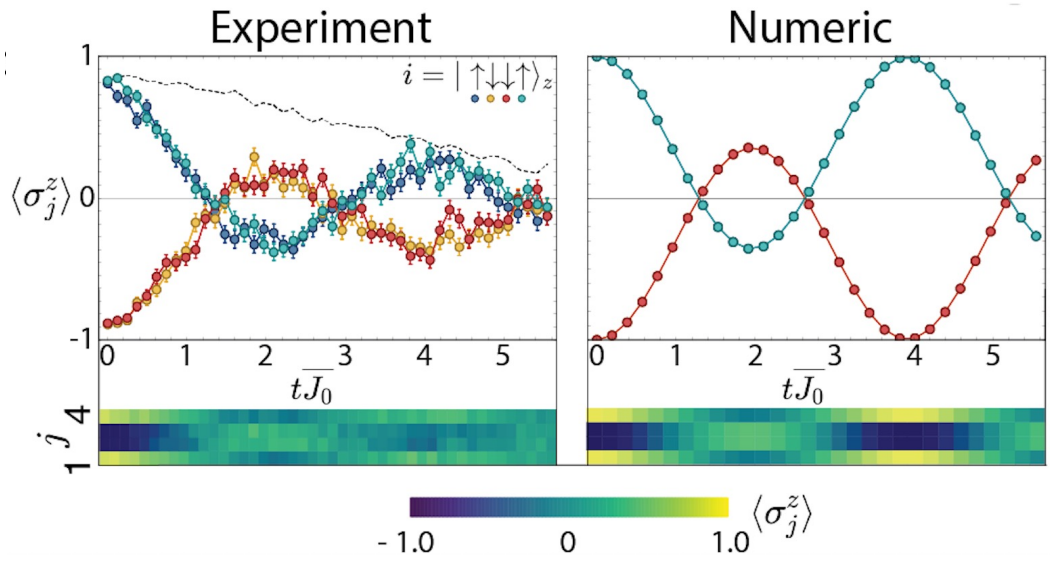


Figure 5.9. Additional Haldane-Shastry data. Approximate Haldane-Shastry experiment, using a different initial state than in Fig. 5.7b that shows especially simple recurrences. Experimental points are the average of 200 repetitions, with error bars of 1 SEM.

expected oscillatory behavior in the measure dynamics for the alternate initial state, despite the reduction of the oscillation amplitudes, around $\overline{J_0}\tau \sim 3$, of the first and fourth ion magnetizations. As a result, we have shown the ability to realize approximate Hamiltonian dynamics for a model that is physically possible to realize.

Furthermore, utilizing the flexibility of Floquet Hamiltonian Engineering, we modify the

driving sequence to engineer a less-symmetric thermalizing model in order to contrast the Haldane-Shastry results. The modified sequence retains the decoupling of the Haldane-Shastry sequence, but results in an target Hamiltonian that has an anisotropic XY form:

$$\mathcal{H}_{HSmod} = \sum_{i<j} \frac{J}{3\,|i-j|^2}(2X_iX_j + Y_iY_j). \tag{5.28}$$

$\mathcal{H}_{HSmod}$ lacks the integrability of the Haldane-Shastry model as well as the conservation laws for each spin projection. Correspondingly, we see dynamics that do not show simple oscillations

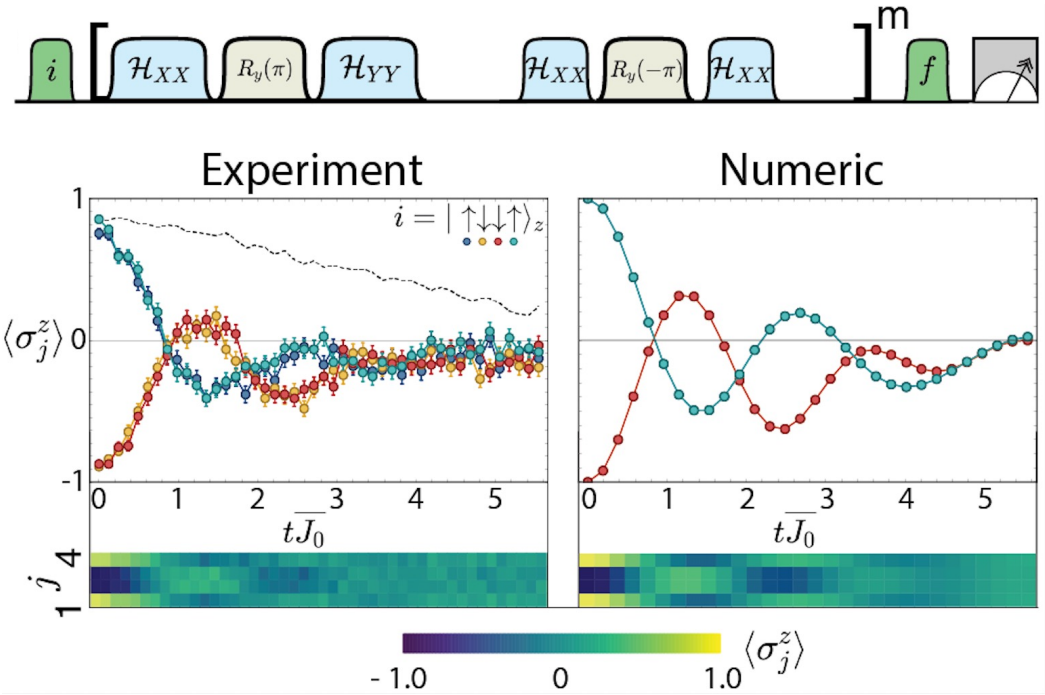


Figure 5.10. Modified Haldane-Shastry sequence results. **(a)** The modified pulse sequence breaks the symmetries of the Haldane-Shastry sequence. The dynamics no longer exhibit the simple recurrences characteristic of near-integrability, and $\langle Z_i\rangle$ is no longer conserved. **(b)** The data (left) compared to ideal numerics using the experimental parameters (right) for the modified approximate Haldane-Shastry pulse sequence for the initial state $|i\rangle = |\uparrow\downarrow\downarrow\uparrow\rangle$. The experimental points are the average of 200 repetitions, with error bars of 1 SEM.

with revivals or conserve total spin.

Approximate realization of the Haldane-Shastry model opens up a number of exciting possibilities. These include studies of prethermalization and relaxation in a near-integrable sys-

tem [99–101], and of the thermodynamic consequences of the expected fractionalized quasiparticles [102]. We leave a full theoretical and experimental study of the trapped-ion implementation of this model to future work.

5.7 Summary: Adding Dynamical Decoupling to the Simulation Toolbox

We have demonstrated a general strategy to extend dynamical decoupling to quantum simulators undergoing unitary many-body evolution. Applied to a trapped-ion experimental platform, we have shown that this technique may extend its coherence time and accessible parameter regime and can be integrated with Floquet Hamiltonian engineering to expand further simulation possibilities. We expect that these decoupling strategies will be useful in systems with other noise sources as well. For example, our experimental qubit is insensitive to external magnetic fields, making decoherence from physical magnetic field fluctuations (as opposed to simulated magnetic fields from qubit energy shifts) negligible. However, fluctuating magnetic fields are a leading source of decoherence in other types of trapped ion experiments and are amenable to the techniques developed here. These methods are also potentially relevant to other platforms with similar control, including quantum simulators based on neutral atoms [103–105] or superconducting circuits [106]. Extensions of this approach, in general, including rotations on individual spins rather than global rotations [107, 108], can be applied to decouple essentially any noise that can be modeled as arising from a slowly-varying Hamiltonian with undesired couplings, while preserving a target Hamiltonian of arbitrary symmetry properties.

Our results also help to clarify the limiting noise in various regimes of our simulator's operation, suggesting possible paths forward. With dynamical decoupling, our noise model suggests

that the limiting noise over most regimes of interest is slow drifts in the motional trap frequencies, possibly due to temperature fluctuations that shift the resonant frequency of the rf trap voltages or small shifts in the electronic grounding. Therefore, future improvements should target this noise, which we have not investigated as extensively as other error sources. We can further predict that operating at $\delta/(\eta\Omega) = 3.5$, if we can reduce these errors arising from motional frequency drifts by about a factor of 5 so that they are below other error sources, we will be able to increase our coherence to $\overline{J_0}\tau \approx 30$. In addition to hardware improvements, errors from motional decoherence can be reduced by utilizing automated and efficient re-calibration procedures of experimental parameters, which are already in use in similar experiments [109]. Once achieved, assuming that an experimental signal typically persists up to time $t = 2\tau$, we estimate that reducing the these errors would correspond to a time of $\overline{J_0}t \approx 60$ available for quantum simulation.

While we have focused on demonstrations with small systems, the fundamental error sources we have studied couple to each ion equally, providing promising fundamentals for system size scaling. For sufficiently long ion chains, the decreasing axial frequency leads to an additional source of decoherence [110] that may ultimately require moving to a modular architecture [111]. However, even direct scaling has led to quantum simulations with up to about 50 ion chains [85, 112]. Maintaining this noise up to comparable sizes would enable our simulator to investigate reliably dynamics that are highly challenging to access either for classical simulation or near-term gate-based quantum computers [113].

Chapter 6: Spectral Form Factor

The experiment presented in this chapter ultimately demonstrates the analog-digital quantum simulation features of QSim's trapped ion system. In addition, the spectral form factor project challenged our system in ways that had not been experienced before. The outline of this chapter is first introducing the spectral form factor and partial spectral form factor followed by implementing the experimental protocol to measure these observables. Lastly, the results of the experiment will be presented. We are currently working on writing a paper on this project with our theory collaborators and as a result the presentation of the SFF project in a future article may differ from the initial conclusions that are discussed in this work.

6.1 What is the Spectral Form Factor?

The spectral form factor, abbreviated SFF, is an observable that provides information about the statistics of energy eigenvalues of a quantum many-body system [114]. More specifically, the SFF is defined as the Fourier transform of the two-point correlator of the energy level density of a time-independent Hamiltonian H:

$$K(t) \equiv \frac{1}{D^2}\overline{\sum_{i,j} e^{i(E_i - E_j)t}} = \frac{1}{D^2}\overline{\mathrm{Tr}[T(t)]\,\mathrm{Tr}[T^\dagger(t)]}, \tag{6.1}$$

where E_i, E_j are energy eigenvalues of H, D is the Hilbert space dimension of the quantum system, and $T(t) \equiv e^{-iHt}$ is the unitary time-evolution operator of H. The overline in Eq. (6.1) denotes that average over an ensemble of $T(t)$ is required due to the non-self-averaging quality of the SFF [115]. $K(t)$ is normalized such that $K(0) = D^{-2}\mathrm{Tr}[\mathbb{1}]^2 = 1$.

The SFF observable can be generalized into another observable called the partial spectral form factor (PSFF). The PSFF characterizes the statistics of both the energy eigenvalues and energy eigenstates of the time-evolution operator restricted to a subsystem of the entire many-body system. The PSFF of a specific subsystem A within the total system $\mathcal{S}$ is defined as,

$$K_A(t) \equiv \frac{1}{DD_A}\overline{\sum_{i,j} e^{i(E_i-E_j)t}\mathrm{Tr}_B\Big[\rho_B(E_i)\rho_B(E_j)\Big]} = \frac{1}{DD_A}\overline{\mathrm{Tr}_B\Big[\mathrm{Tr}_A[T(t)]\mathrm{Tr}_A[T^\dagger(t)]\Big]}, \quad (6.2)$$

where $A \subseteq \mathcal{S}$, B denotes the subsystem complement to A ($A \cup B = \mathcal{S}$), D_A, D_B are the Hilbert space dimensions of A and B, respectively, where $D = D_A D_B$, and $\rho_B(E_i) = \mathrm{Tr}_A\Big[|E_i\rangle\langle E_i|\Big]$ represents the reduced density matrix after taking the partial trace of the eigenstate $|E_i\rangle$ of the Hamiltonian H with energy E_i. The PSFF $K_A(t)$ is also normalized, similar to $K(t)$, such that $K_A(0) = \mathrm{Tr}_B\Big[\mathrm{Tr}_A[\mathbb{1}]^2\Big]/(DD_A) = 1$.

The SFF and the PSFF of subsystem A are equivalent when $A = \mathcal{S}$. However, when $A \subset \mathcal{S}$, the PSFF $K_A(t)$ contains information about the subsystem purities [Eq. (6.3a)] and overlaps of the reduced eigenstates [Eq. (6.3b)]:

$$\mathrm{Tr}_B\big[\rho_B(E_i)^2\big], \quad (i=j) \quad (6.3a)$$

$$\mathrm{Tr}_B\big[\rho_B(E_i)\rho_B(E_j)\big], \quad (i\neq j). \quad (6.3b)$$

From Eq. (6.3a) and Eq. (6.3b), measurements of the PSFF averaged over the spectrum and ensemble gives access to the statistics of the eigenstates.

So far, the SFF and PSFF observables have been presented in the context of studying the continuous dynamics of a time-evolution operator of a continuous Hamiltonian system of interest. However, these observables are not limited to systems that evolve continuously. In fact, both the SFF and PSFF can be studied in Floquet models where the energy eigenvalues are replaced with quasienergies and the time-evolution operator becomes a time-periodic-evolution operator in which the evolution time t is varied at integer n multiples of the driving period τ, the duration of a single cycle of the Floquet operator V, i.e. $T(t) \rightarrow T(t = n\tau) = V^n$ for all $n \in \mathbb{N}$. It is important to note that the quasienergy eigenvalues $\{E_i\}$ are defined for integer multiples of the driving frequency $\omega = 2\pi\tau^{-1}$ and are fixed to lie in the interval $[0, \omega]$ [116].

6.2 Characteristic Properties of the SFF and PSFF

The energy eigenvalues of chaotic quantum many-body systems are described by Wigner-Dyson statistics [117]. For chaotic systems, the SFF, $K(t)$, will increase linearly, with a slope of $1/D^2$, in time t before reaching a constant value, $1/D$, at time t_H where it continues to remain thereafter:

$$K(t) = \frac{1}{D} \begin{cases} 1/D, & 0 < t \leq t_H, \\ 1, & t > t_H, \end{cases} \tag{6.4}$$

where time t_H is known as the Heisenberg (or plateau) time, which is connected to the mean-inverse spacing of adjacent energies, and it typically scales with the Hilbert space dimension D [114, 118]. The ramp-plateau structure of the SFF stems from energy-level repulsion and spectral rigidity [119]. In fact, this feature is a defining characteristic of quantum chaotic systems and is predicted by RMT [114, 120]. Not surprisingly, the SFF is known to be a key diagnostic of many-body quantum chaos [114, 119, 121].

Meanwhile, the PSFF of subsystem A, $K_A(t)$ has a general shift-ramp-plateau structure [116]. In fact, predictions of RMT for the behavior of the PSFF for large subsystems A and B gives:

$$K_A(t) = \frac{1}{D_A^2} + \frac{1}{D} \begin{cases} 1/D, & 0 < t \leq t_H, \\ 1, & t > t_H. \end{cases} \tag{6.5}$$

From Eq. (6.5), the dynamics of the PSFF contain similar features as that of the full system SFF. The slope of the PSFF ramp is similar to the full SFF and the onset of the PSFF plateau also occurs at t_H. In addition, the PSFF has an additive offset that's dependent on the subsystem Hilbert space dimension. The authors of Ref. [116] show that the shift-ramp-plateau in the PSFF behavior is a genuine feature when the subsystem is contained in a chaotic quantum many-body system and is connected subsystem ETH. In fact, ETH places constraints on a chaotic system's eigenstate statistics [116] which is observed in the subsystem dependent shift of the PSFF when the reduced eigenstates obey Wigner-Dyson statistics.

In comparison, we know that integrable and localized models have energy eigenvalues that are described by Poissonian statistics [122–125]. The SFF of a localized system will have a flat-line constant in time, after some initial transient behavior at early time. The value of the localized SFF is: $K(t \gg 0) = 1/D$. The localized subsystem PSFF also remains at a constant value that can be much larger than the $1/D_A^2$ scaling observed in the chaotic PSFF of the same subsystem size. The flat line behavior of the subsystem PSFFs for localized systems is not surprising since the eigenstate statistics of localized systems violate ETH.

Recently, the authors of Ref. [116] have introduced the SFF and PSFF as feasible experimental probes of universal random matrix theory (RMT) predictions for the statistics of energy eigenvalues [114, 120, 126–129] and predictions of the eigenstate thermalization hypothesis (ETH) for the statistics of energy eigenstates [130–136] of quantum chaotic many-body systems.

In addition, both the SFF and PSFF can be used to distinguish many-body chaotic systems from many-body localized (MBL) ones [122, 137].

6.3 Proposed Protocol and Requirements for Measuring SFF and PSFF

Our theory collaborators on this project and authors of Ref. [116] have proposed a protocol to measure the SFF and PSFF within the framework of randomized measurements. In this section, the procedure from Ref. [116] will be introduced and expressions for calculating unbiased estimators of the SFF and PSFF observables are also, presented. Lastly, experimental and statistical requirements for implementing the protocol will be discussed.

The time-evolution operator T is assumed to describe the unitary dynamics of a quantum system evolving under a Hamiltonian H that has at least one local randomized term, such as a ion-dependent random disorder (RD) potential in the z direction. Assuming this form of T, enables a natural ensemble average over many different instances of T, each with a different local RD, such that a disorder-averaged SFF/PSFF can be calculated. With this form of T in mind, recall that the SFF is an observable of the time-evolution operator $T(t)$ and measuring the SFF requires measuring the full trace of $T(t)$, i.e. summing over all of its weighted eigenstates [116]. Sampling T might seem like a daunting task, but our collaborators Joshi, *et al.* recognized that methods from the random measurement toolbox [138] could be utilized. Thus, the following protocol features the application of a local random unitaries (RUs) at various times in order to obtain statistical correlations between the random operations. The SFF and PSFF can be estimated from projective measurements by running the proposed SFF sequence as many times as possible using a different random set of local random unitaries and different set of local random disorder

strengths (a different instance of T) each time.

For a system $\mathcal{S}$ consisting of a fixed system size of N qubits, the following protocol is the proposed SFF experimental sequence for a single instance of the time-evolution operator T which is applied for a given time t.

1. System $\mathcal{S}$ is prepared in an initial N-qubit product state $\rho_0 = |\mathbf{0}\rangle\langle\mathbf{0}|$ where $|\mathbf{0}\rangle \equiv |0\rangle^{\otimes N}$.
2. Next, a random unitary (RU), denoted by the operator U, is applied to the initial state.
3. Then, the time-evolution operator $T(t)$ is applied for some time t.
4. The corresponding adjoint of RU, denoted by $U^\dagger$, is applied to the time-evolved system in which the final state at time t is $\rho_f(t) = U^\dagger T(t) U \rho_0 U^\dagger T^\dagger(t) U$.
5. Finally, a single-shot measurement in the computational basis is performed obtaining the bit string at time t $\boldsymbol{s}(t) = \{s_1, \ldots, s_N\}(t)$ where $s_i \in \{0, 1\}$ for $i = 1, \ldots, N$.

The local RU operator, $U = \otimes_{i=1}^{N} u_i$, is the tensor product of N individual 2×2 RUs where u_i is the RU applied only on the i^{th} qubit. Each u_i is independently randomly sampled from a unitary 2-design on the single qubit Hilbert space $\mathbb{C}^2$. The time-evolution operator $T(t)$ is naturally implemented by applying a Hamiltonian H for the duration t or from applying the Floquet operator V for an integer n times corresponding to a duration $t = n\tau$ where τ is driving period of a single Floquet cycle. The interactions described by H or V have at least one or more randomly sampled disorder potentials.

In order to take an ensemble average over $T(t)$, Steps 1–5 are repeated M times where each sequence uses a new RU and random disorder (RD) corresponding to a new instance of $T(t)$. At the end of M repetitions, a set of measured bit strings $\boldsymbol{s}^{(r)}(t)$ are gathered where $r = 1, \ldots M$ is the index denoting the different instances of T. Of course, to measure the dynamics of $T(t)$ as a function of duration t, Steps 1–5 should be repeated using the same RU and RD while varying the

value of t in Step 3, mapping out the dynamics of the system from t_{start} to t_{end} before repeating the entire process M times for M different instances of $T(t)$.

6.3.1 Estimators of the SFF and PSFF Observables

Both the SFF and PSFF can be calculated from the same set of collected bit strings $\boldsymbol{s}^{(r)}(t)$ using,

$$\widehat{K}(t) = \frac{1}{M}\sum_{r=1}^{M}(\text{-}2)^{-\left|\boldsymbol{s}^{(r)}(t)\right|}, \qquad \left|\boldsymbol{s}^{(r)}(t)\right| \equiv \sum_{i=1}^{N} s_i^{(r)}(t), \tag{6.6}$$

$$\widehat{K_A}(t) = \frac{1}{M}\sum_{r=1}^{M}(\text{-}2)^{-\left|\boldsymbol{s}_A^{(r)}(t)\right|}, \qquad \left|\boldsymbol{s}_A^{(r)}(t)\right| \equiv \sum_{i\in A} s_i^{(r)}(t), \tag{6.7}$$

where $\widehat{K}(t)$ and $\widehat{K_A}(t)$ are unbiased estimators of the SFF $K(t)$ [Eq. (6.1)] and the PSFF of a particular subsystem $K_A(t)$ [Eq. (6.2)], respectively, for a finite number of experimental runs M. Both estimators converge to their corresponding observable in the limit of infinite experimental runs:

$$\lim_{M\to\infty}\widehat{K}(t) = K(t) \qquad \& \qquad \lim_{M\to\infty}\widehat{K_A}(t) = K_A(t). \tag{6.8}$$

Note that the estimator equation for the PSFF of a given subsystem A, Eq. (6.7), is equivalent to the SFF estimator equation when $A = \mathcal{S}$.

6.3.2 General Requirements

The experimental requirements to be able to implement the proposed SFF experimental procedure are less daunting in comparison to the statistical requirements, mainly the finite number of experimental runs M. The experimental requirements will be discussed first, followed by the statistical requirements.

6.3.2.1 Experimental Requirements

An important claim made by Joshi, *et al.* regarding their protocol is that it can be implemented on today's existing experimental platforms [116]. Importantly, the experimental quantum simulator must be able to apply individual (local) RUs and be able to projectively measure each qubit. Ref. [116] emphasizes that applying global RUs and their inverses realizes a different goal from their proposal. Global RUs and their inverses are used in randomized benchmarking experiments in which the goal is to characterize decoherence acting during the global operations. In contrast, application of individual RUs is used to characterize the time evolution operator $T(t)$. The trapped-ion quantum simulator in QSim can apply local RUs to each ion using the individual addressing beam discussed in Sec. 3.4.2.

6.3.2.2 Statistical Requirements

The finite number of experimental runs M and the variance of the estimator observables give rise to the associated statistical errors. For a fixed relative error, the number of measurements needed to access the PSFF of a subsystem size N_A scales as $M \sim 10^{N_A} \approx 2^{3.32 N_A}$ [116]. In comparison, for quantum process tomography of the full time-evolution operator $T(t)$, the number of measurements needed is at least $\sim 2^{5N_A}$ [116]. More details about the analysis of the statistical errors can be found in Ref. [116].

The exponential scaling in M for a particular subsystem PSFF with size N_A is due to the scaling in the SFF observable when the entire system size N is increased (see Eq. (6.4)). Unfortunately, the SFF estimator $\widehat{K(t)}$ signal will drop exponentially as N is increased since the SFF $K(t)$ scales as $1/D^2$ for a chaotic systems at early times and $1/D$ for localized systems. For

a spin-1/2 system (i.e. $^{171}Yb^{+}$ ions) with N spins, the dimension of the Hilbert space is defined as $D \equiv 2^N$, and thus, the slope of the ramp of the SFF for a chaotic system scales as $K(t) \sim 2^{-2N}$ which is a small signal for several ions already.

It is true that M is substantially better for the PSFF protocol than for quantum process tomography; however, it does place a limit on the full system size N where measuring the SFF still remains feasible. On the other hand, measuring the PSFF for small values of N_A within a much larger system of size N remains promising since the PSFF provides information on the statistics of eigenvalues and eigenstates of the reduced subspace. As a result, ETH predictions of subsystems can still be investigated [136]. In addition, the PSFF observable will exhibit the same distinguishing feature as the SFF, if the system is chaotic or localized.

6.4 Two Methods to Rescale the Raw Data from Decoherence Errors

Authors in [116] discuss two sources of decoherence from experimental imperfections of the SFF sequence. First, errors can occur during the application of the random local unitaries U and $U^\dagger$. Second, errors can occur during the time-evolution operator $T(t)$ dynamics. Regardless of when errors occur in the SFF sequence, the decoherence will affect the measured bit string $\boldsymbol{s}^{(r)}(t)$ resulting in a reduced value of the PSFF estimator $\widehat{K_A}(t)$. Thus, decoherence during $T(t)$ and imperfections in the U and $U^\dagger$ will decrease the measured estimator signal and will not create a false-positive ramp signal. Our theory collaborators (the authors of [116]) have proposed two additional measurement sequences to perform in which their corresponding results can be used to rescale partially the raw data via post-processing analysis. Each error mitigation technique will be discussed next by considering the time-periodic-evolution operator $T(t = n\tau) = V_r^n$, describing

the dynamics of the r^{th} Floquet operator V_r where the number of Floquet cycles n is varied at integer multiples of the drive period τ (the duration of V_r).

6.4.1 Imperfections from U and $U^\dagger$

Errors during the application of the random unitaries and their corresponding adjoints can stem from miscalibration or local depolarization. These types of errors will cause a decorrelation between U_r and $U_r^\dagger$ where r denotes the random set. The r^{th} SFF experimental sequence is: $|\mathbf{0}\rangle = |\downarrow\rangle^{\otimes N} \rightarrow U_r \rightarrow T(t = n\tau) = V_r^n \rightarrow U_r^\dagger \rightarrow \boldsymbol{s}^{(r)}(t) = \left\{ s_1^{(r)}(t), \ldots, s_N^{(r)}(t) \right\}$. This sequence becomes trivial when $t = 0$: $|\mathbf{0}\rangle \rightarrow U_r \rightarrow U_r^\dagger \rightarrow \boldsymbol{s}^{(r)}(0) = \{0, \ldots, 0\}$, since $T(t = 0) = \mathbb{1}$ and the corresponding SFF estimator value is $\widehat{K}(t = 0) = 1$, which matches the normalization of the SFF observable $K(t)$. The measured bit string at $t = 0$, $\boldsymbol{s}^{(r)}(0)$ corresponds to the final state, equaling the initial state of all spins prepared in $|0\rangle$ for any instance r assuming an ideal implementation of U_r and $U_r^\dagger$ and no detection errors.

Measurement results of $T(t = 0)$, within the randomized measurement toolbox, can be used to estimate the effect of the noise during the preparation of the random local product state and corresponding measurement in the random basis since there is a one-to-one mapping to the probability of measuring each ion in $|0\rangle$. A robust formula can be developed to use the individual ion fidelity for $T(t = 0)$ averaged over different local random unitaries and corresponding adjoints as a way to correct against imperfect U and $U^\dagger$. The calibration sequence is a measurement of the state overlap between the application of U_r and $U_r^\dagger$ separated by a delay time t, which is scanned over integer multiples of the Floquet period. The SFF, K, corresponds to the measurement of the

operator $\mathcal{O} = \otimes_i \mathcal{O}_i$ where,

$$\mathcal{O}_i(t) = \frac{p_i(0,t)+1}{2[2p_i(0,t)-1]}\left(|0\rangle\langle 0|\right)_i + \frac{p_i(0,t)-2}{2[2p_i(0,t)-1]}\left(|1\rangle\langle 1|\right)_i \tag{6.9}$$

where $p_i(0,t)$ denotes the individual fidelity of ion i averaged over random local unitaries as a function of the delay time t between u_i and $u_i^\dagger$ scanned over integer multiples n of the Floquet period τ when $T(t=0)$, and $\left(|0\rangle\langle 0|\right)_i$ and $\left(|1\rangle\langle 1|\right)_i$ are the i^{th} ion's qubit state projection operators. Equation (6.9) can be written into a more data analysis-friendly-form shown below to mitigate errors that occur from imperfect preparation and measurement of the "raw" data:

$$\left(\widehat{K_A(t)}\right)_{\text{RUCor}} = \frac{1}{M}\sum_{r=1}^{M}\prod_{i\in A}\left[a_i(t)\right]^{1-s_i^{(r)}}\left[b_i(t)\right]^{s_i^{(r)}}, \tag{6.10}$$

where $s_i^{(r)}$ is the raw measured bit of ion i in subsystem A at time t from the r^{th} instance of $T(t)$. Coefficients $a_i(t)$ and $b_i(t)$ corresponding to ion i are defined as,

$$a_i(t) \equiv \frac{p_i(0,t)+1}{2[2p_i(0,t)-1]} \qquad \& \qquad b_i(t) \equiv \frac{p_i(0,t)-2}{2[2p_i(0,t)-1]}. \tag{6.11}$$

In the ideal situation where the average fidelity of ion i is $p_i(0,t)=1$, the coefficients in Eq. (6.11) become $a_i(t)=1$ and $b_i(t)=\frac{-1}{2}$ and substituting them into Eq. (6.10), one finds that the argument of the summed product reduces to: $(1)^{1-s_i^{(r)}}\,(-1/2)^{s_i^{(r)}}$. Comparing this result to the expression $(-2)^{-s_i^{(r)}}$, we see that they are equivalent to one another. Thus, for the ideal case of perfect implementation of the local random unitaries, the corrected PSFF estimator given in Eq. (6.10) simplifies to the "raw" PSFF estimator from Eq. (6.7).

6.4.2 Imperfections During $T(t)$

Errors occurring during the time-evolution of $T(t)$ in the SFF experimental sequence such as global depolarization will affect the measured bit string results, and thus, estimations of the

SFF and PSFF of the system. Joshi, *et al.* propose a way to rescale the decohered raw experiment SFF and PSFF estimators from measurement results of the purity [116]. Demonstrated in different types of random measurement protocols, depolarization or readout errors can be corrected from randomized measurements of the purity [139–142]. The strength of the noise can be extracted from the purity measurement, which then can be used to correct partially decoherence errors during the dynamics of $T(t)$. The equations related to obtaining an estimate of the decoherence from the purity and the way to rescale the raw SFF and PSFF estimator signals are presented next. The experimental sequence to measure the SFF purity will be presented later in Sec. **??**.

The error mitigation technique to correct partially the SFF and PSFF estimators from decoherence is presented in the context of a Floquet system. In addition, the authors in Ref. [116] assume that the type of decoherence in $T(t = n\tau)$ is a *global depolarization* that occurs at each period τ with strength p. The effect of this type of noise alters the final state $\rho_f(t)$ to $\rho_{\text{dec}}(t)$ which is defined as,

$$\rho_{\text{dec}}(t) = \alpha_n \rho_f(t) + (1 - \alpha_n) D^{-1} \mathbb{1}, \tag{6.12}$$

where $\rho_f(t) = U^\dagger T(t) U \rho_0 U^\dagger T^\dagger(t) U$, which was introduced in the proposed SFF experimental protocol and $\alpha_n = (1-p)^n$. Note, the parameter α_n should not be confused with the decaying power law fit exponent α that we use to describe the range of our spin-spin interactions. From the measurement protocol, the erroneous (measured) PSFF is,

$$(K_A)_{\text{dec}}(t) = \alpha_n K_A(t) + D_A^{-2}(1 - \alpha_n), \tag{6.13}$$

where $K_A(t)$ is the actual PSFF value at time $t = n\tau$ and $(K_A)_{\text{dec}}(t)$ is the erroneous PSFF measured value. Equation (6.13) shows that the measured PSFF value will be smaller than the

actual PSFF value as time increases due to the decoherence.

Measurement of the purity P_n of the time-evolved state will enable an estimation of the noise p. Knowing the value of p, the measured estimators can be rescaled. The value of α_n as a function of time t (or integer n) is obtained from the value of the SFF purity P_n:

$$P_n = \mathrm{Tr}\left[\rho_{\mathrm{dec}}^2(t)\right] = \alpha_n^2 + D^{-1}\left(1-\alpha_n^2\right), \tag{6.14}$$

$$\alpha_n = \sqrt{\frac{DP_n - 1}{D-1}}. \tag{6.15}$$

Finally, the measured PSFF signal can be rescaled using the following equation:

$$(K_A)_{\mathrm{res}}(t) = \frac{(K_A)_{\mathrm{dec}}(t) - D_A^{-2}(1-\alpha_n)}{\alpha_n}, \tag{6.16}$$

where the value of α_n is calculated using the measured value of the SFF purity P_n using Eq. (6.15). This PSFF rescaling formula can be used in partnership with the error-mitigation strategy proposed for the imperfect local random unitaries to obtain a "complete" partially rescaled PSFF signal. The word "complete" in the previous sentence refers to a rescaled PSFF signal that includes correction for errors occurring from imperfect preparation and measurement as well as decoherence during the dynamics of the time-evolution operator.

6.5 Implementing the SFF Sequence in QSim

One of the goals of the SFF project is to demonstrate that the SFF and PSFF observables can be realized experimentally on today's NISQ-era system. To be able to demonstrate this goal, the SFF and PSFF estimators given by Eq. (6.6) and Eq. (6.7) of a chaotic system should be distinctly different from the measured estimators of a localized model. As a result, we implemented the SFF protocol for a quantum many-body chaotic model and a quantum MBL system in which both

systems are described by a periodic time-evolution operator $T(t=n\tau)=V_r^n$ with $\hbar=1$.

The general form of the periodic-time-evolution operator $T(t)$ describing the dynamics of r^{th} random Floquet operator V_r are each defined as the following,

$$T(t=n\tau)=V_r^n, \tag{6.17a}$$

$$V_r = e^{-iH_4 t_{\text{SIR}}} e^{-iH_3 t_{\text{Int}}} e^{-iH_2 t_{\text{SIR}}} e^{-iH_1 t_{\text{Int}}}, \tag{6.17b}$$

$$\begin{aligned} H_1 &= \textstyle\sum_{i<j} J_{ij} X_i X_j + B_x \sum_i X_i, \quad H_2 = \sum_i g_i Z_i, \\ H_3 &= \textstyle\sum_{i<j} J_{ij} X_i X_j + B_y \sum_i Y_i, \quad H_4 = \sum_i h_i Z_i, \end{aligned} \tag{6.17c}$$

where $\tau = 2(t_{\text{Int}} + t_{\text{SIR}})$ is the Floquet period corresponding to applying V_r once ($n = 1$), $n = t/\tau$ is the number (an integer) of applied Floquet cycles, J_{ij} is the long-range Ising interaction strength between ions i and j, B_x, B_y are the strengths of uniform magnetic fields along the x- and y-directions, respectively, g_i, h_i are the strengths of two separate individual RD fields that are along the z-direction applied to ion i, and X_i, Y_i, Z_i are ion i's Pauli operators. For the SFF experiment we define $J_0 \equiv J_{\text{avgNN}}$ as the average nearest-neighbor spin-spin interaction strength. Both the uniform and individual random magnetic field strengths are proportional to J_0 and mathematically they are expressed as:

$$B_x,\ B_y \approx J_0 \tag{6.18}$$

$$g_i,\ h_i \in [0, 2J_0\xi]\,, \quad \xi \in \mathbb{Z} \tag{6.19}$$

where ξ is a positive scale factor and the individual RDs are independently randomly sampled from the uniform distribution.

The Floquet period τ of a single cycle of an SFF instance V_r will be the what distinguishes whether the SFF sequence is "chaotic" vs. localized. More specifically, by changing the value of t_{Int}, $T(t = n\tau)$ and V_r will either describe a chaotic system or a localized model. For a

chaotic system, $t_{\rm Int} \approx J_0^{-1}$ while for a localized model, $t_{\rm Int} \approx (1000 J_0)^{-1}$. On the other-hand, the duration that the individual RDs terms are evolved fore remains fixed between the two cases with $t_{\rm SIR} \approx (J_0 \xi)^{-1}$. As a result, the localized system time-evolution operator $T(t = n\tau)$ will effectively describe a system in which each ion experiences a disorder field in the z-direction with a strength equal to the sum of the RDs, $g_i + h_i$.

The experimentally implemented SFF sequence for a given instance of $T(t = n\tau)$ follows the sequence outlined in Sec. 6.3 (which was summarized from Ref. [116]) exactly except for one modification. The proposed sequence just requires a single-shot measurement of each instance of the time-evolution operator scanned in time. We will instead take a total of 100 measurements ($N_m = 100$) total at each value of t (or n since $t = n\tau$) for a given instance of the Floquet operator V_r where index r labels the random sets used. Thus, the SFF sequence of a given instance of V_r will correspond to running two scans of the sequence in which the number of applied Floquet cycles, $n = t/\tau$, is changed in Step 3. Steps 1–5 will be run 50 times for each value of n in a scan, thus corresponding to 100 shots measured for each data point in a single instance of V_r. Table 6.1 displays the $r^{\rm th}$ instance of the SFF sequence implemented in our LabView experimental software control. The part of the SFF sequence highlighted in yellow generates the time-evolution operator $T(t = n\tau)$ for the $r^{\rm th}$ Floquet operator V_r. These four chapters create a single Floquet cycle, $n = 1$, and thus, when $n \geq 1$, n Floquet cycles are applied to evolve the operator $T(t = n\tau) = V_r^n$ in between the applications of U_r and $U_r^\dagger$. In addition, unless indicated otherwise, a single instance of the SFF sequence will also encompass a given set of random angles, $\{\theta_i\}_r$ and $\{\phi_i\}_r$, as well as two different sets of individual ion RDs, i.e., $\{g_{z_i}\}_r \neq \{h_{z_i}\}_r$. All four random sets labeled by index r corresponding to V_r will remain fixed during the scanned SFF sequence.

Using all of the measured bit strings corresponding to step $n = t/\tau$, across all random

SFF Sequence	
Purpose	Chapter/Operator
Initialize State $\|\psi_0\rangle$	Doppler Cool
	Optical Pump
	SB Cool
Apply RU $U_r = \{u_i\}_r$	Global $R_{-x}(\pi/2)$
	SIR 3 $\{R_{-z}(\theta_i)\}_r$
	Global $R_x(\pi/2)$
	SIR 4 $\{R_{-z}(\phi_i)\}_r$
Time-Evolve $T(t=n\tau)=V_r^n$	Int 1 H_1, t_{Int}
	SIR 7 H_2, t_{SIR}
	Int 2 H_3, t_{Int}
	SIR 8 H_4, t_{SIR}
Apply RU† $U_r^\dagger = \{u_i^\dagger\}_r$	Global $R_{-x}(\pi)$
	SIR 5 $\{R_{-z}(\phi_i)\}_r$
	Global $R_{-x}(\pi/2)$
	SIR 6 $\{R_{-z}(\theta_i)\}_r$
	Global $R_{-x}(\pi/2)$
Measure $\boldsymbol{s}^{(r)}(t)$	Detect

Table 6.1. LabView SFF sequence. This is the actual experimental sequence implemented using our LabView control software to realize the SFF protocol. The four chapters highlighted in yellow correspond to the four terms of the Floquet operator V_r where the index r labels both the random unitary set and random disorder sets used in the sequence. The number of applied Floquet cycles, n, is scanned starting from $n=0$ such that the SFF observable can be probed for $T(t=n\tau)=V_r^n$. Surrounding the Floquet dynamics are the individual random unitaries $\{u_i\}_r$ and $\{u_i^\dagger\}_r$, respectively.

instance r SFF sequence can then be calculated using the equation below: The disorder-averaged (and unitary-averaged) PSFF estimator at step $n = t/\tau$ can be calculated using the following equation:

$$\widehat{K_A}(n=t/\tau) = \frac{1}{M}\sum_{r=1}^{M}\left[\frac{1}{N_m}\sum_{m=1}^{N_m}\left(\prod_{i\in A}(1)^{1-s_i^{(r_m)}}\left(\text{-}\tfrac{1}{2}\right)^{s_i^{(r_m)}}\right)\right], \tag{6.20}$$

where $\widehat{K_A}(n=t/\tau)$ is the disorder-averaged PSFF estimator of a particular subsystem $\mathcal{A}$, r is the

index of the SFF sequence corresponding to the random instance r, M

6.5.1 Implementing and Testing the Individual RUs

We need to apply a different RU to N ions initially all polarized down along the z axis in order to prepare a completely random product state outlined in Step 2 of the SFF protocol. A completely random N-ion product state cannot be visualized using the Bloch sphere representation of a single qubit. However, the individual single qubit states (or Bloch vectors) of each of the N ions can be. Recall that an arbitrary single qubit pure state $|\psi\rangle = a\,|\downarrow\rangle + b\,|\uparrow\rangle$ with $|a|^2 + |b|^2 = 1$ can be visualized as a point (θ, ϕ) on the surface of the Bloch sphere where $a = \cos(\theta/2)$ and $b = e^{i\phi}\sin(\theta/2)$ and the Bloch vector $\vec{v} = \{\sin\theta\cos\phi, \sin\theta\sin\phi, \cos\theta\} = \{x, y, z\}$ points from the origin to (θ, ϕ). The ranges of θ and ϕ are on $[0, \pi]$ and $[0, 2\pi]$, respectively. Thus, each individual RU $u_i(\theta_i, \phi_i)$ can be parameterized by angles θ_i and ϕ_i and Step 2 of the SFF procedure with a given RU, $U\,|\mathbf{0}\rangle$ can be thought as preparing N random points on the surface of the Bloch sphere. This subsection will first present how each U is generated followed by results testing the implementation of a finite number of RUs and checking that the sampled values of θ and ϕ are random and independent.

In past experiments run in QSim, we have used our individual addressing beam to prepare basic initial product states such as a N-ion Néel state along the z axis. This simple initial product state preparation using the individual addressing beam was presented in Ch. 3 but I will briefly discuss it again. Let's consider that there are $N = 5$ ions that have just been prepared in the all $|\downarrow\rangle$ product state, $|\downarrow\downarrow\downarrow\downarrow\downarrow\rangle = |\downarrow\rangle^{\otimes N}$. Also, let's assume that we have calibrated the individual addressing beam such that we know the AOD frequencies corresponding to the five individual

ion positions and the corresponding AWG amplitudes to apply a 5 kHz SS to each ion's qubit frequency. Now we want to prepare the 5-ion product state $|\downarrow\uparrow\uparrow\uparrow\downarrow\rangle = |\downarrow_1\rangle\otimes|\uparrow_2\rangle\otimes|\uparrow_3\rangle\otimes|\uparrow_4\rangle\otimes|\downarrow_5\rangle$ which is obtained by running a SIR-Ramsey sequence:

$$|\downarrow\downarrow\downarrow\downarrow\downarrow\rangle \rightarrow R_{-x}(\pi/2) \rightarrow R_{z_2}(\pi)R_{z_3}(\pi)R_{z_4}(\pi) \rightarrow R_x(\pi/2) \rightarrow |\downarrow\uparrow\uparrow\uparrow\downarrow\rangle\,, \tag{6.21}$$

where the sequence in time (operator application) flows from left to right. The first $\pi/2$ pulse is a global rotation in which all the ions will rotate from $|\downarrow\rangle$ to $|\downarrow\rangle_y$, all pointing along the $-y$ axis. Then, only the AOD frequencies mapped to ions 2, 3, and 4 are turned on, denoted by $R_{z_i}(\pi)$ for $i = \{2, 3, 4\}$, where the AWG amplitude for each frequency has been calibrated to apply a 5 kHz SS. In addition, the duration of this single-ion rotation (SIR) is applied for 0.1 ms which corresponds to a π time of a 5 kHz sine wave. As a result, ions 2, 3, and 4 will experience a π pulse about the z axis causing ions 2, 3, and 4 to rotate from $|\downarrow\rangle_y$ to $|\uparrow\rangle_y$. Meanwhile, ions 1 and 5 are unaffected by the individual addressing beam and remain pointing along the $-y$ axis. Finally, the second $\pi/2$ pulse rotates the ion's spins back along the z axis preparing the desired product state, $|\downarrow\uparrow\uparrow\uparrow\downarrow\rangle$.

As seen from the SIR-Ramsey sequence with the duration of the individual addressing beam set to the π time of a 5 kHz signal, $R_x(\pi/2)R_z(\pi)R_{-x}(\pi/2) = R_{-y}(\pi)$ corresponds to a rotation about the $-y$ axis for an angle $\theta = \pi$. This SIR-Ramsey sequence can be generalized into a set of individual random θ rotations, $\{R_{-y}(\theta_i)\} \equiv \{R_x(\pi/2)R_z(\theta_i)R_{-x}(\pi/2)\}$, which corresponds to a given set of random θ values $\{\theta_i\}$. Following immediately, a different SIR chapter generating a set of individual random ϕ rotations, $\{R_z(\phi_i)\}$, corresponding to a given set of ϕ values $\{\phi_i\}$ can be applied. Thus, the individual RU operator for the i^{th} ion with random angles θ_i and ϕ_i is given by, $u_i(\theta_i, \phi_i) = R_z(\phi_i)R_{-y}(\theta_i)$. The form of $u_i(\theta_i, \phi_i)$ is similar to the form of an arbitrary

unitary (rotation) operator for a single qubit [see Eq. (6.22)] except our form has dropped both the initial rotation, $R_z(\varphi_i)$, and the global phase factor $e^{i\alpha}$, in comparison to Eq. (6.22). We can drop the first individual rotation about the z axis since all of the ions are already aligned along the $-z$ axis, and thus, a rotation about the z axis has no effect.

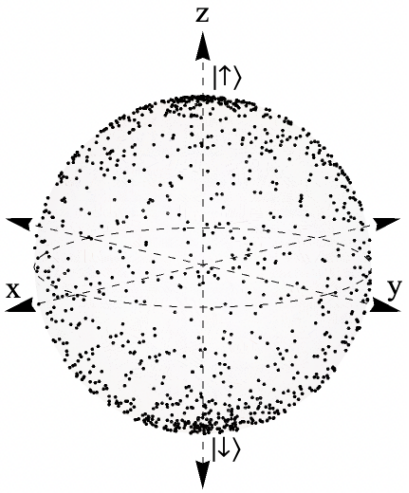
$$U = e^{i\alpha} R_z(\beta) R_y(\gamma) R_z(\delta), \tag{6.22}$$

where α, β, γ, and δ are a set of real numbers. Equation (6.22) is called the Z–Y decomposition for a single qubit [143].

Picking random angles the "correct" way:

To generate the random θ and ϕ values, we used Mathematica's *RandomReal* function that chooses a pseudorandom real number with a uniform probability distribution [144]. We naively used the *RandomReal* function to sample 1000 values of θ from the uniform distribution on $[0, \pi]$ and 1000 values of ϕ from the uniform distribution on $[0, 2\pi]$. We then took each pair of random angles (θ_i, ϕ_i) (spherical coordinates) and plotted them as points lying on the surface of a unit sphere with Cartesian coordinates $\{\sin\theta_i \cos\phi_i, \sin\theta_i \sin\phi_i, \cos\theta_i\}$ where $i = 1, 2, \ldots, 1000$. Figure 6.1 shows our original attempt to sample the surface of the Bloch sphere uniformly by choosing 1000 angle pairs randomly sampled from uniform distributions over their allowed value ranges. We observed that there were more random points around the north and south poles of the Bloch sphere as seen by the density of black points in those regions. In addition, this "clumping" of points was not a problem of under sampling since the same clumping behavior was still present when the number of shots was increased to 5000.

Upon a quick Google search, we found the answer and the solution. The clumping behavior




```
shots = 1000;
θi = π RandomReal[{0, 1}, shots];
ϕi = 2 π RandomReal[{0, 1}, shots];
```

Figure 6.1. Uniform sampling of θ and ϕ but nonuniform distribution of points on a sphere. 1000 random points are plotted on the surface of the Bloch sphere (left). The coordinates of the i^{th} point are given by $\{\sin\theta_i\cos\phi_i, \sin\theta_i\sin\phi_i, \cos\theta_i\}$ in which angles θ_i and ϕ_i are each randomly and independently sampled from uniform distributions of their allowed value ranges, using the Mathematica code that is also displayed (right). Despite sampling each angle uniformly, the points are not uniformly distributed on the sphere's surface, but clustered around its north and south poles.

about the poles of the Bloch sphere is due to the fact that the sphere's differential surface area element dA is a function of θ itself since $dA = \sin\theta d\theta d\phi$ [145]. The correct way to obtain uniformly distributed points on a sphere, which we care the most about, is to sample randomly θ using the function $\theta = \arccos(2\text{RandomReal}[\{0,1\}] - 1)$ corresponding to a non-uniform distribution on $[0, \pi]$ [145]. Thus, we changed our incorrect formula to this correct expression for randomly sampling θ. Figure 6.2 shows the random angle functions that we defined in Mathematica. The

```
(* functions for generating random angles *)
NonUniformRandomTheta[s_] := ArcCos[2 RandomReal[{0, 1}, s] - 1]
UniformRandomPhi[s_] := 2 π RandomReal[{0, 1}, s]
```

Figure 6.2. Defined random angle functions. These are the user-defined random angle functions written in Mathematica, that will generate random θ (top) and ϕ (bottom) values that when used together as angular coordinates (θ, ϕ) will return a random point on the surface of a unit sphere. Being able to generate random points on a sphere's surface is analogous to being able to prepare an arbitrary state $|\psi\rangle$ on the Bloch sphere specified by a random unit-length Bloch vector formed from randomly chosen angles θ and ϕ.

function for picking a random ϕ value is still sampled from the uniform distribution of its allowed value range. Lastly, to verify for ourselves, and to confirm that we were using the right formula, which was indeed the case, we randomly sampled both1000 new ϕ values and 1000 new θ values, using the definitions displayed in Fig. 6.2, and again plotted them on the surface of the Bloch sphere which is shown in Fig. 6.3.

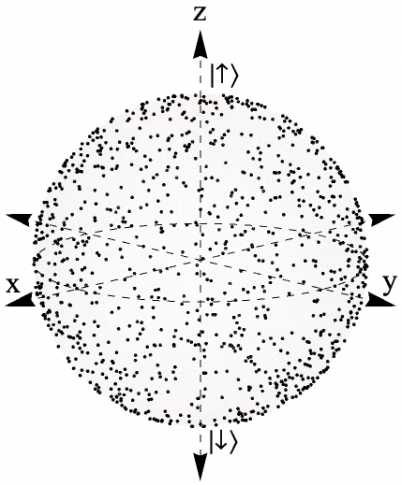


Figure 6.3. Uniform sampling of points on the Bloch sphere. 1000 random points are plotted on the surface of the Bloch sphere using the correct formula, shown in Fig. 6.2, to randomly sample the θ values. The random points are now uniformly distributed across the Bloch sphere's surface. We have now confirmed that we can indeed correctly write minimal code to choose randomly pairs of angles (θ_i, ϕ_i) that as a collection will uniformly sample the Bloch sphere.

Mapping random angles to random Stark shifts to random AWG RF amplitudes:

Having determined the correct way to generate random θ_i and ϕ_i values, we next need to convert these angles into an AC Stark shift seen by the ion. The way we map the random θ_i and ϕ_i values to the applied AWG amplitude of the AOD frequency corresponding to addressing ion i is discussed next. The general procedure for calibrating the individual addressing beam as detailed in Ch. 3 is performed first. As a reminder, this process establishes three sets of relations.

First, we obtain a relationship between the measured single ion individual addressing beam Stark shift and the corresponding AWG amplitude driving the single ion AOD center frequency by fitting the data to a sine-to-the-fourth function with three fit parameters. By inverting this fit function and using the best-fit parameters, we obtain a way to roughly determine what AWG amplitude value is required to measure a particular AC SS. This relationship between the AWG power versus measured SS is a vital tool that is used in calibrating the individual addressing beam intensity corresponding to the AOD frequency value. Second, we determine the N AOD frequency values corresponding to the individual addressing beam centered on a given ion in the chain by scanning the AOD center frequency across the entire length of the N-ion chain. The center frequencies of the N frequency dips are extracted by fitting each dip to a Lorentzian function. Lastly, we calibrate the AWG amplitudes of each ion's AOD frequency such that all N ions are driven at the same target rate by the individual addressing beam at the same time. This last step in the general calibration sequence of the individual addressing beam requires that we raster (quickly change) the frequency of the AOD across all N center frequency values in order to have a linear dependence on the maximum possible AC SS that can be applied to each ion as a function of system size N. See Sec. 3.4.2 for more details on the dependence on the strength of the fourth-order AC Stark shift due to intensity and number of ions being addressed. We typically set the rasterized target AC SS value to be about 5 kHz with a maximum tolerance of $\pm 5\%$ or 5 ± 0.25 kHz for each ion. Thus, we fix the total duration that each SIR chapter is turned on for 0.1 ms which corresponds to a π time of a 5 kHz sine wave. At the end of the general individual addressing beam calibration procedure, we have a list of individual addressing beam frequencies corresponding to the position of each ion, a list of the calibrated AWG amplitudes for each AOD frequency, and a list of the corresponding measured calibrated AC SS values.

In the Mathematica notebook specifically designed for running through the general calibration sequences of the individual addressing beam, these three lists of calibrated values are called, IonAODFreqs, TargetSSAWGAmp, and TargetSSFitFreqs, respectively. Figure 6.4 shows the functions defined in Mathematica which uses the three fitted parameters (StarkAWGFitAmp, StarkAWGFitFreq, and StarkAWGFitOff) of the $\sin^4$ function that was fit to the single-ion individual addressing beam Stark shift vs. applied AWG amplitude data. When this $\sin^4$ best-fit

```
(* functions to convert SS to AWG amplitudes *)
AWGPower[a_, k_, b_, Stark_] := 1/k ArcSin[((Stark - b)/a)^(1/4)]
RandomAWGPower[SS_, AWGAmp_, randomSS_] :=
 AWGPower[StarkAWGFitAmp (SS - StarkAWGFitOff)/StarkAWGFit[AWGAmp] - StarkAWGFitOff, StarkAWGFitFreq, StarkAWGFitOff, randomSS]
```

Figure 6.4. Converting random Stark shifts to AWG amplitudes

function is inverted, it gives an equation that returns an AWG amplitude that should be applied to measure the SS value.

For a given set of random angles $\{\theta_i\} = \{\theta_1, \ldots, \theta_N\}$, each individual θ_i angle is converted into a SS value by dividing each angle by $(2\pi * 0.1)$ where the 0.1 ms is the duration of the SIR chapter. Then, each of the θ angle SS values are plugged in to the AWG power versus measured SS function using the calibrated *TargetSSAWGAmp* and *TargetSSFitFreqs* values found for each ion's individual addressing beam. A similar procedure is done for a given set of random $\{\phi_i\} = \{\phi_1, \ldots \phi_N\}$ angles. The Mathematica code that we have written for this conversion from angles to AWG amplitudes is shown in Fig. 6.5 using the functions in Fig. 6.4.

In Fig. 6.5, we have $N = 5$ and are generating 20 random angle sets for both θ and ϕ. In addition, we export the random angle values for all 20 sets for both θ and ϕ in two separate ".dat" files corresponding to thetaVals and phiVals, respectively. We also export each row of elements

```
NumIons = 5;(* number of ions *)
NUsets = 20;(* number of RU sets *)
PulseDuration = 0.1;(* π-time [ms] of 5 kHz Rabi Freq. *)

(* generate random angles *)
Do[angle[i] = NonUniformRandomTheta[NumIons], {i, NUsets}]
thetaVals = Array[angle, NUsets];
Do[angle[i] = UniformRandomPhi[NumIons], {i, NUsets}]
phiVals = Array[angle, NUsets];
(* convert random angles to random SS *)
thetaSS = thetaVals / (2 π PulseDuration);
phiSS = phiVals / (2 π PulseDuration);
(* convert random SS to random AWG amplitudes *)
thetaAWGExport =
  Table[{RandomAWGPower[TargetSSFitFreqs[[ion]], TargetSSAWGAmp[[ion]], thetaSS[[set, ion]]],
    IonAODFreqs[[ion]]}, {set, NUsets}, {ion, NumIons}];
phiAWGExport =
  Table[{RandomAWGPower[TargetSSFitFreqs[[ion]], TargetSSAWGAmp[[ion]], phiSS[[set, ion]]],
    IonAODFreqs[[ion]]}, {set, NUsets}, {ion, NumIons}];
```

Figure 6.5. Converting Stark shifts to corresponding AWG amplitudes. User-defined functions written in Mathematica, allows us to convert a given AC Stark shifts value to a corresponding AWG amplitude by inverting the analytically function that describes the measured Stark shift experienced by an ion for an applied AWG amplitude on the AOD.

contained in the list thetaAWGExport into their own ".csv" files such that each random θ set can eventually be imported into our LabView SIR chapters. Similarly, each row of elements contained in the list phiAWGExport are also exported into their own ".csv" files corresponding to the random ϕ sets. None of these file export commands are shown in Fig. 6.5 though.

Testing with the ions; they will always let you know if it works (most of the time).

Having developed a way to independently sample random angles θ_i and ϕ_i to prepare a random uniformly distributed point on the Bloch sphere and a way to convert these angles into corresponding AWG amplitudes to drive ion i's individual addressing beam center frequency

tone, it was now time to verify experimentally with the ions that our scheme to implement the different RU sets $\{u_i\}$ are indeed random and independent. We performed what I call a "Measure X, Y, Z" test for $N_U = 20$ different RU sets with $N = 5$ ions. For each RU set $U_r = \{u_i\}_r$ with index r denoting the random sets, we ran the experimental sequence applying U_r to the 5 ions all initially prepared in $|\downarrow\rangle$ in which we projectively measured each ion's average magnetization in a fixed basis (X, Y, or Z). The experimental sequences for measuring along the X, Y, Z axes after $U_r \, |\downarrow\rangle^{\otimes N=5}$ are shown in Table 6.2. The experimental sequences for making projective mea-

Measure X	**Measure Y**	**Measure Z**	**Sequence Description**
Doppler Cool	Doppler Cool	Doppler Cool	
Optical Pump	Optical Pump	Optical Pump	
AWG SB Cool	AWG SB Cool	AWG SB Cool	
AWG GR 1	AWG GR 1	AWG GR 1	$R_{-x}(\pi/2)$
AWG SIR 2	AWG SIR 2	AWG SIR 2	$\{R_z(\theta_i)\}_r$
AWG GR 2	AWG GR 2	AWG GR 2	$R_x(\pi/2)$
AWG SIR 3	AWG SIR 3	AWG SIR 3	$\{R_z(\phi_i)\}_r$
AWG GR 9	AWG GR 13	Detect	For X: $R_{-y}(\pi/2)$. For Y: $R_x(\pi/2)$.
Detect	Detect		

Table 6.2. Measure X, Y, Z experimental sequences. After the initialization process (Doppler cooling, optical pumping, and Raman sideband cooling), the set of individual ion random unitaries (all the chapters highlighted in color) are applied to the prepared all $|\downarrow\rangle$ product state. The three chapters highlighted in blue generates the random $\{\theta_i\}_r$ rotations while the chapter highlighted in orange represents the random $\{\phi_i\}_r$rotations. Lastly, depending on the measurement basis an additional $\pi/2$ pulse is required to project the desired measurement basis onto the z axis before detecting the ion states.

surements of the random product state along any axis are all very similar (same seven chapters) until the actual detection is done. In Table 6.2 the first three processes in each of the sequences, Doppler Cool $\rightarrow$ Optical Pump $\rightarrow$ AWG SB Cool, represent the initialization or state preparation that is done at the beginning of any experimental sequence run in the lab which results

in cooling the ions spin and motion to their ground states. Next, the chapters GR 1 $\rightarrow$ SIR 2 $\rightarrow$ GR 2 $\rightarrow$ SIR 3 with the "AWG" prefix dropped, implement the individual ion RUs from the r^{th} random unitary set in which the three chapters highlighted in blue generate the random θ_i rotations followed by the random ϕ_i rotation with the chapter highlighted in orange. Finally, once the individual $(u_i)_r$ have been implemented "simultaneously," the projective measurement is performed. For the measurements along X or Y as shown in Table 6.2, an additional $\pi/2$ pulse with the appropriate carrier phase is required to project the $-x$ axis or $-y$ axis onto the $-z$ axis before turning on the detection beam. For a measurement in the Z basis, no additional rotation is required before the detection beam is turned on.

For a given random set r, each measurement sequence was run as a "dummy scan" (see Sec. 3.5 explaining the terminology) for 10 times where each scan consisted of two steps with 100 measurements at each step. In total, 2000 experiments were performed for each RU set's Measure X, Y, Z sequence corresponding to a total of $N_U \times 2000 = 40,000$ measurements along each direction. Figure 6.6 shows the individual ion RU ensemble average magnetizations in each of the three directions. The results of the RU ensemble average of each Measure X, Y, Z data set for each ion shows values that are very close to zero considering only 20 finite sets were sampled. Ideally, in the limit of infinite RU sets sampled, the average magnetization of a given ion in any direction is expected to be zero. One thing to point out is that the error bars of the experimental data should not be compared to the error bars of the theoretical values since they reflect different comparisons. The error bars on the experimental data were calculated in order to try to show the spread of the individual ion's average magnetization across the 20 different random sets. In comparison, the theoretical error bars are given by the standard error of the mean for each ion's ideal ensemble average magnetization.

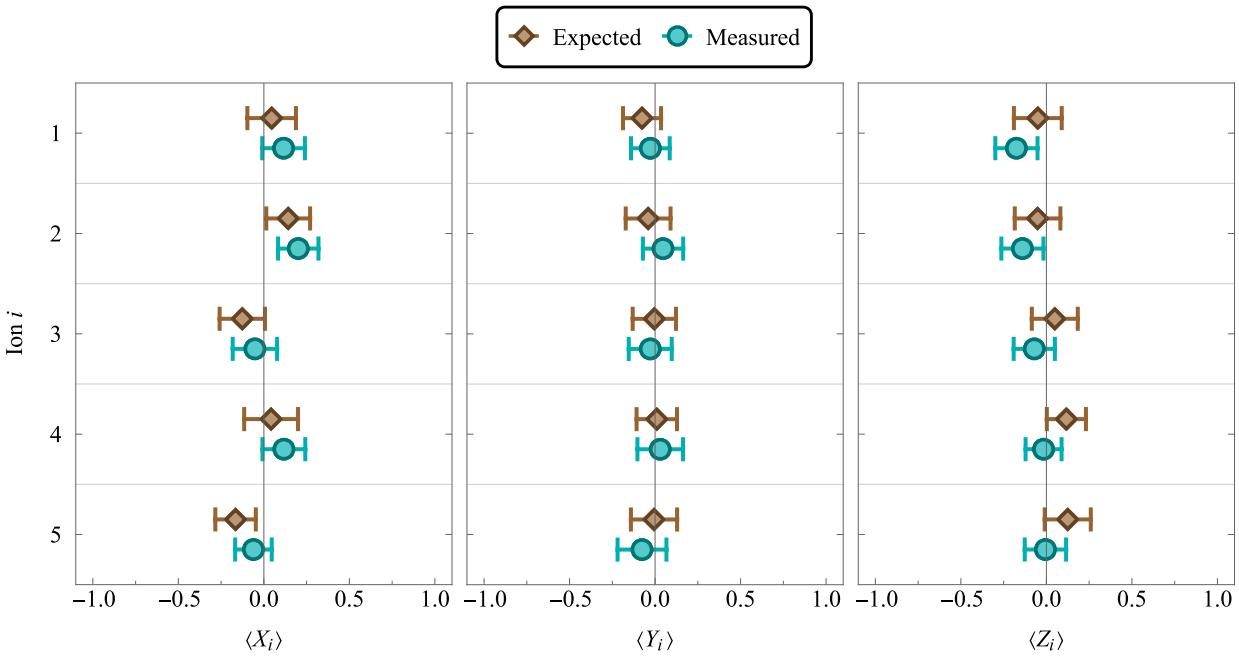


Figure 6.6. Individual ion average measure x, y, z results. The average magnetization along each direction calculated from measurements of the sampled 20 RUs are displayed for each ion (teal circles). In comparison, the expected average magnetization for each ion along x, y, z are plotted (brown diamonds) as well. The associated error bars that are shown for measured values and the expected values should not be compared to each other since they represent different measures. The expected error bars represent the standard uncertainty of the mean of the 20 RUs while the experimental errors bars were calculated in order to show the spread of the 20 random values.Instead each data set's error bars should be compared to how close they are to zero.

We also calculated the RU ensemble average connected correlation in each direction to make sure that the random values sampled were independent from one another. These results are displayed in Fig. 6.7. As observed in Fig. 6.7, very few correlations exist. So, using the ions

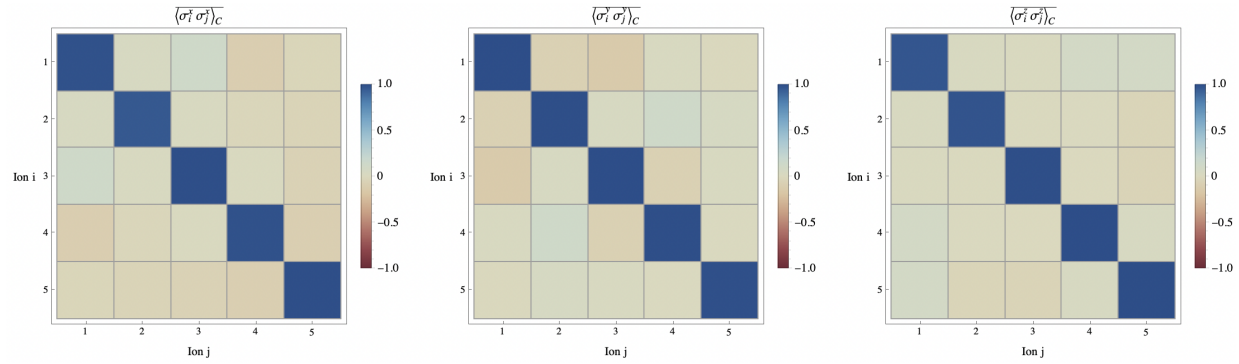


Figure 6.7. RU ensemble average connected correlations.

as our final witness, our methods for generating and implementing the independently randomly

sampled angles seems to work fine.

From the RU measure x, y, and z sequences it turns out that both $R_z(\theta_i)$ and $R_z(\phi_i)$ are actually $R_z(-\theta_i) = R_{-z}(\theta_i)$ and $R_z(-\phi_i) = R_{-z}(\phi_i)$ which is required to match the signs of the measured average x, y, and z magnetization values in each RU set since we trust the QSim Bloch sphere which governs what phase the carrier rotation should have in order to rotate about the $-x$ axis, y axis, x axis, or $-y$ axis. This also means that the individual RU $u_i(\theta_i, \phi_i)$ applied to ion i initially in $|\downarrow\rangle$ will be rotated to a state described by the Bloch vector $\vec{v} = \{-\sin\theta_i \cos\phi_i, \sin\theta_i \sin\phi_i, -\cos\theta_i\}$. The full form of the individual random unitary for the i^{th} ion with random angles θ_i and ϕ_i is defined as:

$$\begin{aligned} u_i(\theta_i, \phi_i) &= R_{-z}(\phi_i) R_x(\pi/2) R_{-z}(\theta_i) R_{-x}(\pi/2) \\ &= R_{-z}(\phi_i) R_y(\theta_i) = e^{i(\phi_i/2)Z_i} e^{-i(\theta_i/2)Y_i} \\ &= \begin{bmatrix} e^{i\phi_i/2}\cos(\theta_i/2) & -e^{i\phi_i/2}\sin(\theta_i/2) \\ e^{-i\phi_i/2}\sin(\theta_i/2) & e^{-i\phi_i/2}\cos(\theta_i/2) \end{bmatrix}. \end{aligned} \tag{6.23}$$

The full form of the corresponding individual random unitary adjoint for the i^{th} ion with random angles θ_i and ϕ_i is defined as:

$$\begin{aligned} u_i^\dagger(\theta_i, \phi_i) &= R_{-x}(\pi/2) R_{-z}(\theta_i) R_{-x}(\pi/2) R_{-z}(\phi_i) R_{-x}(\pi) \\ &= e^{i(\pi/4)X_i} e^{i(\theta_i/2)Z_i} e^{i(\pi/4)X_i} e^{i(\phi_i/2)Z_i} e^{i(\pi/2)X_i} \\ &= \begin{bmatrix} -e^{-i\phi_i/2}\cos(\theta_i/2) & -e^{i\phi_i/2}\sin(\theta_i/2) \\ e^{-i\phi_i/2}\sin(\theta_i/2) & -e^{i\phi_i/2}\cos(\theta_i/2) \end{bmatrix}. \end{aligned} \tag{6.24}$$

For those checking whether Eq. (6.23) and Eq. 6.24 satisfy the definition of a unitary matrix, $U^\dagger U = \mathbb{1}$, the answer is "yes, they do" with a global phase factor of $e^{-i\pi} = -1$.

The state overlap measurement, initially described in Sec. 6.4.1, is implemented using the

sequence shown in Table 6.3. This state overlap sequence was run for only half of 20 total RU

State Overlap Sequence	
Purpose	Chapter/Operator
Initialize State $\|\psi_0\rangle$	Doppler Cool Optical Pump SB Cool
Apply RU $U_r = \{u_i\}_r$	Global $R_{-x}(\pi/2)$ SIR 3 $\{R_{-z}(\theta_i)\}_r$ Global $R_x(\pi/2)$ SIR 4 $\{R_{-z}(\phi_i)\}_r$
Wait Time $t = n\tau$	Blank
Apply RU† $U_r^\dagger = \{u_i^\dagger\}_r$	Global $R_{-x}(\pi)$ SIR 5 $\{R_{-z}(\phi_i)\}_r$ Global $R_{-x}(\pi/2)$ SIR 6 $\{R_{-z}(\theta_i)\}_r$ Global $R_{-x}(\pi/2)$
Measure $\boldsymbol{s}^{(r)}(t)$	Detect

Table 6.3. LabView state overlap sequence. This is the actual experimental sequence implemented using our LabView control software to estimate the error due to imperfect preparation and measurement of the random unitaries.

sets ($r = 11, \ldots, 20$). The wait time duration t was varied from 0–20 ms broken into 16 steps and 200 measurements were performed at each wait time value for each RU set r. Figure 6.8 shows the individual ion average fidelity obtained from the state overlap scan results.

6.5.2 Implementing Local Random Disorders

The disorder strengths g_{z_i} and h_{z_i} are independently randomly sampled from the uniform distribution on $[0, 2J_0\xi]$. The random disorder (RD) strengths are generated in a similar fashion

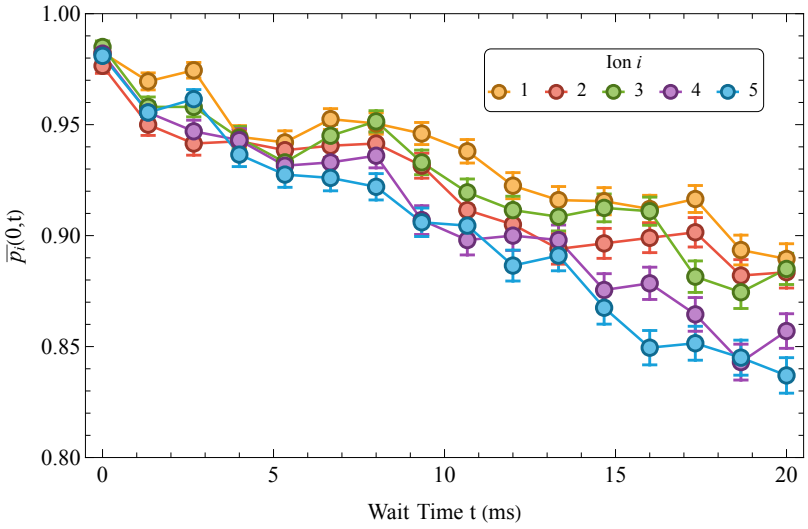


Figure 6.8. Individual ion average state overlap. The ensemble average is only over 10 of the RU sets. Each data point is the mean of 2000 measurements total and the error bars correspond to the standard error of the mean.

to the method used for the random angles. Figure 6.9 shows the code written in Mathematica to generate the RD sets using the functions shown in Fig. 6.4. Not shown in Fig. 6.9 are the

```
NumIons = 5;(* number of ions *)
NBsets = 20;(* number of RD sets *)
JavgNN = 0.430485;(* [kHz]/(2π) *)
ξ = 6; (* disorder scale factor *)
(* B-field values must be multiplied by 2 for LabView *)
JLabView = 2 * (JavgNN * ξ);
(* generate random disorder strengths gzi and hzi *)
Do[gg[i] = RandomReal[{0, 2 JLabView}, NumIons], {i, NBsets}]
gziSSVector = Array[gg, NBsets];
Do[hh[i] = RandomReal[{0, 2 JLabView}, NumIons], {i, NBsets}]
hziSSVector = Array[hh, NBsets];

(* generate corresponding AWG amplitudes from random disorder strengths gzi & hzi *)
gziAWGExport =
  Table[{RandomAWGPower[TargetSSFitFreqs[[ion]], TargetSSAWGAmp[[ion]], gziSSVector[[set, ion]]],
    IonAODFreqs[[ion]]}, {set, NBsets}, {ion, NumIons}];
hziAWGExport =
  Table[{RandomAWGPower[TargetSSFitFreqs[[ion]], TargetSSAWGAmp[[ion]], hziSSVector[[set, ion]]],
    IonAODFreqs[[ion]]}, {set, NBsets}, {ion, NumIons}];
```

Figure 6.9. Converting random disorder strengths to AWG amplitudes.

lines of code that exports all of the RD sets for both g_{z_i} and h_{z_i} into ".dat" files corresponding to the gziSSVector/2 and hziSSVector/2, respectively. In addition, each row in the lists

gziAWGExport and hziAWGExport are exported into their own ".csv" files such that each random $\{g_{z_i}\}_r$ and random $\{h_{z_i}\}_r$ set can be eventually imported into our LabView SIR chapters.

6.5.3 SFF Purity Sequence and Calculating the Purity

In Sec. 6.4.2, measuring the purity of the SFF sequence was proposed as a way to mitigate decoherence errors occurring during the dynamics of $T(t = n\tau)$. Here, we present the experimental sequence to measure the SFF purity and how the purity observable is calculated from the results of the measured sequences.

The SFF purity experimental sequence is very similar to the SFF experimental sequence shown in Table **??**, but without the application of the initial random unitary U. Table 6.4 displays the experimental sequence to measure the purity of the r^{th} SFF instance corresponding to V_r^n. The purity sequence for the r^{th} instance of V_r uses the same sets of individual random values—$\{\theta_i\}_r$, $\{\phi_i\}_r$, $\{g_{z_i}\}_r$, and $\{h_{z_i}\}_r$—that were used in the corresponding SFF sequence. As seen in Table 6.4 and from Table **??**, both sequences begin with preparing the same initial state $|\psi_0\rangle$. Each purity sequence data point (or time step $t = n\tau$) for a given instance r will also have 100 measurements collected before the scanned duration of $T(t=n\tau)$ is incremented to the next value at $t=(n+1)\tau$ and the r^{th} purity sequence displayed in Table 6.4 is repeated 100 more times, etc.

To calculate the disorder-averaged SFF purity, we used the purity equation that Brydges, *et al.* [139] derived in the article's supplementary material in which the purity of a subsystem A in the total system $\mathcal{S}$ is inferred from randomized measurements. Equation (6.25) gives the expression of the disorder-averaged purity of the entire system $\mathcal{S}$,

$$P_n = \text{Tr}\left[\rho^2(t=n\tau)\right] = 2^N \sum_{k,l} (\text{-}2)^{-D[\boldsymbol{s}_k,\boldsymbol{s}_l]} \overline{P(\boldsymbol{s}_k)P(\boldsymbol{s}_l)} \tag{6.25}$$

SFF Purity Sequence	
Purpose	Chapter/Operator
Initialize State $\|\psi_0\rangle$	Doppler Cool Optical Pump SB Cool
Time-Evolve $T(t=n\tau)=V_r^n$	Int 1 H_1, t_{Int} SIR 7 H_2, t_{SIR} Int 2 H_3, t_{Int} SIR 8 H_4, t_{SIR}
Apply RU† $U_r^\dagger=\{u_i^\dagger\}_r$	Global $R_{-x}(\pi)$ SIR 5 $\{R_{-z}(\phi_i)\}_r$ Global $R_{-x}(\pi/2)$ SIR 6 $\{R_{-z}(\theta_i)\}_r$ Global $R_{-x}(\pi/2)$
Measure $\boldsymbol{s}^{(r)}(t)$	Detect

Table 6.4. LabView purity sequence. This is the actual experimental sequence implemented using our LabView control software to measure the SFF purity. The experimental sequence for to measure the purity of random set r is very similar to the SFF sequence. However, it differs slightly since the interactions are applied immediately after preparing the initial state.

where $D[\boldsymbol{s}_k, \boldsymbol{s}_l]$ is the Hamming distance between the k^{th} and l^{th} basis states, and $\overline{P(\boldsymbol{s}_k)P(\boldsymbol{s}_l)}$ is the ensemble average of cross correlations [139]. It is important to note that the cross correlations of the r^{th} random set, $P[\boldsymbol{s}_k^{(r)}]P[\boldsymbol{s}_l^{(r)}]$, corresponding to a time $t = n\tau$ are unbiased estimators [142].

The probability of measuring the k^{th} basis state, $\boldsymbol{s}_k^{(r)}(t)$ at time t in the r^{th} purity sequence is $P[\boldsymbol{s}_k^{(r)}(t)]$ and is an unbiased estimator [142]. However, the corresponding probability squared, $P[\boldsymbol{s}_k^{(r)}(t)]^2$, is a biased estimator since for finite measurements it gives an overestimate of the expectation value. Thus, when calculating the cross correlation of the r^{th} random set at time t

the following formula must be used when $k=l$:

$$P[\boldsymbol{s}_k^{(r)}(t)]^2 = \frac{P[\boldsymbol{s}_k^{(r)}(t)]\left(P[\boldsymbol{s}_k^{(r)}(t)]N_m - 1\right)}{N_m - 1} \tag{6.26}$$

where Eq. (6.26) now gives a faithful estimation of the probability squared for measuring the outcome bit string $\boldsymbol{s}_k^{(r)}(t)$.

Similar to the being able to calculate the full system SFF and the subsystem PSFFs from the r^{th} instance of the SFF sequence, subsystem purities can also be calculated from the results of the r^{th} purity sequence via post-processing. Equation (6.25) can be generalized to calculate the purity of a specific subsystem A contained in the entire system $\mathcal{S}$ using the equation that was derived by Brydges, *et al.* in the supplementary material of [139] which is shown below as Eq. (6.27).

$$\text{Tr}\left[\rho_A^2(t=n\tau)\right] = 2^{N_A}\sum_{k,l}(\text{-}2)^{-D[\boldsymbol{s}_{A_k},\boldsymbol{s}_{A_l}]}\overline{P(\boldsymbol{s}_{A_k})P(\boldsymbol{s}_{A_l})}, \tag{6.27}$$

where N_A is the number of ions in the subsystem and state labels k and l now refer to the subsystem A basis states that span the Hilbert subspace dimension of 2^{N_A}. Even though we don't necessarily care about the subsystem purities, we can calculate them anyway to try to gain more insight about our system and decoherence effects.

Purity Properties: The purity observable is easiest to understand by considering two cases of the density operator ρ. The first case is when the density operator describes the system in a pure state such as an initialized N-ion product state. The purity of a pure state is 1. In comparison, when ρ describes a fully mixed state where the probability of measuring the system in any of the 2^N basis states is equally likely, the corresponding purity is $1/2^N$.

6.6 $N = 5$ SFF

We initially began running the SFF, purity, and state overlap experimental sequences for a chaotic system with $N = 5$ ions. The SFF and purity sequences were measured for 30 random sets. A state overlap sequence was only measured for seven of sets. The seven state overlap sets were dispersed throughout the entire data taking process. Figure 6.10 shows the raw experimental results for the chaotic disorder-averaged SFF for $N = 5$ ions. The error bars shown in Fig. 6.10

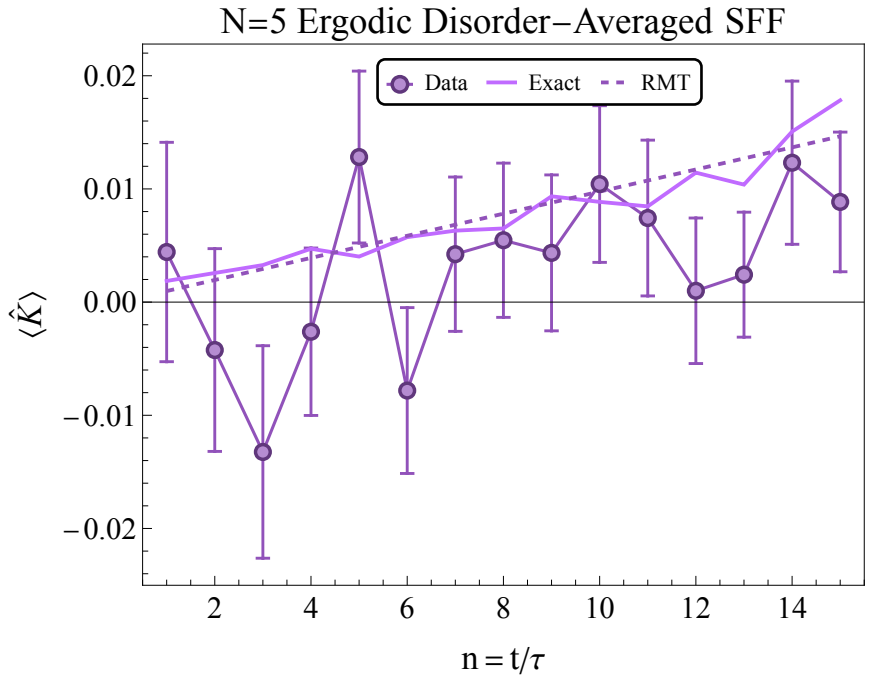


Figure 6.10. $N = 5$ ergodic SFF.

represent the standard error of the mean over the random sets. The solid purple line corresponds to the ideal SFF using the actual experimental parameters and calculated exactly using Eq. (6.1).

Figure 6.11 shows the $N = 5$ ergodic disorder-averaged PSFF results. Each PSFF is actually the mean subsystem size N_A PSFF corresponding to averaging over all the disorder-averaged subsystems A for fixed N_A.

Figure 6.12 shows the raw experimental results for the individual ion average random uni-

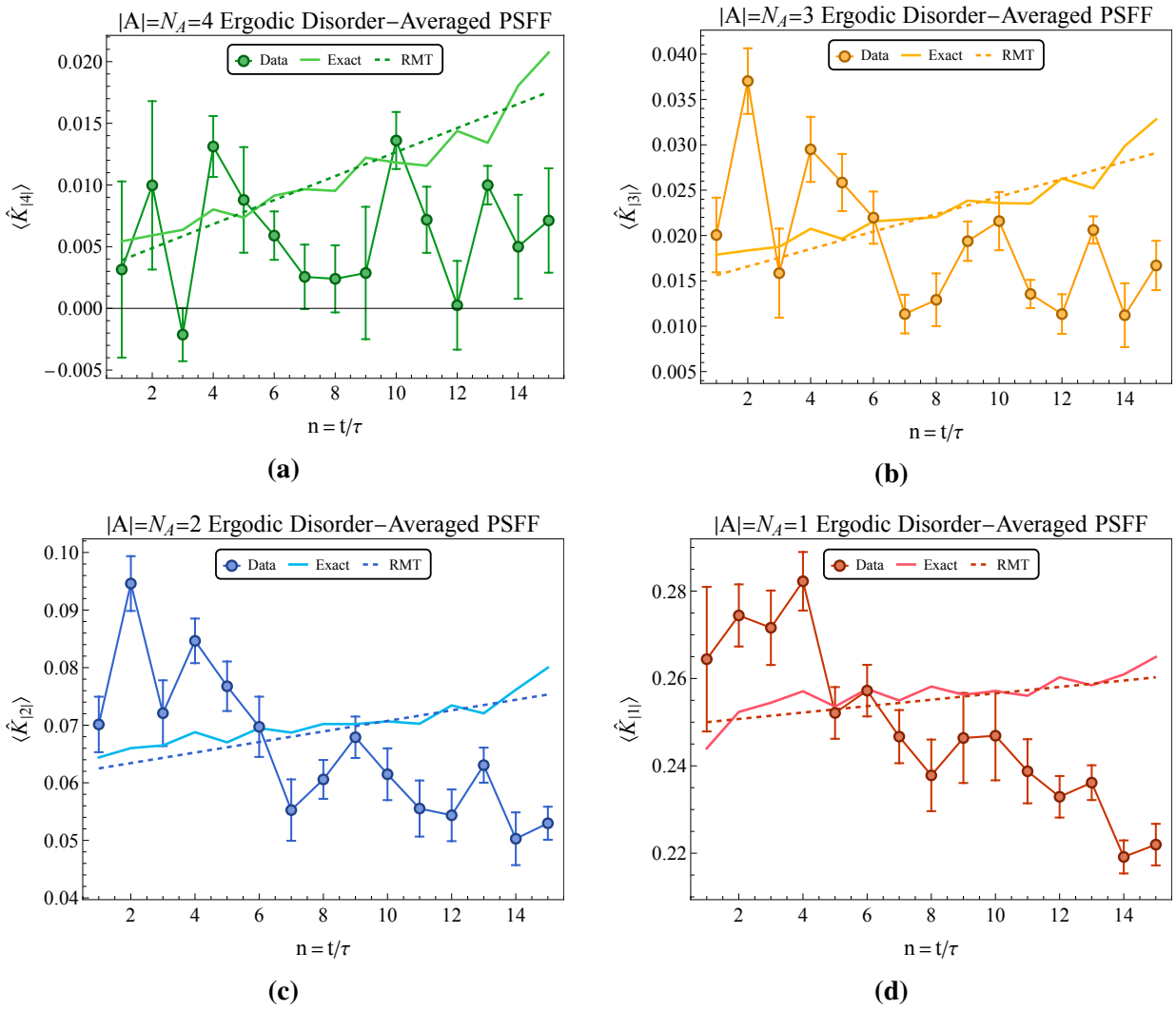


Figure 6.11. $N = 5$ ergodic average subsystem size PSFF.

tary fidelity for $N = 5$ ions. while Fig 6.13 shows the raw experimental results for the ergodic disorder-averaged SFF purity for $N = 5$ ions. The value of the dashed line in Fig. 6.13 corresponds to the expected purity of a fully mixed $N = 5$ ion system, at $1/2^5 = 1/32 = 0.03125$.

6.7 Variations of the Purity Sequence

Before continuing to run more $N = 5$ SFF sequences using a different RU set and different RD sets for each new instance, we wanted to try to understand the observed decoherence. The

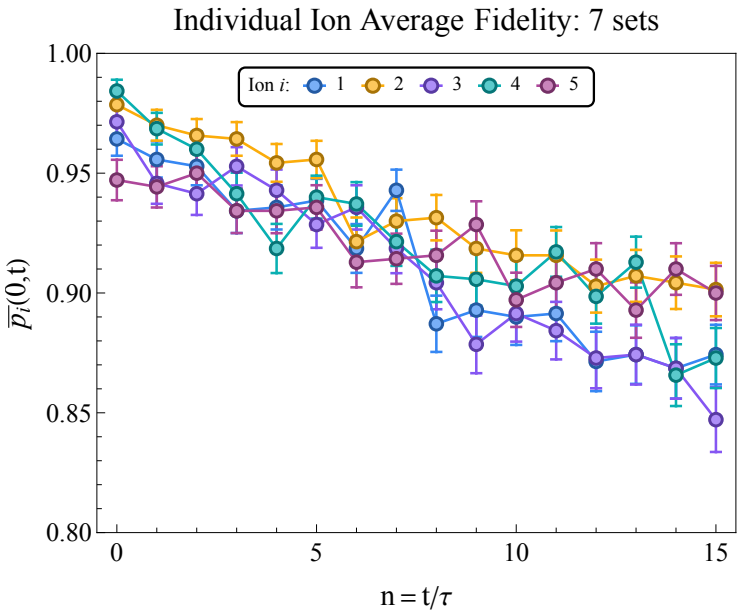


Figure 6.12. $N = 5$ individual ion average fidelity. The state overlap sequence was performed for only 7 RUs. We made sure to run this sequence throughout the data taking process in order to calculate and accurate individual ion fidelity measurement.

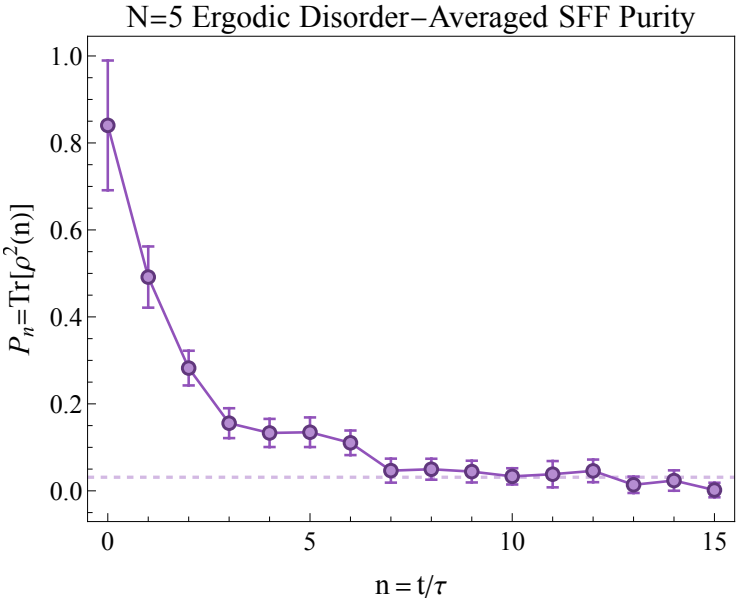


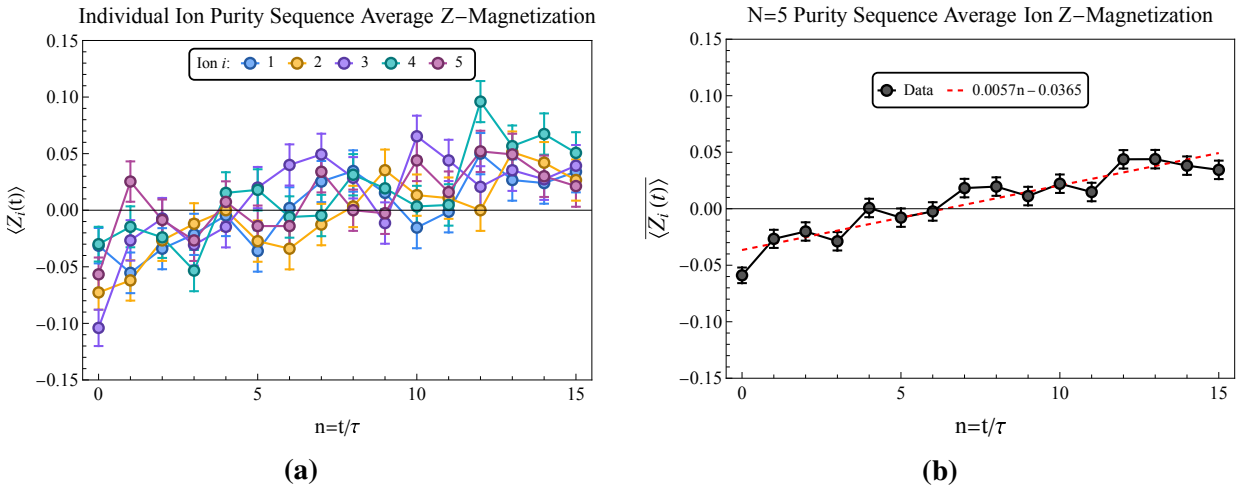
Figure 6.13. $N = 5$ ergodic SFF purity.

decoherence seems to begin around $n = 5, 6$ and is most evident from the average subsystem $N_A = 1, 2$ PSFF plots, Fig. 6.11d and Fig. 6.11c, respectively. The full system purity data in Fig. 6.13, also, shows the influence of decoherence effecting the system after $n = 6$. We decided to begin our investigation by looking at the calculated $N = 5$ SFF purity and the purity sequence

data itself.

In the late time limit, we would expect that the average individual ion ensemble averaged z-magnetization of the purity sequence would tend to zero and remain around that value as the sequence is run for longer durations. This expectation stems from two observations. First, we would naturally expect that the measured purity would eventually decrease towards the fully mixed state purity value as time increases because experimental quantum simulators are not ideal systems. The decrease in the measured purity is due to decoherence which tends to increase at longer experimental run times and leads to a loss coherent of information in the system. Recall that a fully mixed system is equally likely to be measured in any of its 2^N basis states which corresponds with the expectation that the average z-magnetization of any given ion at late times is around zero. Second, each r^{th} instance of the experimental purity sequence applies the r^{th} RU adjoint operator before detecting the outcome bit string in the z-basis, similar to the Measure Z sequence that was implemented to verify that the random unitaries applied to the ions were random. As previously discussed in Sec. 6.5.1, the average magnetization along any given direction for any ion is expected to be around zero assuming the number of random unitaries sampled is large enough.

From Fig. 6.6, the individual ion magnetizations along each direction, averaged over the 20 RU sets sampled, were already yielding results around zero and so, it seemed natural to calculate the ensemble averaged z-magnetization of each ion i, $\langle Z_i \rangle$, and the average ion z-magnetization, $\overline{\langle Z_i \rangle} = \sum \langle Z_i \rangle$, of the measured SFF purity sequences in which 30 random sets were sampled. Plots of these results are shown in Fig. 6.14. At early times t (when $n \leq 6$) both $\langle Z_i(t) \rangle$ and $\overline{\langle Z_i(t) \rangle}$ gradually approach zero matching the behavior of the SFF purity P_n observed in Fig. 6.13 in which $P_n \to 0.03125$ approaches the fully mixed state purity value for $n \leq 6$. However, in both



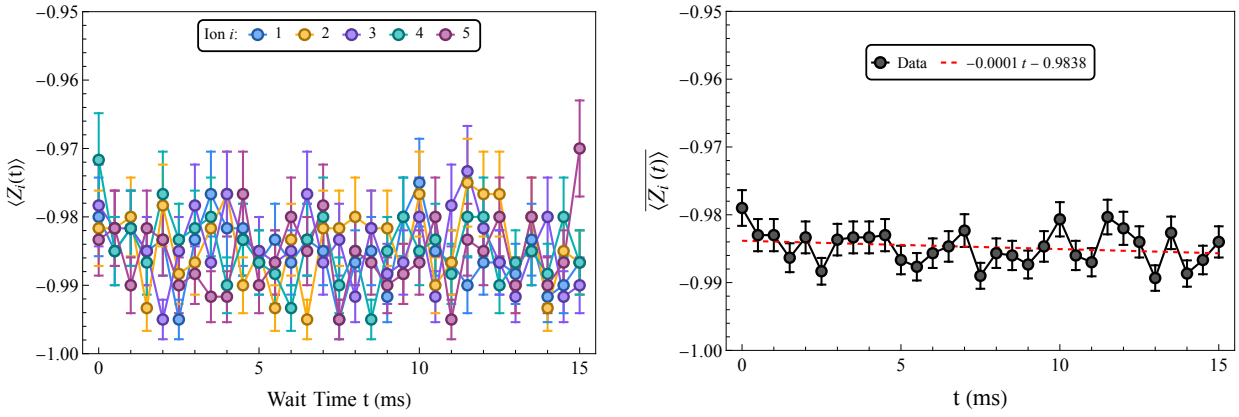
(a) **(b)**

Figure 6.14. $N=5$ ergodic SFF purity sequence z-magnetizations.

Fig. 6.14a and Fig. 6.14b, the average z-magnetization begins to become slightly more positive, especially for larger values of n, $n \geq 12$. We fit the purity sequence average ion z-magnetization to a linear function obtaining the best-fit depicted by the red dashed line and functional form displayed in the legend of Fig. 6.14b. The slope of 0.0057 is given with respect to n, the number of applied Floquet cycles. The change in the average ion z-magnetization with respect to time t in ms is 0.0065. At $n=15$, the corresponding total duration was $t=13.125$ ms.

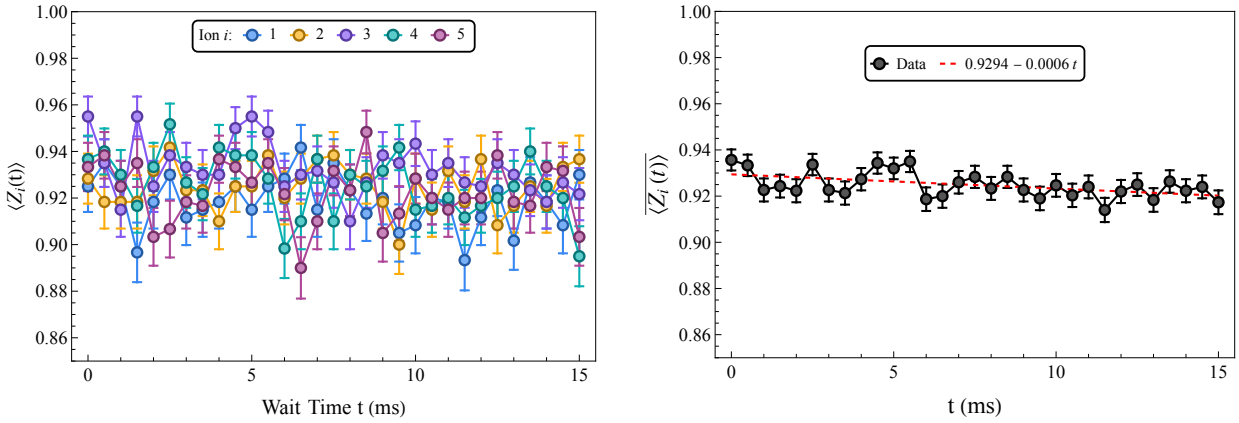
The small positive slope observed in the average ion z-magnetization dynamics of the purity sequence was surprising and puzzling. We decided to break down the entire purity sequence into its simplest form to investigate the origins of the positive slope. As a reminder, the SFF purity sequence can be broken into four steps: i) prepare all ions in their down state, ii) apply $T(t=n\tau)=V_r^n$, iii) apply $U_r^\dagger=\{u_i^\dagger\}_r$, and iv) detect (measure z). Thus, a simple form of the purity sequence involves preparing $N=5$ ions in the all down (dark) product state, wait for some variable time t (i.e. do nothing to or with the ions), and then, detect the ions in the z-basis. Similarly, instead of preparing $|\downarrow\downarrow\downarrow\downarrow\downarrow\rangle$ as the initial state, we could prepare the all up (bright) product state, $|\uparrow\uparrow\uparrow\uparrow\uparrow\rangle$, and detect the ions after waiting for time t. We performed each of these two simple

sequences varying the delay time t from 0 ms to 15 ms before detecting the ions. Figures 6.15 and 6.16 show the individual ion average z-magnetization and average ion z-magnetization dynamics for the ions initially prepared in $|\downarrow\downarrow\downarrow\downarrow\downarrow\rangle$ and $|\uparrow\uparrow\uparrow\uparrow\uparrow\rangle$, respectively. The results of these two sim-



(a) **(b)**

Figure 6.15. Average z-magnetizations of dark product state.



(a) **(b)**

Figure 6.16. Average z-magnetizations of bright product state.

ple purity-like sequences shows a constant or very small decrease in the average z-magnetization dynamics over the varied delay time. We then decided to introduce the application of the individual random unitaries back into the simplified sequence in which we start with the five ions all down, wait for some time t, apply a set of individual random unitaries labeled by r to the system before measuring the ions. This sequence was performed for 30 different RUs over the same wait

time duration of $t = 0, \ldots, 15$ ms and the results are shown in Fig. 6.17. The wait-prepare RU

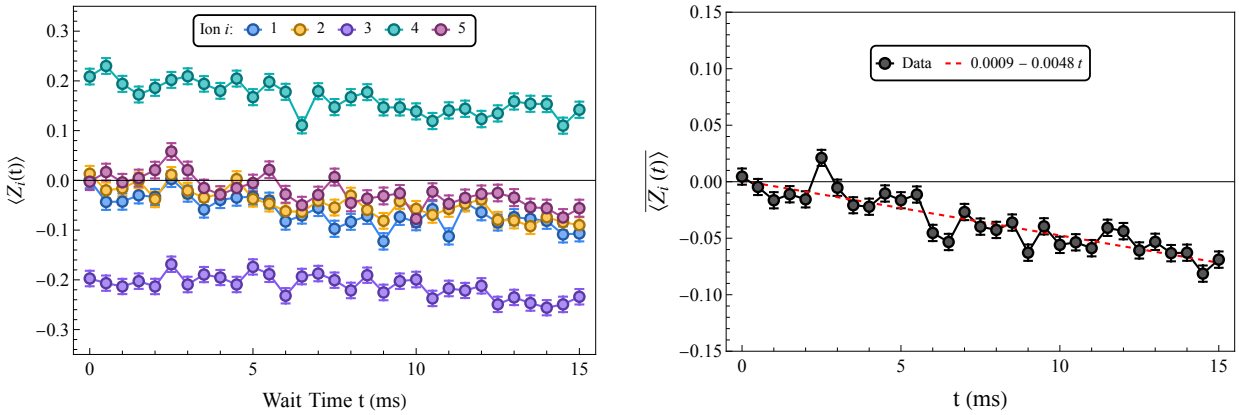


Figure 6.17. Average z-magnetizations of arbitrary product state.

measure sequence has a larger negative slope in the average ion z-magnetization. Still none of the simplified purity-like sequences measured so far have an increase in the average z-magnetization over time. We then investigated the average z-magnetization of the SFF purity sequence in which only the random disorder terms in the Floquet operator were applied in V_r while replacing the global interaction terms with blank chapters. More specifically, the modified purity sequence was the following: $|\downarrow\downarrow\downarrow\downarrow\downarrow\downarrow\rangle \rightarrow$ (blank chapter for $t_{\text{Int}} \rightarrow H_2(\{g_{z_i}\}_r)$ for $t_{\text{SIR}} \rightarrow$ blank chapter for $t_{\text{Int}} \rightarrow H_4(\{h_{z_i}\}_r)$ for $t_{\text{SIR}})^n \rightarrow$ apply $U_r^\dagger = \{u_i^\dagger\}_r \rightarrow$ measure z. The average z-magnetization results of only having the RDs in the purity sequence are shown in Fig. 6.18. Still no sign of a positive slope. Similarly to the RD only purity sequence, we also ran the SFF purity sequence with only the global interaction terms in V_r^n with blank chapters inserted for the random disorder terms. The sign of the positive slope in the average z-magnetization of the purity sequence has been identified at last. The global interactions are causing this effect. Recall, that we define the bight state or $|\uparrow\rangle$ state as the hyperfine ground state $^2\text{S}_{1/2}$ $|F=1,\, m_F=0\rangle$. However, the detection beam contains both sigma and pi polarized light in order to pump population out of the

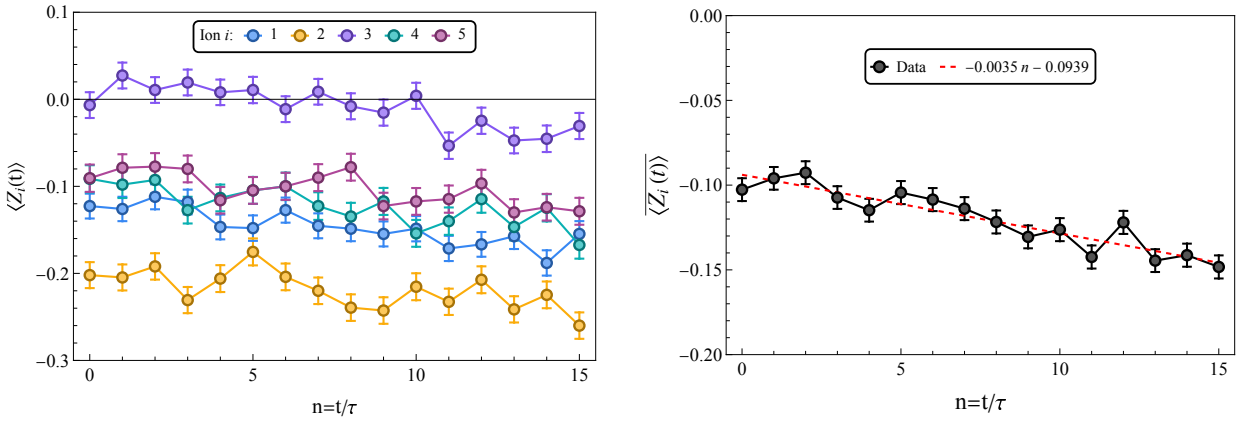


Figure 6.18. Average z-magnetizations of SFF purity sequence with only random disorders.

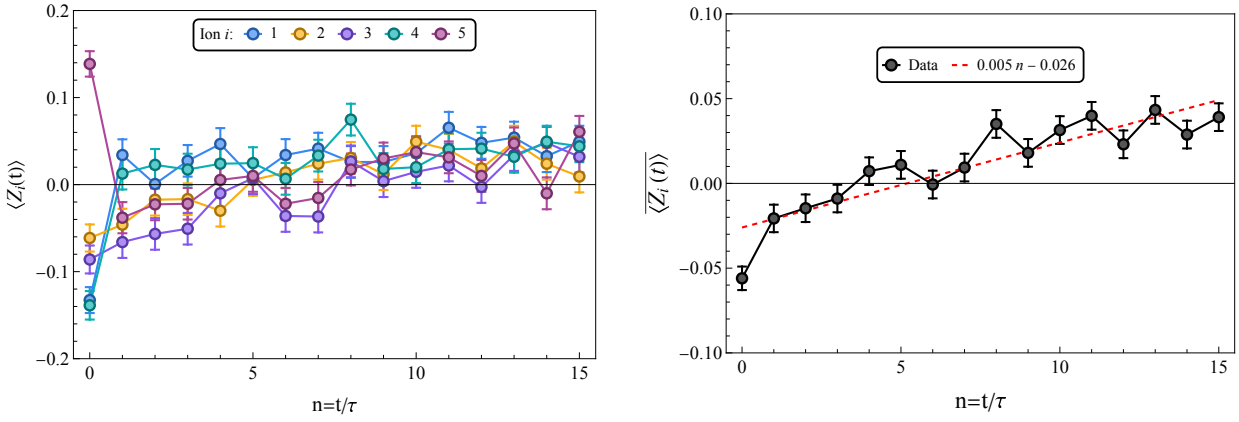


Figure 6.19. Average z-magnetizations of SFF purity sequence with only global interactions.

Zeeman $m_F = \pm 1$ levels. Population in the Zeeman levels will also appear bright and if we are (unintentionally) coupling to these levels, this effect would explain why we observe more bright spins at late times than dark spins.

As a result of the positive slope origin, we decided to check the coupling to the Zeeman levels. It turned out there was significant amount of coupling to the Zeeman sublevels and that our usual method of measuring the Zeeman sublevels presence was in fact not the right method to use. These coupling were actually about ∼20-30% coupling to the $^2S_{1/2}$ Zeeman $|F=1,\ m_F=\pm 1\rangle$ levels in comparison to the maximum carrier Rabi frequency. As a consequence, we made sure

that the Raman QWP and HWP were each optimized for each beam. We reduced the Zeeman percent coupling to about $\sim$3% and $\sim$6% for the respective Zeeman $|F=1,\ m_F=\pm 1\rangle$ states in the $^2\mathrm{S}_{1/2}$. We remeasured the purity-like sequence with only global interactions after minimizing the coupling and the average ion magnetization results are shown in Fig. 6.20.

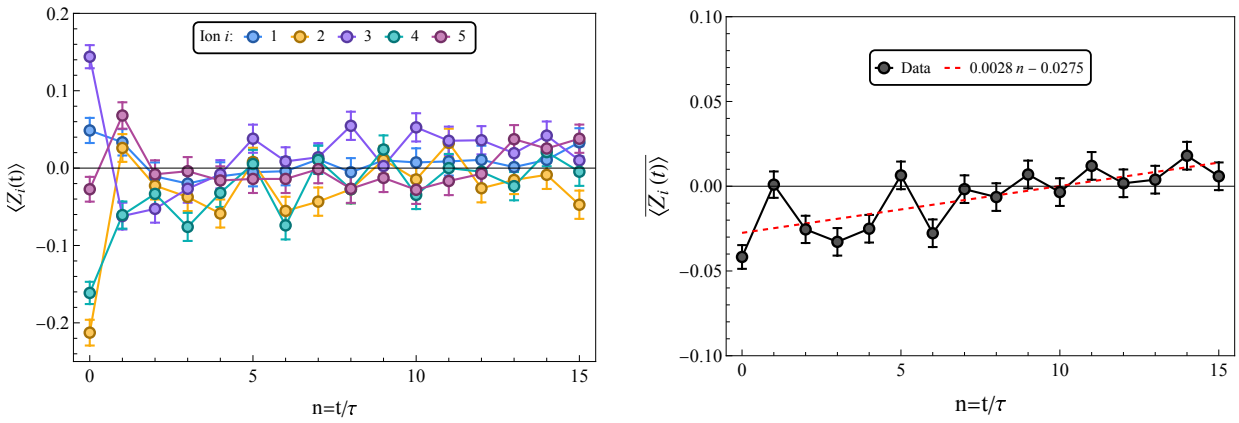


Figure 6.20. Average z-magnetizations of SFF purity sequence with only global interactions take two.

6.8 $N=4$ SFF Results

After minimizing the off-resonant Zeeman coupling, we decided to measure SFF for a slightly smaller sized system consisting of $N=4$ ions. There were a couple of reasons for this decision. The main reason why is simply the fact that $2^{-4}=0.0625$ is bigger than $2^{-5}=0.03125$ by a factor of two. The larger expected amplitude of the SFF ramp, we hoped would be slightly easier to measure since it is farther away from zero, and thus hopefully more distinguishable from noise. The other reason why is that the statistical requirements were slightly less daunting, $M\sim 10,000$ measurements per point, which we thought we would be able to sample a larger percentage of in comparison to the requirement for $N=5$ ions ($M\sim 100,000$).

6.8.1 Disorder-Averaged Ergodic SFF

We initially ran 30 random instances of the chaotic SFF sequence with four ions in which the sequence also incorporated dynamical decoupling following the scheme presented in Ch. 5. Figure 6.21 displays the unscaled experimental results. We decided not to got with this method,

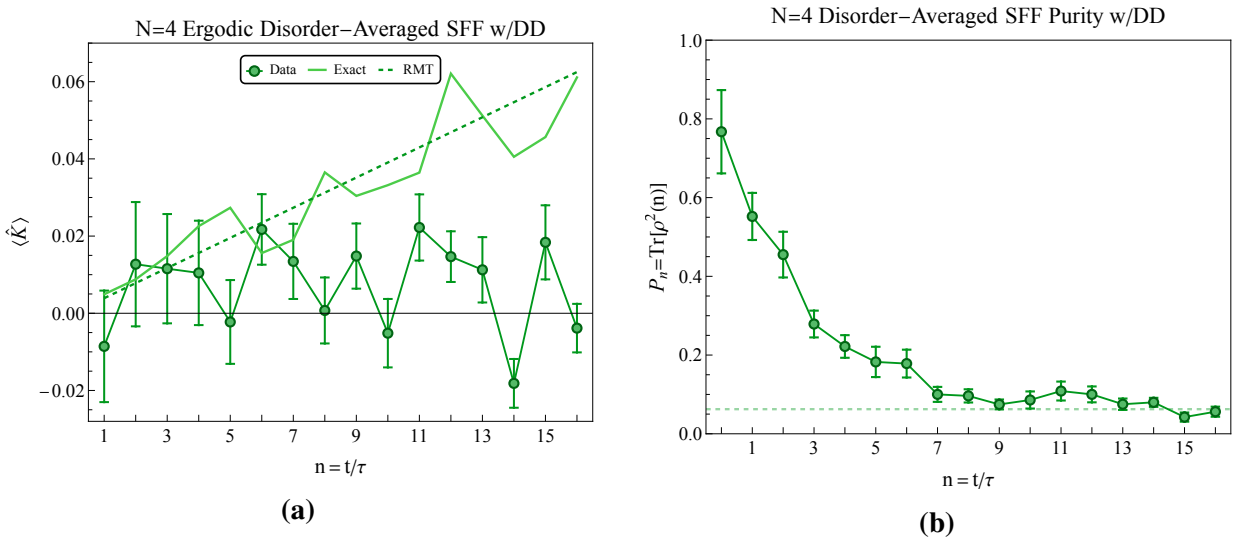


Figure 6.21. $N = 4$ dynamically decoupled results.

which I regret now.

Figure 6.22 shows the raw normalized experimental results for the ergodic disorder-averaged SFF/PSFF estimators for $N = 4$ ions. In total, 213 random sets were sampled, each with 100 experiments per data point. As a result, each data point plotted in Fig. 6.22a corresponds to the ensemble averaged SFF of 213,000 measurements in total. We are able to observe some initial feature of a ramp before decoherence cause the signal to decay, but the ramp feature occurs over two short a timescale to make any claim about quantum chaos. However, however, we cannot claim that this is the SFF of a chaotic system. the rescaling methods proposed by Ref [116], is not a good model for the types of errors that are experiment experience. It would be nice if the decoherence in our system was as simple as a global depolarization error.

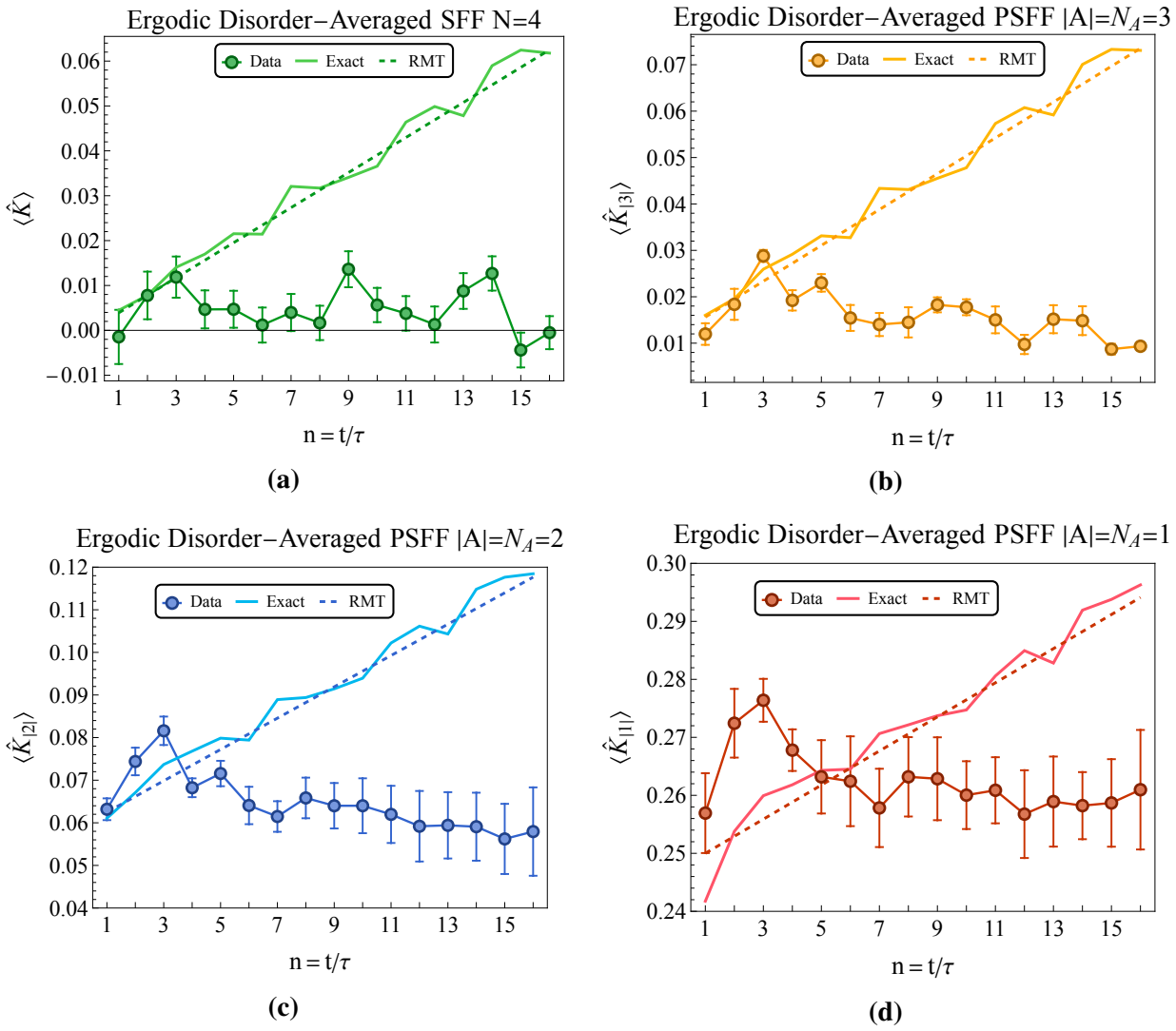


Figure 6.22. $N = 4$ ergodic disorder-averaged average subsystem size PSFF.

Despite not being able to use the rescale methods to correct the data, we still found the purity sequence data useful. The purity sequence provides a good diagnostic tool to examine where decoherence occurs in an experimental sequence. It also can indicate other possible errors such as unwanted off-resonant coupling to the Zeeman levels. Figure 6.23 shows the average SFF purity and the individual ion average fidelity results calculated from the purity sequences that were performed for each of the 213 random sets and measuring 52 RU state overlap sequences, respectively. The decay in the ergodic purity, Fig. 6.23b matches the decay in the ergodic SFF.

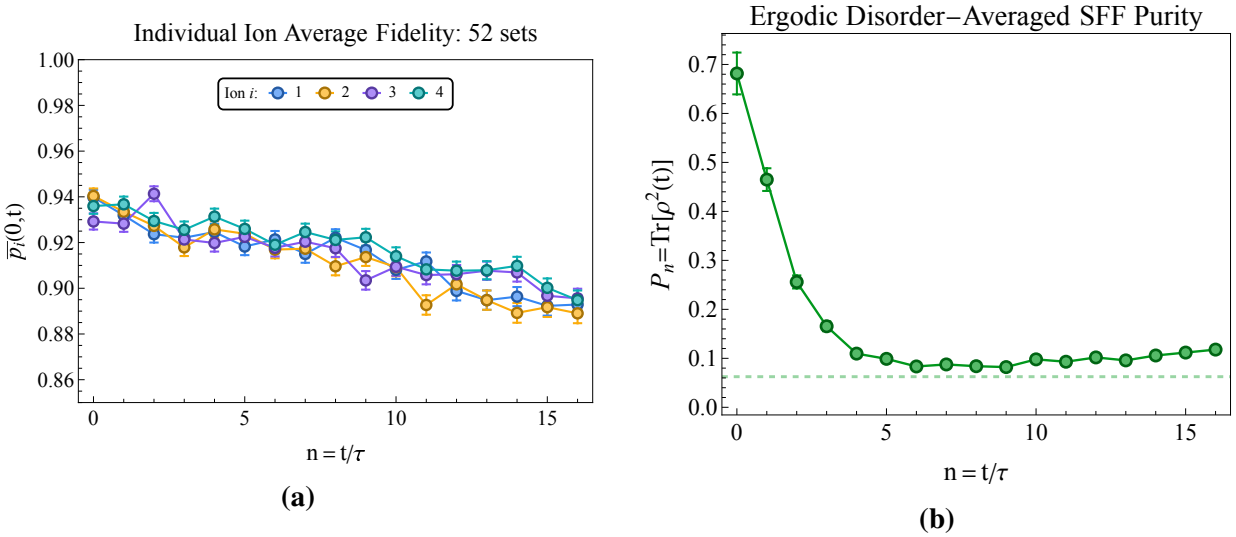


Figure 6.23. $N = 4$ ergodic SFF purity and individual ion average fidelity.

Unfortunately, we are unable to successfully observe a clear ramp feature.

6.8.2 Disorder-Averaged Localized SFF

Figure 6.24 shows the raw normalized experimental results for a localized disorder-averaged SFF and PSFFs for system $\mathcal{S}$ with $N = 4$ ions. From these result, we are able to observe a significantly different behavior in the SFF and PSFFs. This has a tremendous consequence: measuring distinct features of the SFF and PSFF is feasible in current quantum simulators. However, a strong ramp feature is limited by the technical challenges that each individual NISQ era system battles. For the localized disorder-average data only a 100 random sets were sampled and 100 experiments per random set data point were still measured. As a result, each data point in Fig. 6.24a represents the average of 100,000 measurements. The subsystem size PSFF plots are each averaged over all possible unique subsystem combinations within N_A. The error bars in each of the plots represent the standard of the mean while the solid colored lines correspond to the exact PSFF using the experimental parameters and assuming no decoherence.

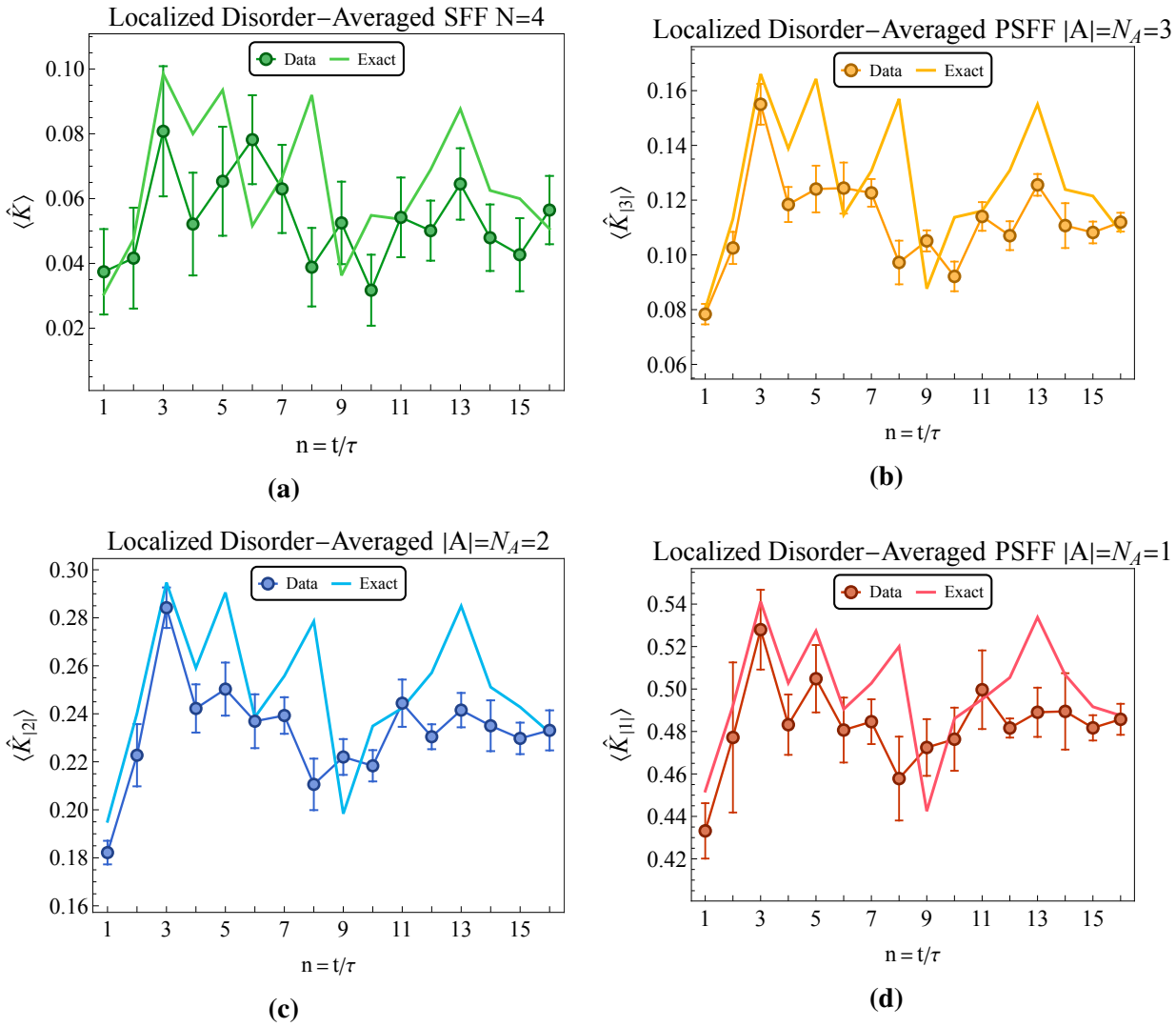


Figure 6.24. $N = 4$ localized disorder-averaged average subsystem size PSFF.

Figure 6.25 shows the raw experimental results for the localized disorder-averaged SFF purity for $N = 4$ ions. The localized purity is consistent with the localized SFF in which we don't observe any fast decay caused by decoherence in comparison to the ergodic system dynamics.

6.8.3 Single-Disorder Localized SFF

Figure 6.26 shows the (raw) normalized experimental SFF and average subsystem size PSFFs for a localized system with a fixed pair of single-disorder sets for $N = 4$ ions. Unlike

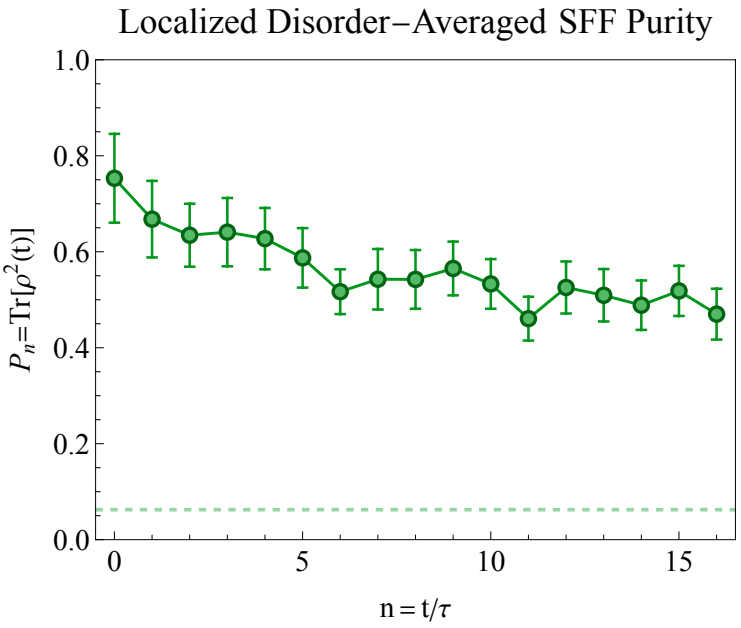


Figure 6.25. $N = 4$ localized disorder-averaged SFF purity.

the previous two SFF measurements, the time-evolution operator T was not sampled, but held fixed. Instead, only the local RUs were changed for each SFF experimental sequence in order to measure a non-disorder averaged SFF and PSFF observables. As observed in each of the plots shown in Fig. 6.26, large oscillations are not "averaged away" and this persistence exemplifies the non-self averaging behavior of the SFF and PSFF observables.

We also ran the corresponding single-disorder purity for each RU instance in which the averaged SFF purity for the single-disorder is displayed in Fig. 6.27. Like the disorder-averaged localized purity, the single-disorder purity does not appear to decay as fast to the fully mixed system value.

6.9 Summary

In this section we aim to summarize the main conclusions that can be drawn from the experimental implementation of the SFF sequence on a trapped-ion quantum simulator. One

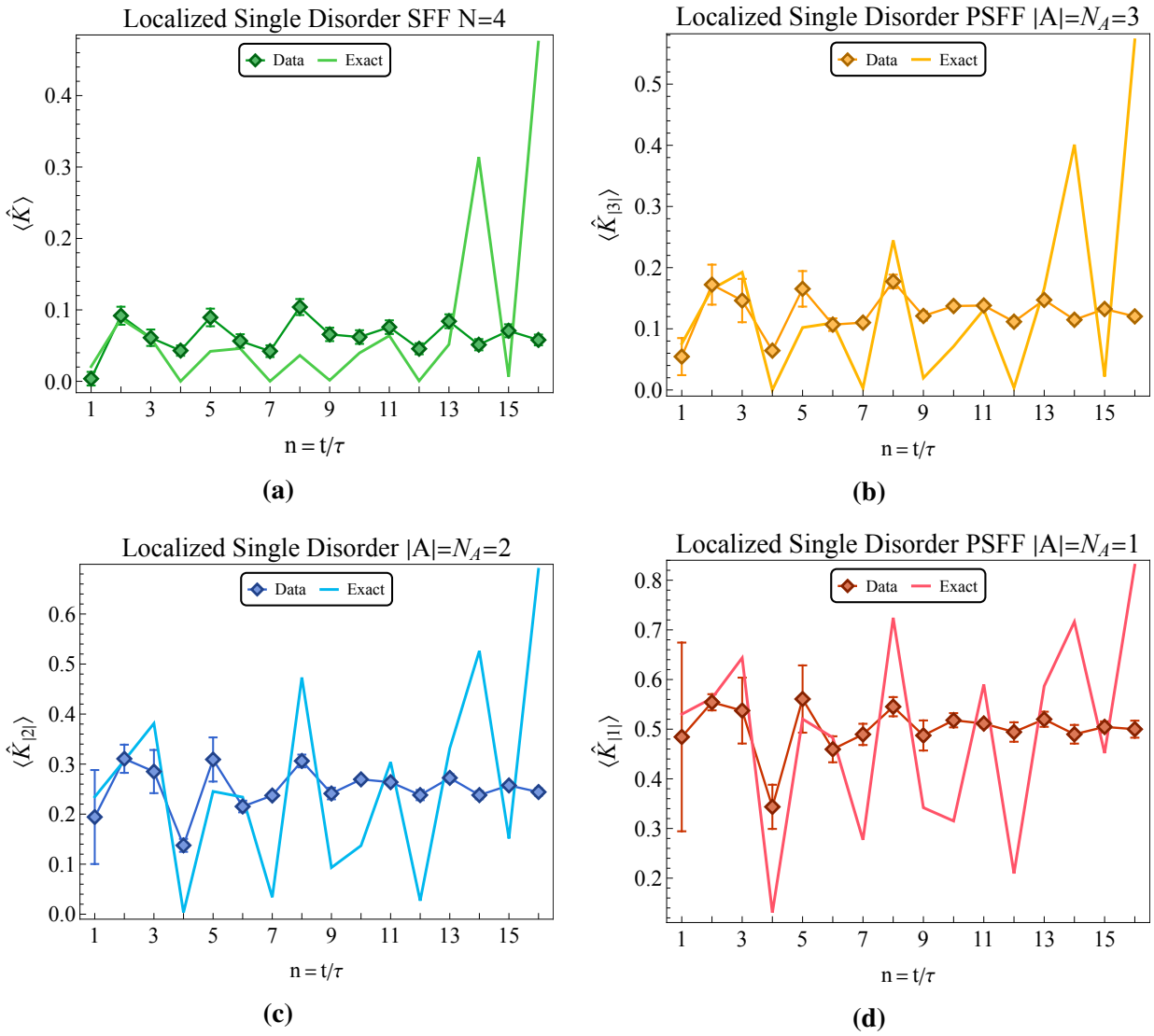


Figure 6.26. $N = 4$ localized single-disorder unitary-averaged average subsystem size PSFF. In comparison to the results shown in Fig. 6.24, non-self averaging oscillations are observed in each subsystem size echoing the dynamics observed in the full SFF.

main result from the SFF project is that we are able to demonstrate the ability to measure the SFF and PSFF observables on a NISQ-era quantum system. The dynamics of the SFF and PSFF are quite different between the ergodic and localized systems.

Unfortunately, the decoherence in our quantum simulator limits our ability to observe a ramp in the chaotic model that we implement. Instead, ergodic dynamics that are outside the chaotic subspace are realized which in fact generalizes the definition of the SFF observable. The

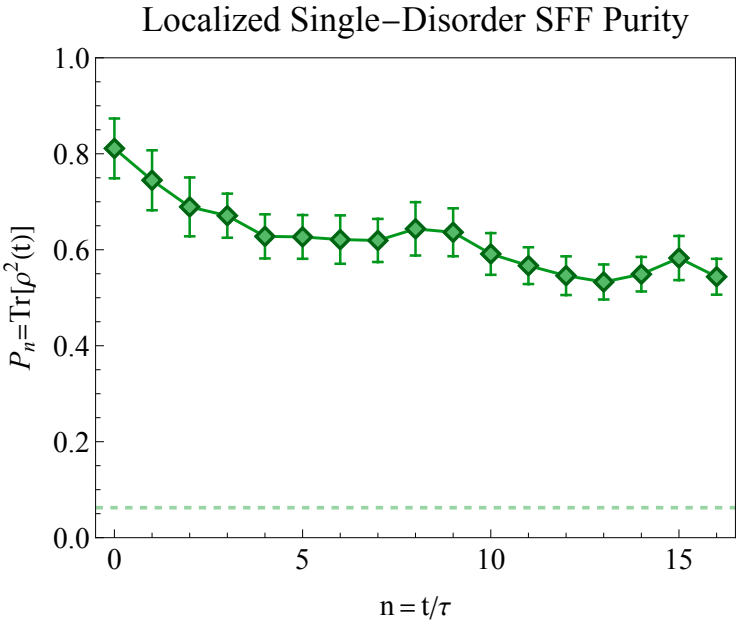


Figure 6.27. $N = 4$ localized single-disorder SFF purity.

SFF observable can be used to measure ergodicity in a quantum system and not just restricted to a chaotic unitary dynamics. The ergodic disorder-averaged SFF and PSFFs are examples of observable-independent signatures of many-body quantum ergodicity.

In comparison, the localized disorder-averaged and single disorder averaged SFFs are able to be measured successfully even with the presence of decoherence in the system. The calculated SFF displays features that are observed in the exact SFF calculated by averaging over the trace of each of the random instances of the time-evolution operator in which measured experimental parameters are used. The non-self averaging behavior of the localized SFF is able to be probed as well.

In realizing the SFF project, the trapped-ion quantum simulator presented in this dissertation utilized "digital" quantum computation techniques along with its traditional "analog" capabilities to simulate "cutting-edge" ideas and topics. Future implementations of the SFF sequence should consider utilizing the dynamical decoupling pulse sequence to extend the coherence of the

target unitary dynamics while suppressing the unwanted slow noise. Combining the method of dynamical decoupling and measuring the spectral form factor enables current quantum simulator platforms to explore even more problems that are currently unanswered.

Bibliography

[1] J. Preskill. "Quantum Computing in the NISQ era and beyond". Quantum **2**, 79 (2018).

[2] A. Kyprianidis. "Simulating Many-Body Quantum Spin Models with Trapped Ions". PhD thesis. University of Maryland, College Park. (2021).

[3] P. M. Becker. "Non-Integrable Dynamics in a Trapped-Ion Quantum Simulator". PhD thesis. University of Maryland, College Park. (2021).

[4] J. E. Sansonetti, W. C. Martin, and S. L. Young. "Atomic Data for Ytterbium (Yb)". In Handbook of Basic Atomic Spectroscopic Data, version 1.1.2. National Institute of Standards and Technology, Gaithersburg, MD (2005).

[5] J. J. Sakurai and J. Napolitano. "Modern Quantum Mechanics". Addison-Wesley. (1994). 2 edition.

[6] C. Foot. "Atomic Physics". Oxford University Press. (2005).

[7] H. J. Metcalf and P. van der Straten. "Laser Cooling and Trapping". Springer. (1999).

[8] P. T. H. Fisk, M. J. Sellars, M. A. Lawn, and G. Coles. "Accurate measurement of the 12.6 GHz "clock" transition in trapped $^{171}Yb^{+}$ ions". IEEE Trans. on Ultrasonics, Ferroelectrics, and Frequency Control **44**, 344–354 (1997).

[9] Chr. Balzer, A. Braun, T. Hannemann, Chr. Paape, M. Ettler, W. Neuhauser, and Chr. Wunderlich. "Electrodynamically trapped Yb^{+} ions for quantum information processing". Phys. Rev. A **73**, 041407 (2006).

[10] S. Olmschenk, K. C. Younge, D. L. Moehring, D. N. Matsukevich, P. Maunz, and C. Monroe. "Manipulation and detection of a trapped Yb^{+} hyperfine qubit". Phys. Rev. A **76**, 052314 (2007).

[11] N. Yu and L. Maleki. "Lifetime measurements of the $4f^{14}5d$ metastable states in single ytterbium ions". Phys. Rev. A **61**, 022507 (2000).

[12] S. Olmschenk, D. Hayes, D. N. Matsukevich, P. Maunz, D. L. Moehring, K. C. Younge, and C. Monroe. "Measurement of the lifetime of the $6p\ ^2P^o_{1/2}$ level of Yb^{+}". Phys. Rev. A **80**, 022502 (2009).

[13] A. S. Bell, P. Gill, H. A. Klein, A. P. Levick, Chr. Tamm, and D. Schnier. "Laser cooling of trapped ytterbium ions using a four-level optical-excitation scheme". Phys. Rev. A **44**, R20–R23 (1991).

[14] R. W. Berends, E. H. Pinnington, B. Guo, and Q. Ji. "Beam-laser lifetime measurements for four resonance levels of Yb II". J. Phys. B: At. Mol. Opt. Phys. **26**, L701 (1993).

[15] E. Biémont, J.-F. Dutrieux, I. Martin, and P. Quinet. "Lifetime calculations in Yb II". J. Phys. B: At. Mol. Opt. Phys. **31**, 3321 (1998).

[16] D. J. Wineland and W. M. Itano. "Laser cooling of atoms". Phys. Rev. A **20**, 1521–1540 (1979).

[17] W. M. Itano and D. J. Wineland. "Laser cooling of ions stored in harmonic and Penning traps". Phys. Rev. A **25**, 35–54 (1982).

[18] D. J. Berkeland and M. G. Boshier. "Destabilization of dark states and optical spectroscopy in Zeeman-degenerate atomic systems". Phys. Rev. A **65**, 033413 (2002).

[19] R. W. P. Drever, J. L. Hall, F. V. Kowalski, J. Hough, G. M. Ford, A. J. Munley, and H. Ward. "Laser phase and frequency stabilization using an optical resonator". Appl. Phys. B **31**, 97–105 (1983).

[20] E. D. Black. "An introduction to Pound–Drever–Hall laser frequency stabilization". Am. J. Phys. **69**, 79–87 (2001).

[21] S. Olmschenk. "Quantum Teleportation Between Distance Matter Qubits". PhD thesis. University of Michigan. (2009).

[22] J. A. Mizrahi. "Ultrafast Control of Spin and Motion in Trapped Ions". PhD thesis. University of Maryland, College Park. (2013).

[23] A. Chew. "Doppler-Free Spectroscopy of Iodine at 739nm". BS thesis, University of Michigan. (2008).

[24] S. Gerstenkorn, J. Verges, and J. Chevillard. "Atlas du Spectre d'Asorption de la Molecule d'Iode, 11000–14000 cm^{-1}". Laboratoire Aime-Cotton, CNRS II, 91405 Orsay, France. (1982).

[25] K. R. Islam. "Quantum Simulation of Interacting Spin Models with Trapped Ions". PhD thesis. University of Maryland, College Park. (2012).

[26] J. D. Jackson. "Classical Electrodynamics". Wiley. (1999). 3 edition.

[27] C. Monroe, W. C. Campbell, L. M. Duan, Z.-X. Gong, A. V. Gorshkov, P. W. Hess, R. Islam, K. Kim, N. M. Linke, G. Pagano, P. Richerme, C. Senko, and N. Y. Yao. "Programmable quantum simulations of spin systems with trapped ions". Rev. Mod. Phys. **93**, 025001 (2021).

[28] W. Paul. "Electromagnetic traps for charges and neutral particles". Rev. Mod. Phys. **62**, 531–540 (1990).

[29] H. G. Dehmel. "Radiofrequency Spectroscopy of Stored Ions I: Storage". In D. R. Bates and I. Estermann, editors, Advances in Atomic and Molecular Physics. Volume 3, pages 53–72. Academic Press (1968).

[30] M. Madsen. "Advanced Ion Trap Development and Ultrafast Laser-Ion Interactions". PhD thesis. University of Michigan. (2006).

[31] J. Smith. "Quantum Thermalization and Localization in a Trapped Ion Quantum Simulator". PhD thesis. University of Maryland, College Park. (2016).

[32] C. R. Senko. "Dynamics and Excited States of Quantum Many-Body Spin Chains with Trapped Ions". PhD thesis. University of Maryland, College Park. (2014).

[33] D. J. Wineland, C. Monroe, W. M. Itano, D. Leibfried, B. E. King, and D. M. Meekhof. "Experimental Issues in Coherent Quantum-State Manipulation of Trapped Atomic Ions". J. Res. Nat. Inst. Stand. Technol. **103**, 259–328 (1998).

[34] A. Sørensen and K. Mølmer. "Quantum Computation with Ions in Thermal Motion". Phys. Rev. Lett. **82**, 1971–1974 (1999).

[35] A. C. Lee, J. Smith, P. Richerme, B. Neyenhuis, P. W. Hess, J. Zhang, and C. Monroe. "Engineering large Stark shifts for control of individual clock state qubits". Phys. Rev. A **94**, 042308 (2016).

[36] W. Morong, F. Liu, P. Becker, K. S. Collins, L. Feng, A. Kyprianidis, G. Pagano, T. You, A. V. Gorshkov, and C. Monroe. "Observation of Stark many-body localization without disorder". Nature **599**, 393–398 (2021).

[37] J. Smith, A. Lee, P. Richerme, B. Neyenhuis, P. W. Hess, P. Hauke, M. Heyl, D. A. Huse, and C. Monroe. "Many-body localization in a quantum simulator with programmable random disorder". Nat. Phys. **12**, 907–911 (2016).

[38] R. Islam, W. C. Campbell, T. Choi, S. M. Clark, C. W. S. Conover, S. Debnath, E. E. Edwards, B. Fields, D. Hayes, D. Hucul, I. V. Inlek, K. G. Johnson, S. Korenblit, A. Lee, K. W. Lee, T. A. Manning, D. N. Matsukevich, J. Mizrahi, Q. Quraishi, C. Senko, J. Smith, and C. Monroe. "Beat note stabilization of mode-locked lasers for quantum information processing". Opt. Lett. **39**, 3238–3241 (2014).

[39] B. Canuel, E. Genin, M. Mantovani, J. Marque, P. Ruggi, and M. Tacca. "Sub-nanoradiant beam pointing monitoring and stabilization system for controlling input beam jitter in gravitational wave interferometers". Appl. Opt. **53**, 2906–2916 (2014).

[40] G. Pagano, P. W. Hess, H. B. Kaplan, W. L. Tan, P. Richerme, P. Becker, A. Kyprianidis, J. Zhang, E. Birckelbaw, M. R. Hernandez, Y. Wu, and C. Monroe. "Cryogenic trapped-ion system for large scale quantum simulation". Quantum Science and Technology **4**, 014004 (2018).

[41] W. L. Tan. "Cryogenic Trapped-Ion System for Large Scale Quantum Simulation". PhD thesis. University of Maryland, College Park. (2021).

[42] G. Pagano, A. Bapat, P. Becker, K. S. Collins, A. De, P. W. Hess, H. B. Kaplan, A. Kyprianidis, W. L. Tan, C. Baldwin, L. T. Brady, A. Deshpande, F. Liu, S. Jordan, A. V. Gorshkov, and C. Monroe. "Quantum approximate optimization of the long-range Ising model with a trapped-ion quantum simulator". Proc. Natl. Acad. of Sci. USA **117**, 25396–25401 (2020).

[43] E. Farhi, J. Goldstone, S. Gutmann, and M. Sipser. "Quantum Computation by Adiabatic Evolution" (2000). arXiv:quant-ph/0001106.

[44] P. Richerme, C. Senko, J. Smith, A. Lee, S. Korenblit, and C. Monroe. "Experimental performance of a quantum simulator: Optimizing adiabatic evolution and identifying many-body ground states". Phys. Rev. A **88**, 012334 (2013).

[45] E. Farhi, J. Goldstone, and S. Gutmann. "A Quantum Approximate Optimization Algorithm" (2014). arXiv:1411.4028.

[46] Y. Nam, JS. Chen, N. C. Pisenti, K. Wright, C. Delaney, D. Maslov, K. R. Brown, S. Allen, J. M. Amini, J. Apisdorf, K. M. Beck, A. Blinov, V. Chaplin, M. Chmielewski, C. Collins, S. Debnath, K. M. Hudek, A. M. Ducore, M. Keesan, S. M. Kreikemeier, J. Mizrahi, P. Solomon, M. Williams, J. D. Wong-Campos, D. Moehring, C. Monroe, and J. Kim. "Ground-state energy estimation of the water molecule on a trapped-ion quantum computer". npj Quantum Information **6**, 33 (2020).

[47] W. W. Ho and T. H. Hsieh. "Efficient variational simulation of non-trivial quantum states". SciPost Phys. **6**, 29 (2019).

[48] T. Koffel, M. Lewenstein, and L. Tagliacozzo. "Entanglement Entropy for the Long-Range Ising Chain in a Transverse Field". Phys. Rev. Lett. **109**, 267203 (2012).

[49] K. Kim, M.-S. Chang, R. Islam, S. Korenblit, L.-M. Duan, and C. Monroe. "Entanglement and Tunable Spin-Spin Couplings between Trapped Ions Using Multiple Transverse Modes". Phys. Rev. Lett. **103**, 120502 (2009).

[50] D. Dylewsky, J. K. Freericks, M. L. Wall, A. M. Rey, and M. Foss-Feig. "Nonperturbative calculation of phonon effects on spin squeezing". Phys. Rev. A **93**, 013415 (2016).

[51] S. Hadfield. "Quantum Algorithms for Scientific Computing and Approximate Optimization" (2018). arXiv:1805.03265.

[52] S. Jordan and A. Bapat. "Simulator and data analysis tools for Quantum Approximate Optimization Algorithm and Variational Quantum Eigensolvers" (2018). *2local-qaoa_VAR.h*, *2local-qaoa_VAR.c*.

[53] A. Bapat. "A python helper library for QAOA-type optimization" (2018). *qaoaLibrary_VAR.py*.

[54] E. Farhi and A. W. Harrow. "Quantum Supremacy through the Quantum Approximate Optimization Algorithm" (2016). arXiv:1602.07674.

[55] M. J. Bremner, A. Montanaro, and D. J. Shepherd. "Average-Case Complexity Versus Approximate Simulation of Commuting Quantum Computations". Phys. Rev. Lett. **117**, 080501 (2016).

[56] A. Bouland, B. Fefferman, C. Nirkhe, and U. Vazirani. "On the complexity and verification of quantum random circuit sampling". Nat. Phys. **15**, 159–163 (2019).

[57] S.-T. Wang and L.-M. Duan. "Certification of Boson Sampling Devices with Coarse-Grained Measurements" (2016). arXiv:1601.02627.

[58] A. Kandala, A. Mezzacapo, K. Temme, M. Takita, M. Brink, J. M. Chow, and J. M. Gambetta. "Hardware-efficient variational quantum eigensolver for small molecules and quantum magnets.". Nature **549**, 242–246 (2017).

[59] C. Hempel, C. Maier, J. Romero, J. McClean, T. Monz, H. Shen, P. Jurcevic, B. P. Lanyon, P. Love, R. Babbush, A. Aspuru-Guzik, R. Blatt, and C. F. Roos. "Quantum Chemistry Calculations on a Trapped-Ion Quantum Simulator". Phys. Rev. X **8**, 031022 (2018).

[60] J. S. Otterbach, R. Manenti, N. Alidoust, A. Bestwick, M. Block, B. Bloom, S. Caldwell, N. Didier, E. Schuyler Fried, S. Hong, P. Karalekas, C. B. Osborn, A. Papageorge, E. C. Peterson, G. Prawiroatmodjo, N. Rubin, C. A. Ryan, D. Scarabelli, M. Scheer, E. A. Sete, P. Sivarajah, R. S. Smith, A. Staley, N. Tezak, W. J. Zeng, A. Hudson, B. R. Johnson, M. Reagor, M. P. da Silva, and C. Rigetti. "Unsupervised Machine Learning on a Hybrid Quantum Computer" (2017). arXiv:1712.05771.

[61] E. Farhi, J. Goldstone, S. Gutmann, J. Lapan, A. Lundgren, and D. Preda. "A Quantum Adiabatic Evolution Algorithm Applied to Random Instances of an NP-Complete Problem". Science **292**, 472–475 (2001).

[62] V. Giovannetti, S. Lloyd, and L. Maccone. "Advances in quantum metrology". Nat. Photon. **5**, 222–229 (2011).

[63] W. Morong, K. S. Collins, A. De, E. Stavropoulos, T. You, and C. Monroe. "Engineering Dynamically Decoupled Quantum Simulations with Trapped Ions". PRX Quantum **4**, 010334 (2023).

[64] E. L. Hahn. "Spin Echoes". Phys. Rev. **80**, 580–594 (1950).

[65] A. M. Souza, G. A. Álvarez, and D. Suter. "Robust dynamical decoupling". Philos. Trans. R. Soc. A: Math., Phys. Eng. Sci. **370**, 4748–4769 (2012).

[66] L. Viola, S. Lloyd, and E. Knill. "Universal Control of Decoupled Quantum Systems". Phys. Rev. Lett. **83**, 4888–4891 (1999).

[67] M. J. Biercuk, H. Uys, A. P. VanDevender, N. Shiga, W. M. Itano, and J. J. Bollinger. "Optimized dynamical decoupling in a model quantum memory". Nature **458**, 996–1000 (2009).

[68] D. J. Szwer, S. C. Webster, A. M. Steane, and D. M. Lucas. "Keeping a single qubit alive by experimental dynamic decoupling". J. Phys. B: At. Mol. Opt. Phys. **44**, 025501 (2010).

[69] G. de Lange, Z. H. Wang, D. Ristè, V. V. Dobrovitski, and R. Hanson. "Universal Dynamical Decoupling of a Single Solid-State Spin from a Spin Bath". Science **330**, 60–63 (2010).

[70] B. Pokharel, N. Anand, B. Fortman, and D. A. Lidar. "Demonstration of Fidelity Improvement Using Dynamical Decoupling with Superconducting Qubits". Phys. Rev. Lett. **121**, 220502 (2018).

[71] P. Wang, C.-Y. Luan, M. Qiao, M. Um, J. Zhang, Y. Wang, X. Yuan, M. Gu, J. Zhang, and K. Kim. "Single ion qubit with estimated coherence time exceeding one hour". Nat. Commun. **12**, 233 (2021).

[72] H. Y. Carr and E. M. Purcell. "Effects of Diffusion on Free Precession in Nuclear Magnetic Resonance Experiments". Phys. Rev. **94**, 630–638 (1954).

[73] U. Haeberlen and J. S. Waugh. "Coherent Averaging Effects in Magnetic Resonance". Phys. Rev. **175**, 453–467 (1968).

[74] M. M. Maricq. "Application of average Hamiltonian theory to the NMR of solids". Phys. Rev. B **25**, 6622–6632 (1982).

[75] A. Brinkmann. "Introduction to average Hamiltonian theory. I. Basics". Concepts in Magn. Reson. Part A **45A**, e21414 (2016).

[76] W. Magnus. "On the exponential solution of differential equations for a linear operator". Communications on Pure and Applied Mathematics **7**, 649–673 (1954).

[77] T. Kuwahara, T. Mori, and K. Saito. "Floquet–Magnus theory and generic transient dynamics in periodically driven many-body quantum systems". Annals of Physics **367**, 96–124 (2016).

[78] J. Choi, H. Zhou, H. S. Knowles, R. Landig, S. Choi, and M. D. Lukin. "Robust dynamic hamiltonian engineering of many-body spin systems". Phys. Rev. X **10**, 031002 (2020).

[79] S. Geier, N. Thaicharoen, C. Hainaut, T. Franz, A. Salzinger, A. Tebben, D. Grimshandl, G. Zürn, and M. Weidemüller. "Floquet hamiltonian engineering of an isolated many-body spin system". Science **374**, 1149–1152 (2021).

[80] P. Scholl, H. J. Williams, G. Bornet, F. Wallner, D. Barredo, L. Henriet, A. Signoles, C. Hainaut, T. Franz, S. Geier, A. Tebben, A. Salzinger, G. Zürn, T. Lahaye, M. Weidemüller, and A. Browaeys. "Microwave Engineering of Programmable xxz Hamiltonians in Arrays of Rydberg Atoms". PRX Quantum **3**, 020303 (2022).

[81] F. Kranzl, A. Lasek, M. K. Joshi, A. Kalev, R. Blatt, C. F. Roos, and N. Yunger Halpern. "Experimental Observation of Thermalization with Noncommuting Charges". PRX Quantum **4**, 020318 (2023).

[82] N. Hatano and M. Suzuki. "Finding Exponential Product Formulas of Higher Orders". In Quantum Annealing and Other Optimization Methods. Pages 37–68. Springer Berlin Heidelberg (2005).

[83] A. M. Childs, Y. Su, M. C. Tran, N. Wiebe, and S. Zhu. "Theory of Trotter Error with Commutator Scaling". Phys. Rev. X **11**, 011020 (2021).

[84] A. Sørensen and K. Mølmer. "Entanglement and quantum computation with ions in thermal motion". Phys. Rev. A **62**, 022311 (2000).

[85] J. Zhang, P. W. Hess, A. Kyprianidis, P. Becker, A. Lee, J. Smith, G. Pagano, I.-D. Potirniche, A. C. Potter, A. Vishwanath, N. Y. Yao, and C. Monroe. "Observation of a discrete time crystal". Nature **543**, 217–220 (2017).

[86] C. Hempel. "Digital quantum simulation, Schrödinger cat state spectroscopy and setting up a linear ion trap". PhD thesis. University of Innsbruck. (2014).

[87] A. Kyprianidis, F. Machado, W. Morong, P. Becker, K. S. Collins, D. V. Else, L. Feng, P. W. Hess, C. Nayak, G. Pagano, N. Y. Yao, and C. Monroe. "Observation of a prethermal discrete time crystal". Science **372**, 1192–1196 (2021).

[88] K. R. Brown, A. W. Harrow, and I. L. Chuang. "Arbitrarily accurate composite pulse sequences". Phys. Rev. A **70**, 052318 (2004).

[89] W. L. Tan, P. Becker, F. Liu, G. Pagano, K. S. Collins, A. De, L. Feng, H. B. Kaplan, A. Kyprianidis, R. Lundgren, W. Morong, S. Whitsitt, A. V. Gorshkov, and C. Monroe. "Domain-wall confinement and dynamics in a quantum simulator". Nat. Phys. **17**, 742–747 (2021).

[90] F. D. M. Haldane. "Exact Jastrow-Gutzwiller resonating-valence-bond ground state of the spin-(1/2 antiferromagnetic Heisenberg chain with $1/r^2$ exchange". Phys. Rev. Lett. **60**, 635–638 (1988).

[91] B. S. Shastry. "Exact solution of an S=1/2 Heisenberg antiferromagnetic chain with long-ranged interactions". Phys. Rev. Lett. **60**, 639–642 (1988).

[92] M. Greiter, F. D. M. Haldane, and R. Thomale. "Non-Abelian statistics in one dimension: Topological momentum spacings and SU(2) level-k fusion rules". Phys. Rev. B **100**, 115107 (2019).

[93] T. Graß and M. Lewenstein. "Trapped-ion quantum simulation of tunable-range Heisenberg chains". EPJ Quantum Technology **1**, 8 (2014).

[94] A. Bermudez, L. Tagliacozzo, G. Sierra, and P. Richerme. "Long-range Heisenberg models in quasiperiodically driven crystals of trapped ions". Phys. Rev. B **95**, 024431 (2017).

[95] S. Birnkammer, A. Bohrdt, F. Grusdt, and M. Knap. "Characterizing topological excitations of a long-range Heisenberg model with trapped ions". Phys. Rev. B **105**, L241103 (2022).

[96] C. L. Hung, A. González-Tudela, J. Ignacio Cirac, and H. J. Kimble. "Quantum spin dynamics with pairwise-tunable, long-range interactions". Proc. Natl. Acad. Sci. USA **113**, E4946–E4955 (2016).

[97] B. D. Simons and B. L. Altshuler. "Exact ground state of an open S=1/2 long-range Heisenberg antiferromagnetic spin chain". Phys. Rev. B **50**, 1102–1105 (1994).

[98] D. Bernard, V. Pasquier, and D. Serban. "Exact Solution of Long-Range Interacting Spin Chains with Boundaries". Europhys. Lett. (EPL) **30**, 301–306 (1995).

[99] O. A. Castro-Alvaredo, B. Doyon, and T. Yoshimura. "Emergent Hydrodynamics in Integrable Quantum Systems Out of Equilibrium". Phys. Rev. X **6**, 041065 (2016).

[100] K. Mallayya, M. Rigol, and W. De Roeck. "Prethermalization and Thermalization in Isolated Quantum Systems". Phys. Rev. X **9**, 21027 (2019).

[101] J. Lopez-Piqueres, B. Ware, S. Gopalakrishnan, and R. Vasseur. "Hydrodynamics of nonintegrable systems from a relaxation-time approximation". Phys. Rev. B **103**, L060302 (2021).

[102] N. M. Myers, J. McCready, and S. Deffner. "Quantum Heat Engines with Singular Interactions". Symmetry **13**, 978 (2021).

[103] P. N. Jepsen, J. Amato-Grill, I. Dimitrova, W. W. Ho, E. Demler, and W. Ketterle. "Spin transport in a tunable Heisenberg model realized with ultracold atoms". Nature **588**, 403–407 (2020).

[104] D. Bluvstein, A. Omran, H. Levine, A. Keesling, G. Semeghini, S. Ebadi, T. T. Wang, A. A. Michailidis, N. Maskara, W. W. Ho, S. Choi, M. Serbyn, M. Greiner, V. Vuletić, and M. D. Lukin. "Controlling quantum many-body dynamics in driven Rydberg atom arrays". Science **371**, 1355–1359 (2021).

[105] A. Periwal, E. S. Cooper, P. Kunkel, J. F. Wienand, E. J. Davis, and M. Schleier-Smith. "Programmable interactions and emergent geometry in an array of atom clouds". Nature **600**, 630–635 (2021).

[106] K. Xu, J.-J. Chen, Yu Zeng, Y.-R. Zhang, C. Song, W. Liu, Q. Guo, P. Zhang, D. Xu, H. Deng, K. Huang, H. Wang, X. Zhu, D. Zheng, and H. Fan. "Emulating Many-Body Localization with a Superconducting Quantum Processor". Phys. Rev. Lett. **120**, 050507 (2018).

[107] H. Frydrych and G. Alber and P. Bažant. "Constructing Pauli pulse schemes for decoupling and quantum simulation". Phys. Rev. A **89**, 022320 (2014).

[108] D. Hayes, S. T. Flammia, and M. J. Biercuk. "Programmable quantum simulation by dynamic Hamiltonian engineering". New J. of Phys. **16**, 083027 (2014).

[109] L. Egan. "Scaling Quantum Computers with Long Chains of Trapped Ions". PhD thesis. University of Maryland, College Park. (2021).

[110] M. Cetina, L. N. Egan, C. Noel, M. L. Goldman, D. Biswas, A. R. Risinger, D. Zhu, and C. Monroe. "Control of Transverse Motion for Quantum Gates on Individually Addressed Atomic Qubits". PRX Quantum **3**, 010334 (2022).

[111] C. Monroe, R. Raussendorf, A. Ruthven, K. R. Brown, P. Maunz, L.-M. Duan, and J. Kim. "Large-scale modular quantum-computer architecture with atomic memory and photonic interconnects". Phys. Rev. A **89**, 022317 (2014).

[112] M. K. Joshi, F. Kranzl, A. Schuckert, I. Lovas, C. Maier, R. Blatt, M. Knap, and C. F. Roos. "Observing emergent hydrodynamics in a long-range quantum magnet". Science **376**, 720–724 (2022).

[113] S. Flannigan, N. Pearson, G. H. Low, A. Buyskikh, I. Bloch, P. Zoller, M. Troyer, and A. J. Daley. "Propagation of errors and quantitative quantum simulation with quantum advantage" (2022). arXiv:2204.13644.

[114] F. Haake. "Quantum signature of chaos". Springer Series in Synergetics. Springer. (2010).

[115] R. E. Prange. "The Spectral Form Factor Is Not Self-Averaging". Phys. Rev. Lett. **78**, 2280–2283 (1997).

[116] L. Kh Joshi, A. Elben, A. Vikram, B. Vermersch, V. Galitski, and P. Zoller. "Probing Many-Body Quantum Chaos with Quantum Simulators". Phys. Rev. X **12**, 011018 (2022).

[117] D. V. Vasilyev, A. Grankin, M. A. Baranov, L. M. Sieberer, and P. Zoller. "Monitoring Quantum Simulators via Quantum Nondemolition Couplings to Atomic Clock Qubits". PRX Quantum **1**, 020302 (2020).

[118] H. Gharibyan, M. Hanada, S. H. Shenker, and M. Tezuka. "Onset of random matrix behavior in scrambling systems". Journal of High Energy Physics**2018** (2018).

[119] L. Leviandier, M. Lombardi, R. Jost, and J. P. Pique. "Fourier Transform: A Tool to Measure Statistical Level Properties in Very Complex Spectra". Phys. Rev. Lett. **56**, 2449–2452 (1986).

[120] M. L. Mehta. "Random matrices". Elsevier. (2004).

[121] T. Guhr, A. Müller–Groeling, and H. A. Weidenmüller. "Random-matrix theories in quantum physics: common concepts". Physics Reports **299**, 189–425 (1998).

[122] R. Nandkishore and D. A. Huse. "Many-Body Localization and Thermalization in Quantum Statistical Mechanics". Annu. Rev. Condens. Matter Phys. **6**, 15–38 (2015).

[123] M. V. Berry and M. Tabor. "Level clustering in the regular spectrum". Proc. R. Soc. A. **356**, 375–394 (1977).

[124] P. Ponte, A. Chandran, Z. Papić, and D. A. Abanin. "Periodically driven ergodic and many-body localized quantum systems". Ann. Phys. **353**, 196–204 (2015).

[125] A. Prakash, J. H. Pixley, and M. Kulkarni. "Universal spectral form factor for many-body localization". Phys. Rev. Res. **3**, L012019 (2021).

[126] E. P. Wigner. "Characteristic Vectors of Bordered Matrices With Infinite Dimensions". Ann. Math. **62**, 548–564 (1955).

[127] F. J. Dyson. "Statistical Theory of the Energy Levels of Complex Systems. I.". J. Math. Phys. **3**, 140–156 (1962).

[128] G. Casati, F. Valz-Gris, and I. Guarnieri. "On the connection between quantization of nonintegrable systems and statistical theory of spectra". Lettere al Nuovo Cimento **28**, 279–282 (1980).

[129] O. Bohigas, M. J. Giannoni, and C. Schmit. "Characterization of Chaotic Quantum Spectra and Universality of Level Fluctuation Laws". Phys. Rev. Lett. **52**, 1–4 (1984).

[130] J. M. Deutsch. "Quantum statistical mechanics in a closed system". Phys. Rev. A **43**, 2046–2049 (1991).

[131] M. Srednicki. "Chaos and quantum thermalization". Phys. Rev. E **50**, 888–901 (1994).

[132] M. Srednicki. "The approach to thermal equilibrium in quantized chaotic systems". J. Phys. A **32**, 1163 (1999).

[133] M. Rigol, V. Dunjko, and M. Olshanii=. "Thermalization and its mechanism for generic isolated quantum systems". Nature **452**, 854–858 (2008).

[134] L. D'Alessio, Y. Kafri, A. Polkovnikov, and M. Rigol. "From quantum chaos and eigenstate thermalization to statistical mechanics and thermodynamics". Adv. Phys. **65**, 239–362 (2016).

[135] J. M. Deutsch. "Eigenstate thermalization hypothesis". Rep. Prog. Phys. **81**, 082001 (2018).

[136] A. Dymarsky, N. Lashkari, and H. Liu. "Subsystem eigenstate thermalization hypothesis". Phys. Rev. E **97**, 012140 (2018).

[137] D. A. Abanin, E. Altman, I. Bloch, and M. Serbyn. "Colloquium: Many-body localization, thermalization, and entanglement". Rev. Mod. Phys. **91**, 021001 (2019).

[138] A. Elben, S. T. Flammia, H.-Y. Huang, R. Kueng, J. Preskill, B. Vermersch, and P. Zoller. "The randomized measurement toolbox". Nat. Rev. Phys. **5**, 9–24 (2023).

[139] T. Brydges, A. Elben, P. Jurcevic, B. Vermersch, C. Maier, B. P. Lanyon, P. Zoller, R. Blatt, and C. F. Roos. "Probing Rényi entanglement entropy via randomized measurements". Science **364**, 260–263 (2019).

[140] S. J. van Enk and C. W. J. Beenakker. "Measuring $\mathrm{Tr}\rho^n$ on Single Copies of ρ Using Random Measurements". Phys. Rev. Lett. **108**, 110503 (2012).

[141] A. Elben, B. Vermersch, M. Dalmonte, J. I. Cirac, and P. Zoller. "Rényi Entropies from Random Quenches in Atomic Hubbard and Spin Models". Phys. Rev. Lett. **120**, 050406 (2018).

[142] B. Vermersch, A. Elben, M. Dalmonte, J. I. Cirac, and P. Zoller. "Unitary n-designs via random quenches in atomic Hubbard and spin models: Application to the measurement of Rényi entropies". Phys. Rev. A **97**, 023604 (2018).

[143] M. Nielsen and I. Chuang. "Quantum Computation and Quantum Information: 10th Anniversary Edition". Cambridge University Press. (2010). 10 edition.

[144] Wolfram Research. "RandomReal". `https://reference.wolfram.com/language/ref/RandomReal.html` (2007). [version 13.0].

[145] E. W. Weisstein. "Sphere Point Picking". Accessed Mar. 22, 2023 [Online] `https://mathworld.wolfram.com/SpherePointPicking.html`.